

**Titre:** Oxygen Reduction Reaction (ORR) on Mixed Oxy-Nitride Non-Noble  
Catalyst: AB-Initio Simulation, Elaboration and Characterization

**Auteur:** Ali Seifitokaldani  
Author:

**Date:** 2014

**Type:** Mémoire ou thèse / Dissertation or Thesis

**Référence:** Seifitokaldani, A. (2014). Oxygen Reduction Reaction (ORR) on Mixed Oxy-Nitride  
Non-Noble Catalyst: AB-Initio Simulation, Elaboration and Characterization [Thèse  
de doctorat, École Polytechnique de Montréal]. PolyPublie.  
Citation: <https://publications.polymtl.ca/1375/>

 **Document en libre accès dans PolyPublie**  
Open Access document in PolyPublie

**URL de PolyPublie:** <https://publications.polymtl.ca/1375/>  
PolyPublie URL:

**Directeurs de  
recherche:** Oumarou Savadogo, & Michel Perrier  
Advisors:

**Programme:** Génie chimique  
Program:

UNIVERSITÉ DE MONTRÉAL

OXYGEN REDUCTION REACTION (ORR)  
ON MIXED OXY-NITRIDE NON-NOBLE CATALYST:  
AB-INITIO SIMULATION, ELABORATION AND CHARACTERIZATION

ALI SEIFITOKALDANI

DÉPARTEMENT DE GÉNIE CHIMIQUE  
ÉCOLE POLYTECHNIQUE DE MONTRÉAL

THÈSE PRÉSENTÉE EN VUE DE L'OBTENTION  
DU DIPLÔME DE PHILOSOPHIAE DOCTOR  
(GÉNIE CHIMIQUE)

AVRIL 2014

UNIVERSITÉ DE MONTRÉAL

ÉCOLE POLYTECHNIQUE DE MONTRÉAL

Cette thèse intitulée:

OXYGEN REDUCTION REACTION (ORR)

ON MIXED OXY-NITRIDE NON-NOBLE CATALYST:

AB-INITIO SIMULATION, ELABORATION AND CHARACTERIZATION

présentée par : SEIFITOKALDANI Ali

en vue de l'obtention du diplôme de : Philosophiae Doctor

a été dûment acceptée par le jury d'examen constitué de :

Mme. DESCHÈNES Louise, Ph.D. , président

M. SAVADOGO Oumarou, D. d'état, membre et directeur de recherche

M. PERRIER Michel, Ph.D. , membre et codirecteur de recherche

M. YAHIA L'Hocine, Ph.D. , membre

M. TERNAN Marten, Ph.D. , membre

## **DEDICATION**

*This thesis is dedicated to my beloved wife, who is the best friend,*

*To my mother and my sister, who are the kindest,*

*And to my father, who was the best teacher, in my life.*

*I love you Dears*

## ACKNOWLEDGEMENT

I would like to give my sincere gratitude to those who helped me during my PhD to complete this thesis. Undoubtedly the first and the most important is nobody but my supervisor, Professor Oumarou Savadogo, who gave me the chance of working in his group. I learned a lot. Thanks Oumarou for your kind guidance, encouragement and supports.

I would like to give million thanks to my co-supervisor, Professor Michel Perrier, whom I learned from to be supportive, kind and patient. Thanks Michel, I never forget your endless kindness.

I thank to my friends in our group: Eric Nguwuo Petuenju, Bintou Ouedraogo, Majid Talebi Esfandarani, Seyed Mohammad-Amin Shahrestani, Kentaro Oishi, Lina Kafrouni and Maryam Haddad. My special thanks to Madam Carole Massicotte, that working in laboratory without her was a real toil.

I would like to thank Dr. Huimin Tian, Dr. Wanli Wang and Mr. Ramon Martinez, who are not here, but helped me to start my work. Thank you so much for all your valuable helps.

And the last, but not least, I thank my wife, my mother and father, my sisters and brothers, all my friends especially Mohsen Keshavarz Khorasgani, and all my beloved nieces and nephews, who make my life full of love, excitement and energy. I always have a great time with your memories.

Thanks Montréal!

Thanks Canada!

## RÉSUMÉ

Dans ce projet, l'oxy-nitruure de titane ( $\text{TiO}_x\text{N}_y$ ) a été étudié comme un nouvel électro-catalyseur non noble pour la réaction de réduction de l'oxygène (RRO). Une comparaison détaillée entre quatre différentes méthodes de préparation sol-gel a été effectuée pour évaluer les propriétés physicochimiques et électrochimiques des électro-catalyseurs produits. Parmi ces méthodes, un nouveau procédé sol-gel à base d'urée (simplement appelée méthode U) a été introduit pour préparer du  $\text{TiO}_x\text{N}_y$  à une température relativement basse et une durée relativement faible de recuit. Les matériaux fabriqués par cette nouvelle méthode donnent une activité électro-catalytique de la RRO plus élevée de celle des oxy-nitruures de titane préparés par les autres méthodes. Les électro-catalyseurs, préparés avec différents rapports de N/O, ont montré des propriétés différentes allant d'un comportement très peu conducteurs (faible rapport N/O) pour les matériaux riches en oxygène au comportement plus conducteur et stable chimiquement et électrochimiquement pour les oxy-nitruures riches en azote (rapport élevé en N/O), respectivement. Généralement, les électro-catalyseurs préparés par la méthode U avaient plus de nitruure de titane dans leurs structures que les électro-catalyseurs préparés par les autres méthodes. Néanmoins, le traitement thermique a un rôle essentiel dans la composition de cette phase la faisant passer de phase ayant une composition en oxyde à celle ayant une composition élevée de nitruure. Selon l'analyse élémentaire effectuée par spectrométrie à dispersion d'énergie (EDS), le pourcentage d'azote dans le matériau est passé de 9 à 24 pour cent en augmentant la température de recuit de 700 à 1100 °C, tandis que le pourcentage d'oxygène diminuait inversement. En outre, sur la base des données de la diffraction des rayons X (XRD), dans le cas de la méthode de U, les pics caractéristiques de TiN ont été détectés, même à des températures de recuit plus basses. L'augmentation de cette température a également fait apparaître des pics beaucoup plus marqués indiquant la croissance de la taille des cristallites. La taille calculée des cristallites a montré que celle des échantillons préparés par la méthode de U (de 20 à 40 nm de diamètre) était presque dans la même gamme de valeurs que celle de la taille des cristallites de TiN pur. La taille des cristallites des échantillons préparés par les autres procédés sol-gel (de 40 à 60 nm de diamètre) était dans la même gamme de la taille des cristallites de  $\text{TiO}_2$  pur. La microscopie électronique à balayage (MEB) et l'analyseur de surface B.E.T. ont été respectivement utilisés pour évaluer la taille des particules et la surface spécifique des différents échantillons. Ils ont indiqué une plus

petite taille de particules et donc une surface spécifique plus élevée pour les électro-catalyseurs produits par la méthode U.

Outre les caractérisations physicochimiques mentionnées ci-dessus, la voltammétrie cyclique (CV), la polarisation et la spectroscopie d'impédance électrochimique (SIE) ont été utilisées pour évaluer les propriétés électrochimiques des électro-catalyseurs. Les valeurs de la pente de Tafel, la densité de courant d'échange et le potentiel de départ ont révélé que l'électro-catalyseur préparé par le procédé de U et qui a été recuit à 1100 °C, a eu la meilleure activité électro-catalytique de tous les autres échantillons avec une pente de Tafel égale à -203 mV/décade, la densité du courant d'échange autour de 4E-04 mA/mg et le potentiel de départ proche de 0.8 volt par rapport à ENH (électrode normale à hydrogène). Les valeurs obtenues avec la SIE ont également montré que c'est le meilleur électro-catalyseur parce qu'il possède la plus grande capacité spécifique (~ 3.3 F/g). Ce fait est aussi en accord avec la plus grande valeur de sa surface BET et également sa plus faible résistance de transfert de charge.

La stabilité chimique et électrochimique est l'un des facteurs déterminants dans le choix d'un électro-catalyseur pour la RRO. À cet égard, l'ICP-TOF-MS a été utilisé pour évaluer la stabilité chimique et électrochimique, sous l'environnement d'acide corrosif, des électro-catalyseurs préparés, en mesurant la concentration du titane dissous après un certain temps. Jusqu'à présent, la mesure de la concentration des métaux dissous par ICP-TOF-MS a été la seule méthode utilisée dans la littérature pour évaluer sa stabilité chimique. Toutefois, dans ce projet, cette technique a été aussi utilisée après beaucoup de balayages de voltammétrie cyclique pour aussi évaluer la stabilité électrochimique de l'électro-catalyseur; ce qui est plus réaliste et plus proche de l'état de fonctionnement de la PEMFC (Polymer Electrolyte Membrane Fuel Cell). La stabilité du meilleur électro-catalyseur avec l'activité électro-catalytique la plus élevée (préparé par le procédé U) est meilleure que l'électro-catalyseur Pt/C utilisé dans le commerce, à la fois chimiquement et électro-chimiquement. La stabilité électrochimique des électro-catalyseurs préparés a également été étudiée à un potentiel oxydant élevé (plus de 2 volts vs NHE). La spectrométrie photoélectronique des rayons X (XPS) a montré que la quantité d'azote à la surface de l'électro-catalyseur a diminué de 11% avant l'oxydation à 5% après l'oxydation. Une diminution de l'activité électro-catalytique pour la RRO a diminué après l'oxydation. Ainsi, diminuer la quantité de nitrure de titane à la surface de l'oxy-nitrure de titane a réduit son activité électro-catalytique.

Dans la deuxième phase de ce projet, l'activité électro-catalytique du nitrure de titane pour la RRO a été étudiée par le calcul de la théorie de la fonctionnelle de la densité (DFT). Au meilleur de notre connaissance, il n'existe pas d'étude de la chimie quantique théorique et numériques de nitrure de métal de transition comme l'électro-catalyseur dans les piles à combustible PEM. La RRO a été considérée comme ayant lieu en trois différentes étapes séquentielles, à savoir l'adsorption de l'oxygène, la production d'hydroxyde et de désorption de l'eau. Sur la base des résultats de la diffraction des rayons X obtenus sur les meilleurs échantillons préparés qui montrent et qu'ils contiennent TiN(111) et TiN(200) comme les deux principales structures du TiN, la simulation a été sur la surface de ces deux structures. La simulation a été effectuée avec le logiciel «Vienna *ab initio* Simulation Package (VASP)» sur la base des ensembles de fonctions d'ondes planes aux conditions périodiques limites et qui intègre la description des interactions entre les électrons. La comparaison des énergies d'adsorption des espèces liées à la RRO a prouvé l'existence d'une forte adsorption dissociative de l'oxygène sur le TiN(111) quelles que soient les sites d'adsorption. Toutefois, en raison d'une adsorption de OH relativement forte sur TiN(111), cette surface a perdu les sites actifs pour procéder à la RRO, tandis que sur la surface du TiN(200), la production et la désorption d'eau s'effectuent presque facilement. La densité d'états électroniques (DEE) a été obtenue pour calculer le centre de la bande  $d$  et le remplissage fractionnaire dans des situations différentes. Considérant la possibilité d'adsorption sur des sites pont et de haut de la TiN(200), ces informations indiquent que la production d'hydroxyde et la désorption de l'eau sont les mesures déterminantes pour la RRO en site pont et sommet, respectivement. Par conséquent, il est révélé que le TiN, spécialement TiN(200) a une activité électro-catalytique pour la RRO. La perte de ce composant de la surface de l'oxy-nitrure de titane a provoqué la diminution de son activité électro-catalytique.

## ABSTRACT

In this project, titanium oxy-nitride ( $\text{TiO}_x\text{N}_y$ ) has been studied as a new non-noble electro-catalyst for the oxygen reduction reaction (ORR). A comprehensive comparison between four different sol-gel methods was carried out to evaluate the physicochemical and electrochemical properties of the produced electro-catalysts. Among them, a new urea-based sol-gel method (simply called U method) is introduced to prepare  $\text{TiO}_x\text{N}_y$  at a fairly low temperature and duration, with higher electro-catalytic activity for the ORR. The prepared electro-catalysts with different N/O ratios showed different properties from a less conductive behavior in oxygen-rich (low N/O ratio) materials to more conductive electro-catalyst behavior in nitrogen-rich (high N/O ratio) oxy-nitrides, respectively. Generally, electro-catalysts prepared by the U method had more titanium nitride in their structures than the electro-catalysts prepared by the other methods. Nevertheless, heat treatment had a key role in this phase transferring from having high oxide structure to high nitride structure. According to the elemental analysis done by energy dispersive spectroscopy (EDS), nitrogen percentage in the bulk material increased from 9 to 24 percent by increasing the temperature from 700 to 1100 °C, while the oxygen percentage was decreasing inversely. In addition, based on the X-ray diffraction (XRD) data, in the case of U method, the TiN characteristic peaks were obvious, even at lower temperatures. Increasing the temperature also made the peaks much sharper indicating the growth of the crystallite size. The calculated crystallite size showed the crystallite size of samples prepared by U method (20 to 40 nm) was almost in the same range of the TiN crystallite size, but the crystallite size of the samples prepared by the other sol-gel methods (40 to 60 nm) was in the same range of the  $\text{TiO}_2$  crystallite size. Scanning electron microscopy (SEM) and B.E.T. surface area analyzer were used to evaluate the particle size and surface area of different samples, respectively. They indicated a smaller particle size and a higher surface area in the electro-catalysts produced by the U method.

Besides the aforementioned physicochemical characterizations, cyclic voltammetry (CV), polarization, and electrochemical impedance spectroscopy (EIS) were used to evaluate the electrochemical properties of the electro-catalysts. Obtained Tafel slope, exchange current density and onset potential revealed that the electro-catalyst prepared by the U method which was annealed at 1100 °C, had the best electro-catalytic activity among all other samples with Tafel slope of -203 mV/decade, exchange current density around  $4\text{E}-04$  mA/mg and the onset potential

close to 0.8 volt vs. NHE (normal hydrogen electrode). EIS measurements also supported this assertion through revealing the highest specific capacitance ( $\sim 3.3$  F/g). This result was in agreement with the highest B.E.T. surface area and the lowest charge transfer resistance exhibited by this electro-catalyst among the other samples.

Stability is one of the determinant factors in selecting an electro-catalyst for the ORR. In this regard, ICP-TOF-MS was used to evaluate the chemical stability of the prepared electro-catalysts under corrosive acidic environment, by measuring the concentration of the dissolved titanium after a certain time. Heretofore, measuring the dissolved metal concentration by ICP-TOF-MS was done just to evaluate its chemical stability. However, in this project this technique was also used during the CV, to evaluate the electro-catalyst's electrochemical stability as well, which is more realistic and similar to the PEMFC's working condition. Stability of the best electro-catalyst with the highest catalytic activity (prepared by the U method) was better than the commercially used Pt/C electro-catalyst, both chemically and electrochemically. Electrochemical stability of the prepared electro-catalysts has also been studied at a high oxidizing potential (more than 2 volts vs. NHE). X-ray Photoelectron Spectroscopy (XPS) showed that the nitrogen amount on the surface of the electro-catalyst decreased from 11 % before the oxidation to 5 % after the oxidation, whereas the catalytic activity for the ORR decreased after the oxidation. Thus, decreasing the titanium nitride's amount in the titanium oxy-nitride surface reduced its catalytic activity.

In the second phase of this project, electro-catalytic activity of the titanium nitride for the ORR was investigated via a density functional theory (DFT) computation. To the best of our knowledge, there is no theoretical and computational quantum chemistry study of the transition metal's nitride as the electro-catalyst in PEM fuel cells. ORR was considered to take place in three different sequential steps namely oxygen adsorption, hydroxide production and water desorption. Based on the XRD results, TiN(111) and TiN(200) were considered as the two major facets of the TiN. Simulation was done by the Vienna *ab initio* Simulation Package (VASP) based on the Plane-Wave basis sets and periodic boundary condition, while the PBE exchange-correlational functional was used to describe the interactions among electrons. Comparing the adsorption energies proved existence of a strong dissociative adsorption of oxygen on the TiN(111) regardless of the adsorption sites. However, because of a relatively strong OH adsorption, TiN(111) loses the active sites to proceed the ORR, while on the TiN(200) surface,

water production and desorption came about easily. Electron density of states (DOS) was obtained to calculate the d-band center and fractional filling in different situations. Considering two possible bridge and top adsorption sites on the TiN(200), these information indicated the hydroxide production and water desorption as the rate determining steps for the ORR in bridge and top sites, respectively. Therefore, it was shown that the TiN, specially TiN(200) had exhibited good electro-catalytic activity for the ORR. Losing this TiN amount from the titanium oxy-nitride's surface might be responsible for the decrease of the electro-catalytic activity of the titanium oxy-nitride for the ORR.

## TABLE OF CONTENTS

DEDICATION .....	III
ACKNOWLEDGEMENT .....	IV
RÉSUMÉ.....	V
ABSTRACT .....	VIII
TABLE OF CONTENTS .....	XI
LIST OF TABLES .....	XVI
LIST OF FIGURES.....	XVII
LIST OF ABBREVIATIONS .....	XIX
INTRODUCTION.....	1
CHAPTER 1 LITERATURE REVIEW – PART A: PEM FUEL CELL .....	4
1.1 Fuel Cell General Application.....	4
1.2 Fuel Cell Types .....	5
1.3 PEM Fuel Cell.....	7
1.4 Membrane Electrode Assembly .....	9
1.4.1 Membrane.....	10
1.4.2 Gas Diffusion Layer .....	12
1.4.3 Catalyst Layer .....	13
1.5 Hydrogen Oxidation Reaction.....	14
1.6 Oxygen Reduction Reaction.....	16
1.7 Theoretical Background .....	18
1.8 Electrochemical Measuring Techniques .....	21
1.9 Pt-based Catalysts .....	29
1.10 Non-Noble Metal Catalysts.....	31

1.11	Catalysts Preparation (Sol-Gel Method) .....	33
CHAPTER 2 LITERATURE REVIEW – PART B: AB INITIO SIMULATION .....		37
2.1	Schrödinger Equation .....	37
2.2	Born-Oppenheimer Approximation .....	40
2.3	Slater Determinants .....	42
2.4	Hartree-Fock (HF) Method .....	44
2.5	Density Functional Theory .....	48
2.5.1	Orbital-Free DFT Approach .....	49
2.5.2	Kohn-Sham Approach .....	51
2.6	Exchange-Correlation Functional .....	53
2.6.1	Local Density Approximation (LDA) .....	54
2.6.2	Generalized Gradient Approximation (GGA) .....	54
2.7	Basis Sets .....	55
2.7.1	Localized Basis Sets .....	56
2.7.2	Plane Wave Basis Sets .....	57
2.8	Pseudo-Potential (Effective Core Potential) .....	58
2.9	Cluster and Slab Models .....	59
2.10	Brillouin Zone .....	61
2.11	VASP .....	63
2.12	Adsorption Energy Calculation .....	66
2.13	Density of State (DOS) .....	66
2.14	<i>d</i> -Band Theory .....	69
CHAPTER 3 OBJECTIVES .....		72
CHAPTER 4 ARTICLE 1: ELECTROCHEMICAL AND PHYSICOCHEMICAL PROPERTIES OF TITANIUM OXY-NITRIDE ELECTROCATALYST (TiO <sub>x</sub> N <sub>y</sub> ) PREPARED		

BY FOUR DIFFERENT SOL-GEL METHODS FOR THE OXYGEN REDUCTION REACTION (ORR) IN ACID MEDIUM.....	73
4.1 Introduction.....	74
4.2 Experimental Procedure.....	76
4.2.1 Materials.....	76
4.2.2 Sol-Gel Procedure.....	76
4.2.3 Heat-Treatment.....	78
4.2.4 Physicochemical Characterizations.....	78
4.2.5 Electrochemical Measurements.....	78
4.2.6 Chemical Stability.....	79
4.3 Results and Discussions.....	79
4.3.1 Physicochemical Characterizations.....	79
4.3.2 Chemical Stability.....	88
4.3.3 Electrochemical Stability.....	90
4.3.4 Catalytic Activity for the ORR.....	92
4.4 Conclusion.....	96
4.5 References.....	97
CHAPTER 5 ARTICLE 2: STABILITY AND CATALYTIC ACTIVITY OF TITANIUM OXY-NITRIDE CATALYST PREPARED BY IN-SITU UREA-BASED SOL-GEL METHOD FOR THE OXYGEN REDUCTION REACTION (ORR) IN ACID MEDIUM.....	104
5.1 Introduction.....	105
5.2 Experimental Procedure.....	106
5.2.1 Catalyst Preparation.....	106
5.2.2 Characterization.....	107
5.2.3 Electrochemical Measurements.....	107

5.3	Results and Discussions .....	108
5.3.1	Physicochemical Characterizations.....	108
5.3.2	Chemical and electrochemical stability and catalytic activity .....	112
5.3.3	Electrochemical Impedance Spectroscopy (EIS) Analysis .....	117
5.4	Conclusion.....	121
5.5	References .....	122
CHAPTER 6 ARTICLE 3: OXYGEN REDUCTION REACTION (ORR) ON A MIXED TITANIUM AND TANTALUM OXY-NITRIDE CATALYST PREPARED BY THE UREA-BASED SOL-GEL METHOD .....		129
6.1	Introduction .....	130
6.2	Experimental Procedure .....	133
6.2.1	Materials.....	133
6.2.2	Sol-Gel Procedure .....	133
6.2.3	Heat Treatment.....	133
6.2.4	Physicochemical Characterizations.....	135
6.2.5	Electrochemical Measurements.....	135
6.3	Results and Discussions .....	136
6.3.1	Physicochemical Characterizations.....	136
6.3.2	Electrochemical Stability .....	139
6.3.3	Catalytic Activity for the ORR.....	141
6.4	Conclusion.....	149
6.5	Acknowledgements: .....	150
6.6	References .....	150

CHAPTER 7	ARTICLE 4: DENSITY FUNCTIONAL THEORY (DFT) COMPUTATION OF THE OXYGEN REDUCTION REACTION (ORR) ON TITANIUM NITRIDE (TiN) SURFACE.....	154
7.1	Introduction .....	155
7.2	Computational Approach .....	156
7.3	Results and Discussions .....	159
7.4	Conclusion.....	168
7.5	References .....	169
CHAPTER 8	GENERAL DISCUSSION.....	175
	CONCLUSIONS AND RECOMMENDATIONS.....	179
	LIST OF REFERENCES .....	181

**LIST OF TABLES**

Table 1-1: Specifications of different types of fuel cells ([14-16]).....	6
Table 1-2: Different types of hierarchically created polymer electrolyte membranes [27] .....	11
Table 2-1: Comparing advantages and disadvantages of localized and plane wave basis sets.....	59

## LIST OF FIGURES

Figure 1-1: Schematic picture of PEMFC [2] .....	1
Figure 1-1: Different parts of a MEA.....	8
Figure 1-2: MEA preparation modes (a): separate electrode method and (b): catalyst coated membrane method [27] .....	10
Figure 1-3: Structure of Nafion membrane [27] .....	12
Figure 1-4: Schematic mechanism for $4e^-$ and $2e^-$ pathways .....	16
Figure 1-5: Oxygen adsorption models: (a) the Griffiths model, (b) the Pauling model and (c) the Yeager model[47].....	18
Figure 1-6: Polarization curve of the ORR on Pt catalyst at 30 °C.....	22
Figure 1-7: CV of Pt/TiON 30 wt % in 0.5 M sulfuric acid saturated with $O_2$ at room temperature .....	24
Figure 1-8: (left: a) Polarization curve with RDE at different speeds for commercial Pt/C 30 wt % catalyst in a 0.5 M sulfuric acid saturated by 1 bar $O_2$ at 25 °C and (right: b) related Koutecky-Levich plot at different potentials. ....	25
Figure 1-9: Modified Randles–Ershler equivalent circuit model ( $R_s$ : uncompensated ohmic resistance, $R_{ct}$ :charge transfer resistance, $W_s$ : Warburg finite element with short terminal, CPE: constant phase element).....	27
Figure 1-10: EIS in the Nyquist (left) and Bode (right) diagram for the titanium oxy-nitride catalyst at three different bias DC potential: 0 V vs. OCV, -0.3 V vs. OCV and +1.5 V vs. SCE. AC perturbation had amplitude of 10 mV. ....	29
Figure 1-11: Heating schedule of heat treatment process .....	35
Figure 2-1: Ethane molecule (left) and graphite surface (right) both modeled by a periodic boundary condition slab model. ....	60
Figure 2-2: Schematic of self-consistent iteration calculations in VASP.....	64
Figure 2-3: VASP user interface windows to select the desired options and adjust the parameters .....	65

Figure 2-4: DOS of two different atoms in TiN (200) in interaction with O <sub>2</sub> molecule. ....	70
Figure 2-5: Schematic of the effect of d-band state position on the extent of anti-bonding filling .....	71

## LIST OF ABBREVIATIONS

AFC	Alkaline Fuel Cell
ALD	Atomic Layer Deposition
AOs	Atomic Orbitals
APUs	Auxiliary Power Units
bcc	Body Center Cubic
BZ	Brillouin Zone
CCM	Catalyst Coated Membrane
CHP	Combined Heat and Power
CL	Catalyst Layer
CPE	Constant Phase Element
CV	Cyclic Voltammetry
CVD	Chemical Vapor Deposition
DFT	Density Functional Theory
DMFC	Direct Methanol Fuel Cell
DOS	Density Of Electronic State
DSC	Differential Scanning Calorimetry
ECSA	Electrochemical Active Surface Area
EDS	Energy Dispersive X-ray Spectroscopy
EIS	Electrochemical Impedance Spectroscopy
fcc	Face Center Cubic
GDL	Gas Diffusion Layers
GGA	Generalized Gradient Approximation
GTO	Gaussian Type Orbitals
HER	Hydrogen Evolution Reaction
HF	Hartree-Fock
HOR	Hydrogen Oxidation Reaction
KS	Kohn-Sham Approach
LDA	Local Density Approximation
MCFC	Molten Carbonate Fuel Cell

MEA	Membrane Electrode Assembly
MOs	Molecular Orbitals
OCV	Open Circuit Voltage
ORR	Oxygen Reduction Reaction
PAFC	Phosphoric Acid Fuel Cell
PAW	Projected Augmented Wave
PEMFC	Polymer Electrolyte Membrane Fuel Cell
PES	Potential Energy Surface
PFSA	Perfluorosulfonic Acid
PLD	Pulsed Laser Deposition
PTFE	Polytetrafluoroethylene
PW	Plane Wave Basis Sets
RDE	Rotating Disk Electrode
rds	Rate Determining Step
RHE	Reversible Hydrogen Electrode
SCE	Saturated Calomel Electrode
SCF	Self-Consistence-Field
SEM	Scanning Electron Microscope
SOFC	Solid Oxide Fuel Cell
STO	Slater Type Orbitals
TFD	Thomas-Fermi-Dirac Model
TGA	Thermal Gravimetric Analysis
TPB	Three Phase Boundary
USP	Ultra Soft Pseudo-Potential
VASP	Vienna ab Initio Simulation Package
XPS	X-Ray Photoelectron Spectroscopy
XRD	X-Ray Diffraction

## INTRODUCTION

Energy resources and their limitation are probably among the most concerning issues of the postmodern world in both scientific societies and political circles. Besides the limitation of fossil fuels as the main energy sources and rising trend of their price, environmental concerns, security and political sight push the scientists to look for an alternative energy resource. Although, since two decades ago, we see lots of progress in development of wind power, hydropower, solar energy, biomass, geothermal and fuel cells as renewable energy resources, some big challenges in the way of each of these technologies have led to this concern still remained unchanged.

Fuel cells, especially Polymer Electrolyte Membrane Fuel Cell (PEMFC), because of some of their exceptional properties, are among the most promising alternative energy sources. Like an internal combustion engine, a fuel cell uses some kind of chemical fuels; but like a battery, the chemical energy is directly converted to the electricity power, without a flame, combustion, noise or vibration and inefficient combusting step. There are different kinds of fuel cells but generally the mechanism to produce power is same except fuels, materials and operational conditions. Therefore, generally speaking, we can say that a fuel cell directly converts the chemical energy of a fuel into the electricity. Main components of a fuel cell are a cathode, an anode, and an ion conducting electrolyte. These parts are schematically shown for a PEMFC in figure 1-1. A fuel such as hydrogen is brought into the anode side and an oxidant, typically oxygen (and/or air), into the cathode side. The electrolyte assists as an obstacle to gas diffusion and electron, but will let ions transfer across it [1].

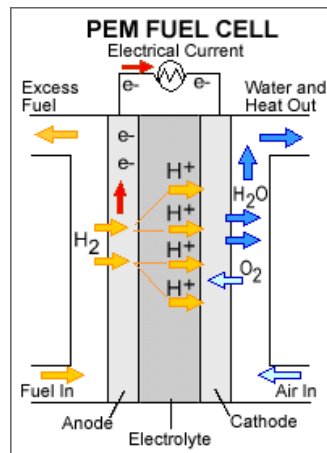
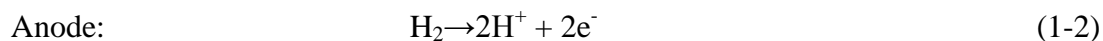
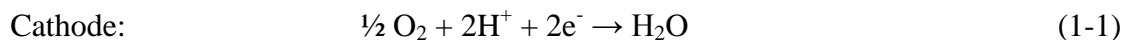


Figure 1-1: Schematic picture of PEMFC [2]

Therefore, two half-cell reactions occur at the anode and cathode, producing ions which can migrate across the electrolyte: the oxidation of hydrogen at the anode and the reduction of oxygen at the cathode for proton conducting electrolyte like PEMFC:



The flow of ionic charge through the electrolyte must be balanced by the flow of electronic charge through an external circuit, and this balance produces electrical power.

The Hydrogen Oxidation Reaction (HOR) in anode is relatively simple involving a single electron transfer process. While, in comparison, at the cathode side, Oxygen Reduction Reaction (ORR) is a complex four-electron transfer process. Therefore the HOR has lower oxidation over potential and a higher kinetic rate than the ORR, so that the ORR rates as measured by the standard state (298K, 1 bar) exchange current density on the cathode catalyst, is 6 orders of magnitude slower than that of its anodic part [3].

Presently, platinum (Pt) nanoparticle on carbon support (Pt/C) is conventional commercial electro-catalyst used in PEMFCs due to its high specific area. The carbon support spaces the Pt particles to prevent agglomeration and also because of high electrical conductivity it is a good current collector. However, the catalytic activity for the ORR is insufficient to obtain the required efficiency even with platinum (specifically in the potential range between 0.75 and 1.0 V ) and the cathodic over potential losses amount to 0.3 – 0.4 V [4, 5].

Therefore, to compensate this high over potential, a large amount of platinum should be used. But, on the other hand, low abundance of Pt natural resources and its high cost is a big obstacle in the future commercialization of PEMFCs. For this reason reducing the utilization of Pt catalyst by a greater dispersion of Pt particles and/or alloying with transition metals may be an appropriate way out. However, because the dissolution and deposition of extremely dispersed Pt particles in the electrolyte decrease the cell performance, the drastic reduction of Pt usage is impossible. But some researchers [6] have revealed that Pt-based alloys with transition metals exhibited higher activity than pure Pt for the ORR as they believed that the presence of the transition metal species changes the electronic structure of Pt, leading to a weaker interaction between the Pt surface and the unwanted Pt-OH intermediate. In this regard, Pt-M (M = Pd, Co,

Ni, Cr, Mn, and Fe) alloys has become attractive to ameliorate the catalytic activity and reduce the cost [4]. However, poor long-term stability due to the dissolution of these transition metals in acidic condition obstructs the practical application. Moreover, the leaching out of metal ions would contaminate the membrane and invalidate the fuel cell. In addition, oxidation of the carbon support during long-term operation brings the stability issue in general to the forefront of the research in this area. All these problems have encouraged the scientists to look for a non-noble catalyst and also a new support with high activity and durability in acidic condition, for more than two decades.

Transition metal nitrides which are well known as valve metals are used as anticorrosion and coating materials, and the group 4 and 5 metal oxides, like Ti, V, Nb and Ta oxides, have high chemical stabilities in acids [7-9]. Therefore, group 4 and 5 metal nitrides, oxides and oxy-nitrides are expected to be stable under an acidic and oxidative atmosphere. In addition it has been reported these compounds have some catalytic activity for the ORR [10-12]. Among them, titanium oxide ( $\text{TiO}_2$ ) is cost effective and has high stability in corrosive medium. Especially compared to the presently being used carbon-supports, it has superior stability [13]. However, low electronic conductivity and small catalytic activity of  $\text{TiO}_2$  are its big drawbacks which should be solved to make it an acceptable electro-catalyst or support of catalysts for PEMFCs. Considering the transition metal nitride's more appropriate electrical conductivity properties, it seems that by producing a special composition of oxy-nitride of these metals, the best catalytic properties might be obtained. Finding the best composition of the transition metal oxide and its nitride, definitely in our case  $\text{TiO}_2$  and  $\text{TiN}$ , to achieve the best electrocatalytic activity of the titanium oxy-nitride ( $\text{TiON}$ ) for the ORR is the main topic of this thesis.

Undeniably having a fundamental insight into the reactions taking place on the electro-catalyst surface would help us to have a profound understanding of the phenomena, which in turn leads to design a more active electro-catalyst with our desired functionality. In this regard, first principal simulation (*ab initio* simulation) is a powerful tool to understand the ORR mechanism on the surface of these catalysts. Following the ORR steps on the catalyst surface proves that the surface electronic structure plays an important role in specifying reaction mechanism. Therefore, different catalyst facets of  $\text{TiN}$ , were analyzed from some basic parameters point of view such as: electronic structure, density of state (DOS), band structure, d-band width, work function and energy of the system.

## CHAPTER 1 LITERATURE REVIEW – PART A: PEM FUEL CELL

The principal of the fuel cell goes back to 1839 when Sir William Grove, a British physical scientist, discovered the possibility of generating electricity from hydrogen and oxygen by reversing water electrolysis process. This principal remains unchanged today and generally speaking, a fuel cell is an electrochemical device that continuously converts the free energy of the chemical fuels directly to the electricity, as long as fuel and oxidant are supplied. Therefore, a fuel cell has similarities to both batteries, because of their similar electrochemical nature of the power generation process, and to combustion engines which — unlike batteries — will work continuously so long as they consume a kind of fuels. Fuel cells are efficient and non-polluting electrical power generators. They have high theoretical performance and energy conversion efficiency, and therefore high power density, operational flexibility, in some case low operating temperature and low environmental impacts.

### 1.1 Fuel Cell General Application

It was after the early stages of space travel that fuel cells were used practically for the first time to generate electricity (and also drinking water) in the Gemini and Apollo programs (1950 ~ 1970). Afterward, nowadays, we imagine that fuel cells will finally come into extensive commercial use through three main applications:

#### *1- Transportation applications*

As mentioned above, a fuel cell *directly* converts the chemical energy of a fuel to the electrical energy. Hence, it has high energy conversion efficiency. In this way, it can help to decrease the consumption of primary energy and the emission of CO<sub>2</sub>. In addition, sulfur is poison to all type of fuel cells and it must be separated from any fuel before feeding to the system; hence, no SO<sub>x</sub> are generated. On the other hand, because there is no combustion, no NO<sub>x</sub> are generated as well. Therefore, the fact that fuel cells are almost zero emission, inspired automotive companies to start (since 1980s) developing fuel cell powered cars and in particular buses. Among all types of fuel cells, PEM fuel cell is the most promising one for automotive applications because it has the highest volumetric power densities of all types and it is easily turned on and off. However, cost issue remains unsolved yet.

## 2- *Stationary power generation applications*

Automotive cost targets, led the other applications including stationary power, benefit from this development and the cheaper multipurpose power source — like Combined Heat and Power (CHP) system — become available. Also, maximizing the amount of electrical power made out of a certain plant and a certain quantity of fuel is the most important consideration for a commercial power generator. Fuel cell technology offers improvements with regard to the hours of operation per year — by reducing the need for maintenance — and the efficiency. Now, a larger number of companies produce fuel cells with possibility of the electricity generation for domestic or small commercial use (1–20 kW range). For instance, in the U.S. or many other developing countries, this type of applications of fuel cells as a remote power generator has found its place in the market, certainly in the location where grid connections are too expensive.

## 3- *Portable applications*

Portable fuel cells regularly include grid-independent applications such as traffic monitoring, demonstrators and toys, camping, yachting, auxiliary power units (APUs) for cars, backup solutions, battery replacements and so forth. Actually because the main motivation behind the past decades of fuel cell research and development (R&D) was the striving for the clean cars, portable application was always in the shadow of transportation application and was considered as a by-product of that technology. It is why this market is less well defined. However, looking at the automotive cost targets at \$50 per kW, stationary targets at approximately \$1000 per kW and portable targets beyond this amount, it seems that it is not reasonable that developers wait until the actual cost reaches the rock-bottom \$50 per kW. So, presently, portable applications are most likely the fastest-growing commerce section for fuel cells.

## **1.2 Fuel Cell Types**

Mainly based on the difference in the electrolyte type it is conventional to sort fuel cells in five different categories namely: Polymer Electrolyte Membrane (PEM) fuel cells, Alkaline Fuel Cell (AFC), Phosphoric Acid Fuel Cell (PAFC), Molten Carbonate Fuel Cell (MCFC) and Solid

Oxide Fuel Cell (SOFC). In addition to the different electrolyte, in each case we encounter different operating temperatures and pressures, different mobile ions, different fuels and consequently different applications. Sometimes somebody add also Direct Methanol Fuel Cell (DMFC) to this list, however from the electrolyte type point of view we can consider this one as a PEM fuel cell as well. The only difference between the conventional well-known PEM fuel cell (Hydrogen Fuel Cell) and DMFC is the feeding fuel to the anode side that is methanol in the later one instead of hydrogen in the earlier one. Table 1 shows all these fuel cell types with some of their important specifications.

Table 1-1: Specifications of different types of fuel cells ([14-16])

Fuel Cell type	PEM FC		AFC
	DMFC	Hydrogen FC	
Electrolyte	Solid polymer membrane (Nafion®)	Solid polymer membrane (Nafion®)	Liquid KOH (30~50 % in H <sub>2</sub> O) immobilized
Anode Reaction	$CH_3OH + H_2O \rightarrow CO_2 + 6H^+ + 6e^-$	$H_2 \rightarrow 2H^+ + 2e^-$	$H_2 + 2OH^- \rightarrow 2H_2O + 2e^-$
Cathode Reaction	$\frac{1}{2}O_2 + 2H^+ + 2e^- \rightarrow H_2O$	$\frac{1}{2}O_2 + 2H^+ + 2e^- \rightarrow H_2O$	$\frac{1}{2}O_2 + H_2O + 2e^- \rightarrow 2OH^-$
Mobile Ion	$H^+$	$H^+$	$OH^-$
Operating Temperature	0 ~ 60 °C	50 ~ 100 °C	50 ~ 200 °C
Catalyst	Pt – Pt/Ru	Pt	Pt
Cell Component	Carbon-Based	Carbon-Based	Carbon-Based
Primary Fuel	Methanol	$H_2$	$H_2$
Start-up Time	Sec ~ min	Sec ~ min	---
Power Density (kW/m <sup>3</sup> )	~ 0.6	3.8 ~ 6.5	~ 1
Main Applications	Portable	Automotive, small CHP systems	Space vehicles, e.g. Apollo, Shuttle

Table 1-2(more): Specifications of different types of fuel cells

Fuel Cell type	PAFC	MCFC	SOFC
Electrolyte	Liquid concentrated $H_3PO_4$ (100 %) immobilized	Molten carbonate ( $CO_3^{2-}$ ) retained in a ceramic matrix of $LiAlO_2$	Yttrium-doped zirconium oxide (YSZ) ceramic
Anode Reaction	$H_2 \rightarrow 2H^+ + 2e^-$	$H_2 + CO_3^{2-} \rightarrow CO_2 + H_2O + 2e^-$	$H_2 + O^{2-} \rightarrow H_2O + 2e^-$
Cathode Reaction	$\frac{1}{2}O_2 + 2H^+ + 2e^- \rightarrow H_2O$	$\frac{1}{2}O_2 + CO_2 + 2e^- \rightarrow CO_3^{2-}$	$\frac{1}{2}O_2 + 2e^- \rightarrow O^{2-}$
Mobile Ion	$H^+$	$CO_3^{2-}$	$O^{2-}$
Operating Temperature	150 ~ 220 °C	600 ~ 700 °C	700 ~ 1000 °C
Catalyst	Pt	Nickel	Perovskites (Ceramic)
Cell Component	Graphite-Based	Stainless based	Ceramic based
Primary Fuel	$H_2$	$H_2, CH_4, CO$	$H_2, CH_4, CO$
Start-up Time	Hours	Hours	Hours
Power Density (kW/m <sup>3</sup> )	0.8 ~ 1.9	1.5 ~ 2.6	0.1 ~ 1.5
Main Applications	Large CHP systems (200 kW)	Medium to large scale CHP systems (up to MW)	Vehicle auxiliary power, all sizes of CHP systems (2 kW to MW)

### 1.3 PEM Fuel Cell

Polymer Electrolyte Membrane fuel cell (PEMFC) — also called Proton Exchange Membrane fuel cell — differentiate itself from the other types of fuel cells in that PEMFC benefits use of a solid phase polymer film as the electrolyte (instead of corrosive aqueous acids or bases), which makes its assembly, usage and handling more easier than the other types, certainly for automotive and portable applications. Generally similar to all electrochemical systems, PEMFC contains two

cathode and anode electrodes and a separating electrolyte between them. Two electron conductive electrodes are porous gas diffusion layers with a thin catalyst layer on their interface with the membrane. These components which compose the heart of a PEMFC are called all together a Membrane Electrode Assembly (MEA) (figure (1-1)).

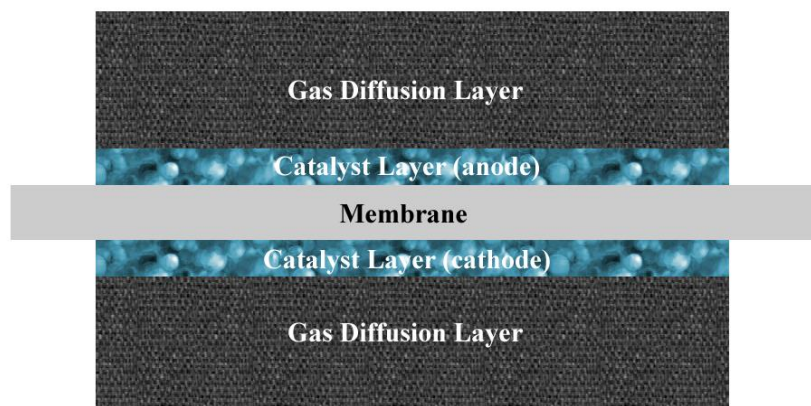


Figure 1-1: Different parts of a MEA

When a PEMFC contains only one cathode and one anode (consequently only one MEA), is called *single* PEMFC. According to the related half reactions, in a single PEMFC the operating voltage is less than 1 volt, which under a given current this voltage is even less. For a state of the art single PEMFC a current density of 1 Amp/cm<sup>2</sup> should be obtained at 0.6 volt. This voltage is far from enough to power a vehicle. Therefore, couple of these single PEMFCs should be assembled into a *stack* PEMFC. In this case, current collectors are bipolar plates where they contain almost 90 % of the volume and 80 % of the mass of a fuel cell stack. Bipolar plates are designed to be anode for one cell in one side and at the same time cathode for the adjacent cell on the other side. They should be very good electrical conductor and impermeable for the reactant gases. Their complex design and these specific properties make the bipolar plate as the most expensive part of the stack fuel cell. There are some challenging discussions related to the distribution of the reactant gases (flow field design in different manner such as: serpentine, parallel or interdigitated models), having a uniform pressure of the reactant gases and stack temperature controlling which are out of the scope of this thesis. In the following section, we talk a little bit more about the most important parts of a PEMFC, the MEA and its components.

## 1.4 Membrane Electrode Assembly

As already mentioned, MEA as the heart of PEMFCs is formed of an ion conducting electrolyte (which is in fact a solid membrane), two gas diffusion layers (GDL) in both sides and a cathode and an anode thin catalyst layer (CL) in interface of the membrane and gas diffusion layers. These components are sandwiched together under a certain temperature, pressure and hot pressing time. These operating conditions play an important role in achieving high-performance MEA. For instance in the case of using the Nafion polymer as the membrane and the Nafion ionomer as the binder in catalyst layer, it is necessary to increase the temperature to recast the ionomer by melting and let it to contact with both the catalyst and the membrane to increase the catalyst utilization and to decrease the ionic resistance. On the other hand, increasing the temperature to more than 125 °C (which is the glassy point of Nafion polymer) decomposes the membrane and dramatically reduces the PEMFC's efficiency. High pressing time also leads to lose the membrane water retention properties. Usually there is an optimum time to have the highest ionic conductivity and three phase reaction area, which after that these properties reduce again. Applied pressure normally depends on the mechanical strength of the gas diffusion layer and its thickness and porosity. One has to measure the total resistance of the MEA while increasing the pressure; the best pressure is at the point that the lowest resistance is achieved [17]. In this thesis operating condition to prepare MEAs was 1~1.5 Kg/cm<sup>2</sup> pressure and the temperature of 110 °C for 4 minutes.

In general there are two modes to make MEA which are depicted schematically in figure (1-2). The first mode is that the catalyst layer is printed to the gas diffusion layer, followed by pressing on the membrane (figure (1-2-a)) [18]. This method is also called *separate electrode method*. In the second way, at first we prepare the catalyst coated membrane (CCM) so that the catalyst layer is directly applied to the membrane followed by adding the gas diffusion layers to both sides (figure (1-2-b)) [19, 20]. In this method pressing is not as crucial as the first method. In this thesis the first mode is the method of choice to prepare the MEA.

To printing the CL on the GDL or membrane there are different methods which are precisely explained in the literature. Here in this part we just address some of those methods in each mode. For the first mode depicted in figure (3-a) we have: Spreading, Spraying [21], Catalyst powder deposition [22], Ionomer impregnation and Electro-deposition methods [23]. We followed the

spreading method in which the catalyst ink was spread on a carbon cloth or carbon paper and then exposed to room temperature to evaporate the solvent. In the second mode depicted in figure (1-2-b) we have: Impregnation reduction [24], Catalyst decal transfer [19, 20], Evaporative deposition [24], Dry spraying [25] and Painting [26] methods.

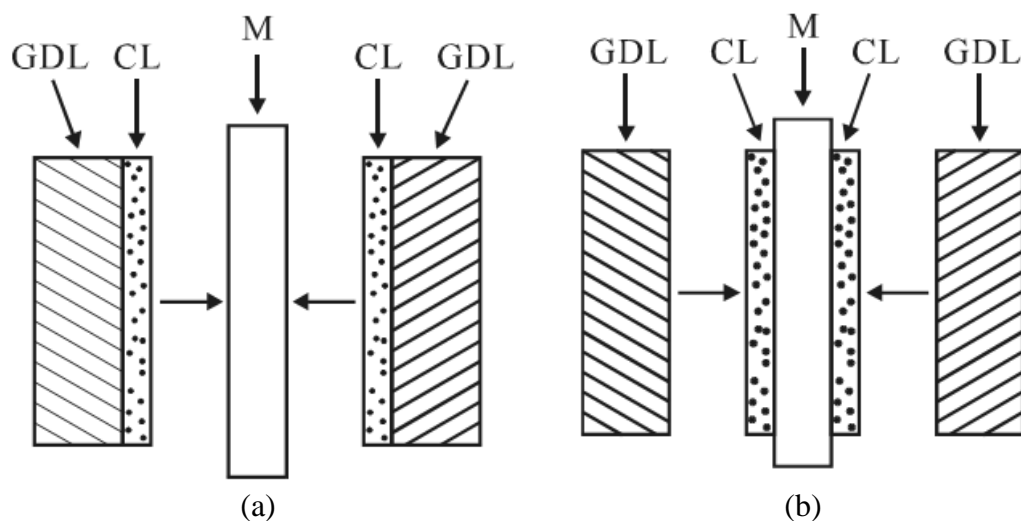


Figure 1-2: MEA preparation modes (a): separate electrode method and (b): catalyst coated membrane method [27]

### 1.4.1 Membrane

The main function of a membrane as the electrolyte in PEMFCs is proton conducting from the anode side to the cathode side. In addition it must separate the fuel and oxidant to prevent the mixture of the gases; it must have a high resistivity for electron transferring, flexibility, strength, chemical and thermal stability, availability and low cost [27]. Although different companies produce different membranes with their own special tricks, which historically we see some important of them in table 2, a common theme in all of them is the use of perfluorosulfonic acid (PFSA) [14]. These hydrophilic ionic groups (sulfonic) are the key for allowing proton passage across the membrane. Ion transport is highly dependent on the free water associated with those groups. So that the ion conductivity increases with the water content up to a point and after that due to diminish of the concentration of protons it decreases. Therefore, moisturizing the membrane is a key to allow ion transport; however on the other hand it limits the operating temperature of the PEMFC. So, systems for thermal and water managements in the cells and

MEAs play an important role to have an efficient operation of the PEMFC [16]. The conductivity of a well-humidified PFSA membrane can be as high as  $0.2 \text{ S.cm}^{-2}$ .

Table 1-2: Different types of hierarchically created polymer electrolyte membranes [27]

Name or structure	Description about life time
1 Phenol-formaldehyde sulfonic acids	Extremely weak and hydrolyzed easily
2 Membranes with a partially sulfonated polystyrene backbone	Short life time (200 hours)
3 “D” membranes, manufactured by grafting styrene-divinylbenzene into a fluorocarbon matrix, followed by sulfonation	500 hours
4 $\alpha\beta$ -trifluoro styrene sulfonic acid	Better chemical and thermal stability, but poor physical properties
5 Triethyl phosphate plasticizer to combine polyvinylidene fluoride with the trifluorostyrene sulfonic acid polymer	5000 h
6 Fluorocarbon matrix grafted with trifluorostyrene	10000 h
7 membrane composed of trifluorostyrene and substituted trifluorostyrene copolymers	15000 h
8 Nafion <sup>®</sup> created by the DuPont <sup>®</sup> company	The most widely used one (high stability and long life time)
9 Membrane created by the Dow <sup>®</sup> Chemical Company	Similar to the Nafion with shorter side chains (better performance but higher price)

Although, due to a smaller thickness (down to  $50 \mu\text{m}$ ), the membrane manufactured by Dow<sup>®</sup> Chemical Company shows better performance, because of the lower cost and ease of fabrication, Nafion<sup>®</sup> is presently the most widely used membrane, even though it is still quite expensive to allow commercialization [28]. Nafion resembles Teflon structure. It is a copolymer of

tetrafluoroethylene and sulfonyl fluoride vinyl ether. This structure gives a long-term chemical and thermal stability. Figure (1-3) shows the general structure of the Nafion membrane.

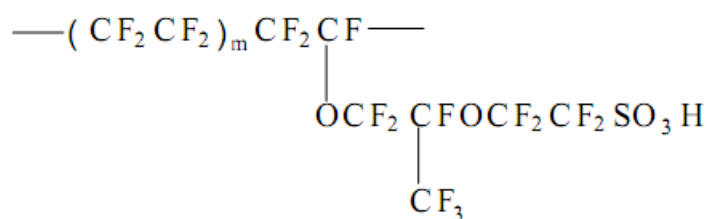


Figure 1-3: Structure of Nafion membrane [27]

In general, the life time of the PEMFC is determined by the life time of its membrane. Although, a thinner membrane improves the performance efficiency by increasing the ion conductivity, due to higher gas permeability and more gas crossover and consequently more degradation, life time of the membrane decreases dramatically. In addition, a thickness smaller than 50  $\mu\text{m}$  (which is the rock-bottom), leads to have lower physical strength [27]. In practice, one needs to treat the membrane before using that. In this regard we followed the standard procedure of treating in  $\text{H}_2\text{O}_2$  3% and then in  $\text{H}_2\text{SO}_4$  1 M for 1 hour each at 80  $^\circ\text{C}$ , followed by washing with boiling deionized water for 1 hour after each step. Hydrogen peroxide is normally used to remove all organic contaminant, while sulfuric acid is used to sulfonate the membrane.

## 1.4.2 Gas Diffusion Layer

Gas diffusion layer (GDL) is typically carbon based material such as carbon cloth or carbon paper. This layer is in fact a mechanical support for the catalyst layer sandwiched between itself and the membrane. It should also provide an electrical pathway for the electrons and a porous pathway for the reactant and product gases. Having all these properties together is a characteristic of carbon which makes it the best candidate for this mission. As already mentioned existence of the water in membrane and feeding gases is crucial to keep the MEA's efficiency at the highest value, but GDL should be able to facilitate the excess water removal — especially in the cathode side — to avoid the gas channel blockage and catalyst occupation. In this regard utilized carbon cloth or carbon paper must be treated by a hydrophobic material such as Polytetrafluoroethylene (PTFE) [28]. Thickness of GDL is almost around 1 mm. It is obvious that the smaller thickness, the smaller ohmic drop.

### 1.4.3 Catalyst Layer

Catalyst Layer (CL) is a very thin layer (ca. micro meter) where the reactions take place on. Based on the heterogeneous electrochemical reactions explained in equations (1-1) and (1-2) it seems clear that there is a need to a three phase boundary (TPB) that brings electrons by an electrical conductive material, reacting gases through a porous volume and reacting ion through a ionic conductive material. Therefore, this layer mainly includes a catalyst — in which the molecular bond in the diatomic gaseous reactant molecules break down — and ionic conductive binder and hydrophobic material that are typically mixed together by a solvent. This mixture that is called in general *catalyst ink* should be printed on the GDL or the membrane by different methods explained in the previous sections. Because of the low temperature operating condition of PEMFCs it is necessary to use a catalyst to overcome the activation energy of the reaction. To avoid the catalyst agglomeration and consequently loss of a big portion of active surface area, it is necessary to disperse the catalyst on a big surface area material. The early use of platinum as the most conventional catalyst was around  $28 \text{ mg/cm}^2$  but now dispersing very small Pt particles on a big surface area carbon powder reduces its utilization down to  $0.1 \text{ mg/cm}^2$ . Carbon powders such as Vulcan XC-72 are among the well-known commercial supports which provide the uniform dispersion of catalyst particles; however, homemade titanium oxy-nitride also was used in this thesis as the catalyst support.

Besides having a big surface area and being electrically conductive, chemical and electrochemical stability of the catalyst support is very important. Although carbon powders provide both high surface area and conductivity, at potentials greater than 1 volt vs. RHE<sup>1</sup> it starts to oxidize. Oxidation of carbon support leads to catalyst agglomeration and losing the catalyst utilization. In this regard, one part of this project was devoted to stability study of the titanium oxy-nitride as an alternative catalyst support compared to the conventional carbon supports.

Catalyst location in interface of the GDL and the membrane is also an affecting parameter which determines the rate limiting factor regarding to the ohmic drop or ionic drop. For instance, for non-porous catalyst layer gas diffusion is a limiting factor and results a big ohmic drop, so the

---

<sup>1</sup> Reversible Hydrogen Electrode

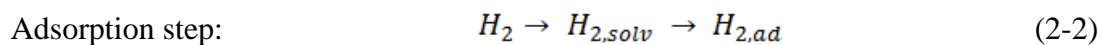
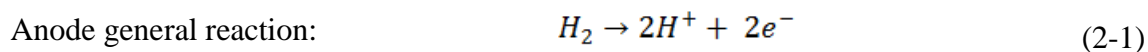
catalyst must be as close as possible to the GDL. Inversely, whit porous catalyst layer, it is the ionic drop which limits the reaction rate and to improve the performance catalyst should be close to the membrane. Therefore, having a thin and porous catalyst layer with preferential location of catalyst close to the membrane, one achieves the optimal catalyst utilization.

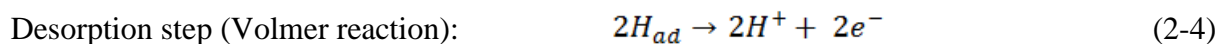
Existence of ionic conductive binder is essential to let the arriving protons from the anode to the interface of cathode and membrane reach the reaction site on the catalyst surface. However, unlike the membrane this material should be permeable for the reacting gas [29-31]. Perfluorosulfonate acid (PFSA) ionomer is normally added to the catalyst ink to provide the media of proton and reactant passage. To repel the condensed water from the catalyst surface at the cathode side and avoiding the catalyst surface occupation and also blockage of the gas transport channels, usually a hydrophobic material such as Polytetrafluoroethylene (PTFE) is also added to the catalyst ink [32, 33].

The ratio of the catalyst, binder, solvent and etc. in the catalyst ink affects the gas permeability, catalytic activity and ionic conductivity which is investigated by Sasikumar [34] and Song [35]. Therefore, to summarize, to achieve a high performance of a PEMFC it is essential to prepare a CL which provides: large three phase interface, easy proton transportation, efficient gas diffusion, easy removal of water and continuous electron passage [27].

## 1.5 Hydrogen Oxidation Reaction

The Hydrogen Oxidation Reaction (HOR) also called Hydrogen Evolution Reaction (HER) is a simple reaction which takes place at the anode side of the PEMFC to generate electrons. This reaction is widely studied and according to the acidic or alkaline medium in which it occurs there are different mechanisms, however, because of our working condition here just those related to the acidic medium are explained. The general form of the HOR is mentioned in equation (2-1) followed by the suggested sequential mechanism in equations (2-2) to (2-4):



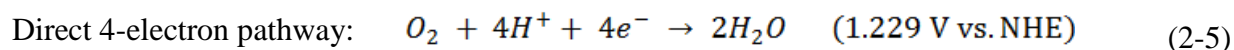


First of all the hydrogen molecule should diffuse through the ionic conductive ionomer (for example PFSA) to the catalyst surface, then it must adsorb on the catalyst surface to form adsorbed hydrogen molecule. The hydrogen-hydrogen bond will be broken to have adsorbed atomic hydrogen on the catalyst surface. This step is well known as the Tafel reaction. Later, via the Volmer reaction this adsorbed atomic hydrogen turns to the proton by releasing an electron. At desorption step this proton starts to migrate through the ion conductive materials to the other side of the membrane. The step that is the slowest one is the rate determining step (rds). There are also other suggested mechanisms such as that offered by Heyrovsky which we address you to study them in the literature [27].

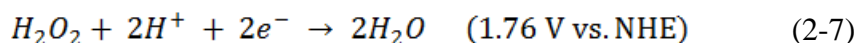
Platinum is the most common used catalyst in the anode side to accelerate the HOR. Although, it constraints the feeding hydrogen purity because of its low tolerance to carbon monoxide. Carbon monoxide which acts as a toxic for platinum may exist in hydrogen (generated by steam reforming of hydrocarbon, certainly natural gas CH<sub>4</sub>). It makes a strong bond with platinum through a bridge-bonding and drastically decreases the number of platinum active sites for the HOR. Also, because of electron capturing by CO and dipole interaction it lowers the activity of the remaining uncovered sites. To overcome this problem and increase the catalyst tolerance to CO, alloying platinum with other transition metals seems a good way out. In this regard different Pt-M binary alloys (M = Ru [36-38], Sn [39], Rh [40], Mo, Ni [41], Re [42], etc.) were investigated. The second metal either by lowering the adsorption of CO or by catalyzing the CO oxidation at lower potential — both because of the electronic structure modification — improves the catalyst tolerance to CO and consequently its performance. Among them Pt-Ru is the most well known to be used as the anode electrocatalyst [27].

## 1.6 Oxygen Reduction Reaction

Oxygen reduction reaction (ORR) is a multi-electron reaction taking place in the cathode side with two main possible pathways in acidic aqueous solution: one pathway involves the transfer of  $2e^-$  to produce hydrogen peroxide ( $H_2O_2$ ), and the other is production of water via a direct  $4e^-$  transfer. In acid media which is operating condition of PEMFCs, these two pathways are mentioned in equations (2-5) to (2-7) and also is depicted schematically in figure (1-4) [43]:



2-electron pathway:



The ORR kinetic is very slow and needs a catalyst to facilitate the reaction by changing the mechanism. A desired catalyst would reduce oxygen molecules to water via the 4-electrons pathway, because an incomplete reduction of oxygen to hydrogen peroxide through 2-electrons route leads to low energy conversion efficiency. In addition hydrogen peroxide further decomposes to harmful free radical species which degrades the ionic conductive materials [44]. The 2-electron pathway is usually used to produce hydrogen peroxide in industry.

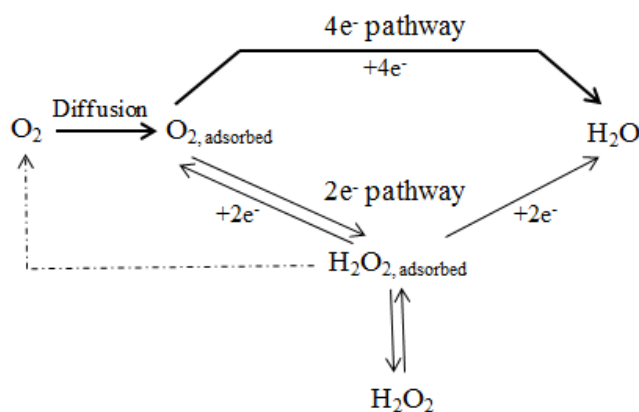
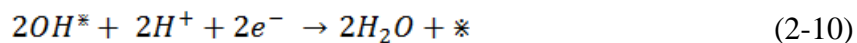


Figure 1-4: Schematic mechanism for  $4e^-$  and  $2e^-$  pathways

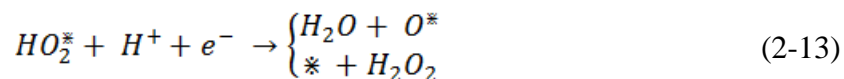
Presently, platinum based materials are the most practical catalysts and certainly, platinum nanoparticle supported on carbon (Pt/C) is accepted commercial electro-catalyst used for the

ORR in PEMFCs. According to the experimental and also theoretical study [45-47] of the electronic structure of platinum — using the Density Functional Theory (DFT) — the ORR on platinum is typically explained by two *dissociative* and *associative* mechanisms including electron transfer steps and chemical steps. *Dissociative* mechanism which is more probable at a low current density leads to a  $4e^-$  pathway; while *associative* mechanism which is more plausible at a high current density causes a  $2e^-$  pathway. Each process may contain a few individual steps which are explained separately in the following sequential equations.

*Dissociative mechanism:*



*Associative mechanism:*



Platinum active sites are denoted by star \*. In these two suggested mechanisms which are implicitly explaining the figure (1-4) there is no  $H_2O_2$  product. However, in the *associative*

mechanism, if the O-O bond not be broken in equation (2-13) this step might be turned to produce  $\text{H}_2\text{O}_2$ , although the  $\text{H}_2\text{O}_2$  could be further reduced to water.

In each of these mechanisms, because of surface geometry and also molecule configuration, one may encounter different possibilities of molecular adsorption. For instance, there are three adsorption models for molecular oxygen adsorption depicted in figure (1-5) [47]:

- ✓ Griffiths model:  $\text{O}_2$  interacts with two bonds on a single surface atom
- ✓ Pauling model: end-on adsorption of  $\text{O}_2$  through a single bond
- ✓ Yeager model: bridge-like adsorption with two bonds interacting with two sites

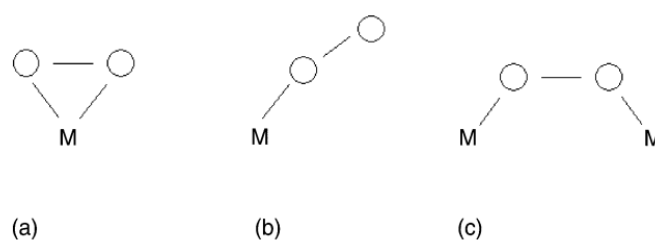


Figure 1-5: Oxygen adsorption models: (a) the Griffiths model, (b) the Pauling model and (c) the Yeager model[47]

These different states have been considered during the calculation; however, the Yeager model approached us to a more stable condition in adsorption than the two other models. Before going through this issue more deeply and unfolding the catalyst effect, types and related problems, it is necessary to explain some theoretical background in electrochemistry and measuring techniques in brief. Following sections are devoted to this matter.

## 1.7 Theoretical Background

As it is obvious from the explained *dissociative* or *associative* mechanisms there are different chemical and electron transfer steps in the way of reaction progress. In both cases the rate of each step is of importance because it determines the rate determining step (rds). Chemical reaction kinetic is well defined in all reaction engineering textbooks, in which the rate of the reaction corresponds to the concentration of the reactants. But, in electrochemical reaction this is a little complex in which one has to consider the electrode potential as well. It seems clear that there is a straightforward relation between the reaction rate and the current in electrochemical reactions. However, it is important to find the relation of the current and the applied potential to complete

this puzzle. A *simple* form of this relation, when there is *no mass transfer effects* (well stirred solution and low current density), is well known as the **Butler-Volmer** equation, which describes the current-potential relationship in each sides (cathode and anode) of a typical electrochemical cell [48]:

$$i = i_0 \left[ \exp\left(\frac{-\alpha n F}{RT} \eta\right) - \exp\left(\frac{(1 - \alpha) n F}{RT} \eta\right) \right] \quad (2-16)$$

where,  $\eta$ ,  $i_0$ ,  $\alpha$ ,  $n$ ,  $F$ ,  $R$  and  $T$  are the over potential, the exchange current density, transfer coefficient, electron transfer number, Faraday's constant, universal gas constant and temperature, respectively.

The exchange current density ( $i_0$ ) is defined as the current while the reaction is in equilibrium; so that the forward and backward reaction rates are similar and there is no net current [48]. Therefore, this value is an indication of reaction rate in one direction at equilibrium and apparently the higher exchange current density, the higher reaction rate. This value mostly depends on the type of the reaction and catalyst (electrode surface), in addition to the reactant concentration, electrode surface area and temperature. For instance, exchange current density of the HOR is 6 orders of magnitude faster than the ORR. As well, this value for the ORR is higher on a platinum electrode than that on a gold electrode. Furthermore, increasing the electrode surface area, temperature and also species concentration at the catalyst surface, increases the value of exchange current density. Exchange current density of the ORR on Pt surface (interface with Nafion) at 30 °C is approximately  $2.8 \times 10^{-4} \text{ mA.cm}^{-2}$  [49]. To achieve these optimum conditions there are different techniques in selecting and producing catalyst which will come in the next upcoming sections.

Over potential ( $\eta$ ) is the deviation of the equilibrium potential (which is obtained by the Nernst equation). Therefore, the Butler-Volmer equation describes the relation between the obtainable current while an over potential is applied to the electrode. In the case that the value of this over potential is very high (could be either negative for cathode or positive for anode) one of the two

terms in the equation (2-16) will be negligible. For the cathode side reaction it could be simplified to the equation (2-17):

$$i = i_0 \exp\left(\frac{-\alpha n F}{RT} \eta\right) \quad (2-17)$$

Rearranging this equation gives us:

$$\eta = \frac{2.303RT}{\alpha n F} \log i_0 - \frac{2.303RT}{\alpha n F} \log i \quad (2-18)$$

Assuming

$$a = \frac{2.303RT}{\alpha n F} \log i_0 \quad (2-19)$$

$$b = -\frac{2.303RT}{\alpha n F} \quad (2-20)$$

Then equation (2-18) will be simplified to:

$$\eta = a + b \cdot \log i \quad (2-21)$$

This equation is the well-known *Tafel* equation [48], which tells us that in a certain current density range, over potential is linearly dependent on the logarithm of the current density. The exchange current density can be obtained from the intercept at the current density axis. The slope of the line is called the *Tafel slope*. The higher the Tafel slope, the slower the reaction kinetics. Relatively same equations might be derived for the anode side reactions; just the Tafel slope for cathode side is negative, when it is positive for the anode side. For the ORR, mostly two Tafel slopes have been reported in literatures: 60 mV/dec and 120 mV/dec, depending on the electrode materials used and on the potential range. It reveals the dependency of the reaction mechanism on both the properties of the catalyst and also working potential.

At a small over potential, the Butler-Volmer equation can be simplified as:

$$i = -i_0 \frac{nF}{RT} \eta \quad (2-22)$$

Therefore, we have:

$$R_p = -\frac{\eta}{i} = \frac{RT}{nFi_0} \quad (2-23)$$

Where  $R_p$  is the charge transfer resistance (or polarization resistance), which refers to the barrier across which the electrons passes from the electrode surface to the adsorbed species or vice versa. The resistance is related to the electrode potential, or more precisely, to the over potential. It is a very important kinetic parameter, describing the speed of the electrode reaction. It can be obtained by AC electrochemical impedance method.

## 1.8 Electrochemical Measuring Techniques

Cyclic Voltammetry (CV), Polarization, Rotating Disk Electrode (RDE) and Electrochemical Impedance Spectroscopy (EIS) are the most frequently used techniques to study the ORR, which were widely used in this thesis.

In **polarization** test, in fact we acquire the responding current density at different potentials from the open circuit voltage to zero. This can be obtained by holding potential of electrode at a certain point and recording the stable current response (steady state polarization) or by slowly sweeping the potential and recording the corresponding currents. The obtained curve (I-V curve) is a characteristic curve to compare the efficiency of different catalysts for the ORR under different circumstances. We can get the Tafel Slope and exchange current density from this curve. Figure (1-6) shows a typical polarization curve of a PEMFC with Pt catalyst at 30 °C.

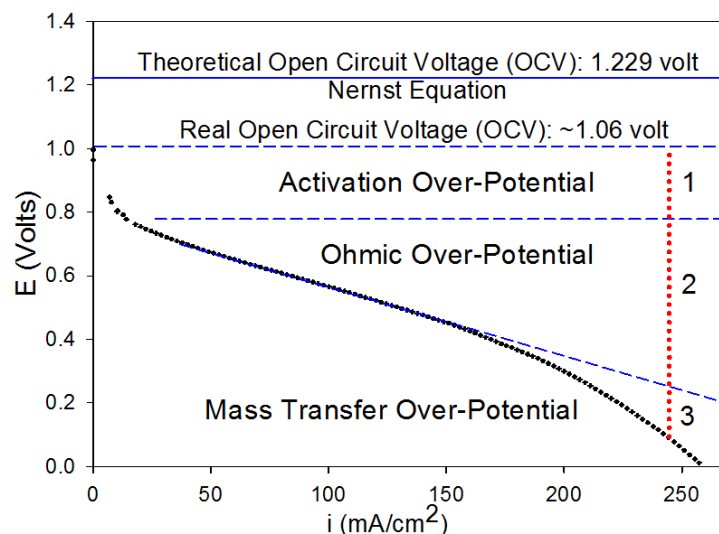
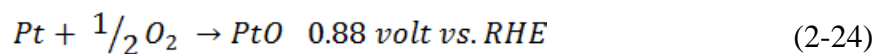


Figure 1-6: Polarization curve of the ORR on Pt catalyst at 30 °C

Theoretically the open circuit voltage (OCV) of a fuel cell should be around 1.229 volt vs. RHE. However, in reality, as depicted in figure (2-6), the OCV is less than this amount (~ 1.06 volt vs. RHE in the case of Pt). This is because of *mixed potential*. In fact, the ORR voltage (1.229 volt vs. RHE) is high enough to oxidize the catalyst surface. In the case of platinum, this oxidation takes place at 0.88 volt vs. RHE. Equation (2-24) shows this oxidation reaction:



Therefore, the real OCV comes from a mixture of this reaction with 0.88 volt and the ORR with 1.229 volt (average ~ 1.06 volt). So, the surface of catalyst is exposed to change with potential changing and an important point inherent in this surface change is that the reaction, for example ORR, will show different behavior at different potential because of this surface change. In preceding sections we mentioned different Tafel slope for the ORR at different potential ranges. Now, it is clearer that because of existence of PtO at a high potential, reaction mechanism is different from that at a low potential, when the reaction takes place on a pure Pt surface. Figure (1-6) also demonstrates voltage lose areas: activation over-potential, ohmic over-potential and mass-transfer over-potential.

Undoubtedly, **Cyclic Voltammetry (CV)** is the most convenient and useful technique in all electrochemical experiments to study the system qualitatively and quantitatively. In this technique, potential is swept linearly between two points and simultaneously the corresponding

current is recorded. The obtained I-V curve is called voltammogram which elaborates different information about the under study system. Sweeping rate can be varied in a wide range, however in this thesis we work at some certain potential rates between 0.1 – 1000 mV/s. Normally we start from an OCV in which there is no considerable Faradaic current (due to the absence of Faradaic reaction<sup>2</sup>), but by receding from this point we will see appearance of the Faradaic current. In fact, according to the Butler-Volmer equation distortion from the equilibrium potential accelerates the reaction rate which consequently leads to more current. Current increases by increasing the absolute value of over-potential until a point in which the rate determining step shifts from electron transfer step to mass transfer phenomenon. The current at this point which in fact appears such a peak in voltammogram is called peak current  $I_P$  or limiting current  $I_L$ . Peak current is a function of potential scan rate ( $v$  in volt/s), number of electron transfer ( $n$ ), electrode surface area ( $A$  in  $\text{cm}^2$ ), diffusion coefficient ( $D$  in  $\text{cm}^2/\text{s}$ ) and bulk concentration ( $C$  in  $\text{mol}/\text{cm}^3$ ) of species. Equation (2-25) shows this relation for a reversible reaction at 25 °C [48]:

$$I_P = (2.69 \times 10^5)n^{3/2}AD^{1/2}Cv^{1/2} \quad (2-25)$$

Therefore, it seems clear that the peak current is proportional to the root square of the potential scan rate. However, in a potential range that there is no Faradaic reaction we may see a small current which is not actually the faradaic current but comes from the charge double layer effects. This current is proportional to the potential scan rate.

A voltammogram is a fast and reliable measurement technique to evaluate the onset potential of different oxidation or reduction reactions. This potential demonstrates the catalytic activity of a catalyst so that the higher onset potential for the ORR, the more active catalyst for this reaction. In addition in the case of platinum, it is possible to measure its electrochemical active surface area (ECSA) by measuring the charge transfer related to the hydrogen desorption process:

---

<sup>2</sup> Faradaic reaction is a reaction in which charge transfer occurs. Sometimes there is no charge transfer in a range of potential, however other chemical processes such as adsorption and desorption can occur and change the electrode-solution interface.

$$ECSA(cm^2_{Pt}/g_{Pt}) = \frac{Q_{H_{desorption}}(C/cm^2_{geometrical})}{210(\mu C/cm^2_{Pt}) \cdot m_{Pt}(g_{Pt}/cm^2_{geometrical})} \quad (2-26)$$

Figure (1-7) shows a typical CV of platinum catalyst on titanium oxy-nitride support (30 wt %) taken at potential scan rate of 50 mV/s.

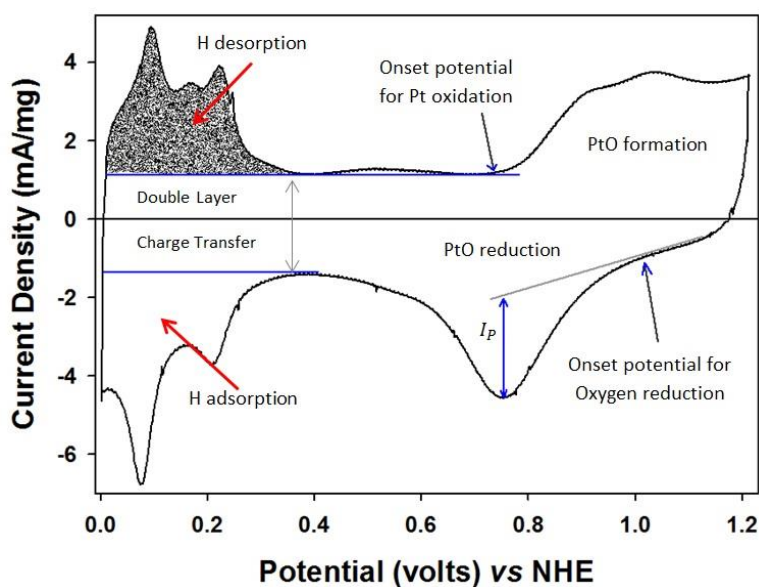


Figure 1-7: CV of Pt/TiON 30 wt % in 0.5 M sulfuric acid saturated with O<sub>2</sub> at room temperature

**Rotating Disk Electrode (RDE)** is a technique belonging to the hydrodynamic method categories used widely in electrochemistry to attain a steady state condition more quickly. This method involves convective mass transport of reactant and products and allows the mass transfer rate at the electrode surface and its ratio to the electron-transfer kinetic increases to be typically larger than the normal non-hydrodynamic methods. If one considers the total resistance in the way of reaction comes from mass transfer resistance and electron transfer resistance, the total current density  $i$  is attributed to the kinetic current density  $i_K$  and Levich current density  $i_{lev}$  by *Koutecky-Levich* equation [48]:

$$\frac{1}{i} = \frac{1}{i_K} + \frac{1}{i_{lev}} \quad (2-27)$$

Where  $i_{lev}$  is proportional to the square root of rotating disk frequency:

$$i_{lev} = 0.62nFAD_{O_2}^{2/3}C_{O_2}\nu^{-1/6}\omega^{1/2} \quad (2-28)$$

In which  $n$  is the overall electron transfer number,  $F$  is the Faraday constant,  $A$  is the electrode surface area,  $D_{O_2}$  is the diffusion coefficient of oxygen,  $C_{O_2}$  is the concentration of dissolved oxygen molecule,  $\nu$  is the kinematic viscosity of solution and  $\omega$  is the angular frequency of rotation. For a 0.5 M sulfuric acid saturated by 1 bar  $O_2$  at 25 °C,  $D_{O_2}$ ,  $\nu$  and  $C_{O_2}$  are  $1.4 \times 10^{-5} \text{ cm}^2 \cdot \text{s}^{-1}$ ,  $0.01 \text{ cm}^2 \cdot \text{s}^{-1}$  and  $1.1 \times 10^{-6} \text{ mol} \cdot \text{cm}^{-3}$ , respectively [50]. Plotting the inverse of electrode current versus inverse of the root square of rotating angular frequency (Koutecky-Levich plot) would give us a line in which the number of electron transfer is inherent in its slop. This method helps us to figure out that the electrode reaction in which mechanism is in progress; for instance, in 2-electron pathway or 4-electron pathway.

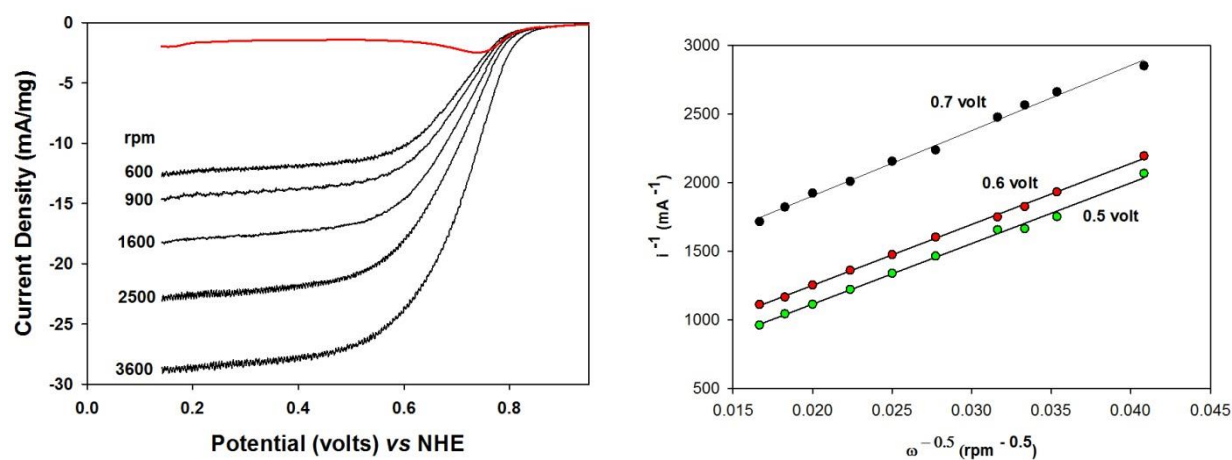


Figure 1-8: (left: a) Polarization curve with RDE at different speeds for commercial Pt/C 30 wt % catalyst in a 0.5 M sulfuric acid saturated by 1 bar  $O_2$  at 25 °C and (right: b) related Koutecky-Levich plot at different potentials.

Figure (1-8-a) shows a polarization curve obtained using RDE for commercial Pt/C 30 wt % catalyst in a 0.5 M sulfuric acid saturated by 1 bar O<sub>2</sub> at 25 °C. The red line is a normal polarization curve when there is no rotation. It seems obvious that the increasing the rotation speed significantly increases the limiting current. Related Koutecky-Levich plot is depicted in figure (1-8-b). According to the slop of these lines, it is possible to obtain the number of electron transfer, in which in this case it is equal to 4 denoting the 4-electron pathway.

In **Electrochemical Impedance Spectroscopy** (EIS) method one in fact applies a DC bias potential with a superimposed small amplitude AC sinusoidal potential to the under study system. In this thesis this method was used to study the ORR in a standard three electrode cell. The frequency of applied AC potential was varied from 1 MHz to 0.01 Hz. Measuring the response sinusoidal current gives us this opportunity to measure the impedance of the system. Some valuable information such as electron transfer resistance, double layer capacitance and also diffusional properties might be extracted from this measurement.

In fact according to the Ohm's law, and considering the applied potential as a sinusoidal function of time and the behavior of response current, the resistance of a system could be represented by an imaginary impedance  $Z$  (including the amplitude and phase lag instead of time):

$$Z = \frac{E}{I} = \frac{E_0 \sin(\omega t)}{I_0 \sin(\omega t + \varphi)} \cong Z_0 \{ \cos(\varphi) + j \cdot \sin(\varphi) \} \quad (2-29)$$

For different electrical element such as ohmic resistance and capacitance there is a certain relation between applied potential and response current which leads to certain impedance:

$$\text{Resistance (R): } I = \frac{E}{R} \rightarrow Z_R(j\omega) = R \quad (2-30)$$

$$\text{Capacitance (C): } I = C \frac{\partial E}{\partial t} \rightarrow Z_C(j\omega) = \frac{1}{j\omega C} \quad (2-31)$$

Plotting  $Z_R$  and  $Z_C$  in Nyquist plane gives us a point on real axis and a line lied on imaginary axis, respectively. However, combination of these elements in series or parallel results different

shapes. Typically we have to make an analogy between the real system and an imaginary electrical circuit to understand the behavior of the system in different frequencies. There are some standard well known equivalent circuits for the ORR; however we have to find the most appropriate one for ours. Normally the basis of developing an equivalent circuit is the *Randles–Ershler* equivalent circuit or its modified versions. Figure (1-9) shows the Modified Randles–Ershler equivalent circuit combined of an uncompensated ohmic resistance ( $R_s$ ) — mostly related to the solution impedance — in series with a parallel set of charge transfer resistance ( $R_{ct}$ ) and diffusional impedance ( $W_s$ ) with a constant phase element ( $CPE$ ) explaining the double layer capacitance ( $R_s-[R_{ct}-W_s]//CPE$ ). This model has been used by several researchers to explicate the impedance of the ORR [51-53].

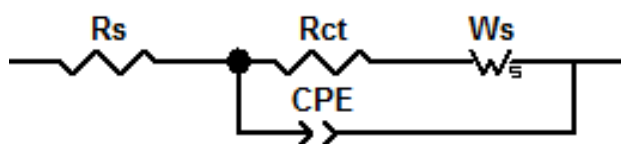


Figure 1-9: Modified Randles–Ershler equivalent circuit model ( $R_s$ : uncompensated ohmic resistance,  $R_{ct}$ : charge transfer resistance,  $W_s$ : Warburg finite element with short terminal,  $CPE$ : constant phase element)

The constant phase element ( $CPE$ ) with the following formula was used to explain the double layer capacitance impedance [54-56]:

$$Z_{CPE} = \frac{1}{Q(j\omega)^n} \quad (2-32)$$

Where  $j$  is an imaginary unit,  $\omega$  is frequency,  $Q$  is the  $CPE$  coefficient explaining the capacitance of the system and exponent  $n$  varies between 0 and 1. If  $n$  equals to 1 then the equation is identical to that of a capacitor. If  $n$  equals 0.5, a 45 degree line is produced on the Nyquist plane. The non-uniform diffusion, the roughness and non-homogeneity effect, distortion of the double layer by Faradaic reactions at the interface, adsorption of impurities through the electrolyte and several other factors, lead to the double layer behaves more like a  $CPE$  than a perfect capacitor. It

produces a depressed semicircle instead of a perfect semicircle in the Nyquist plot. In fact, a capacitor is a constant phase element with a constant phase angle of 90 degrees ( $n = 1$ ).

The diffusional impedance in the model is represented by  $W_s$  recognized as the finite length Warburg element with short circuit terminals (it is terminated in a finite resistance) [54-56]. Following formula shows the generalized Warburg element which was used in the selected equivalent circuit to fit the experimental data in this thesis:

$$Z_{W_s} = R \frac{\tanh(j\omega T)^n}{(j\omega T)^n} \quad (2-33)$$

Where the exponent  $n$  varies again between 0 and 1 and in the case of  $n = 0.5$  one obtains the finite length Warburg element which is the solution of one-dimensional diffusion equation of a particle. Diffusion resistance is presented by  $R$  indicating the impedance at  $\omega \rightarrow 0$ ,  $T = L^2/D$  and  $L$  and  $D$  are effective diffusion thickness and effective diffusion coefficient, respectively.

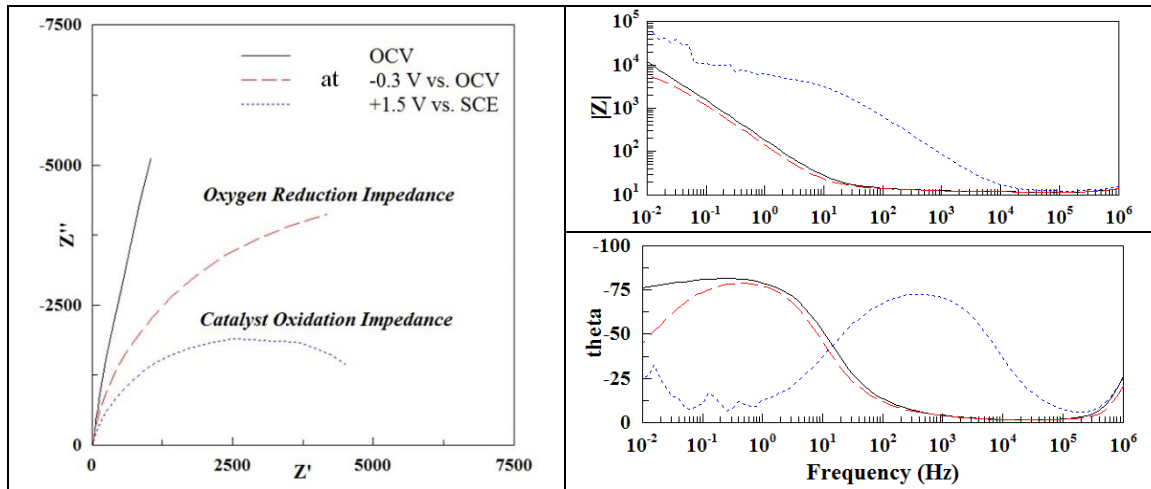


Figure 1-10: EIS in the Nyquist (left) and Bode (right) diagram for the titanium oxy-nitride catalyst at three different bias DC potential: 0 V vs. OCV, -0.3 V vs. OCV and +1.5 V vs. SCE<sup>3</sup>. AC perturbation had amplitude of 10 mV.

In the mentioned model in figure (1-9),  $R_{ct}$  and  $R_s$  are the charge transfer resistance of the working electrode and the uncompensated ohmic resistance of the system including the electrolyte resistance, respectively. The value of  $R_s$  was almost constant in all experiments and equal to  $\sim 10$  ( $\Omega$ ). Figure (1-10) shows a typical EIS diagram in both Nyquist and Bode planes.

## 1.9 Pt-based Catalysts

As already mentioned the desired catalyst for the ORR would reduce oxygen molecules to water via the 4-electrons pathway. In addition having high surface area and consequently more active sites, and also high chemical and electrochemical stability are key parameters to choose a catalyst. Platinum nanoparticles supported on carbon (Pt/C) because of short Pt-Pt bond lead to easy dissociative adsorption of  $O_2$ . Also, because of d-band vacancy of platinum there is a strong interaction between Pt atom and Oxygen atoms which weakens the oxygen-oxygen bond [57]. Considering these geometric and electronic structure factors, the ORR mechanism on Pt typically proceeds through a  $4e^-$  pathway. However, to reach the commercially affordable point it is not enough, certainly because of its short life time, low stability, high price and low abundance.

The first effort is to increase the surface area to mitigate the catalyst usage, by using as small as possible particles. However, it is important to be aware of the particle size effect on the reaction mechanism. With particles larger than  $5 \mu m$ , the formation of  $H_2O_2$  is negligible and process is almost a complete  $4e^-$  reduction of  $O_2$  to  $H_2O$ . At particles smaller than  $5 \mu m$ ,  $H_2O_2$  are produced more than  $H_2O$ , but for particles smaller than  $50 \text{ nm}$ , mass transfer is very fast and the formation rate of  $H_2O_2$  depends on the adsorption/desorption equilibrium and hence is independent of the particle size [43]. It is quite interesting that the shape of nanoparticles also affect the catalytic activity of platinum. So that the results reveal that the hexagonal Pt (111) and (100) nanoparticles exhibit an enhanced activity compared to spherical or cubic nanoparticles [58]. There are also

---

<sup>3</sup> Saturated Calomel Electrode

some studies [59] in which the platinum active sites were increased by making one dimensional platinum nanowires [60] or platinum nanotubes [61] or even porous three dimensional nanostructures. The aspect ratio increases by these methods to let have a less platinum usage.

To decrease the catalyst loading some researchers also use Pt-mono-layered materials or Pt-alloys as the catalyst. In this case it was reported that in addition to the lower Pt usage its catalytic activity also was improved. This improvement is mostly because of an appropriate change in electronic structure of the catalyst surface leading to a weaker Pt-OH interaction. This weakening of the Pt-OH bond makes the OH removal and O<sub>2</sub> adsorption and dissociation much easier with the effect of increasing the ORR activity. Zhang et al. [62] and Zhou et al. [63], showed experimentally and computationally respectively, that deposition of platinum monolayer on palladium surfaces significantly enhances its catalytic activity for the ORR. Vukmirovic et al. [64] went even further by mixing platinum with another late transition metal (Ir, Ru, Rh, Au, Pd, Re or Os) to create this monolayer on the surfaces of palladium nanoparticles or carbon-supported Pd nanoparticles. Comparing to pure Pt, these catalysts showed up to 20-fold increase in a Pt mass activity and are characterized by significantly lower Pt content. This superior activity was mainly due to a lower Pt-OH coverage by modifying the Pt electronic structure. Actually, low OH coverage on Pt is caused by the lateral repulsion between the OH adsorbed on Pt and the OH or O adsorbed on neighboring, other than Pt, late transition metal atoms [65].

Pt alloyed with suitable precious metals such as Ru, Ir, Pd, Rh, Os, Ag, Au or early transition metals such as Cu, Fe, Co, or Ni and even Cr and V have also been developed to overcome the challenging problem of the over-potential loss on cathode in the PEMFCs [46, 66-72]. In this regard Savadogo et al. [73] introduced Pt-Co on carbon as a promising cathode catalyst. In the case of Pt-Cu alloys, these catalysts exhibit 4 times enhancement of the ORR activity compared with that of pure Pt catalysts [74, 75]. This improvement is chiefly due to the effect of the other metals in shortening the Pt-Pt bond distance and consequently influencing the d-band vacancy of Pt [76]. The ORR activity on Pt-oxide alloys such as PtWO<sub>3</sub>/C and Pt-TiO<sub>2</sub>/C, Pt-NbO<sub>2</sub>/C and Pt-CeO<sub>x</sub>/C have also been examined. Among them, Pt-CeO<sub>x</sub> could be a unique system due to the high oxygen storage capacity of CeO<sub>2</sub>. Lim et al. [77] and also Lee et al. [78] reported that the ORR activity on Pt-CeO<sub>x</sub> cathode was higher than that of a commercial Pt cathode.

Core-shell structures are the other multi-component systems which recently have been studied. Among them the Pd/FePt nanoparticles with 5 nm Pd core surrounded with 1 nm FePt shell generate 12 times more current and a significantly higher stability than commercially pure-Pt catalysts for the same total weight [79, 80].

Catalytic activity of other noble metals including the 5<sup>th</sup> and 6<sup>th</sup> period, group 8B elements (Rh, Os, Ru, Ir, Pd and Pt as well) or their alloy with other non-noble transition metals was extensively studied as an alternative catalyst with activity as high as platinum and also much more abundance [81-95]. But, unfortunately even though in some cases they showed impressing activity toward the ORR, their stability is so weaker than the platinum that pushes the researchers to consider the stability parameter as important as the activity factor.

### **1.10 Non-Noble Metal Catalysts**

According to noble-metal catalyst problems such as cost, scarcity and stability in corrosive media, non-noble metal-based catalysts have been considered as the promising alternative. To be an appropriate alternative of Pt catalysts following four characteristics should be satisfied: (1) good catalytic activity, (2) good electrical conductivity, (3) long-term stability under acidic media and (4) low cost. Definitely, the most restrictive of these requirements is the stability. A variety of approaches has been taken to replace Pt/C catalysts and overcome these problems, with organometallic complexes [43, 96-98], chalcogenides [99, 100] and/or transition metals oxides [101-108], carbides [109], nitrides [110], oxy-nitrides [7, 11, 111] and carbo-nitrides [5]. However, so far, none of these catalysts has completely satisfied all the requirements described above.

Organometallic complexes and chalcogenides showed poor stability in acidic media. However, transition metal nitrides which are well known as valve metals are used as anticorrosion and coating materials, and the group 4 and 5 metal oxides, like Ti, V, Nb and Ta oxides, have high chemical stability in acids. Therefore, group 4 and 5 metal nitrides, oxides and oxy-nitrides are expected to be stable under an acidic and oxidative atmosphere. In addition it is reported that these compounds have some catalytic activity for the ORR. For instance, zirconium oxide [103, 105, 112], zirconium oxy-nitride [8], titanium oxide [104], tungsten carbide [113], tungsten carbide with tantalum addition [114], tantalum oxy-nitride [7, 10, 111], tantalum carbo-nitride [5, 102], niobium carbo-nitride [12] chromium carbo-nitride [5, 102], cobalt nitrides and carbo-

nitride [115] have shown a definite catalytic activity for the ORR and acceptable durability in an acid solution.

Titanium dioxide ( $\text{TiO}_2$ ) formed on a Ti plate in both alkaline and acidic medium has shown some catalytic activity for the ORR [116, 117]. The RDE tests confirmed the four-electron pathway in alkaline solutions and two-electron process in acidic solutions. But in both cases the onset potential for the ORR was much smaller than that of the Pt catalyst. The ORR occurred below 0.0 V (versus RHE) in a pH 1.05. Kim et al. [104] showed that heat treatment temperature and time affect its catalytic activity and stability by changing the oxidation state and crystalline structure.

Takasu et al. [108] also examined the binary oxides of Ti, Zr and Ta on Ti substrate in order to improve the ORR activity of these catalysts. Their investigations showed that  $\text{Ti}_{0.7}\text{Zr}_{0.3}\text{O}_x/\text{Ti}$  and  $\text{Ti}_{0.5}\text{Ta}_{0.5}\text{O}_x/\text{Ti}$  provided the highest ORR activity among Ti-based catalysts with onset potential  $E_{\text{ORR}} = 0.86$  V and  $E_{\text{ORR}} = 0.81$  V (vs. RHE) and current density for the ORR at 0.7 V (vs. RHE) equal to  $3.6 \mu\text{A}\cdot\text{cm}^{-2}$  and  $2.3 \mu\text{A}\cdot\text{cm}^{-2}$ , respectively.

$\text{Ta}_2\text{O}_5$  is also currently under assessment as an alternative Pt/C catalyst because of its high ORR activity and outstanding stability in corrosive environments [102, 118]. Analysis of the Pourbaix electrochemical equilibrium database indicates its stability under PEMFC acidic and oxidative condition [118]. Its onset potential ( $\sim 0.95$  V vs. RHE) is comparable to Pt ( $\sim 1.01$  V vs. RHE) but the poor electrical conductivity limits the reduction current.

Adding tungsten as a dopant to the nanoscale tantalum oxide catalysts also assisted the improvement of catalytic performance. The catalyst doped with W up to 32 mol % exhibited a high ORR onset potential of  $\sim 0.94$  V vs. RHE. The oxidation state of the Ta in  $\text{Ta}_2\text{O}_5$  is +5 where for W it is +6 and addition of tungsten cations generates excess oxygen anions in the tantalum oxide structure. These excess oxygen anions can decrease the resistance polarization caused by surface phenomena such as surface diffusion, by enhancing the surface transport mechanisms [101].

Moreover by adding the valve metals such as Ta, Ti, Zr and Nb to ruthenium oxides the stability has been improved [119, 120]. Having long-term stability and corrosion resistivity besides a lower cost, make these alloys promising catalyst materials. The ORR investigations done on vanadium oxides also introduced it as a viable cathode catalyst candidate [121].

Large quantity and low cost besides being environmental friendly material, made  $\text{Mn}_3\text{O}_4$  nanoparticles loaded on mesoporous carbon as a promising catalyst for the ORR in alkaline media. However, its stability in acidic media was insufficient. In addition to manganese oxides, manganese (III) oxo-hydroxide ( $\text{MnOOH}$ ) mixed with carbon also was investigated and showed some ORR catalytic activity. The results confirmed the dependence of the ORR activity to chemical composition, structure, morphology, and even  $\text{MnOOH}$  synthesis method. Whereas by increasing the  $\text{MnOOH}$  content (over 72 wt % up to 90 wt %) the number of electrons involved in the ORR and thus the ORR performance decreased [122].

Partially oxidized group 4 and 5 metal carbo-nitride powders had a definite catalytic activity for the ORR. In particular, Ishihara et al. [5, 102] showed that the partially oxidized  $\text{TaC}_{0.58}\text{N}_{0.42}$  had both high stability and good catalytic activity for the ORR in acid electrolyte. Both  $\text{TaC}_{0.58}\text{N}_{0.42}$  and  $\text{Ta}_2\text{O}_5$  had a poor catalytic activity for the ORR, while the onset potential of the partially oxidized  $\text{TaC}_{0.58}\text{N}_{0.42}$  specimen heat-treated for 8 h was 0.94 V vs. RHE. The main problem of this investigation is related to high energy demanding process of catalyst preparation.  $\text{Ta}_2\text{O}_5$  powder and carbon black were uniformly mixed, and the mixture was heat-treated at 1600 °C under a  $\text{N}_2$  atmosphere to make carbo-nitride [123]. It seems that the oxidation of  $\text{TaC}_{0.58}\text{N}_{0.42}$  introduces specific active sites on the surface which lead to its high onset potential. Also, mixing with the carbon black prepares a sufficient electrical contact between the active sites and the electrical collector to increase the efficiency of these active sites.

Early transition metal carbides including  $\text{TiC}$ ,  $\text{TaC}$ ,  $\text{MoC}$  and  $\text{WC}$  have been widely studied as a non-noble catalyst because of their electrical conductivities [124]. In particular tungsten carbide has electronic structure more like to Pt than to pure tungsten. However,  $\text{WC}$  is not enough stable under ORR conditions. Therefore, tantalum was added to  $\text{WC}$  in order to obtain better characteristics in stability and activity. It was shown that by addition of Ta to the pure  $\text{WC}$  the stability of the  $\text{WC}$  significantly increased. In addition, the onset potential for the ORR in the  $\text{WC} + \text{Ta}$  case was 0.8 V (versus RHE), which was 0.35 V more positive than that of pure  $\text{WC}$  catalyst [114].

### **1.11 Catalysts Preparation (Sol-Gel Method)**

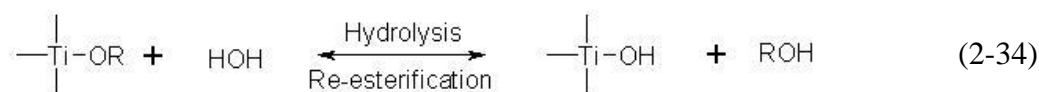
There are so many techniques in used to produce transition metal oxides, nitrides or even oxynitrides in the form of thin films or powders. Some of them which have been mentioned in

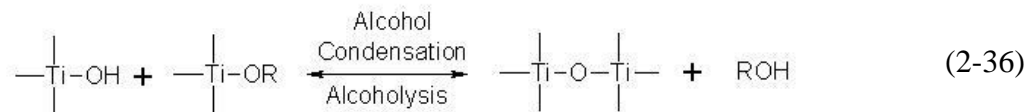
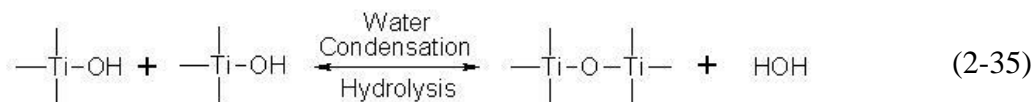
literatures to produce titanium and tantalum oxide or nitride or a mixture of oxide and nitride are summarized here: Electron Beam Evaporation [125, 126], Pulsed Laser Deposition (PLD) [127, 128], Cathodic Arcs Deposition [129], Chemical Vapor Deposition (CVD) [130-132], Atomic Layer Deposition (ALD) [133], Electrophoretic Deposition [5, 111], and Reactive and Magnetron Sputtering methods [7, 103, 114, 134-140]. In almost all these methods there are a heating process either as a post processing step or in situ step. Sometimes, there is a need to very high temperature to achieve the target material, especially when the goal is producing a nitride of titanium or tantalum.

In addition to all these mentioned techniques, Sol-Gel is one of the most appealing methods certainly to produce transition metal oxides because of its simplicity, easy conditional controlling and low cost. The Sol-Gel process or chemical solution deposition as a wet-chemical technique, involves two Sol and then Gel formation steps [141]. The term Sol states the dispersion of colloidal particles of one phase in a fluid medium. For example, when colloidal particles are suspended in air or water, the terms aerosol and hydrosol, respectively, are used [142]. Therefore particles in a Sol, by definition, are colloidal. The precursors for manufacturing these colloids comprise of a metal surrounded by different reactive ligands. Because of readily reaction with water, metal alkoxides — titanium isopropoxide and tantalum (V) ethoxide in this thesis — are the most popular precursors. But alkoxides and water are immiscible and usually a solvent such as an alcohol — ethanol in this thesis — is utilized to facilitate the reaction.

In the second step, by aggregating the Sol particles a wet network (Gel) in a continuous liquid phase is formed which after drying the trapped volatiles like water and alcohol leave out and the network shrinks to form the dry Gel [141]. Gel here is defined as a material containing a three-dimensional network of a solid phase mixed with a trapped and motionless continuous liquid phase.

Basically, there are two reactions used to describe the Sol-Gel process: hydrolysis and condensation. The result of condensation could be either water or alcohol. The general scheme of these reactions for titanium alkoxide could be seen in beneath:





The rate of hydrolysis and condensation are affected by several factors, however, among them temperature, time, pH, concentration and molar ratio of reactant and solvent are the most important parameters [141]. Therefore, by controlling these variables, structure and properties of the resulted materials could be changed. There are so many studies in which the Sol-Gel method was used to produce titanium oxide [143-148], or tantalum oxide [108, 149-155]. However, as much production of titanium or tantalum oxide by Sol-Gel method is easy, it is difficult to convert the prepared oxide to its nitride or oxy-nitride form. Therefore, these studies mostly followed a certain post processing or in situ steps such as heat treating under certain nitridizing gases (nitrogen or ammonia) at very high temperatures [156-168].

In this thesis a new non-oxide based Sol-Gel method is introduced to directly produce titanium or tantalum oxy-nitride. However, we also used heat treatment; results showed that this method was more effective than the conventional techniques to insert nitride into the oxide structure at relatively lower temperature. In this method which we call it in-situ urea-based Sol-Gel method, urea ( $\text{NH}_2\text{CONH}_2$ ) was used instead of water as a nitrogen source reagent. All steps of reaction were done under nitrogen to decrease the probability of oxygen existence as low as possible.

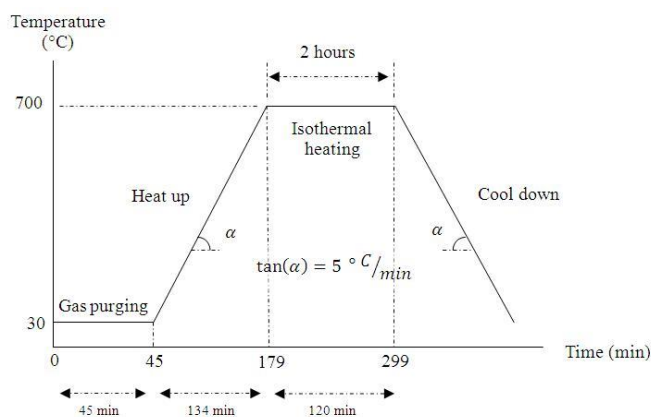


Figure 1-11: Heating schedule of heat treatment process

To change the crystallinity, particle size and specific surface area and also to convert oxide precursor to nitride or oxynitride, heat treatment was done on the yellowish red powders produced at the end of in-situ urea-based Sol-Gel method. In this regard, the dried powder was annealed in silica tube furnace (Model: 55031-A, 800 Watts, 115 Volts, by LINDBERG/HEVIDUTY) at 400 – 1200 °C for couple of hours under a specific atmosphere ( $N_2 + 3\% H_2$ ). Figure (1-11) shows a schematic heating schedule in which the powder was annealed at 700 °C for 2 hours. Heating and cooling rate of 5 °C/min was applied in all heat treatment process in this thesis.

## CHAPTER 2      LITERATURE REVIEW – PART B: AB INITIO SIMULATION

In this chapter all general information about quantum mechanics are extracted from the conventional quantum mechanics textbooks and certainly from [169-172]. In the case of need there are specific references for some of the covered materials.

### 2.1 Schrödinger Equation

At the present time, according to disability of classical mechanics of describing electron — because of its very light weight — there is no substitute for quantum mechanics to give the informative description of the electron distribution in detail. In quantum mechanics, the fundamental equation governing a non-relativistic system, which determines the time-dependent position of a particle by a complex wave-function  $\Psi(\{\mathbf{r}_i\}, t)$ , is the time-dependent Schrödinger equation,

$$i\hbar \frac{d\Psi(\{\mathbf{r}_i\}, t)}{dt} = \hat{H}\Psi(\{\mathbf{r}_i\}, t) \quad (3-1)$$

Where,  $\Psi(\{\mathbf{r}_i\}, t) \equiv \Psi(\mathbf{r}_1, \mathbf{r}_2, \dots, \mathbf{r}_N, t)$  is the many-body wave-function with  $\mathbf{r}_i := (x_i, y_i, z_i, s)$  augmented coordinate including the spin,  $\hat{H}$  is the Hamiltonian operator for the system of electrons and nuclei,  $\hbar = \frac{h}{2\pi} \cong 1.054571726(47) \times 10^{-34} \text{ J}\cdot\text{s}$  is the reduced Planck's constant and  $i = \sqrt{-1}$  is the imaginary unit. The wave-function  $\Psi(\{\mathbf{r}_i\}, t)$  does not have any physical meaning itself, and that is its magnitude-squared which determines the probability density of finding the particle at a certain position  $\mathbf{r}$  and at a given time  $t$ . This relation between the wave-function and probability distribution (P) is an integral over subspace  $\Omega$ , whereas P ought to be equal to 1, when  $\Omega$  covers all the space.

$$P_{(r,t)} = \Psi(\{\mathbf{r}_i\}, t)^* \Psi(\{\mathbf{r}_i\}, t) = |\Psi(\{\mathbf{r}_i\}, t)|^2 \quad (3-2)$$

$$P = \int_{\Omega} P_{(r,t)} d\mathbf{r} = \int_{\Omega} \Psi(\{\mathbf{r}_i\}, t)^* \Psi(\{\mathbf{r}_i\}, t) d\mathbf{r} \quad (3-3)$$

$$P = 1 \text{ when } \Omega = (-\infty, +\infty)$$

Where  $\Psi(\{\mathbf{r}_i\}, t)^*$  is the complex conjugate of the wave-function  $\Psi(\{\mathbf{r}_i\}, t)$ . In general, there are different approaches to solve the Schrödinger equation, however, those methods in which the solutions are found without reference to experimental data, are called *ab initio* (in Latin: *from the beginning*) or *first-principle* methods. Theoretically, chemical information and properties of a system might be obtained by solving this equation for all relevant electrons in the system. Before starting to explain different approaches to solve the Schrödinger equation, we simplify the time-dependent equation to the time-independent Schrödinger equation.

Time-dependent Schrödinger equation is a homogeneous partial differential equation in terms of time  $t$ , and spatial coordinates  $\mathbf{r}_i$  which could be solved by separation of variables method, with the proviso that Hamiltonian is independent of time. Therefore, one can write

$$\Psi(\{\mathbf{r}_i\}, t) = \Psi_r(\{\mathbf{r}_i\}) \times \Psi_t(t) \quad (3-4)$$

Substitution of this form of wave-function into time-dependent Schrödinger equation gives us:

$$i\hbar \frac{\partial \Psi_t(t)}{\partial t} = \frac{\hat{H} \Psi_r(\{\mathbf{r}_i\})}{\Psi_r(\{\mathbf{r}_i\})} = E \text{ (constant)} \quad (3-5)$$

It is trivial that two different functions of two independent variables could be equal if and only if they are equal to a constant. Therefore, according to that the left hand side of the equation (3-5) is a pure function of time  $t$ , and on the other hand, the right hand side of this equation is a pure function of space  $\mathbf{r}$ , they should be equal to a constant with the dimensions of energy (in consistent with the dimensions of the Hamiltonian), where we call that  $E$ . The related differential equation to the  $\Psi_t(t)$  (the left hand side of the equation (3-5)) is a first order homogeneous ordinary differential equation that can be easily solved, which gives us:

$$\Psi_t(t) = \Psi_{t_0} \times e^{\left(-\frac{i\hbar}{E}t\right)} \quad (3-6)$$

Substitution of the equation (3-6) into the definition of the probability density in equation (3-2), gives us:

$$\begin{aligned} P_{(r,t)} &= |\Psi(\{\mathbf{r}_i\}, t)|^2 = |\Psi_r(\{\mathbf{r}_i\})|^2 \times |\Psi_t(t)|^2 = |\Psi_r(\{\mathbf{r}_i\})|^2 \times \Psi_t(t)^* \Psi_t(t) \\ &= |\Psi_r(\{\mathbf{r}_i\})|^2 \times \left[ \Psi_{t_0} \times e^{\left(-\frac{i\hbar}{E}t\right)} \right]^* \left[ \Psi_{t_0} \times e^{\left(-\frac{i\hbar}{E}t\right)} \right] \\ &= |\Psi_r(\{\mathbf{r}_i\})|^2 \times |\Psi_{t_0}|^2 \times e^{\left(+\frac{i\hbar}{E}t\right)} \times e^{\left(-\frac{i\hbar}{E}t\right)} = |\Psi_r(\{\mathbf{r}_i\})|^2 \times |\Psi_{t_0}|^2 \end{aligned} \quad (3-7)$$

Considering that  $|\Psi_{t_0}|^2$  is a constant that can just accompany the  $\Psi_r(\{\mathbf{r}_i\})$  function, equation (3-7) implies the particle probability density's independency of time. Therefore, the remaining exponential part in equation (3-6), just introduces a phase-shift in the general  $\Psi(\{\mathbf{r}_i\}, t)$ , and it does not affect its magnitude. So, the main question would be the answer of the time-independent Schrödinger equation rather than its time-dependent form. Henceforward, we drop the subscript  $\mathbf{r}$  from  $\Psi_r(\{\mathbf{r}_i\})$ . Now, rewriting the right hand side of the equation (3-5) brings us to the time-independent Schrödinger equation in the following form.

$$\hat{H}\Psi(\{\mathbf{r}_i\}) = E\Psi(\{\mathbf{r}_i\}) \quad (3-8)$$

Definition of  $\mathbf{r}_i$  as  $\mathbf{r}_i := (x_i, y_i, z_i, s)$  and considering  $N$  particles in a system, gives us a system of partial differential equations, which according to the Hamiltonian form, are non-linear. This system of equations cannot be solved analytically and need a number of approximations and numerical tricks. Before introducing these approximations let us to define the Hamiltonian by more detail. Hamiltonian for a system of electrons and nuclei inside an external potential field (electromagnetic field) can be written as kinetic and potential energies of these particles:

$$\hat{H} = \hat{T}_n + \hat{V}_{n-n} + \hat{T}_e + \hat{V}_{n-e} + \hat{V}_{e-e} + (\hat{V}_{n-field} + \hat{V}_{e-field}) \quad (3-9)$$

Omitting the electromagnetic field effects (last two parameters in equation (3-9)) all other energies are defined in the following equations. To consider the external electromagnetic field effects see the reference [173].

$$\text{Kinetic energy of nuclei} \quad \hat{T}_n = - \sum_{l=1}^{N_{nuclei}} \frac{\hbar^2}{2M_l} \nabla_l^2 \quad (3-10)$$

$$\text{Kinetic energy of electrons} \quad \hat{T}_e = - \frac{\hbar^2}{2m_e} \sum_{i=1}^{N_{electrons}} \nabla_i^2 \quad (3-11)$$

$$\text{Nucleus-Nucleus coulomb interaction} \quad \hat{V}_{n-n} = + \frac{1}{2} \sum_{l \neq j}^{N_{nuclei}} \frac{Z_l Z_j e^2}{4\pi \epsilon_0 |\mathbf{R}_l - \mathbf{R}_j|} \quad (3-12)$$

$$\text{Electron-Electron coulomb interaction} \quad \hat{V}_{e-e} = + \frac{1}{2} \sum_{i \neq j}^{N_{electrons}} \frac{e^2}{4\pi \epsilon_0 |\mathbf{r}_i - \mathbf{r}_j|} \quad (3-13)$$

$$\text{Nucleus-Electron coulomb interaction} \quad \hat{V}_{n-e} = - \sum_{i,l}^{N_{electrons}, N_{nuclei}} \frac{Z_l e^2}{4\pi \epsilon_0 |\mathbf{r}_i - \mathbf{R}_l|} \quad (3-14)$$

Electrons are denoted by lower case subscripts and nuclei with charge  $Z_l$  and mass  $M_l$ , denoted by upper case subscript. Also  $\nabla^2$  is the Laplacian operator.

$$\nabla_i^2 = \left( \frac{\partial^2}{\partial x_i^2} + \frac{\partial^2}{\partial y_i^2} + \frac{\partial^2}{\partial z_i^2} \right) \quad (3-15)$$

## 2.2 Born-Oppenheimer Approximation

In a system of electrons and nuclei, electrons possess a very small part of the total mass. For instance, in the case of titanium containing 22 protons and 26 neutrons in each nucleus the

average nucleus mass is almost 100,000 times an electron mass. So, assuming a moderately uniform distribution of kinetic energy between the particles within a molecule — based on the equipartition law — the ratio of electrons and nuclei velocity is proportional to the inverse square root of their mass ratio. In the case of titanium, it means that electrons move almost 300 times faster than the nuclei. Therefore, from the electrons view point, nuclei are a kind of fixed points applying a steady force field (attraction) while electrons have enough time to arrange themselves based on the nuclei position. In contrast, electrons are not distinguishable particles for the nuclei but rather a kind of Potential Energy Surface (PES).

Born-Oppenheimer or adiabatic approximation allows us to consider the nuclei as fixed points and consequently as parameters for the electrons. Thereafter, it is trivial to take the  $\mathbf{R}$  as a parameter — we show it by symbolic  $\mathbb{R}$  — to find the related *electronic* wave-function, namely  $\Psi_e(\mathbf{r}, \mathbb{R})$ . So, the related acting Hamiltonian on  $\Psi_e(\mathbf{r}, \mathbb{R})$ , namely  $\hat{H}_e$ , will include  $\hat{T}_e, \hat{V}_{e-e}$  and  $\hat{V}_{n-e}$ , where in the last one we see the parameter  $\mathbb{R}$ . Because  $\hat{V}_{n-n}$  is a constant one can also add this to the electronic Hamiltonian, without affecting the electronic wave function. Solving the electronic Schrödinger equation explained in equation (3-16), gives us the electronic energy  $E_e(\mathbb{R})$  which acts as the Potential Energy Surface (PES) for the nuclei.

$$\hat{H}_e \Psi_e(\mathbf{r}, \mathbb{R}) = (\hat{T}_e + \hat{V}_{e-e} + \hat{V}_{n-e} + \hat{V}_{n-n}) \Psi(\mathbf{r}, \mathbb{R}) = E_e(\mathbb{R}) \Psi(\mathbf{r}, \mathbb{R}) \quad (3-16)$$

Therefore, to find the *nuclei* wave-function, namely  $\Psi_n(\mathbf{R})$ , we have to add this potential energy resulted from the electronic structure, to the nuclei Hamiltonian,

$$\hat{H}_n \Psi_n(\mathbf{R}) = (\hat{T}_n + E_e(\mathbf{R})) \Psi_n(\mathbf{R}) = E_{total} \Psi_n(\mathbf{R}) \quad (3-17)$$

Combination of equations (3-16) and (3-17) with the general Schrödinger equation explained in equation (3-9) gives the following simple result:

$$\Psi_{total}(\mathbf{r}, \mathbf{R}) = \Psi_e(\mathbf{r}, \mathbb{R}) \cdot \Psi_n(\mathbf{R}) \quad (3-18)$$

Therefore, instead of solving a complex system containing electrons and nuclei, with benefit of this adiabatic approximation, one should solve two, though coupled, simpler eigenvalue equations. This approximation is the first starting step in almost all computational quantum chemistry, and almost always solving the electronic Schrödinger equation and finding the electronic wave-function is the most demanding part. Now, it is time to attack this equation by introducing different approaches. However, one should be always aware to observe the Pauli Exclusion Principle. Based on the Pauli Exclusion Principle two electrons with a same set of quantum numbers cannot exist in an orbital while their spin is similar. In other word, if two electrons with similar spin were in one orbital, the obtained wave-function is not acceptable. How one can apply this restriction while trying to solve the electronic Schrödinger equation, is the subject of the next section.

### 2.3 Slater Determinants

Pauli Exclusion Principle is in fact a special case of a more general principal, namely antisymmetry principle, in which the wave-function should be antisymmetric with respect to the exchange of any two electrons,

$$\Psi(\mathbf{r}_1, \mathbf{r}_2, \dots, \mathbf{r}_i, \dots, \mathbf{r}_j, \dots, \mathbf{r}_{N_e}) = -\Psi(\mathbf{r}_1, \mathbf{r}_2, \dots, \mathbf{r}_j, \dots, \mathbf{r}_i, \dots, \mathbf{r}_{N_e}) \quad (3-19)$$

So, now the question is that how one can enforce this antisymmetric restriction to the electronic Schrödinger equation? John C. Slater had a very clever idea to do this, and it is using the slater determinant. Before explaining the slater determinant, it is need to recall the roll of atomic orbitals in this approach.

One of the most successful methods in describing a wave-function of a molecule or a system is using the atomic wave-function of the participating elements, in which we consider the atomic wave-functions ( $\chi(\mathbf{r}_i)$ ) or Atomic Orbitals (AOs) when in isolated atoms. These AOs actually play the role of mathematical basis sets to describe the molecular wave-functions or Molecular Orbitals (MOs). Considering  $N_e$  atomic orbitals for all the electrons in a molecule, and remembering that an orbital is a space function for an electron which determines the probability of finding the electron in a given region, now one can imagine any distribution of electrons inside

these non-interacting orbitals. Equation (3-20) shows one arbitrary distribution of electrons by assigning individual electrons to a product of the orbitals, although in general there is no preference which electron occupies which orbital.

$$\chi_1(\mathbf{r}_1) \cdot \chi_2(\mathbf{r}_2) \cdot \cdots \cdot \chi_{N_e}(\mathbf{r}_{N_e}) \quad (3-20)$$

In this regard, for  $N_e$  orbitals, there is  $N_e!$  permutation to be occupied by the electrons. Therefore, the total wave-function or in fact the MO must be described by a combination of these states. Slater determinant gives such a combination, in addition to satisfying the antisymmetry principle. The defined MO by this way is normalized as well by the normalizing factor  $\sqrt{N_e!}$ .

$$\Psi = \frac{1}{\sqrt{N_e!}} \begin{vmatrix} \chi_1(\mathbf{r}_1) & \chi_1(\mathbf{r}_2) & \cdots & \chi_1(\mathbf{r}_{N_e}) \\ \chi_2(\mathbf{r}_1) & \chi_2(\mathbf{r}_2) & \cdots & \chi_2(\mathbf{r}_{N_e}) \\ \vdots & \vdots & \ddots & \vdots \\ \chi_{N_e}(\mathbf{r}_1) & \chi_{N_e}(\mathbf{r}_2) & \cdots & \chi_{N_e}(\mathbf{r}_{N_e}) \end{vmatrix} \quad (3-21)$$

So, if one interchanges the coordinates of two electrons, it means that two columns inside the slater determinant is interchanged, which in turn according to the determinant properties it results to the minus of the previous one to the antisymmetry principle be satisfied. So far, the number of orbitals was same as the number of electrons, while in practice one can choose them from a given set of orbitals — consider an orbital as a mathematical space function. This way, for each combination of  $N_e$  orbital from a given set of  $N$  orbitals — as basis sets — we will have a wave function, namely  $\Psi_i$ . Finally the total wave-function described in the equation (3-22) should be obtained using minimization method applied by the variation principle.

$$\Psi = \sum_i \alpha_i \Psi_i \quad (3-22)$$

## 2.4 Hartree-Fock (HF) Method

Hartree-Fock (HF) approximation is based on a single Slater determinant, in which the atomic orbitals ( $\chi_i(\mathbf{r}_j)$ ) are obtained by applying the variational principle to minimize the related energy. In equation (3-16) we see that  $\hat{T}_e$  and  $\hat{V}_{n-e}$  are depends only on one electron coordinate while  $\hat{V}_{e-e}$  includes two electrons coordinates. By the following definitions for  $\hat{h}_i$  and  $\hat{g}_{ij}$  with advantage of the atomic unit we will have a new explain for the electronic Hamiltonian:

$$\hat{h}_i = -\frac{1}{2}\nabla_i^2 - \sum_l^{N_{nuclei}} \frac{Z_l}{|\mathbf{r}_i - \mathbf{R}_l|} \quad (3-23)$$

$$\hat{g}_{ij} = -\frac{1}{|\mathbf{r}_i - \mathbf{r}_j|} \quad (3-24)$$

$$\hat{H}_e = \sum_i^{N_{electrons}} \hat{h}_i + \sum_{j>i}^{N_{electrons}} \hat{g}_{ij} + \hat{V}_{n-n} \quad (3-25)$$

On the other hand by using the  $\mathbf{P}$  as a permutation operator, one can expand the total wave-function  $\Psi$  based on the atomics orbitals ( $\chi_i(\mathbf{r}_j)$ ). Where the sum over  $\mathbf{P}_{ij}$  generates all possible permutations of 2 electron coordinates and so forth.

$$\Psi = \frac{1}{\sqrt{N_e!}} \left[ \mathbf{1} - \sum_{ij} \mathbf{P}_{ij} + \sum_{ijk} \mathbf{P}_{ijk} - \dots \right] [\chi_1(\mathbf{r}_1) \chi_2(\mathbf{r}_2) \dots \chi_{N_e}(\mathbf{r}_{N_e})] = \frac{1}{\sqrt{N_e!}} \mathbf{P} \Pi \quad (3-26)$$

$$\mathbf{P} = [\mathbf{1} - \sum_{ij} \mathbf{P}_{ij} + \sum_{ijk} \mathbf{P}_{ijk} - \dots] \text{ and } \mathbf{P}\mathbf{P} = N_e! \mathbf{P} \text{ and } \mathbf{P}\hat{H}_e = \hat{H}_e \mathbf{P}$$

$$\Pi = [\chi_1(\mathbf{r}_1) \chi_2(\mathbf{r}_2) \dots \chi_{N_e}(\mathbf{r}_{N_e})]$$

According to the quantum mechanics principles and using the Dirac notations any observable like E can be obtained using its related operator by the following formula, when the wave-functions are orthonormal:

$$E = \langle \Psi | \hat{H}_e | \Psi \rangle = \int \Psi^* \hat{H}_e \Psi \quad (3-27)$$

Where based on the orthonormality we know that:

$$\int \chi_i(\mathbf{r}_1) \chi_j(\mathbf{r}_1) \cdot d\mathbf{r}_1 = \delta_{ij} = \begin{cases} 0 & \text{when } i \neq j \\ 1 & \text{when } i = j \end{cases} \quad (3-28)$$

Now, putting the equations (3-25) and (3-26) into the equation (3-27) and meanwhile using the orthonormality properties in equation (3-28) gives us:

$$\begin{aligned} E &= \langle \Psi | \hat{H}_e | \Psi \rangle = \left\langle \frac{1}{\sqrt{N_e!}} \mathbf{P}\Pi \left| \hat{H}_e \right| \frac{1}{\sqrt{N_e!}} \mathbf{P}\Pi \right\rangle \\ &= \sum_P (-1)^P \langle \Pi | \hat{H}_e | \mathbf{P}\Pi \rangle \\ &= \sum_P (-1)^P \left\langle \Pi \left| \sum_i^{N_{electrons}} \hat{h}_i + \sum_{j>i}^{N_{electrons}} \hat{g}_{ij} + \hat{V}_{n-n} \right| \mathbf{P}\Pi \right\rangle = \\ &\sum_P (-1)^P \langle \Pi | \sum_i^{N_{electrons}} \hat{h}_i | \mathbf{P}\Pi \rangle + \sum_P (-1)^P \langle \Pi | \sum_{j>i}^{N_{electrons}} \hat{g}_{ij} | \mathbf{P}\Pi \rangle + \sum_P (-1)^P \langle \Pi | \hat{V}_{n-n} | \mathbf{P}\Pi \rangle \\ &= \sum_i^{N_{electrons}} \langle \chi_i(\mathbf{r}_i) | \hat{h}_i | \chi_i(\mathbf{r}_i) \rangle \quad \rightarrow \{ \sum_i^{N_{electrons}} h_i \} \\ &+ \sum_{j>i}^{N_{electrons}} \langle \chi_i(\mathbf{r}_i) \chi_j(\mathbf{r}_j) | \hat{g}_{ij} | \chi_i(\mathbf{r}_i) \chi_j(\mathbf{r}_j) \rangle \quad \rightarrow \left\{ \frac{1}{2} \sum_i^{N_{electrons}} \sum_j^{N_{electrons}} J_{ij} \right\} \\ &- \sum_{j>i}^{N_{electrons}} \langle \chi_i(\mathbf{r}_i) \chi_j(\mathbf{r}_j) | \hat{g}_{ij} | \chi_j(\mathbf{r}_i) \chi_i(\mathbf{r}_j) \rangle \quad \rightarrow \left\{ \frac{1}{2} \sum_i^{N_{electrons}} \sum_j^{N_{electrons}} K_{ij} \right\} \\ &+ V_{n-n} \end{aligned} \quad (3-29)$$

$$\therefore E = \sum_i^{N_{\text{electrons}}} h_i + \frac{1}{2} \sum_i^{N_{\text{electrons}}} \sum_j^{N_{\text{electrons}}} (J_{ij} - K_{ij}) + V_{n-n} \quad (3-30)$$

In equation (3-30)  $h_i$  is in fact sum of the kinetic energy and attraction potential energy of the non-interacting electrons,  $J_{ij}$  is the repulsion potential energy of the electrons — namely coulomb integral — but there is no physical interpretation for the  $K_{ij}$  which in the Hartree-Fock formulation is called the exchange energy, because it comes from the exchanging electrons between two orbitals. Note that in the above formulation because of the orthonormality the phrases containing  $P_{ijk}$  and bigger permutations lead to zero.

At this point, using the variational method to minimize the energy  $E$ , will give us a set of MOs which should remain orthonormal. The result of the variational method is the following formulations:

$$\hat{F}_i \chi_i = \varepsilon_i \chi_i \quad (3-30)$$

Where, the Fock operator is defined as:

$$\hat{F}_i = \hat{h}_i + \sum_j^{N_{\text{electrons}}} (\hat{J}_j - \hat{K}_j) \quad (3-31)$$

In which  $\hat{h}_i$ ,  $\hat{J}_i$  and  $\hat{K}_i$  are the related operator to the already defined kinetic and potential attraction energy  $h$ , coulomb energy  $J$  and exchange energy  $K$  of the electron  $i$ , respectively.

Equation (3-30) — Hartree-Fock equation — is an eigenvalue equation, in which the energy  $\varepsilon_i$  of the orbital  $\chi_i$  is obtained by:

$$\varepsilon_i = \langle \chi_i | \hat{F}_i | \chi_i \rangle = h_i + \sum_i^{N_{\text{electrons}}} \sum_j^{N_{\text{electrons}}} (J_{ij} - K_{ij}) \quad (3-32)$$

So, the total energy would be:

$$E = \sum_i^{N_{\text{electrons}}} \varepsilon_i - \frac{1}{2} \sum_i^{N_{\text{electrons}}} \sum_j^{N_{\text{electrons}}} (J_{ij} - K_{ij}) + V_{n-n} \quad (3-33)$$

The importance of the Hartree-Fock equation (3-30) is that it has introduced a set of one-electron orbital equations instead of the multi-electron equation (3-16). To solve the Hartree-Fock equation iterative methods must be employed and a set of functions that is a solution to this equation is called Self-Consistent Field (SCF) orbitals.

So far the general formulation of the Hartree-Fock approach is described; however there are many other different methods based on this formulation which explaining them in detail is out of the scope of this thesis. In all of those methods expansion of the wave-function based on the Slater determinants is the main cornerstone. But using all possible determinants to reach a reasonable accuracy for big systems is computationally too expensive and time-consuming. On the other hand, there is another approach which is based on the Density Functional Theory (DFT). Because of relatively low computational cost and superior results for a many-electron system, DFT is becoming the technique of choice for large computational chemistry problems [174].

## 2.5 Density Functional Theory

Density Functional<sup>4</sup> Theory (DFT) is a way to solve the electronic Schrödinger equation, an alternative to the Hartree-Fock (HF) method or others which are not explained here such as Configuration Interactions. In fact, it is very similar to the HF approach by borrowing some of its technologies to solve the problem; however the accuracy is almost always better than the HF method while the computational cost — because of the explained reasons in the following paragraphs — is cheaper than the HF method. Therefore, in most of the computational quantum chemistry programs, the DFT module is on the HF module with some extra-subroutine to make it a DFT code.

The main idea of the DFT is work with  $\rho(\mathbf{r})$  which is the charge density not with the wave-functions  $\Psi(\mathbf{r}_1, \mathbf{r}_2, \dots, \mathbf{r}_i, \dots, \mathbf{r}_j, \dots, \mathbf{r}_{N_e})$  used in HF approach. It seems clear that working with a function of three spatial coordinates independent of the number of electrons  $N_e$  is much effective than working with a function which depends on  $4N_e$  coordinates, certainly for big molecules, from the computational point of view. The problem is that we know how to formulate the quantum mechanics in terms of the wave-function not of the density of electrons. For instance how could one calculate the energy or other properties of a system with density while we calculate all these properties with wave-function? That was a great advance made by Hohenberg and Kohn in which they realized that we could actually work with density. They proved that there is in principal a unique functional  $E[\rho(\mathbf{r})]$  that if we give the density we will get back the energy, and this is a one-to-one relation between the electron density of a system and its ground state energy. Hohenberg and Kohn first article at 1964 [175] explained in brief the following two theorems:

- The first one expresses that the ground state wave function and all properties of a many-electron system are a function of the total electronic charge density. According to this theory, the

---

<sup>4</sup> Functional is a function of another function, in which we use (square) brackets [] instead of parenthesis ()

properties of a system could be obtained by using functional, which in this case is the 3 spatial coordinates' dependent electron density.

- The second theorem defines energy functional for the system and according to variational principle it proves that the correct density is the one that minimizes this energy functional.

The only problem is that this functional is not known, and it is the main mission of the DFT to design these functionals. So the first work of Hohenberg and Kohn was a kind of existent theorem not a derivation method. However, it was enough to inspire the scientist to work with approximate functionals, so that presently there are a lot of approximations of DFT even though one cannot obtain the exact energy but a reasonable accuracy. These approximations are tested by experiments, and unfortunately there is not any hierarchy of complications or adding more terms to the approximated functional to give back a better result, such what we see in perturbation theory or in coupled clusters theory in which by adding more term we arrive to more accuracy.

### 2.5.1 Orbital-Free DFT Approach

Compared with the wave-function approach, Hamiltonian that describes the energy functional may be divided into three parts:

$$\hat{\mathbf{H}}_e = \hat{\mathbf{T}}_e + \hat{\mathbf{V}}_{e-n} + \hat{\mathbf{V}}_{e-e} \quad (3-34)$$

And based on that, energy functional would be written as the summation of kinetic energy functional  $T[\rho]$ , attraction between the nuclei and electrons  $E_{e-n}[\rho]$ , and electron-electron repulsion functional  $E_{e-e}[\rho]$ :

$$E[\rho] = T[\rho] + E_{e-n}[\rho] + E_{e-e}[\rho] \quad (3-35)$$

The nuclear-nuclear repulsion is a constant, so we just drop it here. The second term in equation (3-35) is fairly easy to determine. It is a coulomb attraction between a nuclear and density rather than an electron, thus one has to integrate of the coulomb equation over the all possible space smeared out with electrons:

$$E_{e-n}[\rho] = - \sum_l^{N_{nuclei}} \int \frac{Z_l \cdot \rho(\mathbf{r})}{|\mathbf{r} - \mathbf{R}_l|} d\mathbf{r} \quad (3-36)$$

For the last term in equation (3-35) in some level we expect something like equation (3-36). In fact, for instance, electron  $i$  has some density, electron  $j$  has some density as well, and they repel each other by the classical coulomb's law, in which a density times the other density divided by the distance between the electrons and finally integrate over the all possible locations of two electrons to give a six dimensional integral:

$$J[\rho] = \frac{1}{2} \int \int \frac{\rho(\mathbf{r}) \cdot \rho(\mathbf{r}')}{|\mathbf{r} - \mathbf{r}'|} d\mathbf{r} d\mathbf{r}' \quad (3-37)$$

We call this term  $J$  to be consistent with HF notation. In HF approach the antisymmetry principle was satisfied by using the Slater determinant in which we saw its contribution in the exchange operator  $K$ . In early attempts of deducing energy functionals for this exchange energy and also kinetic energy, a uniform electron gas model was considered. These attempts, in fact predating wave mechanics, in which Thomas and Fermi (1927) tried to express all the energy components as a functional of the electron density, however their method had a poor performance because of neglecting applying the exchange energy (at that time the existence of a unique energy functional of density was not yet proved). In Thomas-Fermi-Dirac (TFD) model this was compensated by insertion of the exchange part  $K_D[\rho]$ . For the uniform electron gas model we would have:

$$E_{TFD}[\rho] = T_{TF}[\rho] + E_{e-n}[\rho] + J[\rho] + K_D[\rho] \quad (3-38)$$

Where,

$$T_{TF}[\rho] = C_F \int \rho^{5/3}(\mathbf{r}) d\mathbf{r} \quad C_F = \frac{3}{10} (3\pi^2)^{2/3} \quad (3-39)$$

$$K_D[\rho] = -C_x \int \rho^{4/3}(\mathbf{r}) d\mathbf{r} \quad C_x = \frac{3}{4} \left( \frac{3}{\pi} \right)^{1/3} \quad (3-40)$$

Using a uniform electron gas model results fairly good for the valence electrons in certain metallic systems, however it fails for atoms and molecules because of its disability for predicting the bonding. Kinetic energy using this model is underestimated by ~10 % which could be reduced to ~1 % by adding another terms (Taylor expansion of T respect to the density as a variable). But again, the calculated energy has much lower accuracy than the HF method and also there is divergence problem of high order corrections.

## 2.5.2 Kohn-Sham Approach

Actually before Walter Kohn and Lu Jeu Sham's article in 1965 [176], DFT was not practical because of difficulties related to suggesting an appropriate and reasonable functional for the kinetic energy and exchange terms. They realized that if the electrons are non-interacting (quasi-independent) in the Hartree-Fock sense — in HF approach each electron just sees an average charge field of the all other electrons and there is no correlation between electrons — then one could just use the HF expression for the kinetic energy employing the orbitals. However, it should be just an approximation, not an exact kinetic energy, because electrons in reality are interacting. But, to the extent that HF approximation works pretty well, it is a reasonable approximation as well.

So, Kohn-Sham (KS) approach inserts back the orbitals into the DFT, in which one can easily calculate the kinetic energy by considering the quasi-independency condition,

$$T_S = \sum_i^{N_e} \left\langle \chi_i \left| -\frac{1}{2} \nabla^2 \right| \chi_i \right\rangle \quad (3-41)$$

The subscript  $S$  stands here for the Slater type orbitals. Therefore, mathematical complexity increases from 3 to  $3N_e$ . Now the question is that how one connect the density to the orbitals? Equation (3-42) explains this relation, in which the density is a sum over all occupied orbitals square's:

$$\rho = \sum_i^{N_e} |\chi_i|^2 \quad (3-42)$$

This is again an approximation because the orbitals are not arising from the *exact* density matrix. In fact, in this view one considers that all orbitals are completely occupied (occupation number = 1) or completely empty (occupation number = 0), however, in *Natural Orbitals* the orbital occupation number may be between 0 and 1.

To compensate all these missing kinetic energies and also to count the exchange energy, we use a new functional, namely Exchange-Correlation functional. So that, it is a summation of the difference between real kinetic energy and the kinetic energy obtained by the non-interacting concept, and the difference between the real electron-electron interaction and defined coulomb interaction:

$$E_{XC}[\rho] = (T[\rho] - T_S[\rho]) + (E_{e-e}[\rho] - J[\rho]) \quad (3-43)$$

And consequently,

$$E_{DFT}[\rho] = T_S[\rho] + E_{e-n}[\rho] + J[\rho] + E_{XC}[\rho] \quad (3-44)$$

So, Kohn-Sham reduced the problem of interacting electrons to an imaginary system of non-interacting electrons by introducing the exchange-correlation term. Presently, in all DFT programs first three terms in equation (3-44) are almost same and straight forward and different flavors of the DFT approaches arise from the difference in exchange-correlation functionals. Unfortunately we do not know what form exactly the exchange-correlation functional has, but because the exchange-correlation energy is roughly 10 times smaller than the kinetic energy, KS theory is much less sensitive to inaccuracy than the orbital-free approach. In this regard KS-DFT equation which looks like the HF equation (3-30) gives us the orbitals by the following equation:

$$\hat{h}_{KS}\chi_i = \varepsilon_i\chi_i \quad (3-45)$$

Where the Kohn-Sham electronic operator  $\hat{h}_{KS}$  is defined as:

$$\hat{h}_{KS} = -\frac{1}{2}\nabla^2 + V_{eff} \quad (3-46)$$

$$V_{eff}(\mathbf{r}) = V_{e-n}(\mathbf{r}) + \int \frac{\rho(\mathbf{r}')}{|\mathbf{r} - \mathbf{r}'|} d\mathbf{r}' + V_{XC}(\mathbf{r}) \quad (3-47)$$

These operators are consistent with the functionals in equation (3-44) and just the last piece  $V_{XC}(\mathbf{r})$  is the mysterious term which should be defined approximately. This term is in fact the derivative of the related exchange-correlation functional respect to the density:

$$V_{XC}(\mathbf{r}) = \frac{\partial E_{XC}[\rho]}{\partial \rho} \quad (3-48)$$

Therefore, as it was mentioned previously, specifying the exchange-correlation functional would give us the exchange-correlation potential and in turn the KS operator, which consequently gives back the orbitals by the KS equation (3-45).

## 2.6 Exchange-Correlation Functional

Normally, one breaks down the Exchange-Correlation functional into two parts: Exchange functional and Correlation functional:

$$\begin{aligned} E_{XC}[\rho] &= E_X[\rho] + E_C[\rho] \\ &= \int \rho(\mathbf{r})\varepsilon_X[\rho(\mathbf{r})]d\mathbf{r} + \int \rho(\mathbf{r})\varepsilon_C[\rho(\mathbf{r})]d\mathbf{r} \end{aligned} \quad (3-49)$$

Where,  $\varepsilon_X$  and  $\varepsilon_C$  are the exchange and correlation energy, respectively. There are a lot of approximations for these two energies or related functionals which explaining them is not possible here. However, just to have a flavor of different classes of these approximations some of the simpler kinds of them are explained in two categories: Local Density Approximation (LDA) and Generalized Gradient Approximation (GGA).

### 2.6.1 Local Density Approximation (LDA)

Local Density Approximation (LDA) means that the formulas just worry about what is happening in where the density is and not somewhere else. The main concept behind this approximation is lied on the uniform electron gas model, in which one supposes that the density is a slowly varying function (it is same everywhere). It is not super accurate, but somehow accuracy is acceptable. In this way, exchange functional is same as that in the orbital-free DFT approach:

$$E_X^{LDA}[\rho] = -C_x \int \rho^{4/3}(\mathbf{r}) d\mathbf{r} \quad C_x = \frac{3}{4} \left( \frac{3}{\pi} \right)^{1/3} \quad (3-50)$$

Therefore, we have:

$$\varepsilon_X^{LDA}[\rho] = -C_x \rho^{1/3} \quad (3-51)$$

This approximation for the exchange functional which has a very simple appearance is sometimes called the Slater exchange functional “S” or even Dirac expression. For the correlation part, the formula constructed by *Vosko, Wilk and Nusair (VWN)* [177] and by *Perdew and Wang (PW)* [178] is considered to be accurate fits. So, when one sees an exchange-correlation functional like *S-VWN* or *S-PW* it means that the exchange part is a Slater type exchange functional while the correlation part is the formula introduced by *VWN* or *PW*, respectively.

### 2.6.2 Generalized Gradient Approximation (GGA)

A way to achieve a better accuracy than what one obtains by LDA is expanding the functional at a certain point with adding the derivatives of the density at that point, exactly same as what we do in Taylor expansion of a function. It seems clear that by adding the first derivative of the density as a new variable we would specify the density at that point much more accurate. This approximation for developing functionals is usually called Generalized Gradient Approximation (GGA) or Gradient-Corrected methods [179]. Therefore, if in general we consider the LDA based functional such as:

$$E_{XC}^{LDA}[\rho] = \int f(\rho) d\mathbf{r} \quad (3-52)$$

In the case of GGA we have:

$$E_{xc}^{GGA}[\rho] = \int f(\rho, \nabla\rho) d\mathbf{r} \quad (3-53)$$

There are different types of GGA functional which could be found in literatures and just the name of some of them is mentioned here<sup>5</sup>. *PBE* (Perdew, Burke and Ernzerhof) is the one that is mostly used in our calculation as the both exchange and correlation functionals.

## 2.7 Basis Sets

To start the calculation, using the basis sets to describe the unknown orbitals or in general functions is unavoidable. Basis sets are different mathematical functions to describe the atomic or molecular orbital. Orbitals are usually expanded as a linear combination of these functions with proper weights or coefficient. Just remember the Fourier expansion of a periodic function  $f(x)$  with a wave length  $L$ , where we had:

$$f(x) = \sum_{n=0}^{\infty} \left\{ a_n \cos\left(\frac{2\pi n}{L} x\right) + b_n \sin\left(\frac{2\pi n}{L} x\right) \right\} \quad (3-54)$$

Expanding an unknown molecular orbital with an infinite set of known functions, namely a basis set, is exactly same as what we do in expanding a function with *cos* and *sin* functions in Fourier series. It is obvious that when one uses an infinite number of basis functions — complete basis set — there is no approximation. However, computationally it is not possible to use infinite number of basis functions and we have to enter approximation in our calculation using a finite number of basis functions to reduce the computational cost. The computational effort of first principal methods is roughly proportional to  $M_{basis}^4$ , in which  $M_{basis}$  is the number of functions in

a basis set. Therefore, reducing the number of functions of a basis set as small as possible is of prime importance. The possible minimum set of functions is normally called a *minimum basis*

---

<sup>5</sup> Such as LYP (Lee, Yang and Parr), PW91 (Perdew and Wang), P86 (Perdew), BPW91 (Becke, Perdew and Wang), BLYP and B3LYP (Becke, Lee, Yang and Parr), PBE (Perdew, Burke and Ernzerhof) and RPBE (Revised-Perdew–Burke–Ernzerhof) functional.

set. In addition to the number of basis sets, the type of basis functions also affects the accuracy. There are different types of basis sets, but according to the surface model (will be discussed in the next sections) they could be classified into two categories: the localized basis set and the plane wave basis set.

### 2.7.1 Localized Basis Sets

There are different types of localized basis sets — including functions with their origin at the center of atoms — but two most famous ones are: *Slater Type Orbitals* (STO) and *Gaussian Type Orbitals* (GTO). Slater type orbitals which are atomic orbitals (with quantum numbers  $n$ ,  $l$  and  $m$ ) are explained in equation (3-55) in spherical coordinate:

$$\chi_{\zeta,n,m,l}^{STO}(r, \theta, \varphi) = NY_{l,m}(\theta, \varphi)r^{n-1}e^{-\zeta r} \quad (3-55)$$

Where,  $Y_{l,m}$  are spherical harmonic functions determining the angular orientation of the orbital,  $\zeta$  controls the diffusivity of the radial component and  $N$  is the normalization constant described in equation (3-56):

$$N = \frac{(2\zeta)^{\frac{n+1}{2}}}{\sqrt{(2n)!}} \quad (3-56)$$

Equation (3-55) easily reveals that slater type orbitals have no radial points, but by combination of different STOs one could provide such nodes. This type of basis set has not any convergence problem because of existence of the exponential part, but exactly because of this part, taking two-electron integrals — introduced in for example exchange energy — is not analytically possible and increases the computational cost. These types of basis sets are usually used for small atomic and diatomic systems in which there is a need to a high accuracy. Otherwise, in most of the quantum programs this is the Gaussian type orbitals which are widely used. In this type of basis functions which are very similar to STOs changing the exponential part leads to possibility of evaluating the two-electron integrals analytically. Equation (3-57) and (3-58) demonstrate the GTO in both spherical and Cartesian coordinate:

$$\chi_{\zeta,n,m,l}^{GTO}(r, \theta, \varphi) = NY_{l,m}(\theta, \varphi)r^{2n-2-l}e^{-\zeta r^2} \quad (3-57)$$

$$\chi_{\zeta,l_x,l_y,l_z}^{GTO}(x, y, z) = Nx^{l_x}y^{l_y}z^{l_z}e^{-\zeta(x^2+y^2+z^2)} \quad (3-58)$$

Where, the sum of  $l_x + l_y + l_z$  defines the type of orbital. Therefore, according to this summation it is possible to define different types of GTOs such as s-type GTO, p-type GTO and d-type GTO. Although, GTOs significantly reduce the computation time, unlike the STOs they cannot explain the orbitals behavior's at two limits of distance: center of atom and far from the atom. At center of an atom, GTOs instead of having a cusp, like what we see with STOs, possess a zero slope. On the other hand, by increasing the distance far from the nuclear, GTOs fall off too rapidly and consequently are not able to express the real behavior of the tail of wave-functions. To compensate this weakness and achieve similar accuracy as STOs, one should normally employ GTOs three times the required STOs. Nevertheless, again computational cost with GTOs is yet much smaller than that with STOs, and it is why they are almost universally used basis functions in quantum chemistry calculations. There are also different techniques and methods in employing localized basis sets such as split-valance basis sets (double, triple and quadruple-zeta basis sets) — to split the valence electron from the core electrons — and polarized and diffuse basis sets, but it is out of the scope of this thesis to explain them here.

## 2.7.2 Plane Wave Basis Sets

In addition to localized functions (STOs and GTOs), delocalized *Plane Wave* (PW) basis sets are usually applied for the slab model and periodic boundary condition problems. A plane wave is the solution of one-electron Schrödinger equation in which the external potential is zero (wave equation). If we consider a free electron in one dimension with energy of E, the solution of Schrödinger equation could be written as:

$$\chi(x) = Ae^{+ikx} + Be^{-ikx} \quad (3-59)$$

or

$$\chi(x) = A \cos(kx) + B \sin(kx) \quad (3-60)$$

Where,  $k$  ( $k = \sqrt{2E}$ ) is the one-dimensional wave factor. Expanding this function into three dimensions and using wave vector  $\mathbf{k}$  gives us the plane wave's basis set:

$$\chi_{\mathbf{k}}(\mathbf{r}) = e^{i\mathbf{k}\cdot\mathbf{r}} \quad (3-61)$$

Because plane wave functions have infinite range and are in fact periodic functions, they are the most suitable choice of basis sets for infinite systems or in the other word for systems with periodic boundary conditions. In solid state and condense matter systems we see frequently the effect of this periodicity of structure and boundary conditions in determining the properties of the system. For instance, electrons in the valence bond of metals behave like a free electron which does not belong to any specific atomic center. They build band energy in which localized basis sets cannot properly explain that, and therefore, plane wave functions might be a good basis set to describe it. Plane Wave basis set is used in this thesis.

Normally, a limited number of plane-wave functions are used down to a specific cut off energy, because there is a relation between the size of the basis set and the value of the biggest wave vector  $\mathbf{k}$ . A typical spacing between  $\mathbf{k}$  vectors is  $\sim 0.01$  eV, therefore a cut off energy of 300 eV corresponds to a basis set with  $\sim 30\,000$  functions. Although at first glance PW size seems to be significantly larger than typical GTOs, the size of a PW basis set depends only on the size of the periodic cell not on the actual system, whereas the size of GTO basis set increases linearly by the size of the system. Table (2-1) compares generally some of advantages and disadvantages of two localized basis set and plane wave basis set.

## 2.8 Pseudo-Potential (Effective Core Potential)

Systems involving heavy elements such as  $\text{Ti}^{22}$  ( $[\text{Ar}^{18}].3d^2.4s^2$ ) or  $\text{Pt}^{78}$  ( $[\text{Xe}^{54}].4f^{14}.5d^9.6s^1$ ) contains a large number of core electrons which are unimportant in chemical sense for chemists. However, to correctly explain the valence electrons — due to the electron-electron repulsion between the valence electrons and core electrons — it is necessary to use a large number of basis functions to expand corresponding orbitals of the core electrons. On the other hand, core electron's speed is near to the speed of light and using the relativistic relations is unavoidable. To overcome this mathematical complexity and reduce the excessive and unessential computational

cost, using an alternative function to describe the core electrons is the method of choice in most of the well-known *ab initio* programs. Chemists usually call this function the “*Effective Core Potential*” while it is called “*Pseudo-Potential*” in physics community. This idea is also called “*frozen-core*” approach, in which the core electrons participate in calculations but their corresponding orbitals are fixed at their atomic values.

Table 2-1: Comparing advantages and disadvantages of localized and plane wave basis sets

Localized basis sets (STOs and GTOs)	Plane Waves basis sets
<p><i>Advantages:</i></p> <ul style="list-style-type: none"> <li>• fast convergence with respect to basis set size</li> <li>• no problem with finite systems</li> <li>• easy to parallelize by distributing the large data-set on different compute nodes</li> </ul> <p><i>Disadvantages:</i></p> <ul style="list-style-type: none"> <li>○ difficult to evaluate convergence quality (no systematic way to improve convergence)</li> <li>○ difficult to use (two- and three-center integrals)</li> <li>○ difficult to calculate forces</li> </ul>	<p><i>Disadvantages:</i></p> <ul style="list-style-type: none"> <li>○ slow convergence with respect to basis set size</li> <li>○ require super cells with finite systems</li> </ul> <p><i>Advantages:</i></p> <ul style="list-style-type: none"> <li>• easy to evaluate convergence quality (just increase cut off)</li> <li>• easy to use (Fourier transform)</li> <li>• easy to calculate forces</li> </ul>

When one uses GTOs as a basis set to expand the valence orbitals, because these functions are continues it is rational to use also Gaussian functions to describe the effective core potential. In the case of plane wave basis sets there are two main functions to describe the effective core potential: *Ultra Soft Pseudo-potential* (USP) and the *Projected Augmented Wave* (PAW). The latter is mostly used in our calculations.

## 2.9 Cluster and Slab Models

During the simulation there are two possibilities to model a surface: cluster and slab models [47]. In cluster model a limited number of atoms (10-50) — in order to decrease the computational cost — are presented to describe the surface. This model is appropriate for investigation of the small molecule properties and transition states of reactant on a surface and also for evaluating the chemisorption bond. In electrochemistry point of view, this model is attractive because of its

ability to account the solvent effect easier than the slab model. However, in solid states that we work with semi-infinite systems, to achieve an accurate electronic structure size of the cluster must increase significantly then convergence problem will appear.

To solve this problem, on the other hand, periodic boundary condition is used in the slab model to describe the surface. This periodic condition is applied along the surface in three spatial dimensions, so that each element in a cell exists exactly in corresponding places in adjacent cells. Normally, three or four slabs are needed to construct the so-called “super-cell” to obtain an effective model. The size of the surface unit cell determines the computational effect. If we want to investigate a reaction between a molecule and a surface, which is the case that we follow in this thesis, normally there is a reasonably big vacuum space on top of the slab inside a cell to avoid the effects of the adjacent cells on top of the surface. The same reason, if we want to use periodic condition to model a molecule (cluster) we have to choose a big unit cell including the molecule in middle of the cell. In slab model, in general, calculations give more plausible binding energies. But, because of the periodic condition, we cannot easily study the low adsorbate coverage cases by this model, and usually the solvent is ignored [27]. Figure (2-1) demonstrates an ethane molecule (cluster) and a graphite surface (slab) modeled both by periodic condition. For the ethane molecule the unit cell is big enough in all three dimensions, while in the case of graphite surface it is just elongated in  $z$  axis to avoid its interaction with periodic neighbours.

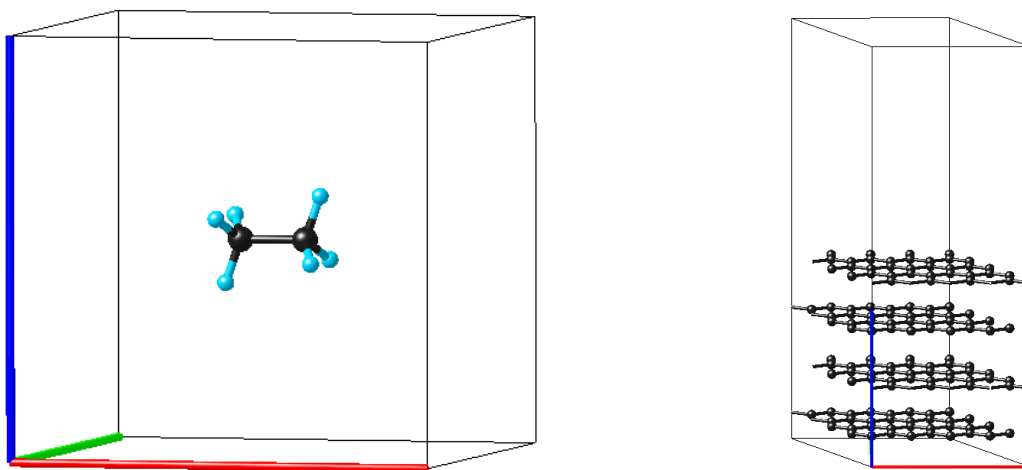


Figure 2-1: Ethane molecule (left) and graphite surface (right) both modeled by a periodic boundary condition slab model.

## 2.10 Brillouin Zone

Before defining the Brillouin Zones and talking directly about its importance in electronic structure calculations, it is necessary to explain a new framework, “reciprocal space”, for demonstrating a crystal (a structure with periodicity) rather the conventional using real space frame work. Normally, a crystalline system defines by three unit vectors namely  $\vec{a}_1$ ,  $\vec{a}_2$  and  $\vec{a}_3$  in real space coordinate. All dimensions in this real space coordinate (including unit cell vectors and the wave length of electrons,  $\lambda$ ) have dimension of length [ $m$ ]. However, reciprocal space is a different framework with dimension of inverse of length  $\left[\frac{1}{m}\right]$ . It is related to  $k$ -vector ( $k = \frac{2\pi}{\lambda}$ ) in the sense of both have same dimension and one may found the reciprocal space also with the name of  $k$ -space<sup>6</sup>. Following equations relate the unit vectors in reciprocal space to those in real space:

$$\begin{aligned}\vec{b}_1 &= 2\pi \frac{\vec{a}_2 \times \vec{a}_3}{\mathbb{V}} \\ \vec{b}_2 &= 2\pi \frac{\vec{a}_3 \times \vec{a}_1}{\mathbb{V}} \\ \vec{b}_3 &= 2\pi \frac{\vec{a}_1 \times \vec{a}_2}{\mathbb{V}}\end{aligned}\tag{3-62}$$

Where,  $\mathbb{V}$  is defined as the cell volume in real space:

$$\mathbb{V} = \vec{a}_1 \cdot (\vec{a}_2 \times \vec{a}_3)\tag{3-63}$$

This framework conveys certain detail of how interactions occur between a crystal structure and the waves much more elegantly than real space. It is able to highlight specific details much better than the real space information does. Based on the relations in equation (3-62) one can generate a

---

<sup>6</sup> In some text books, one may find a difference between the reciprocal space and  $k$ -space, so that  $k$ -space is defined by equation (3-62) but in reciprocal space one has to omit the  $2\pi$  term.

unit cell in reciprocal space equivalent to the crystal unit cell in real space. Therefore, for each lattice point in real space there is an equivalent in reciprocal space. However, these two unit cell may take completely two different shapes. For example, a Face Center Cubic (fcc) crystal in real space, has a Body Center Cubic (bcc) form in reciprocal space and vice versa.

Now, consider the region in the space that is closest to a given lattice point (in real space) than to any other lattice point. This region is called “Wigner-Seitz” cell. Generating this region is very simple and straightforward, so that one just need to draw the perpendicular bisector of any segment line connecting the considered lattice point to any other lattice points. The most inner region created by these planes is the Wigner-Seitz cell. So, now, doing the same procedure but in reciprocal space will give us the *first Brillouin Zone*. Therefore, the first Brillouin Zone is in fact the Wigner-Seitz cell about a lattice point in reciprocal space. Those perpendicular bisectors defined in the real space are called *Bragg Planes* in the reciprocal space. Keeping in mind the Bragg Planes definition, the first Brillouin Zone is the region in space which one can reach from the given lattice point in reciprocal coordinate (origin) without crossing a single Bragg Plane. By this definition one can obtain also the  $n^{th}$  Brillouin Zone by crossing exactly  $n-1$  Bragg Planes and no more. However, in study of the electronic structure of materials it is just the first Brillouin Zone which is used normally and by convention we call this only *Brillouin Zone* or (BZ). It seems clear that the Bragg Planes are the boundaries of the Brillouin Zone and using the Ewald’s sphere one can easily prove that the diffraction occurs in these planes.

According to the relation between the energy of an electron and its  $\mathbf{k}$ -vector ( $E = \frac{\hbar^2 \mathbf{k}^2}{2m}$ ), so it is easily possible to demonstrate this energy in different Brillouin Zones of a structure extended in  $\mathbf{k}$ -space. But the most attracting part in working in  $\mathbf{k}$ -space is related to the *Bloch’s theorem* which states that the wave-function value at equivalent positions in different cells of a periodic system are related together by a phase factor involving the lattice vector and the wave vector. Equation (3-64) explains the Bloch’s theorem in one dimensional periodic system:

$$\Psi(x + a) = e^{-ika} \cdot \Psi(x) \quad (3-64)$$

In which  $a$  is the lattice periodicity length. So, the problem of treating an infinite number of electrons transformed to only treating those within the unit cell and the first Brillouin Zone represents all zones or in the other word all energy bands are repeated of that in the first Brillouin Zone.

Working in the Brillouin Zone with  $k$  vectors significantly reduces the computational cost. However, to evaluate the introduced integrals in both HF and DFT approaches, we need to use numerical methods in which the  $k$  vector should be divided to more parts ( $k$ -points). Although, increasing the grid number ( $k$ -points) returns a better accuracy, it leads to more computational efforts and sometimes to divergence problem. In this thesis, all calculations were done in reciprocal space with a  $4 \times 4 \times 1$  grid mesh of  $k$ -vector in  $x$ ,  $y$  and  $z$  directions, respectively.

## 2.11 VASP

There are several different atomic scale codes that are commercially or freely available [180]. Vienna *ab initio* Simulation Package (VASP) [181-184] is the one that was used in this thesis to simulate the different steps of the ORR on titanium oxide, titanium nitride and platinum surface. VASP is a commercial computer program to calculate the ground state electronic structure of the system by an approximate solution to the many-body Schrödinger equation. In addition to both possibility of using DFT to solve the Kohn-Sham equation, and HF approximation to solve the Roothaan equation<sup>7</sup>, it is possible to benefit the hybrid functionals that mix the HF approach with DFT.

In this thesis we used this code to solve the Kohn-Sham equation (DFT approach) with an iterative numeric method<sup>8</sup> depicted in figure (2-2). We used the periodic boundary conditions and Plane-Wave basis sets with a cutoff energy of 400 eV to make sure of the convergence in energy.

---

<sup>7</sup> Roothaan equation is a representation of the Hartree-Fock equation in a non-orthonormal basis sets which can be of Gaussian-type or Slater-type.

<sup>8</sup> Like the Residual Minimization Method with Direct Inversion of the Iterative Subspace (RMM-DIIS) or blocked Davidson algorithms

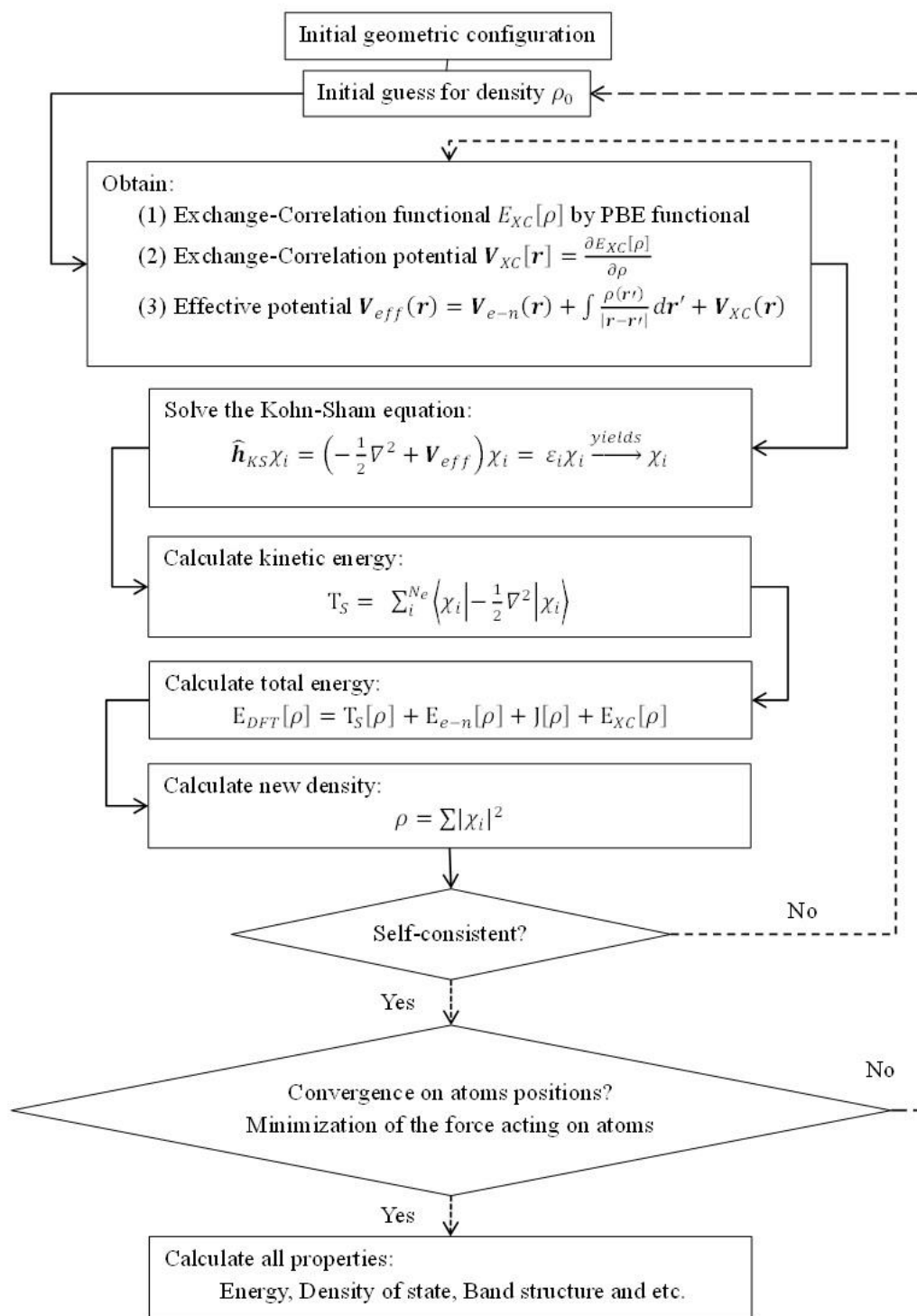


Figure 2-2: Schematic of self-consistent iteration calculations in VASP<sup>9</sup>

<sup>9</sup> <http://cms.mpi.univie.ac.at/vasp/vasp.pdf>

Electron-ion core interactions was represented by Projected Augmented Wave (PAW) approach [185, 186], while the General Gradient Approximation (GGA) of *Perdew, Burke and Ernzerhof* [187, 188] which is recognized as PBE was used as the exchange-correlational functional. The Brillouin zone integration was done on a grid of  $4 \times 4 \times 1$  with a Gaussian smearing width<sup>10</sup> of 0.2 eV and a Self-Consistence-Field (SCF) convergence criterion of  $1 \times 10^{-5}$  eV. Figure (2-3) shows the computer user interface windows to select the desired options.

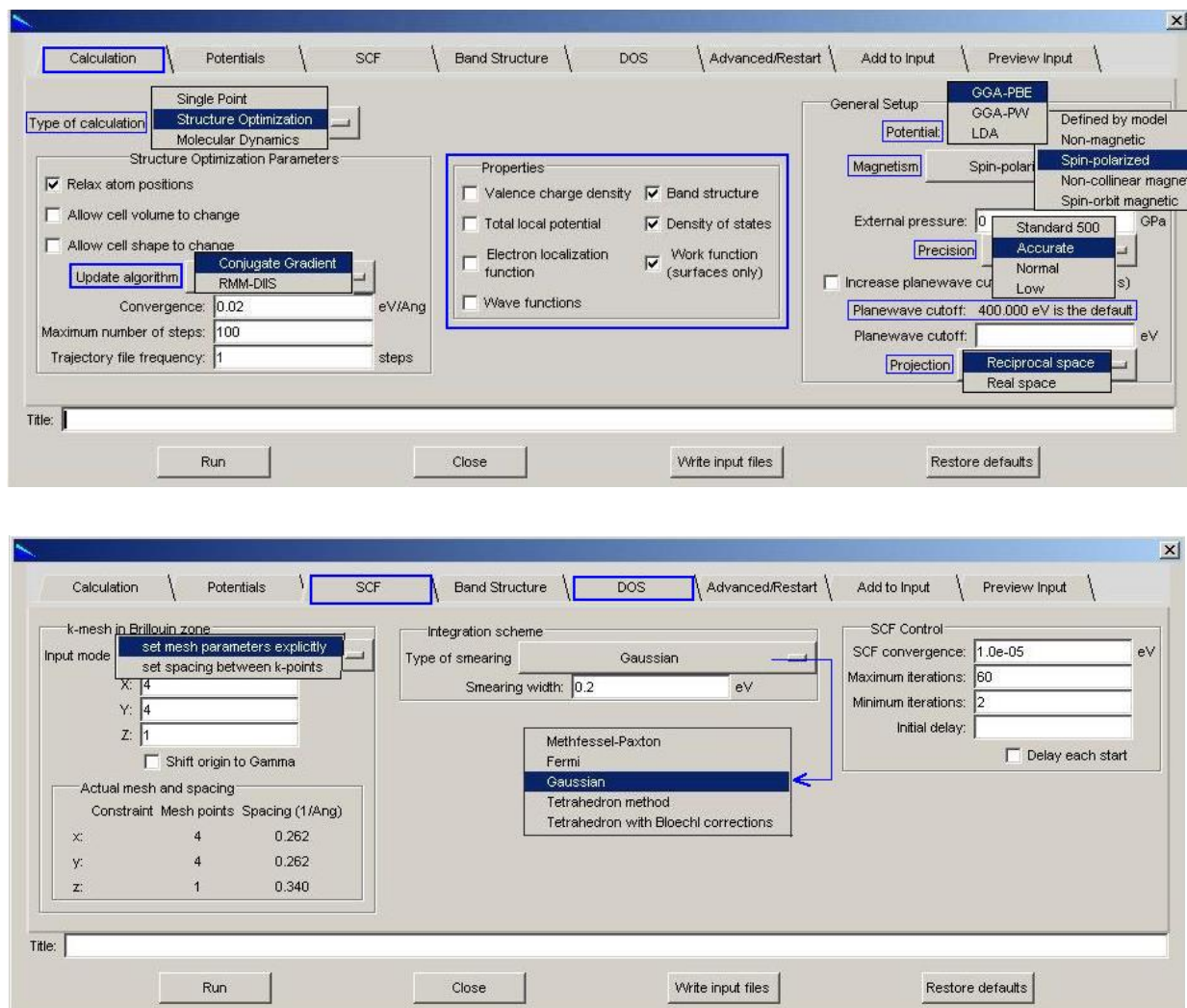


Figure 2-3: VASP user interface windows to select the desired options and adjust the parameters

<sup>10</sup> To determine the electron occupancies

## 2.12 Adsorption Energy Calculation

Adsorption energy is one of the most important parameters to determine the activity of a catalyst for a desired reaction. In the case of ORR strong molecular oxygen ( $O_2$ ) adsorption which followed by a weak hydroxide (OH) adsorption leads to a fast reaction, while a weak oxygen adsorption or a very strong adsorption of hydroxide results the blockage of the catalyst surface and slow reaction rate. In fact strong adsorption between oxygen molecule and catalyst surface weakens the oxygen-oxygen bond in a dissociative way, and afterward weak adsorption between hydroxide molecule and catalyst surface leads to fast desorption and consequently to release the catalyst active sites for the next coming molecules. To calculate the adsorption energy of an adsorbate on a substrate one has to calculate the energy of three systems separately: substrate alone, adsorbate alone and the system of adsorbate on substrate. Following equation gives us the adsorption energy obtained by VASP [27]:

$$E = E_{adsorbate} + E_{substrate} - E_{adsorbedsystem} \quad (3-65)$$

## 2.13 Density of State (DOS)

Before defining the Density of electronic State (DOS) let see what the Fermi energy  $\epsilon_F$  (Fermi level) is and what role in the DOS calculation it has. Fermi energy or Fermi level is the highest energy occupied by an electron at 0K. Therefore, at 0K electrons fill all the available energy state up to the Fermi level. However, increasing the temperature increases the electrons energy and lets them to be able to jump to the higher energy states. Fermi function<sup>11</sup> is used to find the probability that an energy state is occupied by electron at any given temperature:

$$f(\epsilon) = \frac{1}{e^{\frac{(\epsilon - \epsilon_F)}{kT}} + 1} \quad (3-66)$$

Where  $k$  is the Boltzmann's constant and  $T$  is the absolute temperature. It is clear that at temperatures near 0K, all energy states smaller than Fermi energy would be occupied, while the

---

<sup>11</sup> Also called the Fermi-Dirac distribution

higher energy states will be empty. However, increasing the temperature increases the occupation probability of those states. Now, consider a free electron inside a box of length  $L$  and volume  $V$  equal to  $L^3$ . Solving the Schrödinger equation gives the quantized energy levels:

$$\epsilon_n = \frac{\pi^2 \hbar^2 n^2}{2mL^2} \longrightarrow n = \left( \frac{2mL^2}{\pi^2 \hbar^2} \right)^{1/2} \epsilon_n^{1/2} \quad (3-67)$$

Where,  $n$  is the principal quantum number (which determines the energy state) and  $\hbar$  is the reduced Planck's constant. So, at 0K one easily can obtain the highest energy level which is the Fermi level:

$$\epsilon_F = \frac{\pi^2 \hbar^2 n_F^2}{2mL^2} \quad (3-68)$$

To find the number of electrons in a small energy range  $\epsilon$  to  $\epsilon + d\epsilon$  we have to multiply the density of states per unit energy range in that considered energy range. If we define  $D(\epsilon)$  as the density of states per unit energy range, therefore the number of electrons in a volume  $V$  is:

$$D(\epsilon)d\epsilon = \mathcal{N}(n)dn \quad (3-69)$$

In which,  $\mathcal{N}(n)$  is the density of states per unit  $n$  space volume. In fact, equation (3-69) declares that the total number of electron state in a specified volume can be counted over the state number ranges or the related energy ranges. Considering the possibility of existence of two electrons with different spins in a same state, and calculating the space volume between  $n$  and  $n + dn$  we have:

$$\mathcal{N}(n)dn = 2 \times \frac{1}{8} \times 4\pi n^2 \cdot dn = \pi n^2 \cdot dn \xrightarrow{\text{yields}} \mathcal{N}(n) = \pi n^2 \quad (3-70)$$

Therefore, according to equations (3-67) and (3-70) we have:

$$D(\epsilon)d\epsilon = \mathcal{N}(n) \frac{dn}{d\epsilon} d\epsilon = \pi n^2 \cdot \frac{dn}{d\epsilon} \cdot d\epsilon \quad (3-71)$$

$$\therefore D(\epsilon) = \pi n^2 \cdot \frac{dn}{d\epsilon} = \pi \cdot \left\{ \frac{2m\epsilon L^2}{\pi^2 \hbar^2} \right\} \cdot \left\{ \left( \frac{mL^2}{2\pi^2 \hbar^2} \right)^{1/2} \epsilon^{-1/2} \right\} = \frac{V}{2\pi^2} \left( \frac{2m}{\hbar^2} \right)^{3/2} \epsilon^{1/2} \quad (3-72)$$

So, the density of states per volume is:

$$\rho(\epsilon) = \frac{D(\epsilon)}{V} = \frac{(2m)^{3/2}}{2\pi^2 \hbar^3} \epsilon^{1/2} \quad (3-73)$$

Therefore, to find the number of electrons (not the electron states) in a given energy level we have to multiply the  $\rho(\epsilon)$  in  $f(\epsilon)$ . DOS is important because according to the interaction between different band states<sup>12</sup> explained in the next section, we see that it affects the adsorption strength between an adsorbate and a substrate. In this regard before jumping to the next section, we have to be familiar with some concepts: total number of states in a band, number of occupied states, fractional band filling, d-band center and  $d$ -band width. These concepts are defined by the following equations:

The total number of states in the band:

$$\mathcal{N}_{states} = \int_{-\infty}^{\infty} \rho \cdot d\epsilon \quad (3-74)$$

The number of occupied states:

$$\mathcal{N}_{occupied\ states} = \int_{-\infty}^{\epsilon_F} \rho \cdot d\epsilon \quad (62)$$

---

<sup>12</sup> In solid state physics the Band describes those ranges of energy that an electron within a solid may have. According to the quantum mechanics, we expect discretized energy levels, however, overlapping energy states of electrons in neighbouring atoms in a solid, leads to approximately continuous energy ranges that electrons can move through that. For different orbitals ( $s$ ,  $p$ ,  $d$  and  $f$ ) we may have different band states.

And according to equations (61) and (62) fractional d-band filling is:

$$f_d = \frac{\mathcal{N}_{occupied\ states}}{\mathcal{N}_{states}} \quad (63)$$

The  $d$ -band center  $\epsilon_d$  is defined as the average energy of the band:

$$\epsilon_d = \frac{\int_{-\infty}^{\epsilon_F} \rho E \cdot d\epsilon}{\int_{-\infty}^{\epsilon_F} \rho \cdot d\epsilon} \quad (64)$$

And finally the  $d$ -band width is defined as:

$$W_d^2 = \frac{\int_{-\infty}^{\epsilon_F} \rho E^2 \cdot d\epsilon}{\int_{-\infty}^{\epsilon_F} \rho \cdot d\epsilon} \quad (65)$$

Density of states obtained by VASP is based on the Fermi level, therefore in our calculations of  $d$ -band center or  $d$ -band width we have to adjust the upper interval of the integral as zero. Figure (2-4) shows DOS of two different titanium atoms (a and b) in TiN (200) which is in interaction with oxygen molecule. In one of them  $d$ -band center is below the Fermi level (a), while for the other one it is above the Fermi level (b). Position of the  $d$ -band center relative to the Fermi level is of importance in determining the bond strength, which is the topic of the next section.

## 2.14 $d$ -Band Theory

In study of the catalytic activity of a catalyst always physical property of its surface is of importance, especially in the case of transition metal catalyst used in heterogeneous reactions. Before, the local density of one-electron state at the Fermi level [189-192] and also the number of holes in the  $d$ -band [193] were considered as two simple effective parameters in determining the chemical reactivity of a surface. However, in 1995 Hammer and Nørskov [194] (and others in later studies [195-197]) stated that these two simple properties are not sufficient to understand all the system. They showed that considering the interaction between the metal  $d$ -states and both the bonding and anti-bonding molecular states is important to understand the reactivity of the surface. In this regard they mentioned the following three parameters as attributing properties of the surface to its ability of adsorbing or desorbing molecules [27]:

- (1) The position of the molecular bonding and anti-bonding states relative to the  $d$ -band of the metal (position of the  $d$ -band center  $\epsilon_d$ )
- (2) The degree of filling of the  $d$ -band  $f_d$
- (3) And the electronic coupling<sup>13</sup> between the molecular orbitals and the metal  $d$ -states

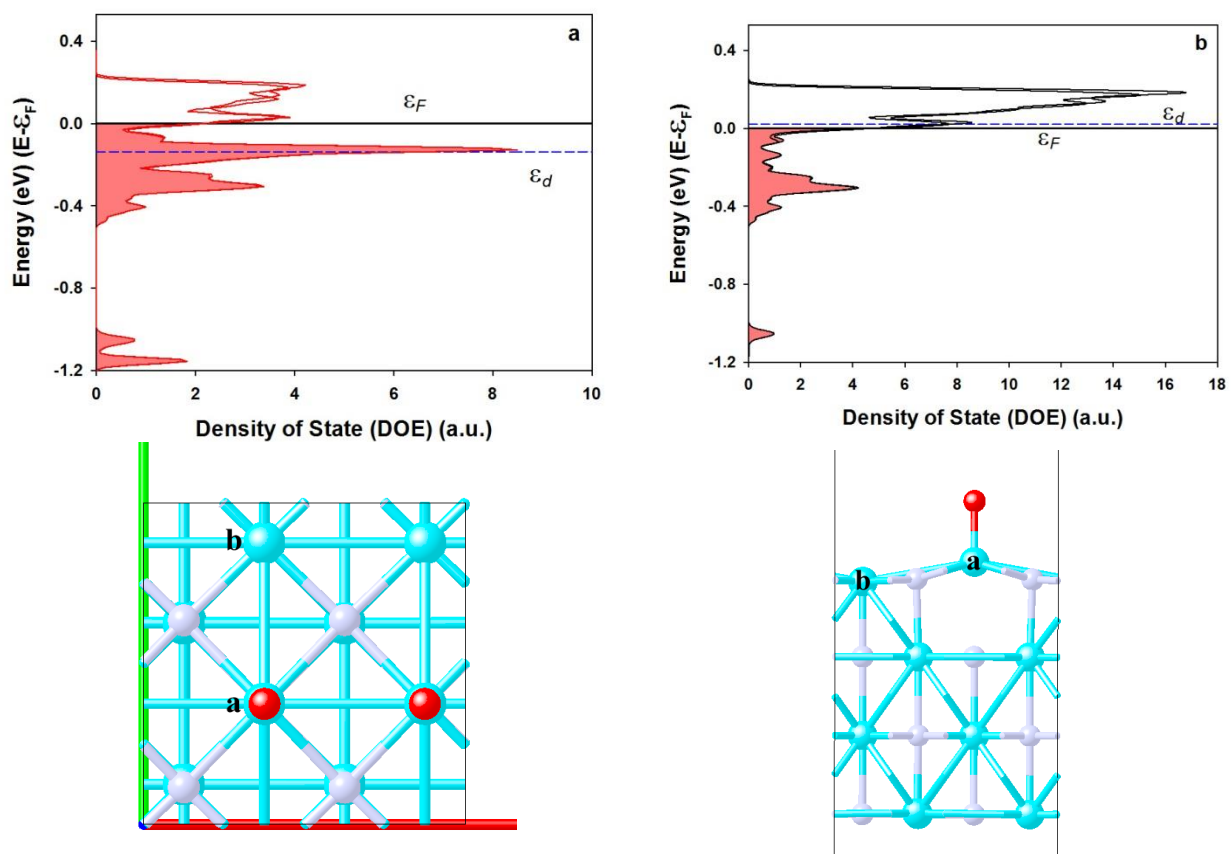


Figure 2-4: DOS of two different atoms in TiN (200) in interaction with O<sub>2</sub> molecule.

To simply explain these effects, consider a hydrogen molecule on top of a transition metal surface. First of all there is an interaction between hydrogen  $1s$  orbital and metal valance  $s$  band which according to the molecular orbital (MO) theory it leads to establishing a filled bonding orbital with lower energy and an empty anti-bonding orbital with higher energy. Although this interaction of  $s$  states is attractive, because the related electron coupling is almost same for a vast

<sup>13</sup> Electronic coupling is the interaction between molecular orbitals (electron donor and acceptor) which it is an important factor in controlling the electron transfer process.

variety of transition metals, it cannot be a determining factor. But, we see there is also an interaction between this hydrogen bonding state, namely called  $\sigma$ , and the  $d$ -band of the metal which leads to form a bonding  $d-\sigma$  state and an anti-bonding  $d-\sigma^*$  states. Filling the bonding state reinforces the adsorption of the hydrogen molecule on the surface, however filling the anti-bonding state destabilises that. The extent of the filling of the anti-bonding state is a function of the density of electron state of the metal surface, which varies from one metal to another and it might be an appropriate factor to evaluate the reactivity of the catalyst. To be aware of the extent of filling of the anti-bonding state, one can consider the position of the  $d$ -band center relative to the Fermi level. Figure (2-5) so beautifully shows the effect of  $d$ -band state position relative to the Fermi level on the extent of the anti-bonding filling. It seems obvious that higher energy of  $d$ -band center leads to less anti-bonding state filling and consequently stronger adsorption bound formation and vice versa.

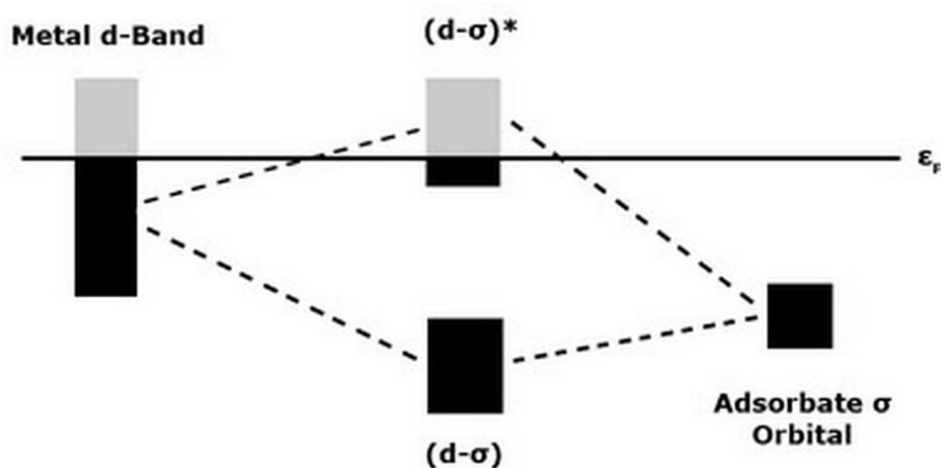


Figure 2-5: Schematic of the effect of d-band state position on the extent of anti-bonding filling<sup>14</sup>

<sup>14</sup> <https://sites.google.com/site/orrcatalysiswithptbasedcsnps/home/d-band-theory>

## CHAPTER 3 OBJECTIVES

Finding a new electro-catalyst for the ORR with high stability, activity and conductivity in addition to low cost and high abundance is the main challenge to commercialize the PEMFC technology. Producing an electro-catalyst with these properties with main focus on stability specification and also having a better understanding of the ORR on this electro-catalyst were the main objectives of this thesis.

Showing some catalytic activity for the ORR besides their high stability in corrosive media made the transition metal oxides and/or nitrides the most promising materials to reach us to our main objective. In this regard, titanium oxide, because of its high abundance and fairly low price, was selected. However, its evidently low electrical conductivity built this idea in mind to use titanium nitride in its structure as well. Therefore, titanium oxy-nitride was selected as the target electro-catalyst in this thesis. Showing a definitely high onset potential for the ORR, tantalum oxide also was considered to be mixed with titanium oxy-nitride to have a mixture of titanium and tantalum oxy-nitride. In this regard, to reach the main objective of this project, following specific objectives were tracked:

- Preparation of titanium and tantalum oxy-nitride by the Sol-Gel method
- Heat treatment under a specific gas ( $N_2 + 3\% H_2$ )
- Physicochemical characterization (XRD, EDS, XPS, SEM, BET)
- Electrochemical measurements (Polarization, CV, EIS)
- Evaluating the chemical and electrochemical stability (ICP-TOF-MS and CV)
- *ab initio* simulations of the reaction steps of the ORR on titanium nitride to find out some basic parameters such as adsorption energy, work functions, density of electronic states and electronic band structure of the system by Vienna *ab initio* Simulation Package (VASP)
- Correlation between the basic parameters of the catalyst and its performance for the ORR

**CHAPTER 4      ARTICLE 1: ELECTROCHEMICAL AND  
PHYSICOCHEMICAL PROPERTIES OF TITANIUM OXY-NITRIDE  
ELECTROCATALYST (TiO<sub>x</sub>N<sub>y</sub>) PREPARED BY FOUR DIFFERENT  
SOL-GEL METHODS FOR THE OXYGEN REDUCTION REACTION  
(ORR) IN ACID MEDIUM**

A. Seifitokaldani <sup>a,b</sup>, K. Oishi<sup>a,b</sup>, M. Perrier <sup>a</sup>, O. Savadogo <sup>a,b</sup>

<sup>a</sup> Chemical Engineering Department, Polytechnique Montréal, Montréal, QC, Canada

<sup>b</sup> Laboratory of New Materials for Electrochemistry and Energy, Polytechnique Montréal,  
C.P.6079, Succursale Centre-Ville, Montréal, Québec H3C 3A7, Canada

Submitted to: Journal of Electroanalytical Chemistry

The titanium oxy-nitride electrocatalysts were fabricated for the first time using four different sol-gel methods. The steps of each method of preparation were identified and optimised. The physicochemical properties (structure, chemical composition, BET surface area, surface morphology, chemical stability and electrochemical stability) were determined. The oxygen reduction reaction (ORR) in acid medium on these electrocatalysts (onset potential, charge density, Tafel slope, exchange current density, mass activity) were characterized and compared to those of Pt/C for this reaction. Their stability was also compared to those of Pt. The effect of the preparation method on the electrocatalytic parameters were investigated from the point of view of catalytic activity and stability. The stability of the titanium oxy-nitride electrocatalysts was correlated to their chemical composition and BET surface area. The effect of the precursors for the electrocatalyst preparation and the heat treatment up to 1100°C on the the chemical composition, surface area and electrocatalyst performances were established. The optimised preparation method, precursor and heating temperature to get the best electrocatalyst were deduced. This electrocatalyst based on TiO<sub>x</sub>N<sub>y</sub> with a high content of nitrogen exhibited one of the best onset potential (0.75 Volt vs NHE) obtained until now from a non-noble electrocatalyst for the ORR in acid medium.

**Key words:** titanium oxy-nitride, sol-gel, physicochemical and electrochemical characterization, oxygen reduction reaction (ORR)

## 4.1 Introduction

A Polymer Electrolyte Membrane Fuel Cell (PEMFC) converts chemical energy (oxygen and hydrogen) directly to electricity by two half electrochemical reactions taking place on the anode (oxidation of the hydrogen) and cathode (the reduction of the oxygen) side [1]. The PEMFC is the most promising alternative energy device in the near future because it exhibits a high theoretical efficiency, and operates at low temperature [2-6].

The platinum nano-particle (or platinum alloys [7, 8]) supported on carbon (Pt/C) is currently accepted as the state of the art commercial electrocatalyst used in PEMFCs, because of its high activity and high specific surface area [9]. However, the electrocatalytic activity for the Oxygen Reduction Reaction (ORR) on Pt based electrocatalyst is insufficient to obtain the required efficiency because the cathodic over-potential losses of this reaction in the cell operating conditions is 0.3 – 0.4 V [10]. As well, low abundances of Pt natural resources and its high cost are significant obstacles in the future commercialization of PEMFCs. On the other hand, sintering, dissolution and deposition of extremely dispersed Pt particles in the electrolyte and oxidation of a carbon support during long-term operation decrease the cell performance [11-16]. Therefore, development of new electrocatalyst with high activity and high durability in acidic conditions becomes one of the most important topics in the PEMFC research area.

Oxides and nitrides of transition metals of groups IV and V (like Ti, V, Nb and Ta, which are well known as valve metals), are used abundantly as anti-corrosion and coating materials and have high chemical stabilities in acidic media [17, 18]. In addition, it has been reported that these compounds have some electrocatalytic activity in the ORR [19, 20]. Transition metal oxides, such as zirconium oxide [21-23], titanium oxide [24-26], manganese oxide [27], tungsten oxide [28, 29], niobium oxide [24, 30, 31], cobalt and tin oxide [31] have been evaluated as electrocatalysts or catalyst-supports for the ORR. In particular, because of abundant natural resources of titanium oxide in comparison to platinum and the demonstration of its electrocatalytic activities for the ORR, titanium oxide has attracted the attention of researchers. It has been found that the catalytic activity of titanium oxide for the ORR might be affected by a surface state change, such as the crystalline structure and the work function [32]. Since an oxygen

molecule hardly adsorbs on a surface of perfect oxides, such as  $\text{TiO}_2$ , it is essential to form some defects in the oxygen adsorption sites on the catalyst surface while the metal is basically kept at the highest oxidation state [31, 33]. These surface defects, which lead to lower ionization potential and work function and, consequently, a higher density of the state of electrons, are mostly made by changing the crystalline during a heat treatment process [34, 35]. With all these, in spite of their high stability in acidic media, because of the low surface area and electrical conductivity, their mass activity was not acceptable for the PEMFC applications. For instance, the ORR hardly proceeds on the tantalum oxide because of the big gap between the upper energy level of the valence band and the Fermi level of tantalum oxide [36]. In order to narrow this wide band-gap of the oxides and make surface defects, it was shown that inserting N and/or C was the most effective method. In addition, transition metal nitrides and/or carbides have high electrical conductivity [37].

The study of the chemical and electrochemical properties of zirconium nitride, niobium nitride [33], cobalt nitride [38], tungsten carbide [39], chromium carbo-nitride and tantalum carbo-nitride [40, 41] showed that as a consequence of a large decrease in the Gibbs energy, transition metal oxides are thermodynamically more stable than carbo-nitrides and nitrides. Thus, these nitrides and carbo-nitrides were essentially unstable under the ORR conditions and easily oxidized at high oxidation potentials [42, 43]. Also, it was observed that the transition metal pure nitrides, such as  $\text{Ta}_3\text{N}_5$ , like those perfect oxides, shows poor catalytic activity for the ORR and the onset potential for the ORR was below 0.4V vs. RHE.

According to the preparation procedures, transition metal oxy-nitrides or partially oxidized carbo-nitrides would have these surface defects to reveal a definite catalytic activity for the ORR besides the chemical and electrochemical stability [10, 18-20, 34, 35, 44-47]. These properties change with the N/O ratio, from semiconductor behavior in oxygen-rich oxy-nitrides to high conductive and stable nitrogen-rich materials. As mentioned earlier, titanium compounds are among those oxy-nitrides, which have been developed as an attractive material. Titanium oxy-nitride has been synthesized by different methods, such as reactive sputtering [48, 49], Chemical Vapor Deposition (CVD) [50], the Solvo-thermal method [51], the hydro-thermal method [52], nitridizing titanium oxide under ammonia gas [53], oxidizing titanium nitride [54], the sol-gel method [55-60].

In this research, we focused on the sol-gel method, which is more widespread than others to produce titanium oxy-nitride. For the first time, a comprehensive comparison between four different sol-gel methods was carried out to evaluate the physicochemical and electrochemical properties of the produced oxy-nitride electrocatalyst for the ORR. For titanium oxides produced without any in-situ insertion of nitrogen sources, the electrocatalyst was labelled “O”. Then, when urea was added after the sol-gel process just to participate in the heat treatment process, the result was called “O+U”. In the two other methods, the nitrogen source took part in the sol-gel process to react with the titanium precursor. In these cases, when the nitrogen source was hydrazine, the result was called “H” and when it was urea, the name was “U”. X-ray diffraction (XRD), scanning electron microscopy (SEM), energy dispersive X-ray spectroscopy (EDS), BET surface analysis, as well as ICP-TOF analysis and other electrochemical measurements were done.

## **4.2 Experimental Procedure**

### **4.2.1 Materials**

Titanium (IV) isopropoxide [ $\text{Ti}(\text{O}i\text{C}_3\text{H}_7)_4$ ] (97%) was purchased from Sigma-Aldrich and used without further purification. Urea (reagent ACS 99%) and hydrazine monohydrate ( $\text{NH}_2\text{NH}_2 \cdot \text{H}_2\text{O}$ , 99%) as the nitrogen source were obtained from Fischer Scientific and Anachemia, respectively. Anhydrous ethanol was used as the mutual solvent.

### **4.2.2 Sol-Gel Procedure**

The flowchart in figure 1(a) describes the experimental procedure to prepare the titanium oxy-nitride precursor by the urea-based or hydrazine-based sol-gel method. The appropriate amount of monohydrated hydrazine or urea was firstly dissolved in 42 mL of absolute ethanol under a nitrogen atmosphere at room temperature. After 30 minutes, a determined amount of titanium (IV) isopropoxide (as the starting material) was added drop by drop to the solution with continuous stirring to achieve a molar ratio of metal source to urea (to obtain “U” sample) or hydrazine monohydrate (to obtain “H” sample) and solvent of 1:2:45. This reaction was very slow, and was allowed to continue through the night at 80 °C under reflux conditions in order to ensure completion of the reaction. However, in the case of hydrazine monohydrated, due to the

presence of water, a fast reaction between the titanium isopropoxide and water was observed. Then, the resulting homogeneous light yellow solution was dried at 140-150 °C while the color of the remnant slowly changed into yellowish red. The yellowish red precipitates were cooled down to room temperature and ground into fine powder. This step was done under nitrogen in a glove box to reduce as low as possible the probability of the presence of oxygen and moisture. The resulting precursors obtained by urea and hydrazine monohydrate were called “U” and “H”, respectively.

On the other hand, figure 1(b) shows the preparation method of the oxide-based catalyst. In this procedure, after dissolving an appropriate amount of titanium (IV) isopropoxide in a certain amount of ethanol (42 mL) under stirring conditions, specified amounts of de-ionized water were added to the solution drop by drop. Unlike the urea-based or hydrazine-based sol-gel method this reaction was very fast and small white particles appeared immediately after the addition of water. However, the reaction was continued for 6 hours. It was carried out in a cold water bath at 5 °C. Finally, using the vacuum filtration method, the white precipitate was separated from the excess of water and electrolyte. This sample, which was called “O”, was dried in a vacuum oven at around 80 °C for 24 hours. When a specified amount of urea was added to the separated precipitation before drying, the sample was called “O+U” and went to the furnace without drying in a vacuum oven. In all cases, the molar ratio of nitrogen source and titanium was two.

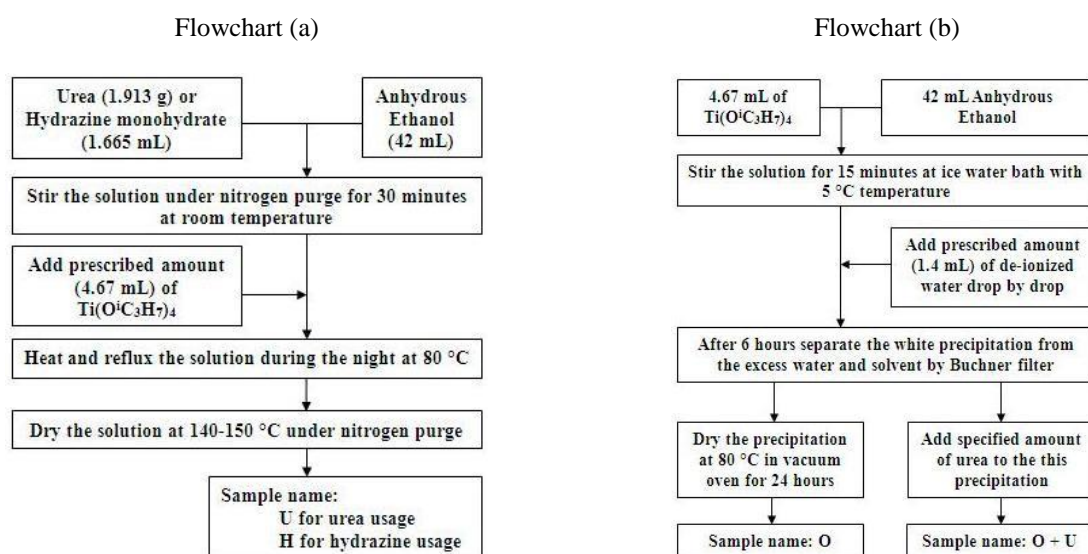


Fig. 1. (a) Schematic flowchart of the preparation of the oxy-nitride based electrocatalyst (b) Schematic flowchart of the preparation of the oxide based electrocatalyst.

### 4.2.3 Heat-Treatment

The obtained precursors were subjected to a specified nitridizing gas ( $\text{N}_2 + 3\% \text{H}_2$ ) with a 200 mL/min flow rate at 700, 900 and 1100 °C. This process was done in a silica tube furnace. Heat treatment converted the precursors to titanium oxy-nitride, and also changed the crystallinity, particle size and specific surface area and therefore, modified the property of the catalyst. After 45 minutes of gas purging, approximately 2 g of the precursors which had been placed in a crucible, were heated up to a desired temperature at a heating rate of 5 °C/min. Isothermal heat treatment time was 2 hours. The sample was then furnace cooled at the cooling rate identical to the heating rate.

### 4.2.4 Physicochemical Characterizations

In order to characterize the crystalline structure and phase identification, powder X-ray diffraction (XRD) data were collected using a Philips X'Pert diffractometer equipped with  $\text{Cu K}\alpha$  radiation ( $\lambda = 1.5406 \text{ \AA}$ ) (at 50 kV and 40 mA) in a scan range ( $2\theta$ ) from 10° to 85° at a speed of  $2^\circ \text{ min}^{-1}$ . Ti, O, N and C contents of different samples were roughly examined through a scanning electron microscope (SEM, JEOL JSM-840) equipped with an Energy Dispersive X-Ray Spectroscopy (EDS). The surface morphologies and particle size were observed through high resolution SEM (JSM-7600 TFE). A BET surface analyzer (Micromeritics Flow Sorb II 2300) was used to obtain the BET surface area of samples.

### 4.2.5 Electrochemical Measurements

All electrochemical experiments were conducted through a conventional 3-electrode cell containing 0.5 M sulfuric acid ( $0.5 \text{ mol}\cdot\text{dm}^{-3} \text{H}_2\text{SO}_4$ ) saturated with  $\text{N}_2$  or  $\text{O}_2$  at atmospheric pressure and 25 °C. Data acquisition was completed using a potentiostat/galvanostat model 273A (EG&G Princeton Applied Research, USA). The saturated calomel electrode ( $\text{Hg}/\text{Hg}_2\text{Cl}_2$  sat. KCl) and the platinum (Pt) mesh were used as the reference and counter electrodes, respectively, while the catalyst was employed as the working electrode. To prepare the working electrode, 10 mg of the prepared catalyst powder was added to a mixture of 480  $\mu\text{L}$  de-ionized water and 20  $\mu\text{L}$  Nafion 5 wt % by ultrasonic treatment for 10 minutes. Then, ca. 20  $\mu\text{L}$  of this ink was placed very slowly, layer by layer on a pre-polished glassy carbon rod (CH Instruments Inc. CHI 104, diameter = 3 mm). Before adding the next layer, the previous one must be dried completely to

have a uniform and fully covered surface. This step is very important to avoid the oxidation and reduction related to the glassy carbon rod during the measurements. The catalyst loading was ca.  $5 \text{ mg/cm}^2$  (geometric). All electrode potentials refer to the Normal Hydrogen Electrode (NHE) scale.

Cyclic Voltammetry (CV) in the range of 0.0 to 1.2 V (versus NHE) was performed to evaluate the electrochemical stability of the prepared catalysts. The scan rate was adjusted to  $100 \text{ mV.s}^{-1}$  and  $\text{N}_2$  gas was bubbled into the electrolyte solution at  $25^\circ\text{C}$ . After the CV had reached a steady state, Slow Scan Voltammetry (SSV) was performed at  $5 \text{ mV.s}^{-1}$  scan rate in both  $\text{N}_2$  and  $\text{O}_2$  atmosphere to evaluate catalytic activity for the ORR. Polarization curves were also obtained under nitrogen and oxygen with a  $0.1667 \text{ mV.s}^{-1}$  scan rate. Since the particle sizes of the specimens are different, the real surface area is hardly estimated. Therefore, the current density reflects the ORR activity for a determined amount of the powder. So, in this article the current density is expressed based on the mass of the working electrode (mass activity).

#### 4.2.6 Chemical Stability

To evaluate the chemical stability of the catalysts, Ti ion concentration was measured by the methods based on the Time of Flight-Inductively Coupled Plasma-Mass Spectrometry (TOF-ICP-MS) (LECO, RENAISSANCE) to figure out the dissolution percentages. The primary solution was  $\text{H}_2\text{SO}_4$  10 mM at  $50^\circ\text{C}$  containing 20 mg of the sample during 24 hours to find its chemical stability under fuel cell conditions.

### 4.3 Results and Discussions

#### 4.3.1 Physicochemical Characterizations

Figures 2-a and b show the XRD patterns of the  $\text{TiO}_x\text{N}_y$  catalysts produced by four different sol-gel methods after calcination at  $700^\circ\text{C}$ ,  $900^\circ\text{C}$  and  $1100^\circ\text{C}$  for 2 hours. Pure anatase  $\text{TiO}_2$  and TiN purchased from Fisher Scientific and Sigma-Aldrich, respectively, were used as references. The five diffraction peaks at  $2\theta$  of  $36.56^\circ$ ,  $42.54^\circ$ ,  $61.71^\circ$ ,  $73.99^\circ$  and  $77.89^\circ$  can be indexed as the cubic Fm3m unit cell of TiN [(111), (200), (220), (311) and (222)] with  $a=4.2417 \text{ \AA}$  and  $\alpha=90^\circ$  cell parameters. As well, strong diffraction peaks at  $25.25^\circ$ ,  $37.75^\circ$ ,  $47.95^\circ$ ,  $53.79^\circ$  and  $55.05^\circ$  are respectively assigned to (101), (004), (200), (105) and (211) facets of the Anatase

structure of titanium dioxide micro powder. All peaks are in good agreement with the standard spectrums (JCPDS No. 38-1420 for TiN and No. 21-1272 for TiO<sub>2</sub>).

In the case of the sample obtained from “O” method, it is obvious that the Anatase phase changed to the Rutile phase in all temperatures, however, in the case of the sample fabricated from “H” a small Anatase 101 peak was observed at 25.25° at 700 °C, which vanished at higher temperatures. This phase change from Anatase to Rutile also took place in the samples obtained from the “U” and “O+U” methods, respectively. In these last cases, the intensity of the Rutile peaks decreased when the heat treatment temperature increased to 900 °C and 1100 °C. After carefully looking at figure 2-a it is evident that there is no sign of the presence of the 5 identified TiN peaks in the electrocatalyst prepared from the “O” and the “H” method. On the other hand, there is a good compatibility with the pure Rutile related peaks. This is an indication that the significant amount of the electrocatalyst prepared using the “O” and “H” methods, was TiO<sub>2</sub> even at high temperatures.

Inversely, the TiN peaks, are obviously observed in the samples fabricated using the “O+U” and “U” methods (Fig. 2-b). The XRD patterns of these samples are not in agreement with those of the Rutile peaks, especially at temperatures higher than 700 °C. This indicates that there was an important amount of TiN in the samples prepared by “U” and the “O+U” methods. For all the samples prepared using these last two methods, the intensity of the TiN related peaks increased with the heat treatment temperature.

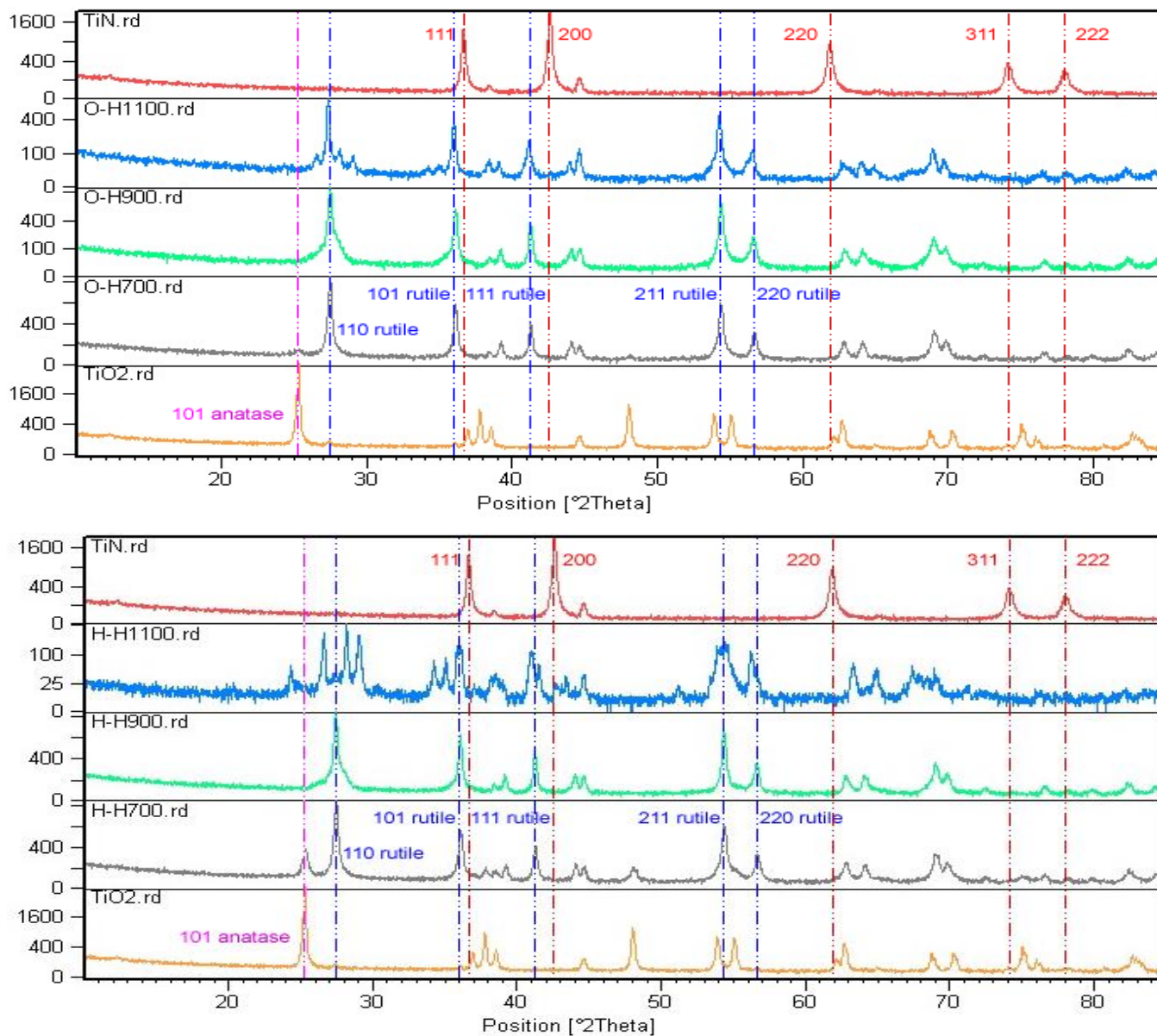


Figure 2-a. XRD results of titanium oxy-nitride powder prepared by “O” (top) and “H” (bottom) methods and annealed at 700, 900 and 1100 °C for 2 hours; TiN (in top) and TiO<sub>2</sub> (in bottom) reference materials.

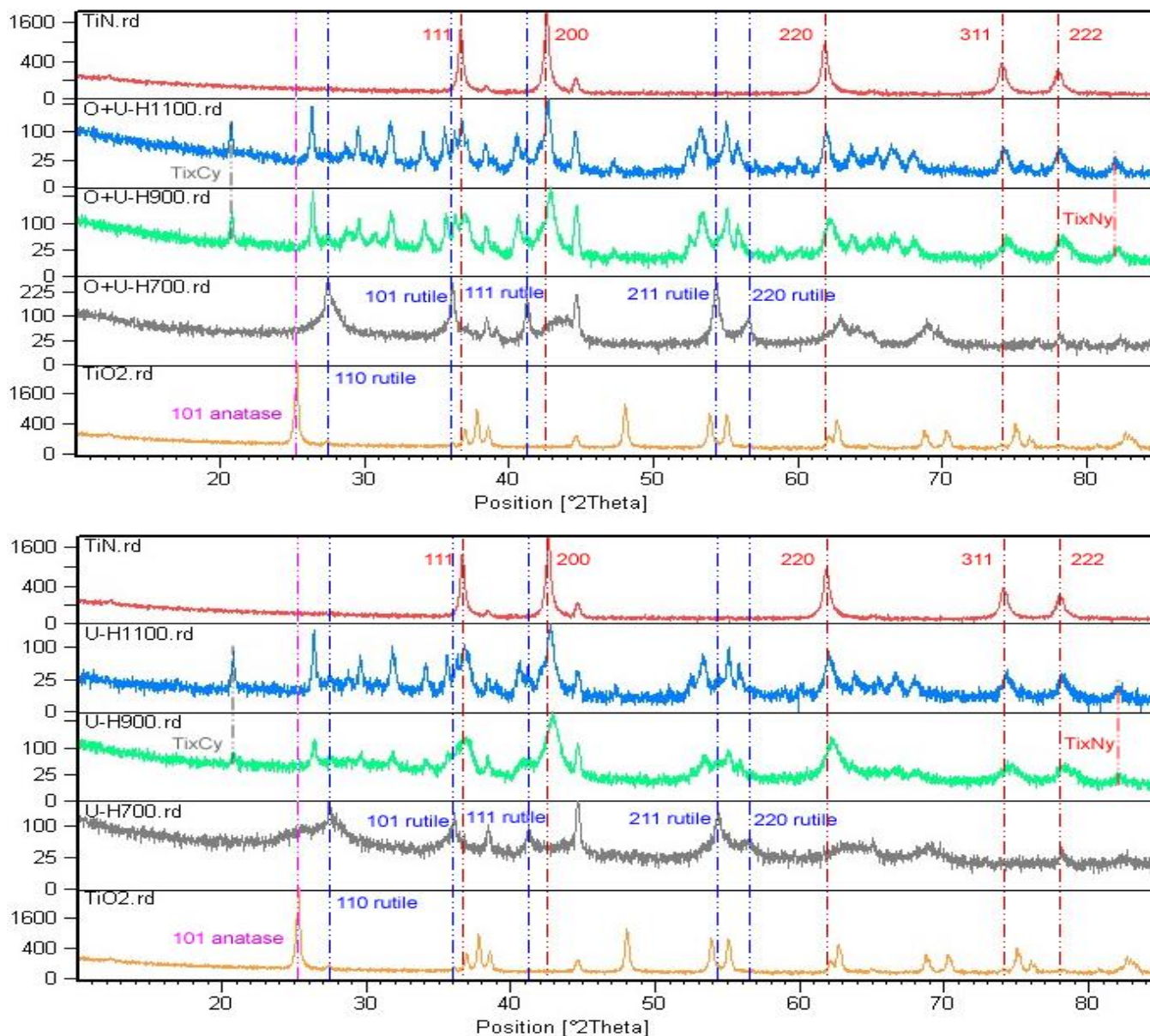


Figure 2-b. XRD results of titanium oxy-nitride powder prepared by “O+U” (top) and “U” (bottom) methods and annealed at 700, 900 and 1100 °C for 2 hours; TiN (in top) and TiO<sub>2</sub> (in bottom) reference materials.

These different XRD patterns show also that the various samples may not contained pure TiN or TiO<sub>2</sub>, but a mixed of TiO<sub>2</sub> and TiN. Effectively, the XRD patterns of Fig.2 show that over the (111) and (200) TiN diffractions, at around 38° and 44°, there are some small peaks in all the samples, which could belong to both TiN and Anatase TiO<sub>2</sub>. According to the Ti and O phase

diagram [61], the possibility of the Anatase existing at temperatures higher than 600 °C is too small. Therefore, these peaks must belong to TiN. The peaks exist in all the samples, and it should be mentioned that the TiN phase may exist in all of them, even those prepared by “O” and “H” methods. Therefore, there were both TiN and Rutile TiO<sub>2</sub> phases with different ratios in the catalysts, and these samples were labelled as TiO<sub>x</sub>N<sub>y</sub> with different amounts of x and y. The amount of x might be higher than that of y in the case of the samples fabricated from the “O” and “H” methods and the amount of y might be higher than that of x in “U” and “O+U” methods. Extracting these peaks, which are indicated by the blue and red dash lines, it is possible to see some other peaks. They do not belong to the pure TiN nor pure TiO<sub>2</sub>, but are characteristic diffractions of TiO<sub>x</sub>N<sub>y</sub>. Certainly, in the case of “O+U” and “U”, in figure 2-b, at 26.3°, 40.5°, 53° and 54.5° these characteristic peaks are evident. These results on the TiO<sub>x</sub>N<sub>y</sub> are in good agreement with those obtained elsewhere [59].

Using Urea in the heat treatment step or during the sol-gel process also led to the imperfect composition of Ti, C and N elements. So that, in both the “U” and “O+U” samples, at 20.8° and 82.7°, there were Ti<sub>8</sub>C<sub>5</sub> and Ti<sub>4</sub>N<sub>x</sub>, respectively. From the XRD patterns we have concluded that the nitrogen content relative to the oxygen content in the prepared “O+U” and “U” samples was considerable. This was proven by taking the EDS analysis of all the samples heat treated at 900 °C. The results are depicted in figure 3. This ratio further increased with rising temperatures.

We might conclude that using urea in the heat treatment step or the sol-gel process was more effective than the other two methods to avoid having the titanium oxide in the catalyst. In addition, the “H” method was in turn more effective than the “O” method. Fewer TiO<sub>2</sub> peaks observed for the “H” method indicates that more defects are present on the electrocatalyst, which in sequence leads to an improved ORR process by easing the oxygen adsorption. In addition, the diffraction intensity increased with increasing particle size. These results suggested that the nano-sized powders were obtained by the sol - gel method and heat treatment, because of their relatively low intensity compared to the TiO<sub>2</sub> and TiN micro powders. However, increasing the temperature made the peaks much sharper, which indicates the growth of the crystalline structures.

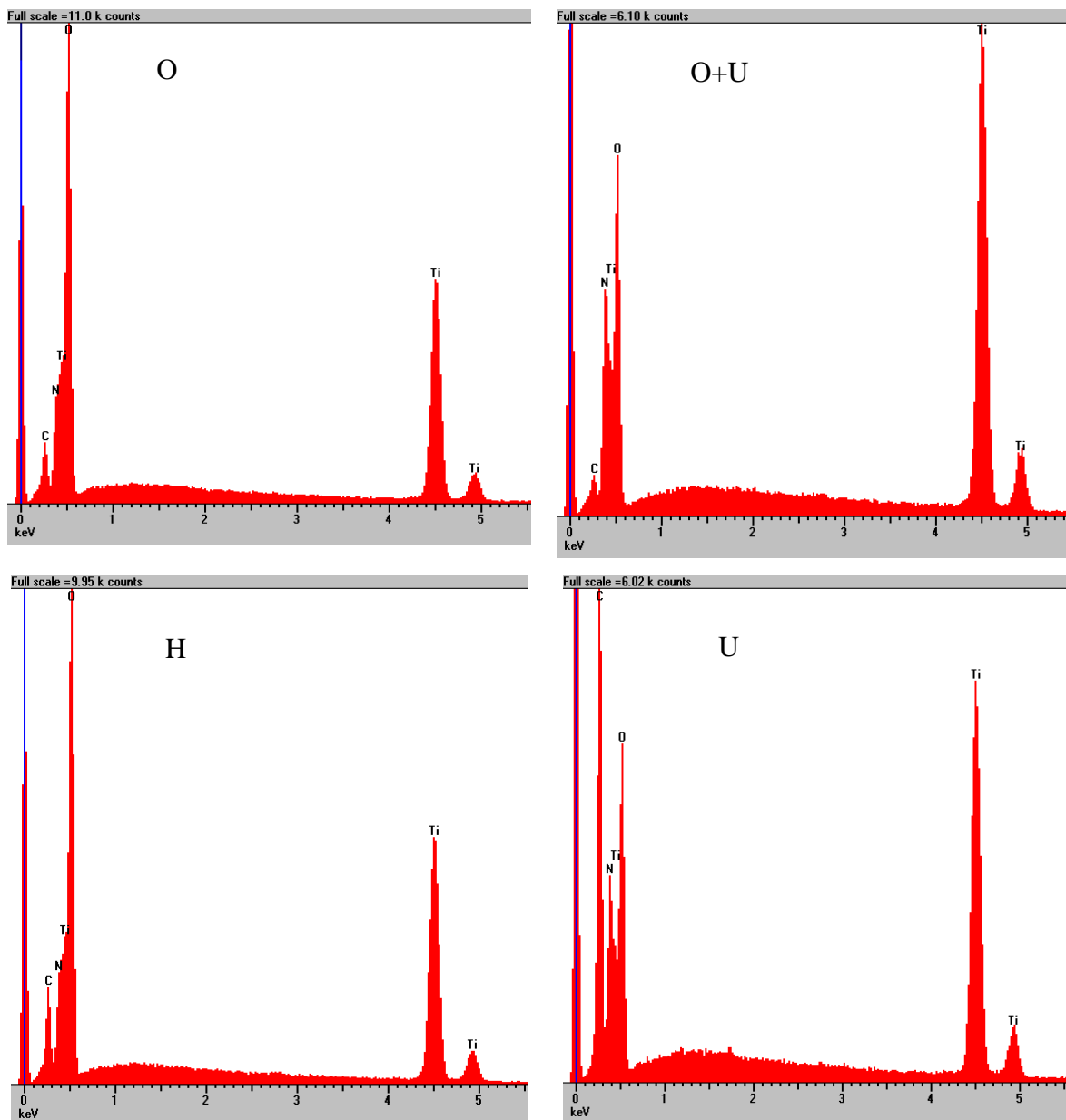


Figure 3. Results of the EDS analysis of the  $\text{TiO}_x\text{N}_y$  prepared by the different methods and heat treated at 900 °C.

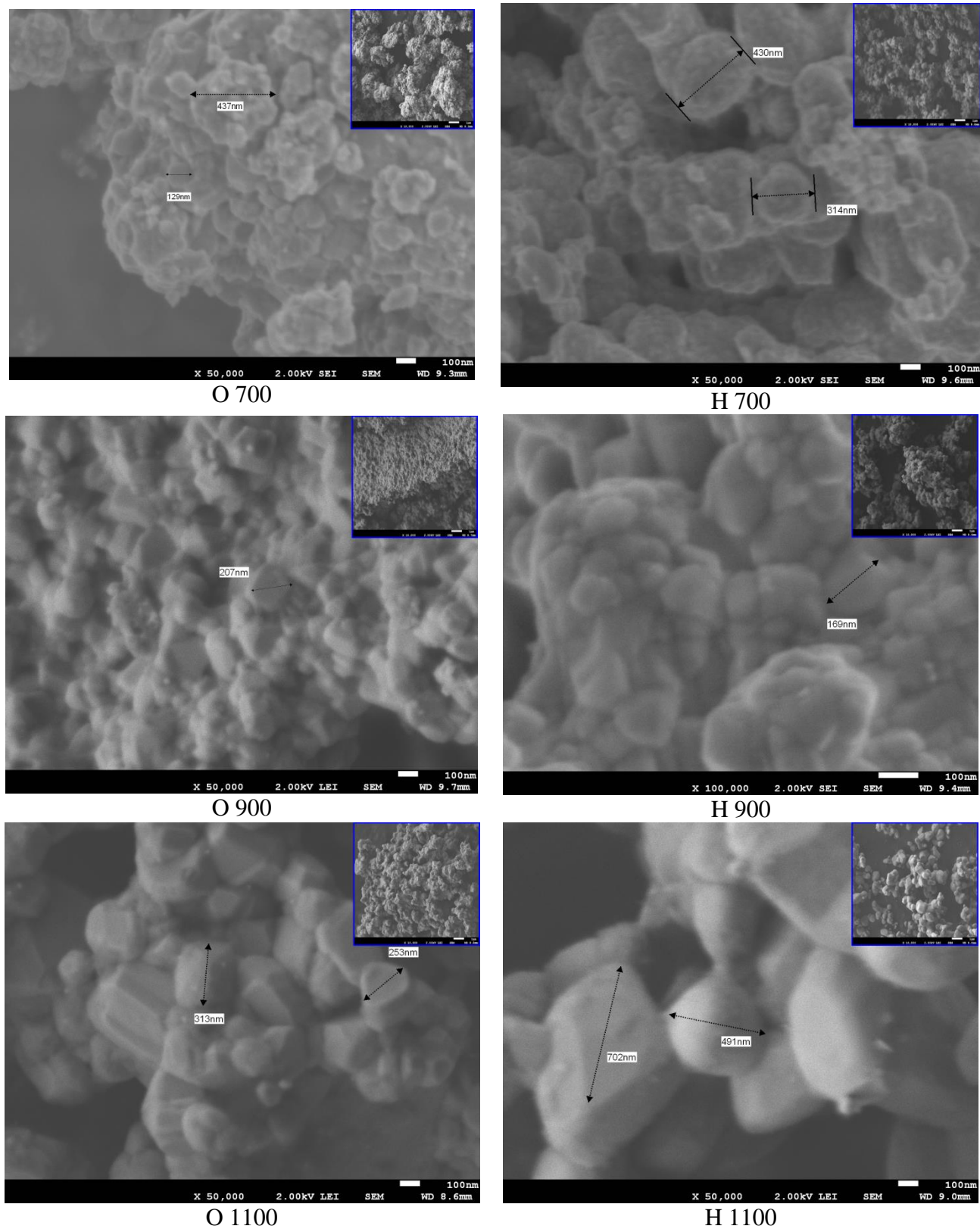


Figure 4-a. Results of the SEM images of the samples prepared by “O” and “H” methods.

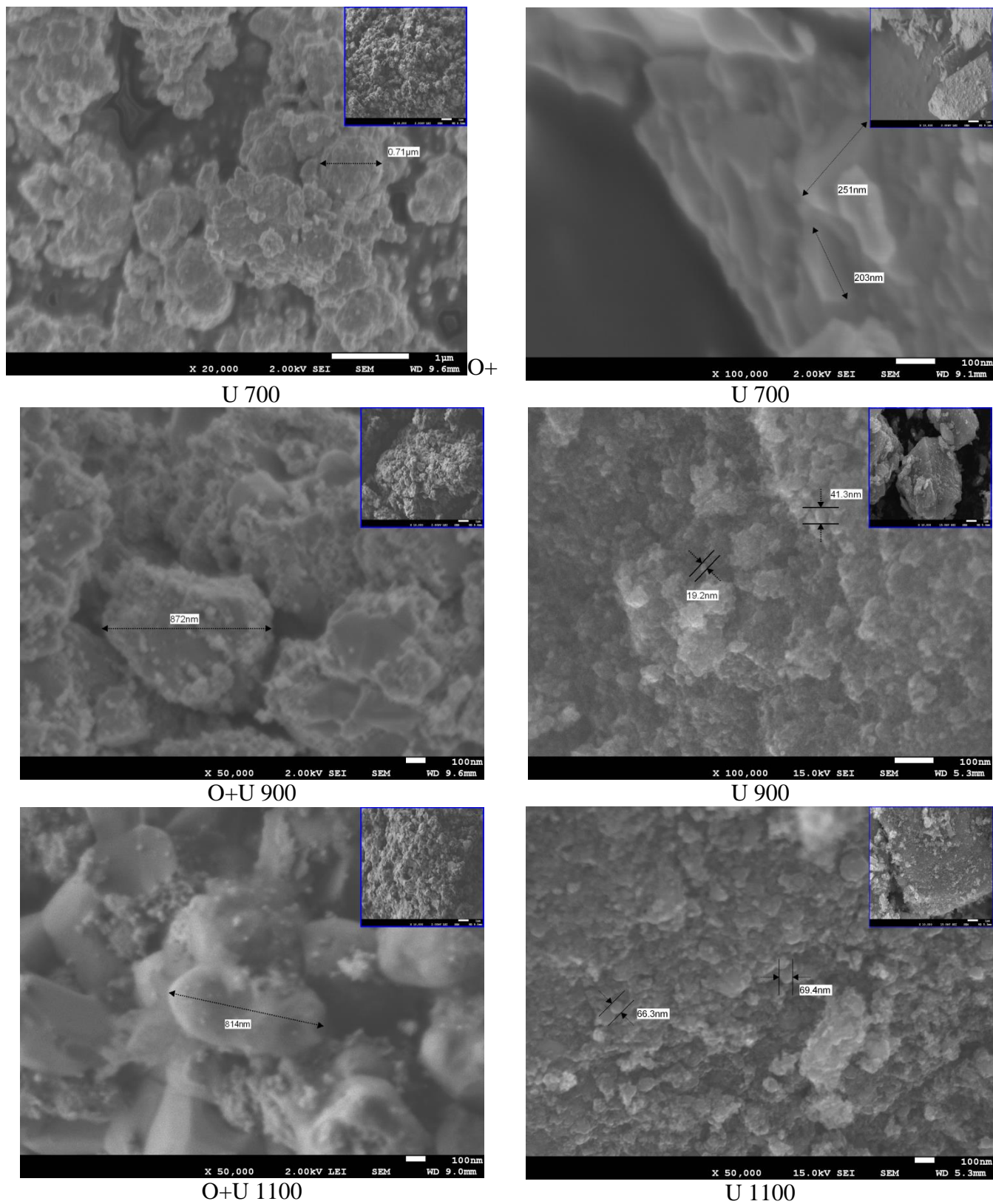


Figure 4-b. Results of the SEM images of the samples prepared by "O+U" and "U" methods.

Figures 4-a and b show the SEM images of the electrocatalysts fabricated in various conditions. There are 4 main varying parameters, which affect the electrocatalyst shape, size, surface area and electrocatalytic properties. These parameters are the particles agglomeration and sintering, the porosity, the particle size and the crystallinity. In each case we studied the variation of these parameters with rising temperatures. In the case of the sample prepared from the process “O” (please see the above paragraph 2.2), the particles agglomeration decreased with rising temperatures, however, porosity and crystallinity increased. This leads to different facets of the crystal be shown in figure 4-a. On the other hand the particle sizes are uniform ( $\sim 300$  nm) in all the temperatures used for the heat treatment. Therefore, this reduction in agglomeration and augmentation in porosity, obviously led to a high surface area at higher temperatures. This conclusion was endorsed by the B.E.T. surface area results depicted in figure 5. For the “H” samples, however there was less agglomeration at higher temperatures, because of the drastic increase in particle size and also sintering we see a low surface area. Thus, all the “H” samples showed almost the same amount in the B.E.T. surface. In these two cases, “O” and “H”, the B.E.T. amount was between 5 to 8  $\text{m}^2/\text{g}$  (except for the O-1100  $^\circ\text{C}$ , which was  $\sim 32$   $\text{m}^2/\text{g}$ ).

Electrocatalysts obtained from the “U” and “O+U” methods, contain many small particles including particles with 10 nanometers in size (figure 4-b). At 700  $^\circ\text{C}$ , we saw almost the same morphology of the samples obtained with the “U” and “O+U” methods. Whereas, in the case of the sample obtained from the “U” method, the quantity of the particle with small size increased with the heat treatment temperature. In the case of the samples prepared from the “O+U” method, by increasing the temperature, these small particles started to vanish through sintering and in addition there was no considerable change in the porosity of the samples and, consequently, the electrocatalyst surface area decreased. Therefore, there was a slight increase in the B.E.T. surface area with the heat treatment temperature of the “U” samples as depicted in figure 5 (from 77 to 94  $\text{m}^2/\text{g}$ ), while, in the case of “O+U”, this amount decreased (from 70 to 14  $\text{m}^2/\text{g}$ ) when the heat treatment increased. The electrocatalyst obtained from these two methods cannot exhibit a definite crystalline facet of  $\text{TiO}_2$ , as well as the “O” and “H” methods.

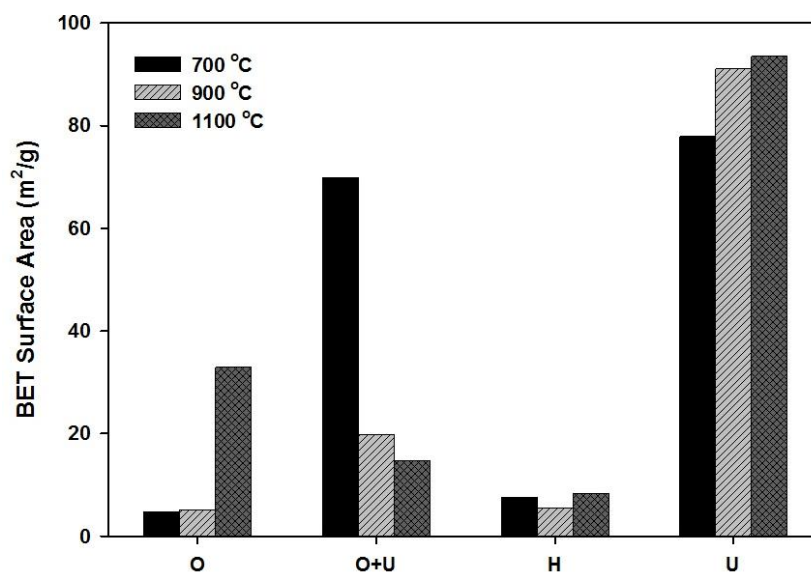


Figure 5. Variation of the BET surface area of the samples prepared by the four different methods and heat treated at various temperatures.

### 4.3.2 Chemical Stability

The chemical stability was evaluated by measuring the concentration of the dissolved Ti ion from 20 mg of the electrocatalysts in 30 mL of 10 mM sulfuric acid at 50 °C after 24 hours under atmospheric conditions. To compare the stability of these electrocatalysts with a reliable reference, those of the commercial 20 % Pt/C (Vulcan XC-72) based electrocatalyst was also evaluated in the same conditions. Our approach is different from the previous study in the literature which determined by the ICP-TOF the concentration of the titanium or platinum ions after dissolution, without giving any information about the initial amount of the catalyst. For example, it was reported that the average Ti concentration after 24 days at 50 °C in 0.1 mol.dm<sup>-3</sup> sulfuric acid under atmospheric conditions was about  $3.5 \times 10^{-7}$  ml.dm<sup>-3</sup> [32]. On the other hand, it is known that putting more catalyst throughout the acid leads to more dissolution and, consequently, higher concentration, and vice versa. Thus, it is not possible to correctly judge the chemical stability of the catalyst. Therefore, in the present work, the ICP-TOF results are referred to an initial electrocatalyst mass in term of percentage according to the initial amount of the electrocatalyst. The results of these ICP-TOF analyses are mentioned in figure 6-a. In this figure, the dissolution percentage means the mass ratio of the dissolved ions (Ti or Pt) to the primary inserted 20 mg of the electrocatalyst throughout the solution.

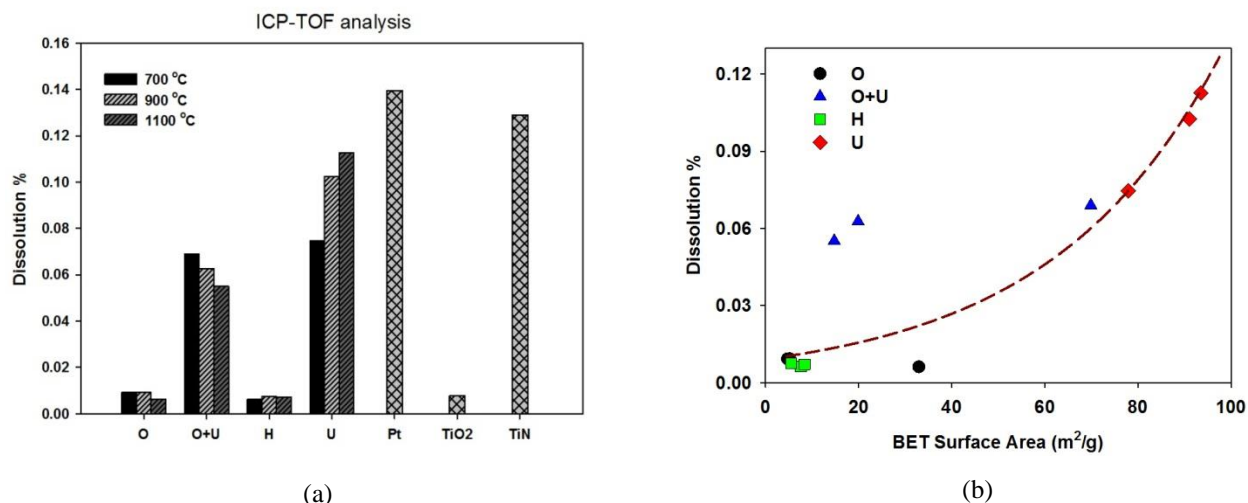


Figure 6.(a) Results of the ICP-TOF analysis of the electrocatalysts prepared using the four different methods, commercial Pt/C catalyst, commercial TiO<sub>2</sub> and TiN. (b) ICP-TOF results vs the BET surface area

The samples prepared using the “O” and the “H” methods exhibited very low and almost the same dissolution rate in this acidic medium. According to the BET surface area results shown in Fig.5, both of these samples had comparatively lower BET surface area to be exposed in the corrosive environment compared to the other two samples prepared using “O+U” and “U” methods. In the case of the sample prepared with the “O” method, the catalyst heat treated at 1100 °C, however had a higher surface area than those that were heat treated at the lower temperatures, displayed also in the same order of magnitude of chemical stability. This is probably due the stable TiO<sub>2</sub> crystalline facets which were apparent in the SEM pictures (Fig. 4.a) and XRD results (Fig.2.a). The chemical stability might be related to these crystal structures. Inversely, in the case of the samples prepared using the “O+U” and “U” methods, the BET surface and consequently the rates of dissolution of the electrocatalyst in acid medium are much higher than those fabricated using the “O” and the “H” methods. This might be due to the small particle size (e.g high surface area) and or lack of stable crystalline structure.

The variation of the relative dissolution, in acid medium, of the electrocatalysts fabricated from the various methods with their BET surface area is shown in figure 6-b. The general trend shows that the electrocatalyst dissolution increases with their BET surface area shown in Fig.5. In particular the samples prepared using the “U” method and heated at 700 °C exhibited a BET surface area of about 80 m<sup>2</sup>/g (Fig.5) and a dissolution rate of 0.08% whereas for samples

prepared with the same method and heated at 1100 °C had a BET surface area of 95 m<sup>2</sup>/g and a dissolution rate of almost 0.12%. On the other hand, the samples prepared with the “O” and the “H” methods exhibited the similar BET surface area in Fig.5 and dissolution rate in Fig.6. In particular Fig. 6.b relates very well the curve of these variations of these dissolution rates which are indicated in Fig.6.a. The general good agreement of the correlation between the dissolution rate of the samples and their BET surface area is shown in Fig.5 and Fig.6 and indicates well that the less stable electrocatalyst in acid medium, are those with of course high surface area and or less stable structures. As an example, the sample prepared with the “O” method and heat treated at 1100 °C exhibited a highly stable crystalline structure with high surface area and is relative stable with a dissolution rate less than 0.01%. Nevertheless, all the samples showed relatively lower dissolution percentages than the commercial Pt/C catalyst. According to these ICP-TOF results, it is possible to conclude that, TiO<sub>x</sub>N<sub>y</sub>, even with a very high surface area, is more stable than the Pt/C catalyst which has the similar surface area as them. The remarkable point here is that the samples prepared by the “O” and “H” methods, which already showed more TiO<sub>2</sub> properties than TiN, in XRD, EDS and SEM, in chemical stability measurements also revealed stability near to the TiO<sub>2</sub> chemical stability. On the other hand the samples prepared with the “U” and “O+U” methods, showed stability more similar to TiN than TiO<sub>2</sub>. These comparative results are shown in Fig. 6.a.

### 4.3.3 Electrochemical Stability

Figure 7 shows the cyclic voltammogram (CV) of the samples prepared with the “O+U” and “U” which were heat treated at 1100 °C. The electrolyte was 0.5 M sulfuric acid at 25 °C stripped with nitrogen. For each sample, the shape of the CV in both cases hardly changed after several potential cycles, so that the first scan and the 100<sup>th</sup> were almost the same for each of the samples. We have also verified experimentally that the CVs of the other samples prepared and heated at the other temperatures reached a steady state immediately and the scan of the 100<sup>th</sup> was almost the same as those of the first scan. These results revealed that the heat treated titanium oxynitrides had high electrochemical stability in acidic solution. Furthermore, there was no specific anodic or cathodic peak (in this potential window) because of the electrochemical oxidation and dissolution or reduction of the electrocatalyst, respectively. The calculated cathodic and anodic

electric charge densities at steady state were almost the same, which confirms the surface stability of the specimens. The electric charges in the CV were calculated using the following equation;

$$Q = \int i \cdot dt = \int i \frac{dE}{v} = \frac{1}{v} \int i \cdot dE$$

Where  $Q$ ,  $i$ ,  $t$ ,  $v$  and  $E$  are charge (C), current density (Amp/mg), time (second), scan rate (mV/second), and electrode potential (Volt), respectively.

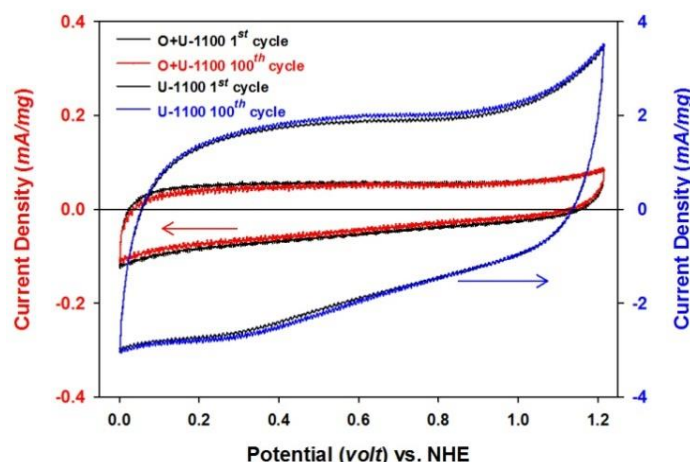


Figure 7. CV under  $N_2$  and  $100 \text{ mV} \cdot \text{s}^{-1}$  scan rate of the O+U and U samples heat treated at  $1100 \text{ }^\circ\text{C}$

Figure 8 shows the variation of the calculated cathodic electrical charge densities with the variation of the calculated anodic electrical charge densities for the various samples. There was a linear relation between the anodic and the cathodic electrical charge densities. This was mostly due to the same charge and discharge of the electric double layer, indicating that no one-way oxidation or reduction reaction of the electrocatalyst occurred.

The comparison of the electrical charge densities in Fig. 8 shows that, except for the samples prepared with the “U” method, the samples prepared with the same method but at different heat treatment temperatures had electric charge densities in the same range of values and consequently the same electrochemical active surface area, if we assume that a real surface area is proportional to the charge of the electric double layer. The electrical charge density is also correlated to the BET surface area. As an example, samples prepared by the “O+U” method showed higher electrical charge densities than the samples prepared by “O” and “H” methods. The  $\text{TiO}_x\text{N}_y$  based electrocatalyst prepared from the “U” method and heated at  $1100 \text{ }^\circ\text{C}$  showed the highest

electrochemical surface area, with more than  $2500 \mu\text{C}\cdot\text{cm}^{-2}$  of electrical charge density. This amount is significantly higher than that indicated elsewhere [32] for the titanium oxide based electrocatalyst which exhibited less than  $100 \mu\text{C}\cdot\text{cm}^{-2}$  of charge density.

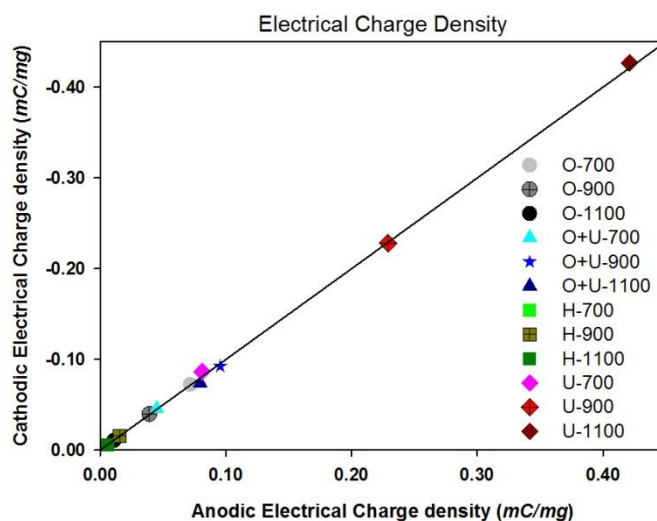


Figure 8. Comparison of the anodic and cathodic charge densities calculated from the CV

#### 4.3.4 Catalytic Activity for the ORR

After the CVs reached steady state, slow scan voltammetry (SSV) (scan rate:  $5 \text{ mV}\cdot\text{s}^{-1}$ , 1.2 V to 0 V vs. NHE) was performed under nitrogen and oxygen atmosphere. However, the potential–current curves in the slow scan voltammetry immediately reached steady state; the curve at the 3<sup>rd</sup> cycle was used to avoid the effect of the initial state. These curves are shown in figure 9. The cathodic current obtained under  $\text{O}_2$  atmosphere increased when the potential was decreasing, however, such an increase in the obtained cathodic current under  $\text{N}_2$  was not observed. The obtained current under  $\text{N}_2$  atmosphere is the charge current of the double layer capacitance. The difference between the current under  $\text{O}_2$  atmosphere ( $i_{\text{O}_2}$ ) and that under  $\text{N}_2$  atmosphere ( $i_{\text{N}_2}$ ) corresponded to the oxygen reduction current ( $i_{\text{ORR}}$ ), that is,  $i_{\text{ORR}} = i_{\text{O}_2} - i_{\text{N}_2}$ . This current density or mass activity is based on the mass density of the working electrode. The onset potential for the ORR,  $E_{\text{ORR}}$ , was defined as the electrode potential at the  $i_{\text{ORR}} = -0.2 \mu\text{A}\cdot\text{cm}^{-2}$  and it is also used to evaluate the catalytic activity for the ORR.

Figure 9-a shows the SSV in sulfuric acid under oxygen atmosphere of the various electrocatalysts heat treated at 700, 900 and 1100 °C. Fig. 9.b shows the polarization curves at a very slow scan rate ( $0.1667 \text{ mV}\cdot\text{s}^{-1}$ ) under  $\text{O}_2$  atmosphere. These curves show that for a given cathodic polarization potential the current density increases significantly. This improvement depends on the sol-gel method. In particular for the samples prepared with the “U” method this improvement is important with a mass activity at 0.0 V vs NHE of  $-0.10 \text{ mA}\cdot\text{mg}^{-1}$  when the sample is heat treated at  $700^\circ\text{C}$  and  $-0.25 \text{ mA}\cdot\text{mg}^{-1}$  for sample heated at  $1100^\circ\text{C}$ . Using the curves in Fig.9, the typical Tafel polarization curve is shown in Fig. 10.a. Two Tafel slopes can be derived from this curve: a slope at very low current density region (near the open circuit voltage) and those at high current density. The Tafel slope at low current (about  $20 \text{ mV}\pm 10 \text{ mV}/\text{decade}$ ) is significantly lower than those at high current density ( $150 \text{ mV}\pm 10 \text{ mV}/\text{decade}$ ). The Tafel plots at high current densities of the ORR derived from the polarization curves of Fig. 9.b are shown in Fig.10.b. These curves show clearly that the lowest current densities are obtained with the samples prepared with the “O” and “H” methods and the highest current densities are obtained with the samples prepared with the “U” method and heat treated at  $900^\circ\text{C}$  and  $1100^\circ\text{C}$ . As an example, the current density at 0.3 V vs NHE is about  $10^{-3} \text{ mA}\cdot\text{mg}^{-1}$  for the sample prepared with the “H” method and heated at  $900^\circ\text{C}$  whereas it is about  $10^{-1} \text{ mA}\cdot\text{mg}^{-1}$  for the sample prepared with the “U” method and heated at  $900^\circ\text{C}$ . The basic kinetic parameters (Tafel slope, exchange current density and onset potential) for the various samples and heat treatment conditions deduced from the polarization curves and the Tafel plots are listed in Table 1. Their variation with the heating temperature is also shown in Fig.11. Table 1 and Figure 11 show clearly that the values of the  $i_{\text{ORR}}$  and  $E_{\text{ORR}}$  increased considerably, in particular in the case of the samples prepared with the “U” method, with the temperature of the heat treatment. For these samples, the onset potential of titanium oxy-nitride increased from ca. 0.44 V to 0.75 V vs NHE when the temperature increased from 700 to  $1100^\circ\text{C}$ . For a given heat treatment temperature, there was at least a 300 mV improvement in the onset potential of the samples prepared with the “U” method when compared to those of sample prepared with the other methods. On the other hand the current density of the sample prepared with the “U” method and heated at  $1100^\circ\text{C}$  is 10 times higher than that of the sample prepared with the “O” method and heated at the same temperature; with a 460 mV improvement in the onset potential.

Based on the above physicochemical characterization results, it seems that the samples which exhibit a high BET surface area and a mixed structure of TiN and TiO<sub>2</sub> (high content of TiN structure rather than only a perfect TiO<sub>2</sub> structure) might have good electrocatalytic properties. This specific mixed structural crystalline created due to the heat treatment is responsible for the capacity of these electrocatalysts to ease the oxygen adsorption. Therefore, the samples prepared with the “U” method and heated at 1100°C exhibit the high BET surface area with the high double layer charge density. They also exhibit the highest onset potential and current density compared to the other samples. However, the results in figure 9-b show that the Titanium oxynitride based electrocatalysts are significantly less efficient for the ORR than the Pt/C based electrocatalyst. There is room to develop strategies in the improvement of these new non noble electrocatalyst for the ORR for PEMFC applications. The determination of the mechanism of the ORR on this class of electrocatalysts using rotating disc electrodes and its comparison to that on Pt based electrocatalyst is under active development.

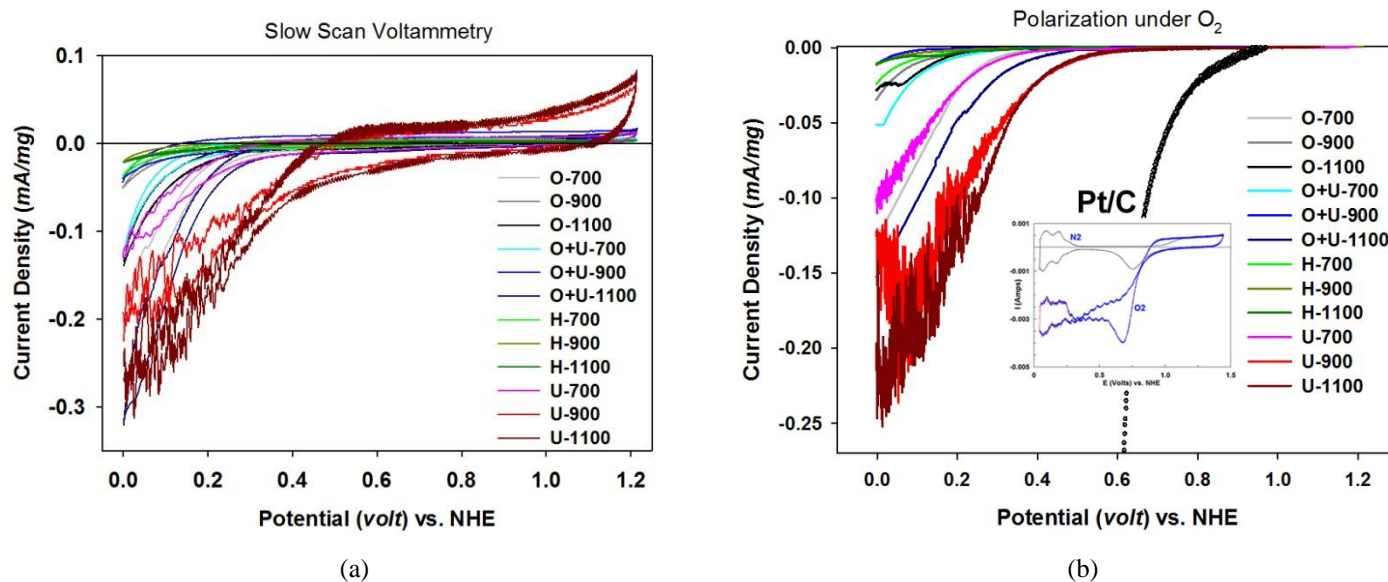


Figure 9. (a) SSV (scan rate: 5 mV/s) and (b) polarization (scan rate: 0.1667 mV/s) under O<sub>2</sub> atmosphere

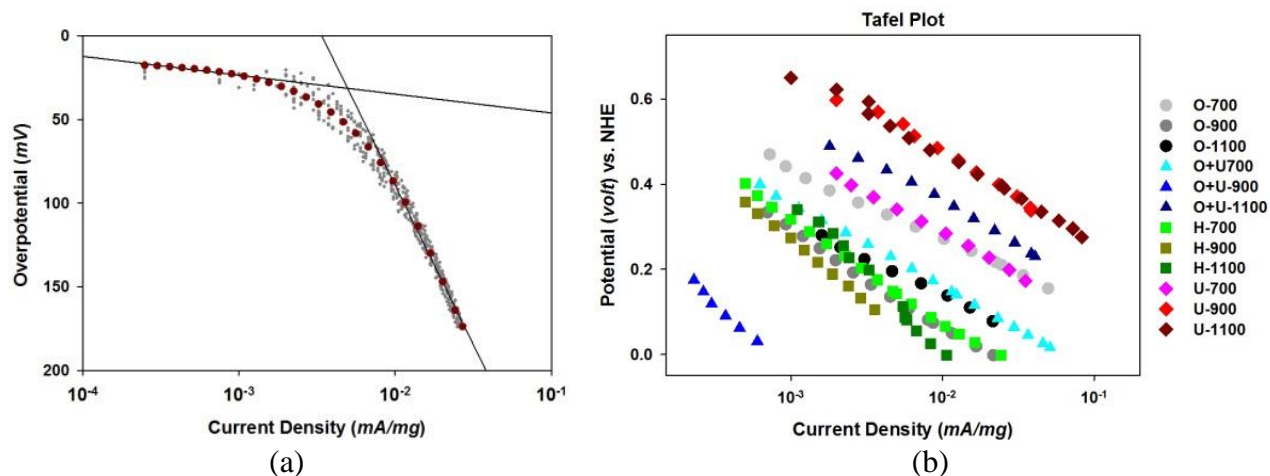


Figure 10. The Tafel plot of (a) U-1100 (b) all prepared  $TiO_xN_y$  samples

Table 1. Tafel slope, Exchange current density, Onset potential and BET surface area of the  $TiO_xN_y$  catalysts

	<i>O-700</i>	<i>O-900</i>	<i>O-1100</i>	<i>H-700</i>	<i>H-900</i>	<i>H-1100</i>
Tafel slope at low Potential (mV/decade)	-161	-230	-168	-242	-290	-366
Exchange Current Density (mA/mg)	<b>1.70E-03</b>	6.20E-04	1.13E-03	7.30E-04	7.00E-04	8.30E-04
Onset Potential (Volt vs. NHE)	0.39	0.34	0.29	0.34	0.3	0.41
BET surface area (m <sup>2</sup> /g)	4.7194	5.1829	32.9377	7.5820	5.4869	8.4007
	<i>O+U-700</i>	<i>O+U-900</i>	<i>O+U-1100</i>	<i>U-700</i>	<i>U-900</i>	<i>U-1100</i>
Tafel slope at low Potential (mV/decade)	-198	-330	-199	-190	-217	-203
Exchange Current Density (mA/mg)	1.20E-03	1.76E-04	2.00E-04	1.50E-03	7.50E-04	4.30E-04
Onset Potential (Volt vs. NHE)	0.33	0.2	0.53	0.44	0.72	<b>0.75</b>
BET surface area (m <sup>2</sup> /g)	69.8682	19.8821	14.7581	77.9177	91.0436	<b>93.5132</b>

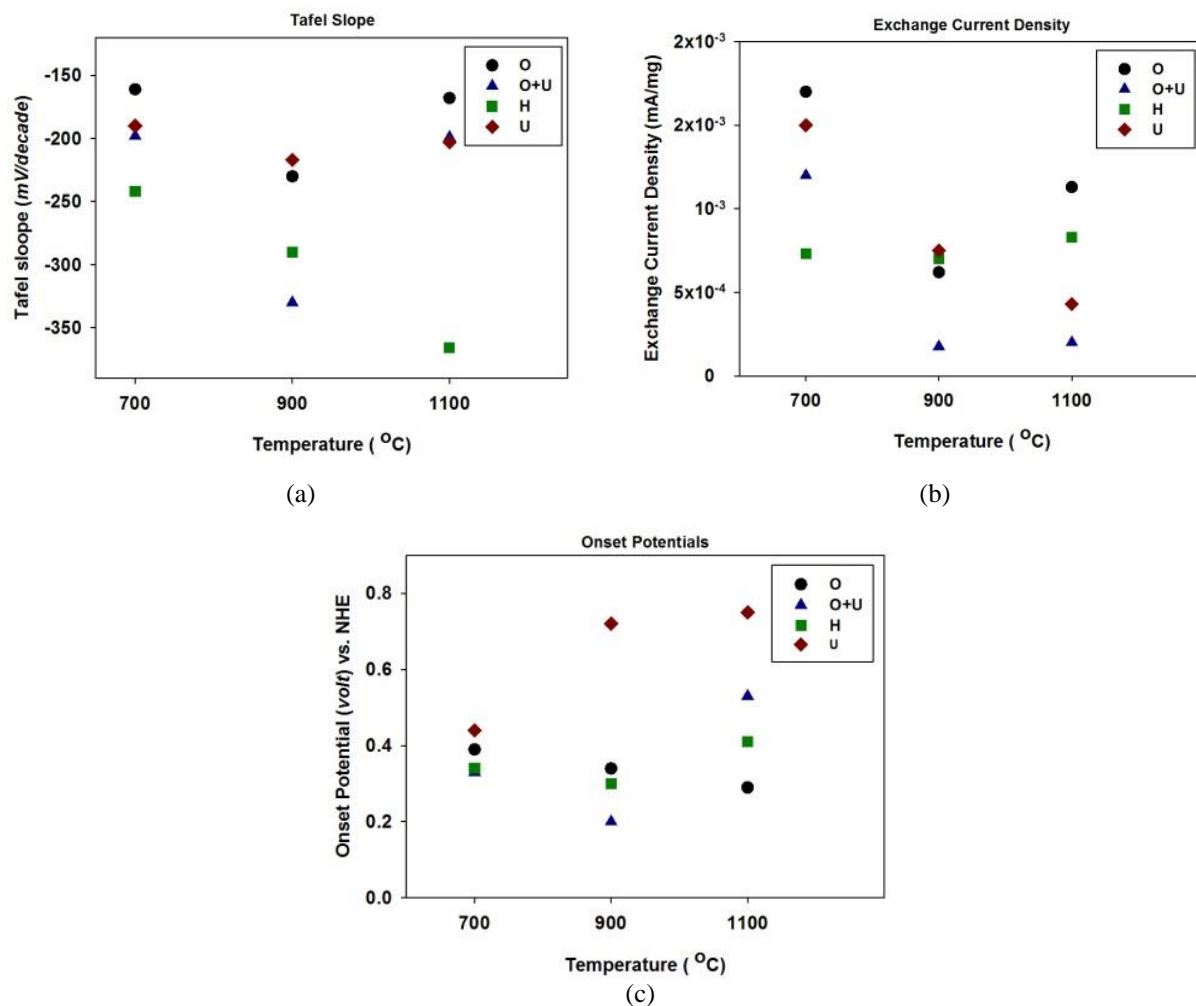


Figure 11. Kinetic parameters of the  $TiO_xN_y$  catalysts (a) Tafel slope, (b) Exchange current density and (c) Onset potential

#### 4.4 Conclusion

The titanium oxy-nitride electrocatalysts with various ratios of oxygen and nitrogen for the oxygen reduction reaction were fabricated for the first time using four different sol-gel methods, various precursors and heat treatments. It was shown that all the prepared electrocatalysts were  $TiO_xN_y$  based materials with different ratios of x and y.

XRD, EDS, SEM and BET results have shown the different correlations between the electrocatalyst structure, chemical composition including surface defects, morphology, surface area and chemical stability of the electrocatalyst. As an example, the electrocatalyst prepared with the urea-based sol-gel method and annealed at 1100 °C showed that a considerable amount

of nitrogen was inserted into the electrocatalyst structure with small particle sizes of around 70 nm leading to the highest BET surface area of around  $95 \pm 5 \text{ m}^2/\text{g}$ .

The chemical stability (dissolution rate) of  $\text{TiO}_x\text{N}_y$  based electrocatalyst measured by ICP-ToF-MS in sulfuric acid has shown that all the electrocatalysts prepared in this work exhibited chemical stability higher than the commercial Pt/C based electrocatalyst.

It was shown that the cyclic voltammetry for a long time (more than 100 cycles) of the different  $\text{TiO}_x\text{N}_y$  based electrocatalyst had high electrochemical stability and there was no peak related to the oxidation or reduction of the electrocatalyst in the PEMFC working potential range.

The electrocatalysts prepared by the in-situ urea-based sol-gel method showed comparatively much higher electrocatalytic activity with a high onset potential of 0.75 Volt vs NHE and a high exchange current density of  $4.3 \times 10^{-4} \text{ mA/mg}$ . This electrocatalyst has demonstrated promising properties to be used as an alternative for a non-noble electrocatalyst in PEM Fuel Cell application.

## 4.5 References

- [1] R. Bashyam, P. Zelenay, A class of non-precious metal composite catalysts for fuel cells, *Nature* 443 (2006) 63-6.
- [2] S.J. Peighambardoust, S. Rowshanzamir, M. Amjadi, Review of the proton exchange membranes for fuel cell applications, *International Journal of Hydrogen Energy* 35 (2010) 9349-84.
- [3] B. Wang, Recent development of non-platinum catalysts for oxygen reduction reaction, *J. Power Sources* 152 (2005) 1-15.
- [4] S.M. Haile, Fuel cell materials and components, *Acta Mater.* 51 (2003) 5981-6000.
- [5] R. Othman, A.L. Dicks, Z. Zhu, Non precious metal catalysts for the PEM fuel cell cathode, *International Journal of Hydrogen Energy* 37 (2012) 357-72.
- [6] Y. Wang, K.S. Chen, J. Mishler, S.C. Cho, X.C. Adroher, A review of polymer electrolyte membrane fuel cells: Technology, applications, and needs on fundamental research, *Applied Energy* 88 (2011) 981-1007.

- [7] H. Wu, D. Wexler, H. Liu, O. Savadogo, J. Ahn, G. Wang, Pt<sub>1-x</sub>Co<sub>x</sub> nanoparticles as cathode catalyst for proton exchange membrane fuel cells with enhanced catalytic activity, *Mater. Chem. Phys.* 124 (2010) 841-4.
- [8] G. Wang, H. Wu, D. Wexler, H. Liu, O. Savadogo, Ni@Pt core-shell nanoparticles with enhanced catalytic activity for oxygen reduction reaction, *J. Alloy. Compd.* 503 (2010) L1-L4.
- [9] D.C. Higgins, D. Meza, Z. Chen, Nitrogen-Doped Carbon Nanotubes as Platinum Catalyst Supports for Oxygen Reduction Reaction in Proton Exchange Membrane Fuel Cells, *The Journal of Physical Chemistry C* 114 (2010) 21982-8.
- [10] A. Ishihara, Y. Shibata, S. Mitsushima, K. Ota, Partially Oxidized Tantalum Carbonitrides as a New Nonplatinum Cathode for PEFC--1, *Journal of The Electrochemical Society* 155 (2008) B400-B6.
- [11] Y. Shao, G. Yin, Y. Gao, Understanding and approaches for the durability issues of Pt-based catalysts for PEM fuel cell, *J. Power Sources* 171 (2007) 558-66.
- [12] D. Wang, H.L. Xin, Y. Yu, H. Wang, E. Rus, D.A. Muller, H.D. Abruña, Pt-Decorated PdCo@Pd/C Core-Shell Nanoparticles with Enhanced Stability and Electrocatalytic Activity for the Oxygen Reduction Reaction, *J. Am. Chem. Soc.* 132 (2010) 17664-6.
- [13] K. Zhang, Q. Yue, G. Chen, Y. Zhai, L. Wang, H. Wang, J. Zhao, J. Liu, J. Jia, H. Li, Effects of Acid Treatment of Pt-Ni Alloy Nanoparticles@Graphene on the Kinetics of the Oxygen Reduction Reaction in Acidic and Alkaline Solutions, *The Journal of Physical Chemistry C* 115 (2010) 379-89.
- [14] F. Fouda-Onana, S. Bah, O. Savadogo, Palladium-copper alloys as catalysts for the oxygen reduction reaction in an acidic media I: Correlation between the ORR kinetic parameters and intrinsic physical properties of the alloys, *Journal of Electroanalytical Chemistry* 636 (2009) 1-9.
- [15] J. Wu, X.Z. Yuan, J.J. Martin, H. Wang, J. Zhang, J. Shen, S. Wu, W. Merida, A review of PEM fuel cell durability: Degradation mechanisms and mitigation strategies, *Journal of Power Sources* 184 (2008) 104-19.
- [16] X. Yu, S. Ye, Recent advances in activity and durability enhancement of Pt/C catalytic cathode in PEMFC: Part II: Degradation mechanism and durability enhancement of carbon supported platinum catalyst, *J. Power Sources* 172 (2007) 145-54.

- [17] S. Venkataraj, D. Severin, S.H. Mohamed, J. Ngaruiya, O. Kappertz, M. Wuttig, Towards understanding the superior properties of transition metal oxynitrides prepared by reactive DC magnetron sputtering, *Thin Solid Films* 502 (2006) 228-34.
- [18] S. Doi, A. Ishihara, S. Mitsushima, N. Kamiya, K.-i. Ota, Zirconium-Based Compounds for Cathode of Polymer Electrolyte Fuel Cell, *Journal of The Electrochemical Society* 154 (2007) B362-B9.
- [19] Y. Maekawa, A. Ishihara, J.-H. Kim, S. Mitsushima, K.-i. Ota, Catalytic Activity of Zirconium Oxynitride Prepared by Reactive Sputtering for ORR in Sulfuric Acid, *Electrochemical and Solid-State Letters* 11 (2008) B109-B12.
- [20] K.D. Nam, A. Ishihara, K. Matsuzawa, S. Mitsushima, K.-i. Ota, Partially Oxidized Niobium Carbonitride as Non-Platinum Cathode for PEFC, *Electrochemical and Solid-State Letters* 12 (2009) B158-B60.
- [21] Y. Suzuki, A. Ishihara, S. Mitsushima, N. Kamiya, K.-i. Ota, Sulfated-Zirconia as a Support of Pt Catalyst for Polymer Electrolyte Fuel Cells, *Electrochemical and Solid-State Letters* 10 (2007) B105-B7.
- [22] Y. Liu, A. Ishihara, S. Mitsushima, N. Kamiya, K.-i. Ota, Zirconium Oxide for PEFC Cathodes, *Electrochemical and Solid-State Letters* 8 (2005) A400-A2.
- [23] Y. Liu, A. Ishihara, S. Mitsushima, K.-i. Ota, Influence of sputtering power on oxygen reduction reaction activity of zirconium oxides prepared by radio frequency reactive sputtering, *Electrochimica Acta* 55 (2010) 1239-44.
- [24] G. Chen, C.C. Waraksa, H. Cho, D.D. Macdonald, T.E. Mallouka, EIS Studies of Porous Oxygen Electrodes with Discrete Particles: I. Impedance of Oxide Catalyst Supports, *Journal of The Electrochemical Society* 150 (2003) E423-E8.
- [25] T. Ioroi, Z. Siroma, N. Fujiwara, S.-i. Yamazaki, K. Yasuda, Sub-stoichiometric titanium oxide-supported platinum electrocatalyst for polymer electrolyte fuel cells, *Electrochemistry Communications* 7 (2005) 183-8.
- [26] L. Timperman, Y.J. Feng, W. Vogel, N. Alonso-Vante, Substrate effect on oxygen reduction electrocatalysis, *Electrochimica Acta* 55 (2010) 7558-63.

- [27] N.R. Elezovic, B.M. Babic, V.R. Radmilovic, L.M. Vracar, N.V. Krstajic, Synthesis and characterization of MoO<sub>x</sub>-Pt/C and TiO<sub>x</sub>-Pt/C nano-catalysts for oxygen reduction, *Electrochimica Acta* 54 (2009) 2404-9.
- [28] M.S. Saha, M.N. Banis, Y. Zhang, R. Li, X. Sun, M. Cai, F.T. Wagner, Tungsten oxide nanowires grown on carbon paper as Pt electrocatalyst support for high performance proton exchange membrane fuel cells, *Journal of Power Sources* 192 (2009) 330-5.
- [29] J. Shim, C.-R. Lee, H.-K. Lee, J.-S. Lee, E.J. Cairns, Electrochemical characteristics of Pt-WO<sub>3</sub>/C and Pt-TiO<sub>2</sub>/C electrocatalysts in a polymer electrolyte fuel cell, *Journal of Power Sources* 102 (2001) 172-7.
- [30] K. Sasaki, L. Zhang, R.R. Adzic, Niobium oxide-supported platinum ultra-low amount electrocatalysts for oxygen reduction, *Physical Chemistry Chemical Physics* 10 (2008) 159-67.
- [31] A. Ishihara, Y. Ohgi, K. Matsuzawa, S. Mitsushima, K.-i. Ota, Progress in non-precious metal oxide-based cathode for polymer electrolyte fuel cells, *Electrochimica Acta* 55 (2010) 8005-12.
- [32] Y. Liu, A. Ishihara, S. Mitsushima, N. Kamiya, K.-i. Ota, Transition Metal Oxides as DMFC Cathodes Without Platinum, *Journal of The Electrochemical Society* 154 (2007) B664-B9.
- [33] K.-i. Ota, Y. Ohgi, K.-D. Nam, K. Matsuzawa, S. Mitsushima, A. Ishihara, Development of group 4 and 5 metal oxide-based cathodes for polymer electrolyte fuel cell, *J. Power Sources* 196 (2011) 5256-63.
- [34] A. Ishihara, S. Doi, S. Mitsushima, K.-i. Ota, Tantalum (oxy)nitrides prepared using reactive sputtering for new nonplatinum cathodes of polymer electrolyte fuel cell, *Electrochimica Acta* 53 (2008) 5442-50.
- [35] A. Ishihara, K. Lee, S. Doi, S. Mitsushima, N. Kamiya, M. Hara, K. Domen, K. Fukuda, K.-i. Ota, Tantalum Oxynitride for a Novel Cathode of PEFC, *Electrochemical and Solid-State Letters* 8 (2005) A201-A3.
- [36] W.-J. Chun, A. Ishikawa, H. Fujisawa, T. Takata, J.N. Kondo, M. Hara, M. Kawai, Y. Matsumoto, K. Domen, Conduction and Valence Band Positions of Ta<sub>2</sub>O<sub>5</sub>, TaON, and Ta<sub>3</sub>N<sub>5</sub> by UPS and Electrochemical Methods, *The Journal of Physical Chemistry B* 107 (2003) 1798-803.

- [37] A. Ishihara, M. Tamura, K. Matsuzawa, S. Mitsushima, K.-i. Ota, Tantalum oxide-based compounds as new non-noble cathodes for polymer electrolyte fuel cell, *Electrochimica Acta* 55 (2010) 7581-9.
- [38] M. Azuma, M. Kashihara, Y. Nakato, H. Tsubomura, Reduction of oxygen to water on cobalt-nitride thin film electrodes prepared by the reactive rf sputtering technique, *Journal of Electroanalytical Chemistry and Interfacial Electrochemistry* 250 (1988) 73-82.
- [39] K. Lee, A. Ishihara, S. Mitsushima, N. Kamiya, K.-i. Ota, Stability and electrocatalytic activity for oxygen reduction in WC + Ta catalyst, *Electrochimica Acta* 49 (2004) 3479-85.
- [40] Jin-Hwan Kim, Akimitsu Ishihara, Shigenori Mitsushima, Nobuyuki Kamiya, K.-i. Ota, New Non-platinum Cathode Based on Chromium for PEFC, *Chem. Lett.* 36 (2007) 514.
- [41] J.-H. Kim, A. Ishihara, S. Mitsushima, N. Kamiya, K.-i. Ota, Oxygen Reduction Reaction of Ta-C-N Prepared by Reactive Sputtering with Heat Treatment, *Electrochemistry* 75 (2007) 166-8.
- [42] S. Shimada, Interfacial reaction on oxidation of carbides with formation of carbon, *Solid State Ionics* 141–142 (2001) 99-104.
- [43] S. Shimada, M. Johnsson, S. Urbonaite, Thermoanalytical study on oxidation of TaC<sub>1-x</sub>N<sub>x</sub> powders by simultaneous TG-DTA-MS technique, *Thermochimica Acta* 419 (2004) 143-8.
- [44] A. Ishihara, M. Tamura, K. Matsuzawa, S. Mitsushima, K.-i. Ota, Partially Oxidized Tantalum Carbonitride as New Cathodes Without Platinum Group Metals for Polymer Electrolyte Fuel Cell, *Journal of Fuel Cell Science and Technology* 8 (2011) 031005-6.
- [45] Y. Shibata, A. Ishihara, S. Mitsushima, N. Kamiya, K.-i. Ota, Effect of Heat Treatment on Catalytic Activity for Oxygen Reduction Reaction of TaO<sub>x</sub>Ny/Ti Prepared by Electrophoretic Deposition, *Electrochemical and Solid-State Letters* 10 (2007) B43-B6.
- [46] A.I. Yoshiro Ohgi, Yohei Shibata, Shigenori Mitsushima and Ken-ichiro Ota, Catalytic Activity of Partially Oxidized Transition-metal Carbide–Nitride for Oxygen Reduction Reaction in Sulfuric Acid, *Chemistry Letters* 37 (2008) 608.
- [47] G. Liu, H.M. Zhang, M.R. Wang, H.X. Zhong, J. Chen, Preparation, characterization of ZrO<sub>x</sub>Ny/C and its application in PEMFC as an electrocatalyst for oxygen reduction, *J. Power Sources* 172 (2007) 503-10.

- [48] S.Y. Kim, D.H. Han, J.N. Kim, J.J. Lee, Titanium oxynitride films for a bipolar plate of polymer electrolyte membrane fuel cell prepared by inductively coupled plasma assisted reactive sputtering, *Journal of Power Sources* 193 (2009) 570-4.
- [49] S.K. Rawal, A.K. Chawla, V. Chawla, R. Jayaganthan, R. Chandra, Effect of ambient gas on structural and optical properties of titanium oxynitride films, *Applied Surface Science* 256 (2010) 4129-35.
- [50] X. Song, D. Gopireddy, C.G. Takoudis, Characterization of titanium oxynitride films deposited by low pressure chemical vapor deposition using amide Ti precursor, *Thin Solid Films* 516 (2008) 6330-5.
- [51] B. Chi, L. Zhao, T. Jin, One-Step Template-Free Route for Synthesis of Mesoporous N-Doped Titania Spheres, *The Journal of Physical Chemistry C* 111 (2007) 6189-93.
- [52] M. Bellardita, M. Addamo, A. Di Paola, L. Palmisano, A.M. Venezia, Preparation of N-doped TiO<sub>2</sub>: characterization and photocatalytic performance under UV and visible light, *Physical Chemistry Chemical Physics* 11 (2009) 4084-93.
- [53] R. Aghababazadeh, A.R. Mirhabibi, B. Rand, S. Banijamali, J. Pourasad, M. Ghahari, Synthesis and characterization of nanocrystalline titanium nitride powder from rutile and anatase as precursors, *Surface Science* 601 (2007) 2881-5.
- [54] Z. Wu, F. Dong, W. Zhao, S. Guo, Visible light induced electron transfer process over nitrogen doped TiO<sub>2</sub> nanocrystals prepared by oxidation of titanium nitride, *Journal of Hazardous Materials* 157 (2008) 57-63.
- [55] C. Di Valentin, E. Finazzi, G. Pacchioni, A. Selloni, S. Livraghi, M.C. Paganini, E. Giamello, N-doped TiO<sub>2</sub>: Theory and experiment, *Chemical Physics* 339 (2007) 44-56.
- [56] T.C. Jagadale, S.P. Takale, R.S. Sonawane, H.M. Joshi, S.I. Patil, B.B. Kale, S.B. Ogale, N-Doped TiO<sub>2</sub> Nanoparticle Based Visible Light Photocatalyst by Modified Peroxide Sol-Gel Method, *The Journal of Physical Chemistry C* 112 (2008) 14595-602.
- [57] Y. Kuroda, T. Mori, K. Yagi, N. Makihata, Y. Kawahara, M. Nagao, S. Kittaka, Preparation of Visible-Light-Responsive TiO<sub>2</sub>-xN<sub>x</sub> Photocatalyst by a Sol-Gel Method: Analysis of the Active Center on TiO<sub>2</sub> that Reacts with NH<sub>3</sub>, *Langmuir* 21 (2005) 8026-34.

- [58] E. Martínez-Ferrero, Y. Sakatani, C. Boissière, D. Grosso, A. Fuertes, J. Fraxedas, C. Sanchez, Nanostructured Titanium Oxynitride Porous Thin Films as Efficient Visible-Active Photocatalysts, *Advanced Functional Materials* 17 (2007) 3348-54.
- [59] W.L. Wang, O. Savadogo, Z.F. Ma, Preparation of new titanium oxy nitride based electro catalysts using an anhydrous sol-gel method for water electrolysis in acid medium, *International Journal of Hydrogen Energy* 37 (2012) 7405-17.
- [60] W. Wang, O. Savadogo, Z.-F. Ma, The oxygen reduction reaction on Pt/TiO<sub>x</sub>N<sub>y</sub>-based electrocatalyst for PEM fuel cell applications, *Journal of Applied Electrochemistry* 42 (2012) 857-66.
- [61] X. Nie, S. Zhuo, G. Maeng, K. Sohlberg, Doping of TiO<sub>2</sub> Polymorphs for Altered Optical and Photocatalytic Properties, *International Journal of Photoenergy* 2009 (2009).

**CHAPTER 5 ARTICLE 2: STABILITY AND CATALYTIC ACTIVITY  
OF TITANIUM OXY-NITRIDE CATALYST PREPARED BY IN-SITU  
UREA-BASED SOL-GEL METHOD FOR THE OXYGEN  
REDUCTION REACTION (ORR) IN ACID MEDIUM**

A. Seifitokaldani <sup>a,b</sup>, M. Perrier <sup>a</sup>, O. Savadogo <sup>a,b</sup>

<sup>a</sup> Chemical Engineering Department, Polytechnique Montréal, Montréal, QC, Canada

<sup>b</sup> Laboratory of New Materials for Electrochemistry and Energy, Polytechnique Montréal,  
C.P.6079, Succursale Centre-Ville, Montréal, Québec H3C 3A7, Canada

Submitted to: International Journal of Hydrogen Energy

Titanium oxy-nitride synthesized by the in-situ urea-based sol-gel method was used as an electrocatalyst for the oxygen reduction reaction (ORR). The chemical, physical and electrocatalytic properties of these prepared electrocatalyst were compared to those of titanium oxy-nitride based electrocatalysts produced by other conventional sol-gel methods. The effect of the materials heating conditions on these properties was determined. Correlations between these chemical, physical and electrocatalytic properties and the nitrogen content of the electrocatalyst were determined. How the nitrogen content, the BET surface area and the particle size affect these properties was systematically evaluated. The correlations were supported by the chemical and electrochemical stability measurement and the Electrochemical Impedance Spectroscopy (EIS) results of the electrocatalyst. From these correlations why a typical composition of the electrocatalyst exhibits a high onset potential of 0.75 V was discussed.

**Key words:** *titanium oxy-nitride, in-situ urea-based sol-gel, oxygen reduction reaction (ORR), catalytic activity, chemical and electrochemical stability*

## 5.1 Introduction

Platinum Nano-particles or Pt-alloys supported on carbon (Pt/C or Pt-M/C) are the most convenient electrocatalysts in Polymer Electrolyte Membrane (PEM) fuel cells, because of their exceptional activity and high surface area [1-25]. However, some problems, such as sintering, dissolution, and the deposition of extremely dispersed Pt nano-particles in the electrolyte and oxidation of the carbon support during long-term operation, are a big obstacle limiting the mass utilization of PEM fuel cells. Moreover, the leaching out of metal ions used in platinum alloys contaminates the membrane and invalidates the fuel cell. As well, it is necessary to consider the low abundance of Pt natural resources and its high cost, which is unavoidable [26-35]. Therefore, developing a new cheaper non-noble electrocatalyst with high activity and certainly high chemical and electrochemical stability under PEM fuel cell corrosive circumstances has engaged researchers in the last decade.

The development of transition metal oxy-nitrides, because of their high chemical stability in acidic media, is an interesting approach for new electrocatalyst development for the ORR, especially after it was reported that these compounds have some catalytic activity for this reaction [36-46]. Due to its great abundance, titanium oxy-nitride ( $\text{TiO}_x\text{N}_y$ ) is one of the most appealing electrocatalysts and has been the subject of many investigations on its preparation, stability, and catalytic activity [47-52]. In this study,  $\text{TiO}_x\text{N}_y$  was prepared by a new in-situ urea-based sol-gel method. For comparison three other titanium oxy-nitrides were prepared using classical sol-gel methods without urea. The specific chemical composition of these electrocatalysts might be the key to successfully identify excellent electrocatalysts for the ORR. The prepared electrocatalysts with different N/O ratios showed different properties from a semiconductor behavior in oxygen-rich materials to more conductive and stable electrocatalyst behavior in nitrogen-rich oxy-nitrides, respectively. As it was already shown by Wang et al. [53], in the in-situ urea-based sol-gel method more nitrogen was inserted into the titanium oxide structure, compared to the other methods. Based on the X-Ray Diffraction (XRD) data, this phase transfer from titanium oxide to titanium nitride was clarified by calculating the lattice parameters.

To the best of our knowledge, there are some studies to evaluate the chemical stability of transition metal oxy-nitrides prepared by the classical sol-gel method [54-57]; however, there is no study on the titanium oxy-nitride synthesized by the in-situ urea-based sol-gel method. On the

other hand there is no study on the electrochemical stability of these electrocatalysts. Therefore, we have tried to determine conditions of the synthesis of the titanium oxy-nitride by the in-situ urea-based sol-gel method and to assess the electrochemical stability of these electrocatalysts at a relatively high anodic potential (ca. 2 volts vs. SCE) in addition to the evaluation of their chemical stability by ICP-TOF-MS measurements. In this regard, X-ray Photoelectron Spectroscopy (XPS) analysis also provided a better understanding of surface changes under oxidizing conditions. Besides stability assessment, kinetic parameters were obtained by polarization experiments and Electrochemical Impedance Spectroscopy (EIS) measurements.

Therefore, evaluating the catalytic activity based on the kinetic parameters and the electrochemical stability based on the surface chemical change of these electrocatalysts is done in this study to identify the best titanium oxy-nitride electrocatalyst for the ORR.

## 5.2 Experimental Procedure

### 5.2.1 Catalyst Preparation

Different Titanium Oxy-Nitrides ( $\text{TiO}_x\text{N}_y$ ) were produced by in-situ and ex-situ, urea-based and non-urea-based sol-gel methods. In all these methods, Titanium (IV) isopropoxide [ $\text{Ti}(\text{O}^i\text{C}_3\text{H}_7)_4$ ] (97%) (Purchased from Sigma-Aldrich) and absolute ethanol were used to prepare the sol. In in-situ urea-based method, urea was dissolved in absolute ethanol under severe stirring and then an appropriate amount of Titanium (IV) isopropoxide was added drop by drop to this solution. This sol was kept for 24 hours under  $\text{N}_2$  atmosphere and reflux conditions at 80 °C and later, by increasing the temperature to 150 °C and evaporating all excess solvent, a yellowish red remnant remained. The catalyst prepared by this method was called U. The same procedure was applied to produce the H catalyst, where monohydrate hydrazine (purchased from Anachemia) was used instead of urea. On the other hand, in the other two methods, first of all Titanium (IV) isopropoxide was added to the ethanol and then de-ionized water was added drop by drop. The electrocatalyst prepared by this procedure was called O. In the ex-situ urea-based sol-gel method, the O+U catalyst was produced by adding urea to the O just before the heat treatment section. These obtained precursors were subjected to a specified nitridizing gas ( $\text{N}_2 + 3\% \text{H}_2$ ) with a 200 mL/min flow rate at 700, 900 and 1100 °C (the corresponding temperature is indicated in the name of the sol-gel method for each sample, e.g., U-1100 is the electrocatalyst prepared by the

in-situ urea-based sol-gel method and heat treated at 1100 °C). Heat treatment converted the precursors (mostly titanium oxide and/or hydroxide) to titanium oxy-nitride and also changed the crystallinity, particle size and specific surface area, thereby, modifying the property of the electrocatalyst. The isothermal heat treatment time was 2 hours and the heating rate was 5 °C/min for both the heating and cooling.

### 5.2.2 Characterization

X-ray diffraction (XRD) data were collected using a Philips X'Pert diffractometer equipped with Cu K $\alpha$  radiation ( $\lambda = 1.5406 \text{ \AA}$ ) (at 50 kV and 40 mA) in a scan range ( $2\theta$ ) from 10° to 85° at a speed of 2° min<sup>-1</sup>. Ti, O and N contents of different samples were roughly examined through a scanning electron microscope (SEM, JEOL JSM-840) equipped with an Energy Dispersive X-Ray Spectroscopy (EDS). X-ray Photoelectron Spectroscopy (XPS) (Kratos Axis Ultra) revealed the oxidation state of Ti and its binding energy with other elements. The surface morphologies and particle size were observed by high resolution SEM (JSM-7600 TFE). The BET surface analyzer (Micromeritics Flow Sorb II 2300) was used to obtain the BET surface area of samples. To evaluate the electrocatalyst chemical and electrochemical stability, Ti ion concentration was measured by the method based on the Time Of Flight-Inductively Coupled Plasma-Mass Spectrometry (TOF-ICP-MS) (LECO, RENAISSANCE) to figure out the dissolution percentages.

### 5.2.3 Electrochemical Measurements

A conventional three-electrode compartment was used to conduct electrochemical experiments using a model 273A potentiostat/galvanostat (EG&G Princeton Applied Research, USA). Saturated calomel electrode (Hg/Hg<sub>2</sub>Cl<sub>2</sub> sat. KCl) and platinum (Pt) mesh as the reference and counter electrodes, respectively. The prepared electrocatalysts served as the working electrode, which was painted on a glassy carbon rod as the support. To prepare the working electrode, 10 mg of the prepared electrocatalyst powder was added to a mixture of 480  $\mu\text{L}$  de-ionized water and 20  $\mu\text{L}$  Nafion 5 % wt by ultrasonic treatment for 10 minutes. Then an appropriate amount of the ink was placed very slowly and layer by layer on a pre-polished glassy carbon rod (CH Instruments Inc. CHI 104, diameter = 3 mm). Electrochemical impedance spectroscopy (EIS)

measurements were implemented with a Solartron SI 1260 (impedance/gain-phase analyzer) in a frequency range of 0.1 Hz to 1 MHz and a DC bias was applied by an Solartron 1470 (battery test unit) instrument. An AC sinusoidal perturbation of 10 mV amplitude was superimposed on the DC potential bias implemented by the battery test unit. The impedance data acquisition monitoring and fitting an appropriate equivalent circuit were done by Zview software. The charge transfer resistance and the capacitance values were calculated.

## 5.3 Results and Discussions

### 5.3.1 Physicochemical Characterizations

Figure 1 shows the XRD results of the catalysts produced by the in-situ urea-based sol-gel method calcinated at 700 °C, 900 °C and 1100 °C for 2 hours. In the other sol-gel methods only the results of the samples calcinated at the highest temperature, 1100 °C are presented, because at the lower temperatures there was no considerable change. The five diffraction peaks at  $2\theta$  of 36.56°, 42.54°, 61.71°, 73.99° and 77.89° were indexed as the cubic Fm3m unit cell of TiN [(111), (200), (220), (311) and (222)] (JCPDS No. 38-1420). The strong diffraction peaks at 25.25°, 37.75°, 47.95°, 53.79° and 55.05° were respectively assigned to (101), (004), (200), (105) and (211) facets of the tetragonal anatase structure of titanium dioxide (JCPDS No. 21-1272). In addition, diffraction peaks at 27.421°, 36.041°, 41.187°, 54.233° and 56.783° were respectively assigned to (110), (101), (111), (211) and (220) of the tetragonal rutile structure of titanium dioxide (JCPDS No. 03-1122). Pure anatase TiO<sub>2</sub> and TiN purchased respectively from Fisher Scientific and Sigma-Aldrich were used as references to compare the crystallite size of the prepared catalysts.

In both the non-urea based sol-gel methods, O and H, increasing the temperature led to a phase change from anatase to rutile. This is evident in figure 1, by the vanishing (101) anatase facet at 25.25° and the (110), (211) and (220) rutile facets appearing at 27.421°, 54.233° and 56.783°, respectively. The lattice parameters mentioned in table 1 also proved that both O-1100 and H-1100 had a tetragonal rutile like structure with almost the same parameters as the rutile TiO<sub>2</sub> reference. In addition there was no significant sign of the presence of the 5 identified TiN peaks in these samples, indicating the lower phase transfer of titanium oxide to titanium nitride. This

means a significant amount of the electrocatalyst prepared by the O and H methods was  $\text{TiO}_2$  even under a nitridizing gas at such a high temperature.

In the case of O+U, increasing the temperature to 1100 °C led to the characteristic peaks of TiN appearing, however, the calculated lattice parameters showed that the electrocatalyst had a more tetragonal anatase structure than a cubic one. So in this case, the calculated  $a$  and  $c$  lattice parameters were too far from each other (4.169 and 9.6217 Ang, respectively) to create a cubic TiN like cell. One might conclude that the presence of urea at the heat treatment step suppressed the phase transformation from anatase to rutile even at a high temperature.

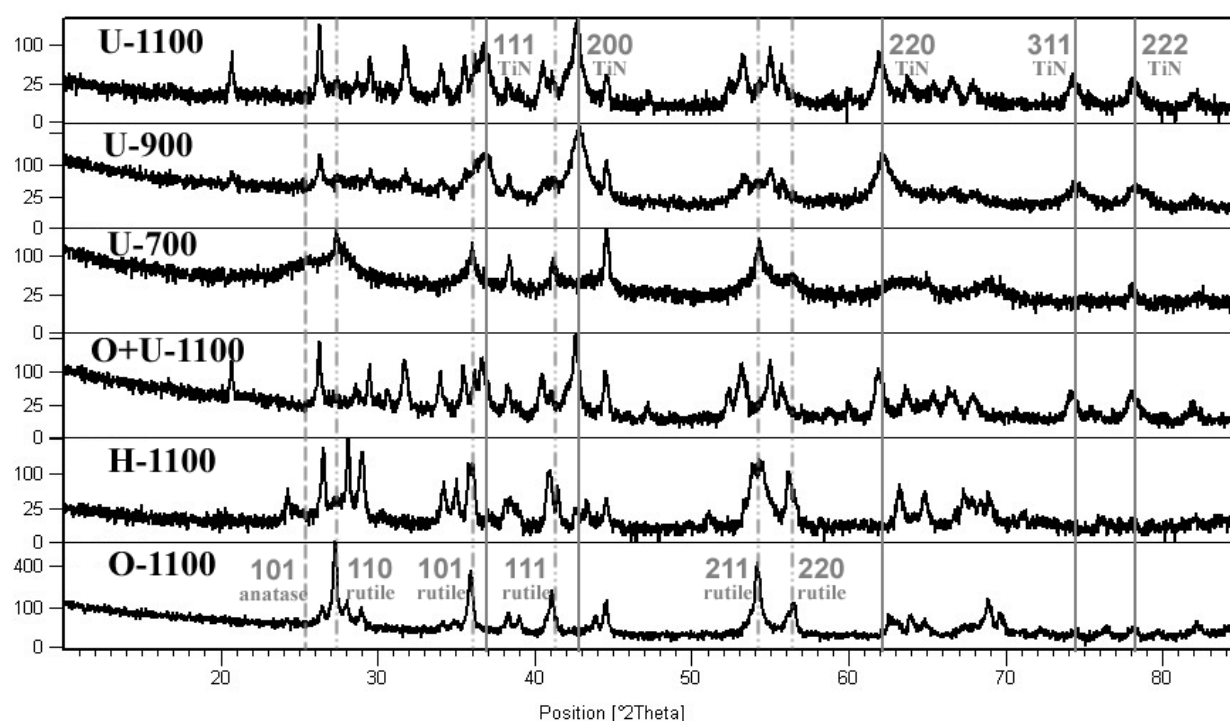


Figure 1. XRD patterns of different samples

Table 1. Lattice parameters of the prepared samples and purchased TiN and anatase  $\text{TiO}_2$

Samples	U-1100	U-900	U-700	O+U-1100	H-1100	O-1100	TiN	$\text{TiO}_2$
Lattice parameters	a	4.4782	4.4052	4.5668	4.169	4.6198	4.6226 (4.2417) <sup>1</sup>	3.8307 (4.5928) <sup>2</sup> , (3.7852) <sup>3</sup>
	c	4.9578	5.2514	2.0117	9.6217	2.9375	2.9603	9.262 (2.9582) <sup>2</sup> , (9.5139) <sup>3</sup>

<sup>1</sup> JCPDS 38-1420 reference of TiN. <sup>2</sup> JCPDS 03-1122 reference of rutile  $\text{TiO}_2$ . <sup>3</sup> JCPDS 21-1272 reference of anatase  $\text{TiO}_2$

In the case of U, the TiN characteristic peaks were obvious, even at lower temperatures. At low temperature the phase transfer took place from anatase to rutile. So that, the U-700 lattice parameters ( $a = 4.5668$  and  $c = 2.0117$  Ang) were consistent with those of the rutile  $\text{TiO}_2$  reference (table 1). In addition, at higher temperatures (900 and 1100 °C) there was another phase transfer from the tetragonal rutile structure to the cubic TiN structure. This was more evident in U-1100. Therefore, there was a considerable amount of TiN in the samples prepared using the in-situ urea-based sol-gel method (U), especially those calcinated at 1100 °C. Increasing the temperature also made the peaks much sharper indicating the growth of the crystallite size. The calculated crystallite size with the Scherrer equation showed the crystallite size of U and O+U catalysts (20 to 40 nm) were almost in the same range of the TiN crystallite size, and the crystallite size of O and H catalysts (40 to 60 nm) were in the same range of the  $\text{TiO}_2$  crystallite size.

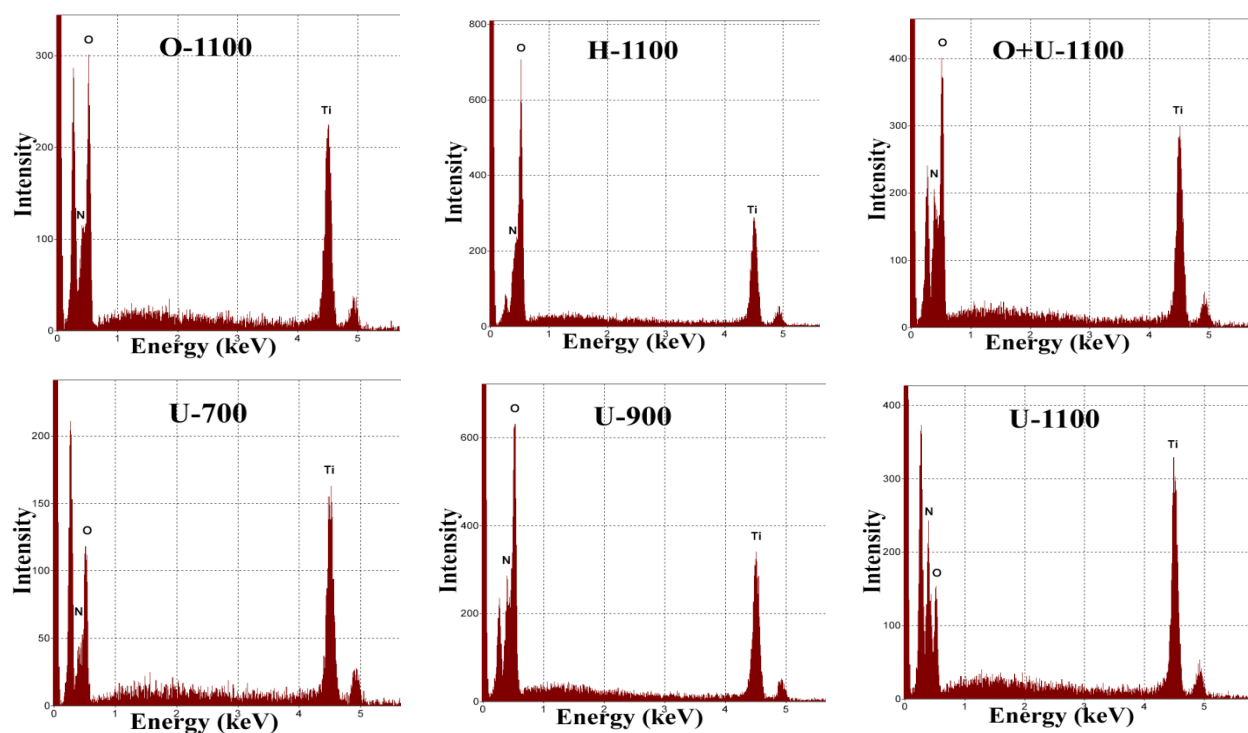


Figure 2. EDS patterns of different samples

So, there were both TiN and  $\text{TiO}_2$  phases with different ratios in the electrocatalysts, and the samples could be called  $\text{TiO}_x\text{N}_y$  with different ratios of  $x$  and  $y$ . Also, calculating the area under the peaks in the EDS elemental analysis graphs (figure 2) revealed that the nitrogen percentage increased from 9 and 17 percent in U-700 and U-900, respectively, to 24 percent in U-1100,

while the oxygen percentage was decreasing inversely. The first peak at around 0.27 keV in these EDS patterns, which was related to the carbon, came mostly from the tape used as a sample holder, thus it was excluded in the calculation.

Figure 3, which is the SEM picture of the prepared samples, demonstrates the agglomeration and sintering, porosity and particle size differences, which affect the electrocatalyst in shape, size, surface area and, consequently, catalytic properties. The particle size was completely dependent on the preparation method and calcination temperature. Therefore, in the case of O, H and O+U, it was ca. 250-300, 400-500 and 700-800 nm, respectively. However, in U catalysts, it was less than 200 nm, and by increasing the temperature it was reduced to 20-40 nm. This particle size reduction is clear in figure 3. Generally, in all samples at high temperatures we saw less agglomeration (despite the more sintering probability at higher temperatures) and more porosity, although from O to H and then to O+U there was more porosity. This factor greatly affected the value of the surface area. Uniformity in particle size is also very important. For instance, O+U-1100 had much bigger particles than O and H, however, unlike the O and H, O+U particles were not uniform and there were a lot of tiny particles, which led to a higher B.E.T. surface area. Having a very high B.E.T. surface area with the U method was also a consequence of particles that were too small. The values of particle size and B.E.T. surface area are mentioned in table 3.

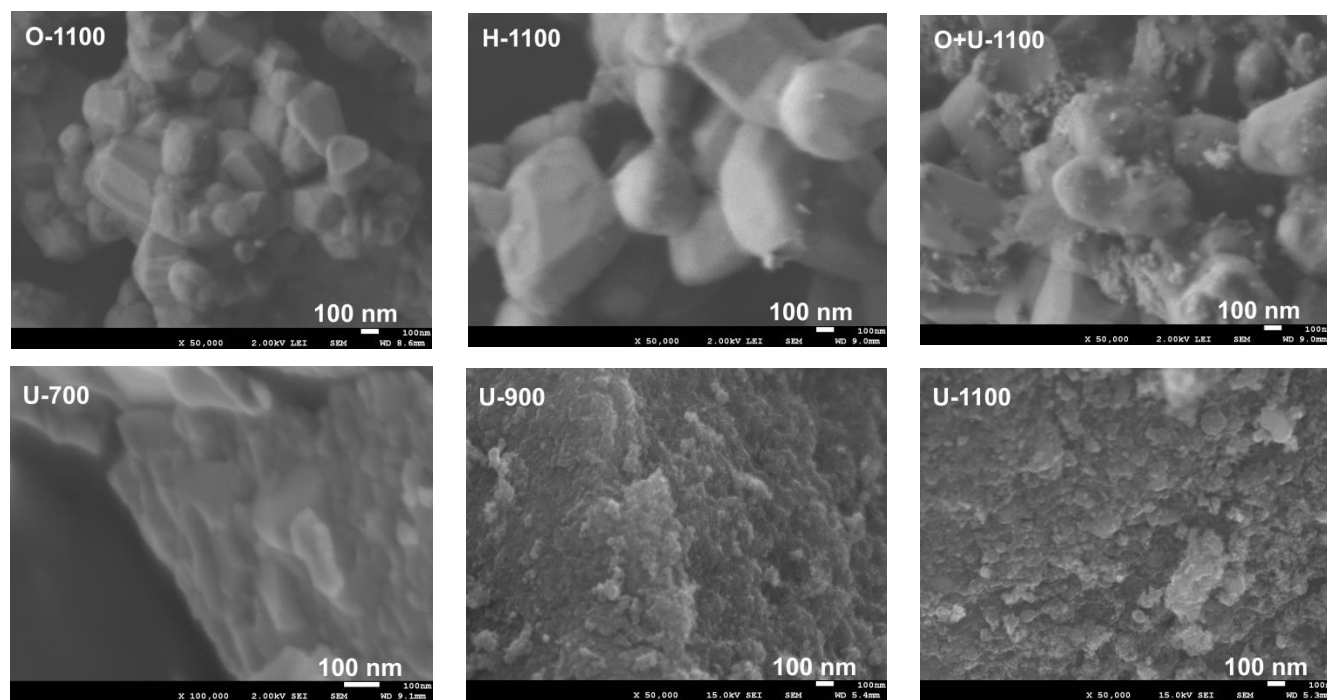


Figure 3. SEM images of the samples prepared by different methods

### 5.3.2 Chemical and electrochemical stability and catalytic activity

Cyclic Voltammetry (CV) with a scan rate of  $100 \text{ mV}\cdot\text{s}^{-1}$  in the range of 0.0 to 1.2 V (versus NHE) was performed to evaluate the electrochemical stability of the prepared electrocatalysts. Sulfuric acid  $0.5 \text{ mol}\cdot\text{dm}^{-3}$  saturated with  $\text{N}_2$  at atmospheric pressure and  $25 \text{ }^\circ\text{C}$  was used as the electrolyte to simulate the PEM fuel cell circumstances as accurately as possible. The shape of the CV hardly changed after 100 cycles, indicating a high electrochemical stability of the heat treated titanium oxy-nitrides in such a corrosive media at this PEM fuel cell working potential range. As well, calculated anodic and cathodic electric charge densities were almost the same, indicating high surface stability of the specimens in the absence of electrocatalyst dissolution or reduction. These calculated electrical charge densities also revealed a high electrochemical surface area of the samples prepared by the U method, so that the catalyst U-1100 showed the highest double layer charge density, with more than  $2500 \text{ }\mu\text{C}\cdot\text{cm}^{-2}$  electrical charge density, which is almost 5 times bigger than the other electrocatalysts. This was consistent with the B.E.T. results and the particle size obtained by the SEM.

To evaluate the electrocatalytic activity Slow Scan Voltammetry (SSV) (scan rate:  $5 \text{ mV}\cdot\text{s}^{-1}$ , 1.2 V to 0 V vs. NHE) was performed under nitrogen and oxygen atmospheres. The obtained current under  $\text{N}_2$  atmosphere was the charge current of the double layer capacitance. The difference between the current under  $\text{O}_2$  atmosphere ( $i_{\text{O}_2}$ ) and that under  $\text{N}_2$  atmosphere ( $i_{\text{N}_2}$ ) corresponded to the oxygen reduction current ( $i_{\text{ORR}}$ ), that is,  $i_{\text{ORR}} = i_{\text{O}_2} - i_{\text{N}_2}$ . The onset potential for the ORR,  $E_{\text{ORR}}$ , was defined as the electrode potential at the  $i_{\text{ORR}} = -0.2 \text{ }\mu\text{A}\cdot\text{cm}^{-2}$ .

To extract the kinetics parameters (Tafel slope and exchange current density) polarization with an extremely slow scan rate ( $0.1667 \text{ mV}\cdot\text{s}^{-1}$ ) was taken under saturated  $\text{O}_2$  atmosphere. Figures 4-a and b show the polarization curves and the Tafel plots of all prepared electrocatalysts, respectively. According to these curves it was evident that the electrocatalytic activity for the ORR was significantly dependent on both the heat-treatment temperature and the selected sol-gel method, so that the onset potential of titanium oxy-nitride increased from ca. 0.44 V to 0.75 V vs. NHE by increasing the temperature from 700 to 1100  $^\circ\text{C}$  in the U samples. As well, there was at least a 300 mV improvement in the onset potential with the electrocatalyst prepared by the U method compared with the others, in addition its significant higher current density was

demonstrated more precisely in figure 4-a. All Tafel parameters are mentioned in table 3. All catalysts showed almost the same range for the Tafel slopes, however, due to a better onset potential and exchange current density, U-1100 showed the best activity for the ORR. Regarding the physicochemical characterization results, it seems that having a high active surface area and more defects on the electrocatalyst surface play a prominent role in its electrocatalytic activity for the ORR. Therefore, U-1100 with both of the high B.E.T. and electrochemical surface area as well as more defects on the surface showed the highest onset potential and current density compared to the other electrocatalysts.

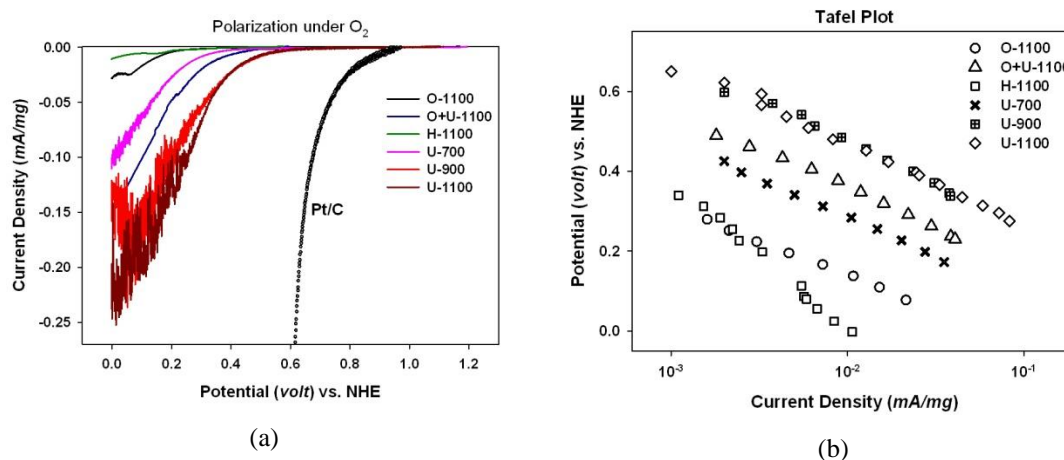


Figure 4. (a) Polarization curves (scan rate  $0.1667 \text{ mV}\cdot\text{s}^{-1}$ ) under  $\text{O}_2$  and (b) Tafel plots of all prepared catalysts

To evaluate the electrochemical stability at higher oxidation voltage than the frequently working potential, CV was taken at a larger potential range from -2 to +2 volts vs. SCE. These CV curves are depicted in figure 5, for the U-1100, U-900 and also for the commercial  $\text{TiO}_2$ . From thermodynamic, at a high oxidizing potential the  $\text{TiO}_2$  surface is more stable than the one with surface defects. There was a huge peak around 1.55 volts vs. SCE in the case of U-1100, showing more defects on its surface. This peak was significantly smaller in U-900, and there was approximately no considerable oxidation peak in the other electrocatalysts. The other electrocatalysts showed almost the same behavior as commercial  $\text{TiO}_2$ , depicted in figure 5. Keeping in mind that the more defects on the electrocatalyst surface, the more tendencies to oxidation, makes it easy to understand this behavior. This result was in complete agreement with those obtained from XRD and EDS to show that U-1100 had more TiN than  $\text{TiO}_2$  in its structure,

leading to more defects on its surface, which consequently improved the oxygen reduction procedure (figure 4-a).

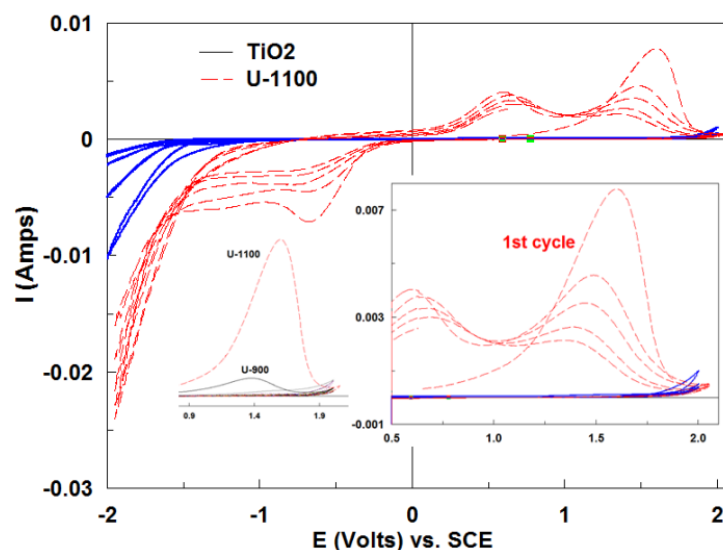


Figure 5. CV (scan rate  $100 \text{ mV}\cdot\text{s}^{-1}$  under  $\text{N}_2$ ) of U-1100, U-900 and commercial  $\text{TiO}_2$ . Under practical PEM fuel cell conditions, although the working potential range is much lower than this oxidizing potential, it is not far from reality to possess such a high oxidation potential for a moment. Therefore, studying the electrocatalyst performance after this oxidation condition is somewhat important. Figure 6 shows the polarization curves before and after the oxidation of our best prepared catalyst, U-1100. Although, the onset potential did not change much, increasing the Tafel slope and inversely decreasing the exchange current density values had a prominent effect on the electrocatalytic activity of this electrocatalyst. As a result, a performance drop after oxidation is clear in figure 6.

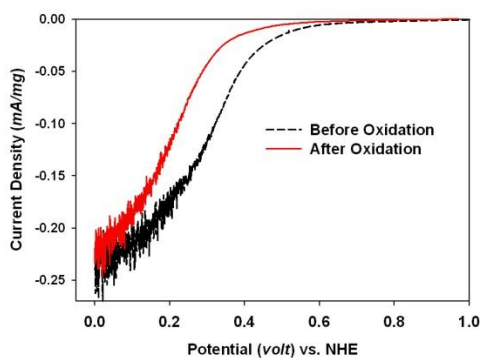


Figure 6. Polarization (scan rate  $0.1667 \text{ mV}\cdot\text{s}^{-1}$  under  $\text{O}_2$ ) of U-1100 before and after oxidation scan up to 2 volts vs. SCE

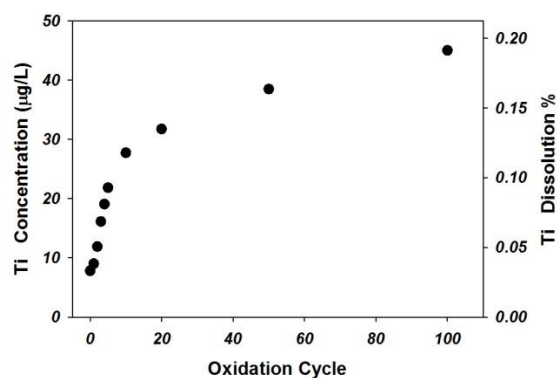


Figure 7. ICP-TOF analysis results of Ti ion concentration after several CV with  $100 \text{ mV}\cdot\text{s}^{-1}$  scan rate

In reverse scans the reduction reaction on the electrocatalyst surface started at -0.3 volts vs. SCE and decreasing potential to less than -1.5 volts vs. SCE led to hydrogen evolution (figure 5). This reduction reaction was not balanced with the oxidation reaction, which led to having more oxidizing current. There were two reasons for this current: the dissolution of Ti into the electrolyte and the oxidizing of TiN to TiO<sub>2</sub>. The latter was proven by measuring the titanium ion concentration through the electrolyte by ICP-TOF, and the former was confirmed by XPS measurements of the surface of the electrocatalyst before and after oxidation up to 2 volts vs. SCE.

Figure 7 shows the Ti concentration in the electrolyte at the end of each oxidizing scan up to 100 cycles. Ti dissolution was sharply increased at the beginning; however, it reached a semi-saturated condition after 20 cycles. This was in accordance with the related CV depicted in figure 5, where we see smaller oxidation peaks after some cycles. Based on the ICP-TOF analysis, this catalyst showed relatively high stability compared to that of the commercial Pt/C electrocatalyst. Therefore to evaluate the chemical stability by putting the catalyst in 10 mM sulfuric acid at 50 °C for 24 hours, without applying any external voltage, Ti dissolution was less than 0.1 percent in U-1100, while Pt dissolution was around 0.15 percent. In addition, under such a high oxidizing potential, titanium dissolution after 100 cycles was less than 0.2 percent, showing relatively high electrochemical stability.

Figure 8 represents the XPS survey scan of the U-1100 catalyst. According to this survey the existence of nitrogen and oxygen besides titanium was proven. A big peak around 290 eV is attributed to the carbon coming from the participating organic sources in electrocatalyst preparation and the carbon dioxide impurities from the environment during the sample preparation. XPS survey scans were taken of a sample before and after oxidation (oxidation at a potential higher than 1.55 volts vs. SCE). Although the shapes of both surveys were almost the same as the one presented in figure 8, calculating the elemental percentages showed a decrease of nitrogen at the surface of the electrocatalyst after oxidation. Therefore, excluding carbon impurities, nitrogen constituted only 5 percent of the TiO<sub>x</sub>N<sub>y</sub> surface composition after oxidation, while it was around 11 percent before oxidation. This is presented more precisely in the high resolution XPS scan in figure 9. Comparing the N 1s peaks before (a) and after (b) oxidation revealed the decrease of the Ti-N bond by oxidation. Decomposition of the high resolution XPS spectra of Ti 2P<sub>3/2</sub> and N 1S<sub>1/2</sub> in figure 9 shows four different Ti bonds in TiO<sub>2</sub>, Ti<sub>2</sub>O<sub>3</sub>, TiO and

TiN components and three N-Ti, N-O and N-C bonds. The related binding energies are mentioned in table 2.

Generally, Ti-N binding energy of ca. 455 eV was lower than titanium oxide compounds binding energy of ca. 459 eV, indicating TiN was less stable than titanium oxide. Furthermore, comparing the lower nitrogen percentage of the electrocatalyst surface composition mentioned in table 2 with the higher nitrogen percentage in the bulk of the electrocatalyst obtained by EDS (ac. 24 percent) revealed that, at least on the surface of the electrocatalyst, TiN tends to be oxidized to titanium oxide compounds, even in the absence of any applied oxidizing potential. Not only the existence of such a low amount of nitrogen was enough to make defects in the electrocatalyst surface to accelerate the ORR, but also the higher amount of TiN in the bulk of the catalyst led to improve the electrical conductivity of the electrocatalyst. The effect of these improvements was obvious in the polarization curve (figure 4), nevertheless, it would be explained more precisely by EIS measurements, in the following section.

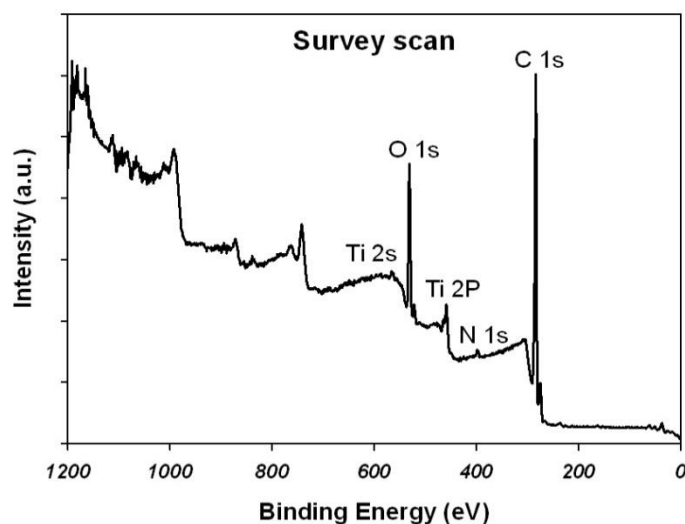


Figure 8. Survey scan XPS

Table 2. Binding energy (eV) of Ti  $2P_{3/2}$  and N  $1S_{1/2}$  before and after oxidation

	before oxidation	after oxidation
<b>TiO<sub>2</sub></b>	459.4	459.8
<b>Ti<sub>2</sub>O<sub>3</sub></b>	457.6	458.2
<b>TiO</b>	456.5	456.9
<b>TiN</b>	455.3	455.6
<b>N-Ti</b>	397	397.3
<b>N-O</b>	402.4	402.7
<b>N-C</b>	400.5	401
<b>Nitrogen percentage</b>	11 %	5 %

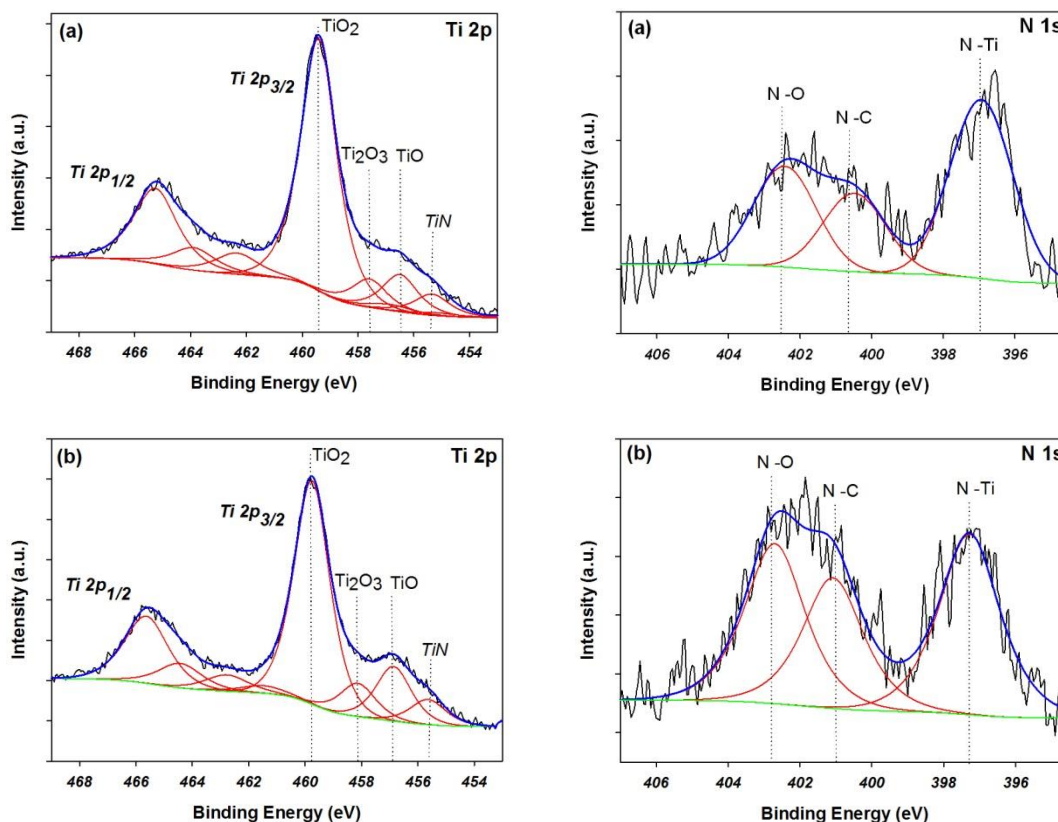


Figure 9. High resolution XPS spectra of the U-1100 catalyst (a) before and (b) after oxidation

### 5.3.3 Electrochemical Impedance Spectroscopy (EIS) Analysis

Using the same three-electrode cell as explained in the previous section, electrochemical impedance spectroscopy analysis was done on the prepared catalysts. DC bias potential had three different values of the open circuit voltage (OCV), -0.3 volts vs. OCV and +1.5 volts vs. SCE, while an AC sinusoidal potential with 10 mV amplitude and a frequency of 1 MHz to 0.01 Hz was superimposed on that. A modified Randles–Erszler equivalent circuit combined with an uncompensated ohmic resistance ( $R_s$ ) in a series with a parallel set of charge transfer resistance ( $R_{ct}$ ) and diffusional impedance ( $W_s$ ) with a constant phase element ( $CPE$ ) explaining the double layer capacitance ( $R_s - [(R_{ct} - W_s) // CPE]$ ) has been used by several researchers to explicate the impedance of the ORR [58-59]. This model is depicted in figure 10 (a). This equivalent circuit is like the one Dhirde et al.[60] used to model a low current PEM fuel cell system.

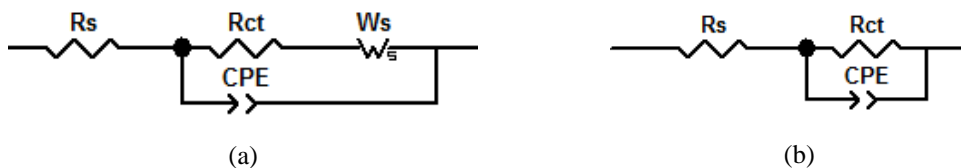


Figure 10. (a) Modified Randles–Ershler equivalent circuit model ( $R_s$ : uncompensated ohmic resistance,  $R_{ct}$ : charge transfer resistance,  $W_s$ : Warburg finite element with short terminal,  $CPE$ : constant phase element), (b) simplified model by ignoring Warburg impedance effects

In this investigation the same model has been used to fit the experimental data, however, due to big charge transfer resistance, the effect of the diffusional impedance was negligible, so that in most of the electrocatalysts the simplified model presented in figure 10 (b) also fitted the obtained impedance spectra very well. The quality of the fitting equivalent circuit was controlled by the Chi-squared (to be less than 0.001) and variance values. As well, the Kramers-Kronig (K-K) data validation test was employed. Overall, the equivalent circuits fitted the experimental data quite well.

The constant phase element (CPE) with the following formula was used to explain the double layer capacitance impedance:

$$Z_{CPE} = \frac{1}{Q(j\omega)^n}$$

Where  $j$  is an imaginary unit,  $\omega$  is frequency,  $Q$  is the CPE coefficient explaining the capacitance of the system and exponent  $n$  varies between 0 and 1. If  $n$  equals 1 then the equation is identical to that of a capacitor. If  $n$  equals 0.5, a 45 degree line is produced on the Nyquist plane. The non-uniform diffusion, the roughness and non-homogeneity effect, the distortion of the double layer by Faradaic reactions at the interface, the adsorption of impurities through the electrolyte and several other factors led to the double layer behaving more like a CPE than a perfect capacitor. It produced a depressed semicircle instead of a perfect semicircle. In fact, a capacitor is a constant phase element with a constant phase angle of 90 degrees ( $n = 1$ ).

The diffusion impedance in the model is presented by  $W_s$  recognized as the finite length Warburg element with short circuit terminals (it is terminated in a finite resistance). The following formula shows the generalized Warburg element, which was used in the selected equivalent circuit to fit the experimental data:

$$Z_{W_s} = R \frac{\tanh(j\omega T)^n}{(j\omega T)^n}$$

Where the exponent  $n$  varies again between 0 and 1 and in the case of  $n = 0.5$  one obtains the finite length Warburg element, which is the solution for the one-dimensional diffusion equation of a particle.  $R$  is diffusion resistance, indicating the impedance at the limit of  $\omega \rightarrow 0$ ,  $T = L^2/D$  and  $L$  and  $D$  are effective diffusion thickness and effective diffusion coefficient, respectively. In the mentioned models in figure 10,  $R_{ct}$  and  $R_s$  are the charge transfer resistance of the working electrode and the uncompensated ohmic resistance of the system including the electrolyte resistance, respectively. The value of  $R_s$  was almost constant in all experiments and equal to ca. 10 ( $\Omega$ ).

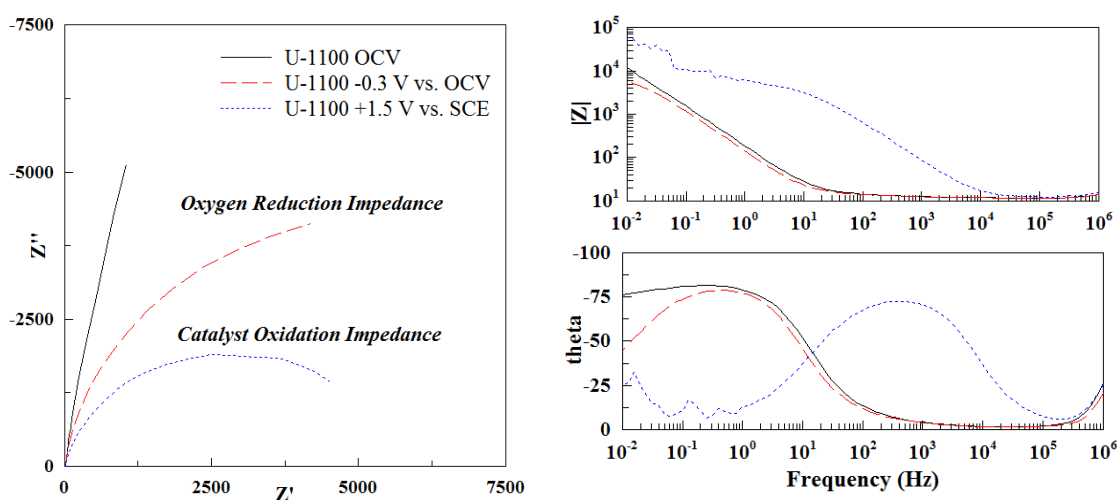


Figure 11. EIS data in the Nyquist (left) and Bode (right) diagram for the U-1100 catalyst at three different bias DC potentials: 0 V vs. OCV, -0.3 V vs. OCV and +1.5 V vs. SCE. AC perturbation had an amplitude of 10 mV.

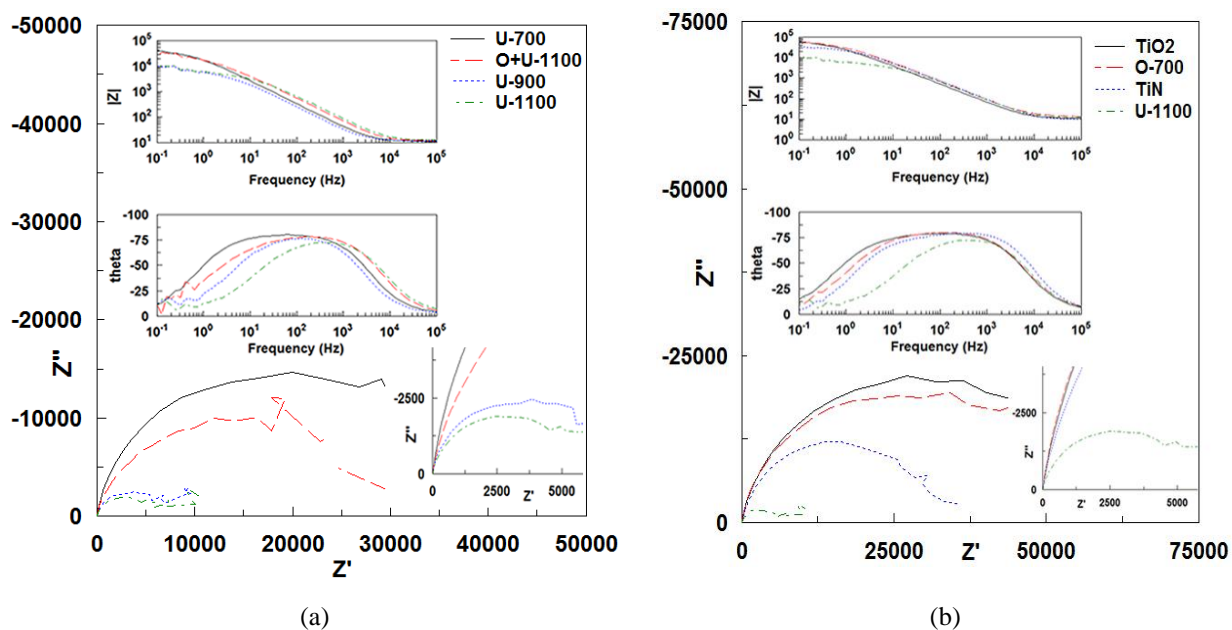


Figure 12. EIS spectra of (a) O+U-1100 and all U catalysts and (b) commercial TiO<sub>2</sub> and TiN and prepared O-700 and U-1100 catalysts. The bias DC potential: 1.5 V vs. SCE and Ac perturbation: 10 mV.

Figure 11 illustrates the behavior of the U-1100 at three different bias potentials of 0 volts vs. OCV, -0.3 volts vs. OCV and +1.5 volts vs. SCE. These spectra are presented in Nyquist and Bode diagrams, at the right and left of figure 11, respectively. Despite the U-1100 showing the best electrocatalytic activity for the ORR according to the polarization curves, at OCV there was a big charge transfer impedance, indicating a too slow rate reaction. It was worse for the other electrocatalysts, however, decreasing the bias potential to -0.3 volts vs. OCV, accelerated the ORR by decreasing the charge transfer resistance from ca. 82 k $\Omega$  at OCV to ca. 8 k $\Omega$  when there was an over-potential of 0.3 volts. The calculated charge transfer resistance and double layer capacitance ( $C_{dl}$ ) of the other catalysts are mentioned in table 3. Comparing the charge transfer resistances indicated that, like the result obtained from the polarization experiment, U-1100 had the best catalytic activity with the lowest charge transfer resistance. The other electrocatalysts with a relatively big resistance confirmed their low activity for the ORR. Although changing the bias potential changed the charge transfer resistance in almost all the electrocatalysts (sometimes by 2 orders of magnitude), it did not affect the double layer capacitances. U-1100 with a specific capacitance of 3.29625 (F/g) showed the biggest surface area, which was consistent with its

B.E.T. surface area. The specific capacitance values of other electrocatalysts are mentioned in table 3.

To compare more precisely the oxidation reaction rate, EIS measurements at a bias DC potential of 1.5 V vs. SCE were carried out. The corresponding results are represented in Figures 11 and 12. The impedance spectrum of U-1100 in Figure 11 proves the tendency of U-1100 to be oxidized at this oxidizing potential. The charge transfer resistance was considerably lower than the others. Figure 12 compares its impedance with the other electrocatalysts and also with commercial TiO<sub>2</sub> and TiN. Like the results obtained from the CV in a wide potential range (depicted in figure 5), in figure 12 the electrocatalysts prepared by the U method and calcinated at a high temperature reveal lower impedance to oxidation than the other catalysts. The catalysts prepared by O, H and O+U methods showed impedance like the impedance of commercial anatase titanium oxide, which indicated lower defects on their surface. These results once again pointed out a relatively higher surface area and more active sites in the case of catalysts prepared by the U method and heat treated at high temperatures.

Table 3. BET, particle size, EIS and Tafel parameters of the TiO<sub>x</sub>N<sub>y</sub> catalysts prepared by different sol-gel methods.

samples	BET surface area (m <sup>2</sup> /g)	Particle size (nm)	Specific Capacitance (F/g)	Charge Transfer Resistance (ohm)		Tafel Slope (mV/decade)	Exchange Current density (mA/mg)	Onset Potential (Volt vs. NHE)
				OCV	-0.3 V vs. OCV			
U-1100	<b>93.5132</b>	<b>20~60</b>	<b>3.29625</b>	8.25E+04	8.81E+03	<b>-203</b>	<b>4.30E-04</b>	<b>0.75</b>
U-900	<b>91.0436</b>	<b>40~60</b>	<b>2.41925</b>	3.04E+06	1.92E+04	<b>-217</b>	<b>7.50E-04</b>	<b>0.72</b>
U-700	<b>77.9177</b>	<b>~200</b>	<b>0.5977</b>	1.71E+06	9.47E+04	<b>-190</b>	<b>1.50E-03</b>	<b>0.44</b>
O+U	<b>15 ~ 20</b>	700~800	< 0.5	~ 1E+06	~ 5E+05	<b>-200 ~ -300</b>	<b>~ 2E-04</b>	<b>0.3 ~ 0.5</b>
H	<b>5 ~ 10</b>	400~500	< 0.02	~ 2E+06	~ 1E+06	<b>-240 ~ -350</b>	<b>~ 8E-04</b>	<b>0.3 ~ 0.4</b>
O	<b>&lt; 5</b>	250~300	< 0.1	> 1E+7	~ 3E+06	<b>-160 ~ -230</b>	<b>~ 8E-04</b>	<b>0.3 ~ 0.4</b>

## 5.4 Conclusion

The feasibility of the preparation of a mixture of titanium oxy-nitride electrocatalyst for the ORR achieved. XRD and EDS results revealed that a considerable amount of nitrogen in the form of a TiN phase was inserted into the metal oxide structure to enhance the electrocatalytic activity by

improving the electrical properties and also introducing the defects on the surface. EDS results show that nitrogen content of ca. 24 % was obtained from the bulk of the electrocatalyst prepared by this method and heat treated at 1100 °C. Its surface was strongly oxidized. Based on the XPS analysis, it was found that the nitrogen amount on the surface was ca. 11 % before oxidizing the sample, and it was decreased even lower than ca. 5 % when the sample was oxidized at a potential of 1.5 V vs. SCE. The results also show that under the applied oxidation potential (up to 2 V vs. SCE) the maximum concentration of the dissolve titanium was smaller than 0.5 µg/L ~ 0.2 wt % after the 100<sup>th</sup> cycle of the cyclic voltammogram curves. This amount was less than 0.1 wt % when there was no applied potential. This indicates a much higher stability of this family of electrocatalysts when compared to those of the commercial Pt/C catalyst. The morphology of the electrocatalyst revealed by the SEM images supported that the high BET surface area of U-1100 (ca. 93 m<sup>2</sup>/g) was a consequence of the very small particle size (ca. 20~60 nm) of the catalyst produced by this method. Based on the amounts of the onset potential, the exchange current density and the Tafel slopes, electrocatalysts prepared by the in-situ urea-based sol-gel method had much higher electrocatalytic activity than the others. Polarization taken in the PEM fuel cell potential range (0 to 1.2 V vs. NHE) showed the biggest onset potential for U-1100 at around 0.75 V vs. NHE. The exchange current density of these electrocatalysts was one order of magnitude higher than that of other electrocatalysts. In particular the best electrocatalytic activity for the ORR of the in-situ urea-based electrocatalyst was supported by the calculated value of the charge transfer resistance determined by the EIS measurements. It was found that its charge transfer resistance was significantly smaller ( $10^4$ ) than the charge transfer resistance of the other electrocatalysts ( $10^6$ ).

## 5.5 References

- [1] Higgins DC, Meza D, Chen Z. Nitrogen-Doped Carbon Nanotubes as Platinum Catalyst Supports for Oxygen Reduction Reaction in Proton Exchange Membrane Fuel Cells. *The Journal of Physical Chemistry C*. 2010;114:21982-8.
- [2] Chen Z, Waje M, Li W, Yan Y. Supportless Pt and PtPd Nanotubes as Electrocatalysts for Oxygen-Reduction Reactions. *Angewandte Chemie International Edition*. 2007;46:4060-3.

- [3] Toda T, Igarashi H, Watanabe M. Enhancement of the electrocatalytic O<sub>2</sub> reduction on Pt–Fe alloys. *Journal of Electroanalytical Chemistry*. 1999;460:258-62.
- [4] Tang Y, Zhang H, Zhong H, Xu T, Jin H. Carbon-supported Pd-Pt cathode electrocatalysts for proton exchange membrane fuel cells. *J Power Sources*. 2011;In Press, Corrected Proof.
- [5] Jung DW, Park S, Ahn CY, Kim JB, Oh ES. Performance Comparison of Pt<sub>1-x</sub>Pd<sub>x</sub>/Carbon Nanotubes Catalysts in Both Electrodes of Polymer Electrolyte Membrane Fuel Cells. *Fuel Cells*. 2012;12:398-405.
- [6] Zhang H, Yin Y, Hu Y, Li C, Wu P, Wei S, et al. Pd@Pt Core–Shell Nanostructures with Controllable Composition Synthesized by a Microwave Method and Their Enhanced Electrocatalytic Activity toward Oxygen Reduction and Methanol Oxidation. *The Journal of Physical Chemistry C*. 2010;114:11861-7.
- [7] Peng Z, Yang H. Synthesis and Oxygen Reduction Electrocatalytic Property of Pt-on-Pd Bimetallic Heteronanostructures. *J Am Chem Soc*. 2009;131:7542-3.
- [8] Yang H, Vogel W, Lamy C, Alonso-Vante N. Structure and Electrocatalytic Activity of Carbon-Supported Pt–Ni Alloy Nanoparticles Toward the Oxygen Reduction Reaction. *The Journal of Physical Chemistry B*. 2004;108:11024-34.
- [9] Stamenkovic VR, Fowler B, Mun BS, Wang G, Ross PN, Lucas CA, et al. Improved Oxygen Reduction Activity on Pt<sub>3</sub>Ni(111) via Increased Surface Site Availability. *Science*. 2007;315:493-7.
- [10] Wang G, Wu H, Wexler D, Liu H, Savadogo O. Ni@Pt core-shell nanoparticles with enhanced catalytic activity for oxygen reduction reaction. *J Alloy Compd*. 2010;503:L1-L4.
- [11] Zhao J, Manthiram A. In Situ Electrochemical Characterization of Proton Exchange Membrane Fuel Cells Fabricated with Pd–Pt–Ni Cathode Catalysts. *Journal of The Electrochemical Society*. 2011;158:B208-B14.
- [12] Wu H, Wexler D, Liu H, Savadogo O, Ahn J, Wang G. Pt<sub>1-x</sub>Cox nanoparticles as cathode catalyst for proton exchange membrane fuel cells with enhanced catalytic activity. *Mater Chem Phys*. 2010;124:841-4.

- [13] Chen S, Ferreira PJ, Sheng W, Yabuuchi N, Allard LF, Shao-Horn Y. Enhanced Activity for Oxygen Reduction Reaction on “Pt<sub>3</sub>Co” Nanoparticles: Direct Evidence of Percolated and Sandwich-Segregation Structures. *J Am Chem Soc.* 2008;130:13818-9.
- [14] Stamenković V, Schmidt TJ, Ross PN, Marković NM. Surface Composition Effects in Electrocatalysis: Kinetics of Oxygen Reduction on Well-Defined Pt<sub>3</sub>Ni and Pt<sub>3</sub>Co Alloy Surfaces. *The Journal of Physical Chemistry B.* 2002;106:11970-9.
- [15] Lee KH, Kwon K, Roev V, Yoo DY, Chang H, Seung D. Synthesis and characterization of nanostructured PtCo-CeO<sub>x</sub>/C for oxygen reduction reaction. *J Power Sources.* 2008;185:871-5.
- [16] Fugane K, Mori T, Ou DR, Suzuki A, Yoshikawa H, Masuda T, et al. Activity of oxygen reduction reaction on small amount of amorphous CeO<sub>x</sub> promoted Pt cathode for fuel cell application. *Electrochimica Acta.* 2011;56:3874-83.
- [17] Mukerjee S, Srinivasan S. Enhanced electrocatalysis of oxygen reduction on platinum alloys in proton exchange membrane fuel cells. *Journal of Electroanalytical Chemistry.* 1993;357:201-24.
- [18] Mani P, Srivastava R, Strasser P. Dealloyed Pt–Cu Core–Shell Nanoparticle Electrocatalysts for Use in PEM Fuel Cell Cathodes. *The Journal of Physical Chemistry C.* 2008;112:2770-8.
- [19] Stephens IEL, Bondarenko AS, Perez-Alonso FJ, Calle-Vallejo F, Bech L, Johansson TP, et al. Tuning the Activity of Pt(111) for Oxygen Electroreduction by Subsurface Alloying. *J Am Chem Soc.* 2011;133:5485-91.
- [20] Stamenkovic V, Mun BS, Mayrhofer KJJ, Ross PN, Markovic NM, Rossmeisl J, et al. Changing the Activity of Electrocatalysts for Oxygen Reduction by Tuning the Surface Electronic Structure. *Angewandte Chemie International Edition.* 2006;45:2897-901.
- [21] Nie M, Shen PK, Wu M, Wei Z, Meng H. A study of oxygen reduction on improved Pt-WC/C electrocatalysts. *J Power Sources.* 2006;162:173-6.
- [22] Toda T, Igarashi H, Uchida H, Watanabe M. Enhancement of the Electroreduction of Oxygen on Pt Alloys with Fe, Ni, and Co. *Journal of The Electrochemical Society.* 1999;146:3750-6.

- [23] Jeon MK, Lee CH, Park GIL, Kang KH. Combinatorial search for oxygen reduction reaction electrocatalysts: A review. *J Power Sources*. 2012;216:400-8.
- [24] Alia SM, Zhang G, Kisailus D, Li D, Gu S, Jensen K, et al. Porous Platinum Nanotubes for Oxygen Reduction and Methanol Oxidation Reactions. *Adv Funct Mater*. 2010;20:3742-6.
- [25] Vukmirovic MB, Zhang J, Sasaki K, Nilekar AU, Uribe F, Mavrikakis M, et al. Platinum monolayer electrocatalysts for oxygen reduction. *Electrochimica Acta*. 2007;52:2257-63.
- [26] Wu J, Yuan XZ, Martin JJ, Wang H, Zhang J, Shen J, et al. A review of PEM fuel cell durability: Degradation mechanisms and mitigation strategies. *Journal of Power Sources*. 2008;184:104-19.
- [27] Yu X, Ye S. Recent advances in activity and durability enhancement of Pt/C catalytic cathode in PEMFC: Part II: Degradation mechanism and durability enhancement of carbon supported platinum catalyst. *J Power Sources*. 2007;172:145-54.
- [28] Shao Y, Yin G, Gao Y. Understanding and approaches for the durability issues of Pt-based catalysts for PEM fuel cell. *J Power Sources*. 2007;171:558-66.
- [29] Rinaldo SG, Lee W, Stumper J, Eikerling M. Model- and Theory-Based Evaluation of Pt Dissolution for Supported Pt Nanoparticle Distributions under Potential Cycling. *Electrochemical and Solid-State Letters*. 2011;14:B47-B9.
- [30] Wang D, Xin HL, Yu Y, Wang H, Rus E, Muller DA, et al. Pt-Decorated PdCo@Pd/C Core-Shell Nanoparticles with Enhanced Stability and Electrocatalytic Activity for the Oxygen Reduction Reaction. *J Am Chem Soc*. 2010;132:17664-6.
- [31] Zhang K, Yue Q, Chen G, Zhai Y, Wang L, Wang H, et al. Effects of Acid Treatment of Pt-Ni Alloy Nanoparticles@Graphene on the Kinetics of the Oxygen Reduction Reaction in Acidic and Alkaline Solutions. *The Journal of Physical Chemistry C*. 2010;115:379-89.
- [32] Zhou Z-M, Shao Z-G, Qin X-P, Chen X-G, Wei Z-D, Yi B-L. Durability study of Pt-Pd/C as PEMFC cathode catalyst. *International Journal of Hydrogen Energy*. 2010;35:1719-26.
- [33] Mazumder V, Chi M, More KL, Sun S. Core/Shell Pd/FePt Nanoparticles as an Active and Durable Catalyst for the Oxygen Reduction Reaction. *J Am Chem Soc*. 2010;132:7848-9.

- [34] Zamel N, Li X. Effect of contaminants on polymer electrolyte membrane fuel cells. *Progress in Energy and Combustion Science*. 2011;37:292-329.
- [35] Bonakdarpour A, Lobel R, Sheng S, Monchesky TL, Dahn JR. Acid Stability and Oxygen Reduction Activity of Magnetron-Sputtered Pt<sub>1-x</sub>Ta<sub>x</sub> (0 ≤ x ≤ 1) Films. *Journal of The Electrochemical Society*. 2006;153:A2304-A13.
- [36] Wang B. Recent development of non-platinum catalysts for oxygen reduction reaction. *J Power Sources*. 2005;152:1-15.
- [37] Maekawa Y, Ishihara A, Kim J-H, Mitsushima S, Ota K-i. Catalytic Activity of Zirconium Oxynitride Prepared by Reactive Sputtering for ORR in Sulfuric Acid. *Electrochemical and Solid-State Letters*. 2008;11:B109-B12.
- [38] Nam KD, Ishihara A, Matsuzawa K, Mitsushima S, Ota K-i. Partially Oxidized Niobium Carbonitride as Non-Platinum Cathode for PEFC. *Electrochemical and Solid-State Letters*. 2009;12:B158-B60.
- [39] Ota K-i, Ohgi Y, Nam K-D, Matsuzawa K, Mitsushima S, Ishihara A. Development of group 4 and 5 metal oxide-based cathodes for polymer electrolyte fuel cell. *J Power Sources*. 2011;196:5256-63.
- [40] Oh T, Kim JY, Shin Y, Engelhard M, Weil KS. Effects of tungsten oxide addition on the electrochemical performance of nanoscale tantalum oxide-based electrocatalysts for proton exchange membrane (PEM) fuel cells. *J Power Sources*. 2011;196:6099-103.
- [41] Ishihara A, Tamura M, Matsuzawa K, Mitsushima S, Ota K-i. Tantalum oxide-based compounds as new non-noble cathodes for polymer electrolyte fuel cell. *Electrochimica Acta*. 2010;55:7581-9.
- [42] Othman R, Dicks AL, Zhu Z. Non precious metal catalysts for the PEM fuel cell cathode. *International Journal of Hydrogen Energy*. 2012;37:357-72.
- [43] Ishihara A, Doi S, Mitsushima S, Ota K-i. Tantalum (oxy)nitrides prepared using reactive sputtering for new nonplatinum cathodes of polymer electrolyte fuel cell. *Electrochimica Acta*. 2008;53:5442-50.

- [44] Ishihara A, Lee K, Doi S, Mitsushima S, Kamiya N, Hara M, et al. Tantalum Oxynitride for a Novel Cathode of PEFC. *Electrochemical and Solid-State Letters*. 2005;8:A201-A3.
- [45] Takasu Y, Suzuki M, Yang H, Ohashi T, Sugimoto W. Oxygen reduction characteristics of several valve metal oxide electrodes in HClO<sub>4</sub> solution. *Electrochimica Acta*. 2010;55:8220-9.
- [46] Ishihara A, Shibata Y, Mitsushima S, Ota K. Partially Oxidized Tantalum Carbonitrides as a New Nonplatinum Cathode for PEFC--1. *Journal of The Electrochemical Society*. 2008;155:B400-B6.
- [47] Ishihara A, Ohgi Y, Matsuzawa K, Mitsushima S, Ota K-i. Progress in non-precious metal oxide-based cathode for polymer electrolyte fuel cells. *Electrochimica Acta*. 2010;55:8005-12.
- [48] Wang W, Savadogo O, Ma Z-F. The oxygen reduction reaction on Pt/TiO<sub>x</sub>N<sub>y</sub>-based electrocatalyst for PEM fuel cell applications. *Journal of Applied Electrochemistry*. 2012;42:857-66.
- [49] Ioroi T, Siroma Z, Fujiwara N, Yamazaki S-i, Yasuda K. Sub-stoichiometric titanium oxide-supported platinum electrocatalyst for polymer electrolyte fuel cells. *Electrochemistry Communications*. 2005;7:183-8.
- [50] Selvarani G, Maheswari S, Sridhar P, Pitchumani S, Shukla AK. A PEFC With Pt--TiO<sub>2</sub>/C as Oxygen-Reduction Catalyst. *Journal of Fuel Cell Science and Technology*. 2011;8:021003-8.
- [51] Shim J, Lee C-R, Lee H-K, Lee J-S, Cairns EJ. Electrochemical characteristics of Pt-WO<sub>3</sub>/C and Pt-TiO<sub>2</sub>/C electrocatalysts in a polymer electrolyte fuel cell. *J Power Sources*. 2001;102:172-7.
- [52] Elezovic NR, Babic BM, Radmilovic VR, Vracar LM, Krstajic NV. Synthesis and characterization of MoO<sub>x</sub>-Pt/C and TiO<sub>x</sub>-Pt/C nano-catalysts for oxygen reduction. *Electrochimica Acta*. 2009;54:2404-9.
- [53] Wang WL, Savadogo O, Ma ZF. Preparation of new titanium oxy nitride based electro catalysts using an anhydrous sol-gel method for water electrolysis in acid medium. *International Journal of Hydrogen Energy*. 2012;37:7405-17.
- [54] Liu Y, Ishihara A, Mitsushima S, Kamiya N, Ota K-i. Zirconium Oxide for PEFC Cathodes. *Electrochemical and Solid-State Letters*. 2005;8:A400-A2.

- [55] Doi S, Ishihara A, Mitsushima S, Kamiya N, Ota K-i. Zirconium-Based Compounds for Cathode of Polymer Electrolyte Fuel Cell. *Journal of The Electrochemical Society*. 2007;154:B362-B9.
- [56] Kim J-H, Ishihara A, Mitsushima S, Kamiya N, Ota K-I. Catalytic activity of titanium oxide for oxygen reduction reaction as a non-platinum catalyst for PEFC. *Electrochimica Acta*. 2007;52:2492-7.
- [57] Shibata Y, Ishihara A, Mitsushima S, Kamiya N, Ota K-i. Effect of Heat Treatment on Catalytic Activity for Oxygen Reduction Reaction of TaOxNy/Ti Prepared by Electrophoretic Deposition. *Electrochemical and Solid-State Letters*. 2007;10:B43-B6.
- [58] Xie Z, Holdcroft S. Polarization-dependent mass transport parameters for orr in perfluorosulfonic acid ionomer membranes: an EIS study using microelectrodes. *J Electroanal Chem*. 2004;568:247-60.
- [59] Itagaki M, Hasegawa H, Watanabe K, Hachiya T. Electroreduction mechanism of oxygen investigated by electrochemical impedance spectroscopy. *J Electroanal Chem*. 2003;557:59-73.
- [60] Dhirde AM, Dale NV, Salehfar H, Mann MD, Han TH. Equivalent Electric Circuit Modeling and Performance Analysis of a PEM Fuel Cell Stack Using Impedance Spectroscopy. *Energy Conversion, IEEE Transactions on*. 2010;25:778-86.

**CHAPTER 6      ARTICLE 3: OXYGEN REDUCTION REACTION (ORR)  
ON A MIXED TITANIUM AND TANTALUM OXY-NITRIDE  
CATALYST PREPARED BY THE UREA-BASED SOL-GEL METHOD**

A. Seifitokaldani <sup>a,b</sup>, M. Perrier <sup>a</sup>, O. Savadogo <sup>a,b</sup>

<sup>a</sup> Chemical Engineering Department, Polytechnique Montréal, Montréal, QC, Canada

<sup>b</sup> Laboratory of New Materials for Electrochemistry and Energy, Polytechnique Montréal,  
C.P.6079, Succursale Centre-Ville, Montréal, Québec H3C 3A7, Canada

Submitted to: Journal of New Materials for Electrochemical Systems

The electrochemical stability and activity of different compositions of titanium and tantalum oxy-nitride nano-catalysts were investigated for the oxygen reduction reaction (ORR). A new sol-gel method was used to produce a nano-powder mixture of Ti and Ta oxy-nitride from their alkoxides using urea as a nitrogen source. The precursors prepared by the sol-gel method were annealed in a N<sub>2</sub> + 3% H<sub>2</sub> atmosphere at determined temperatures (500, 700 and 900 °C) inside a silica tube furnace. X-ray diffraction results proved that by using this method a considerable amount of nitrogen was inserted into the catalyst structure at a relatively low temperature. Energy dispersive spectroscopy showed that the prepared catalyst should be oxidized carbonitride of titanium and/or tantalum. Heat treatment had a major effect on the onset potential by changing the crystallinity of the catalyst, so that the onset potential of titanium oxynitride increased from ca. 0.05 V to 0.65 V vs. NHE by increasing the temperature from 500 to 700 °C. Increasing the Ta concentration also led to a higher onset potential but lower ORR current. For instance, the onset potential for the ORR for tantalum oxynitride heat treated at 700 °C was ca. 0.85 V vs. NHE while this value was ca. 0.65 V vs. NHE for titanium oxynitride. However, the ORR current was 100 times smaller in tantalum oxynitride, most likely because of a low electrochemically active surface area. Electrochemical measurements suggested that an appropriate composition of titanium and tantalum was required to have both a good onset potential and ORR current by improving the catalytic activity and increasing the active surface area and electrical conductivity.

**Key words:** *titanium and tantalum oxy-nitride, urea-based sol-gel, oxygen reduction reaction (ORR)*

## 6.1 Introduction

Fuel cells are one of the most probable interesting alternative energy devices which exhibited high efficiency and environmentally friendly properties. Among them, due to their high energy density, Polymer Electrolyte Membrane Fuel Cells (PEMFC) are the most promising type for commercial fuel cell vehicles applications because they can operate at low temperatures ranging from room temperature to 80 °C [1].

The platinum nano-particle supported on carbon (Pt/C) is the state-of-the art commercial electro-catalyst used in PEMFCs due to its high specific surface area and high electrocatalytic performances for the Hydrogen Oxidation Reaction (HOR) and the Oxygen Reduction Reaction (ORR) [2, 3]. However, the electro-catalytic activity for the ORR is insufficient to obtain the appropriate power with low electrocatalyst loading even with platinum [4]. The limited abundance of Pt natural resources and its high cost are significant obstacles in the future commercialization of PEMFCs [4-9]. On the other hand, the dissolution and deposition of extremely dispersed Pt particles in the electrolyte and oxidation of the carbon support during long-term operation decreases the cell performance. This makes impossible the drastic reduction of Pt usage [8, 10]. Thus, the commercial viability of PEMFCs requires the development of better electro-catalysts to improve the fuel-cell performance.

Some researchers [11-15] have revealed that Pt-based alloys with transition metals exhibited much higher ORR activity than pure Pt as they believed that the presence of the metal species changes the electronic structure of Pt, leading to a weaker interaction between the Pt surface and the unwanted Pt-OH intermediate. In this regard, Pt-M (M= Pd, Co, Ni, Cr, Mn, and Fe) alloys have become attractive to ameliorate the catalytic activity and reduce the cost [16-20]. However, poor long-term stability due to the dissolution of these transition metals in acidic conditions hinders the practical application [21]. Additionally, the leaching out of metal ions would contaminate the membrane and limit the fuel cell performances. Therefore, the development of non-noble electro-catalysts with high activity and durability in acidic conditions becomes one of the most important topics in PEM fuel cell research.

Transition metal nitrides, which are well known as valve metals, are used as anticorrosion and coating materials, and groups 4 and 5 metal oxides, like Ti, V, Nb and Ta oxides, have high chemical stability in acids [21-25]. Therefore, group 4 and 5 metal nitrides, oxides and oxy-

nitrides are expected to be stable under an acidic and oxidative atmosphere. In addition, it has been reported that these compounds have some electro-catalytic activity for the ORR [24-28].

Transition metal carbonitrides have been studied [22-25]. They started with transition metal carbides because of their electrical conductivities. Although, for example, tungsten carbide has electronic properties, like platinum, it has a very low corrosion resistance under acidic and oxidative conditions. They found that in addition to the enhancement of electrocatalytic activity, the chemical stability of the tungsten carbide was significantly increased by the addition of Ta to the pure WC catalyst [29]. This enhancement was most probably because of the passive oxide film formation on the catalyst surface. Therefore, other studies were carried out on the transition and non-transition metal oxides like, like zirconium oxide [30, 31], titanium oxide [32], cobalt oxide, tin oxide and niobium oxide [33]. In particular, because titanium oxide is an abundant natural resource and supports some electrochemical reactions, it is worth being studied. It has been found that the electrocatalytic activity of titanium oxide for the ORR might be affected by a surface state change, such as the crystalline structure and work function [32]. It was shown that the onset potential for the ORR was increased up to 0.65 V for the electrocatalysts heat-treated at 900 °C. The heat-treated electrocatalysts were chemically and electrochemically stable in acid solution, so that the average Ti concentration of the electrocatalysts after 24 days at 50 °C in 0.1 mol.dm<sup>-3</sup> sulphuric acid under atmospheric conditions was about  $3.5 \times 10^{-7}$  mol.dm<sup>-3</sup> [32]. This amount was smaller than the solubility of the platinum black powder under the same electrolyte at a lower temperature (20 °C) after 25 h ( $5.6 \times 10^{-7}$  mol.dm<sup>-3</sup>) [34].

In spite of the high stability in acidic conditions of the metal oxides of groups 4 and 5 transition metals, these oxides were almost insulators and it is clear that the electrocatalysts must have some electrical conductivity. For instance, the ORR hardly proceeds on the tantalum oxide due to the big gap between the upper energy level of the valence band and the Fermi level of tantalum oxide [35]. The most effective means to narrow this wide band-gap of the oxides was to insert N and/or C. In addition, transition metal nitrides and/or carbides have high electrical conductivity (e.g. TaC  $4 \times 10^4$  S.cm<sup>-1</sup>; TaN  $4-7 \times 10^3$  S.cm<sup>-1</sup> [10]). In this regard, Azuma and co-workers studied the electrochemical properties of ZrN, NbN, CoN, TiN and VN prepared by reactive RF sputtering. Ishihara and co-workers also studied chromium carbonitride and tantalum carbonitride prepared by the reactive sputtering [36, 37]. However, as a consequence of a large decrease in the Gibbs energy, transition metal oxides are thermodynamically more stable than their carbonitride

and nitride and thus, these nitrides and carbonitrides are essentially unstable under the ORR conditions [38, 39]. Also, it was seen that the pure nitride of transition metals, such as  $Ta_3N_5$ , show poor catalytic activity for the ORR and the onset potential was below 0.4V vs. RHE. On the other hand, tantalum oxynitrides or partially oxidized tantalum carbonitrides had both chemical and electrochemical stability and definite catalytic activity for the ORR [4, 24, 26, 40-42]. Ishihara and co-workers believe that an oxygen molecule hardly adsorbs on the surface of perfect oxides, such as  $Ta_2O_5$  and/or  $TiO_2$ , and that it is essential to form some defects as the oxygen adsorption sites on a surface while the metal is basically kept at the highest oxidation state [22, 33]. These surface defects, which lead to lower ionization potential, work function and, consequently, a higher density of the state of electrons, are mostly made by changing the crystallinity with a heat treatment process [24, 26]. Zirconium oxy-nitride [25, 27, 43] and partially oxidized niobium carbonitride [28] also were studied as a non-platinum cathode catalyst for the ORR. So far, the obtained current and onset potential for the ORR were much smaller than those for the platinum based electrocatalyst. It is then necessary to continue the investigation of transition metal oxides and/or oxynitrides to improve the electrocatalytic properties.

In previous studies, transition metal nitride and/or carbonitride were normally used as the starting materials to produce partially oxidized metal carbonitride. These nitrides and/or carbonitrides were prepared mostly at high temperatures up to 1600 °C over 8 hours. In this study, a new urea-based sol-gel method is used to prepare a mixture of titanium and tantalum oxynitride at a much lower temperature and duration. The maximum heat treatment temperature in this work is 900 °C. As a result of this sol-gel method there are both metal carbide and nitride besides metal oxide in the catalyst structure. The stability and electrochemical activity of these electrocatalysts were also evaluated in order to use them as a non-platinum electrocatalyst for the ORR. In previous studies, other researchers took electrochemical measurements of the prepared electro catalysts supported by carbon black. It was noted that the mixture of the carbon black as a current collector was required to obtain sufficient electrical conductivity. Using carbon black increased the ORR current as much as 60 times, however, there was no enhancement in onset potential for the ORR which, of course is not affected by the carbon surface area. In fact, carbon black increased the surface area, which acted on the active sites of the electrocatalysts and had sufficient electrical conductivity. In this study the prepared electrocatalysts are characterized without carbon black and, therefore, the ORR current might be much lower compared with those of the other oxides

electrocatalyst in the literature which are supported on carbon black. The aim of our work is to evaluate the ORR intrinsic electrocatalytic parameters of the oxy-nitrides electrocatalysts without any carbon support. The electrocatalysts will be also characterized by X-ray diffraction (XRD), scanning electron microscopy (SEM), and energy dispersive X-ray spectroscopy (EDS).

## 6.2 Experimental Procedure

### 6.2.1 Materials

Titanium (IV) isopropoxide [ $\text{Ti}(\text{O}^i\text{C}_3\text{H}_7)_4$ ] (97%) and tantalum (V) ethoxide [ $\text{Ta}(\text{OC}_2\text{H}_5)_5$ ] (99.8%) were purchased from Sigma-Aldrich and used without further purification. Urea (reagent ACS 99%) was obtained from Fischer Scientific and anhydrous ethanol was used as the mutual solvent.

### 6.2.2 Sol-Gel Procedure

The flowchart in Fig. 1 describes the experimental procedure to prepare a mixture of titanium and tantalum oxy-nitride precursor. First, an appropriate amount of urea was dissolved in 42 mL of absolute ethanol under a nitrogen atmosphere at room temperature. After 30 minutes, the determined amount of titanium (IV) isopropoxide and tantalum (V) ethoxide (as the starting materials) was added drop by drop to the solution with continuous stirring to achieve a molar ratio of metal source to urea and solvent of 1:2:45. This reaction was very slow, and it was allowed to continue through the night at 80°C under reflux conditions in order to ensure completion of the reaction. Then, the resulting homogeneous light yellow solution was dried at 140-150 °C while the color of the remnant slowly changed into yellowish red. The yellowish red precipitates were cooled to room temperature and ground into fine powder. All steps of this procedure were carried out under nitrogen to decrease the probability of oxygen and moisture existence as low as possible.

### 6.2.3 Heat Treatment

The obtained precursors were subjected to a specified nitridizing gas ( $\text{N}_2 + 3\% \text{H}_2$ ) with ca. 180 mL/min flow rate at 500, 700 and 900 °C. This process was done inside a silica tube furnace (Model: 55031-A, 800 Watts, 115 Volts, by LINDBERG/HEVI-DUTY). The precursors were

converted to titanium and tantalum oxy-nitride at high temperature, and crystallinity, particle size and specific surface area changed to modify the property of the catalyst. A heating schedule shown in Fig. 2 (a) was adopted in this study. After 45 minutes of gas purging, approximately 2 g of the precursor, which had been placed in a crucible, were heated up to the desired temperature at a heating rate of 5 °C/min. The isothermal heat treatment time was 2 hours. The sample was then furnace cooled at a cooling rate identical to the heating rate. Figure 2 (b) shows the precursor before and after heat treatment at 700 °C.

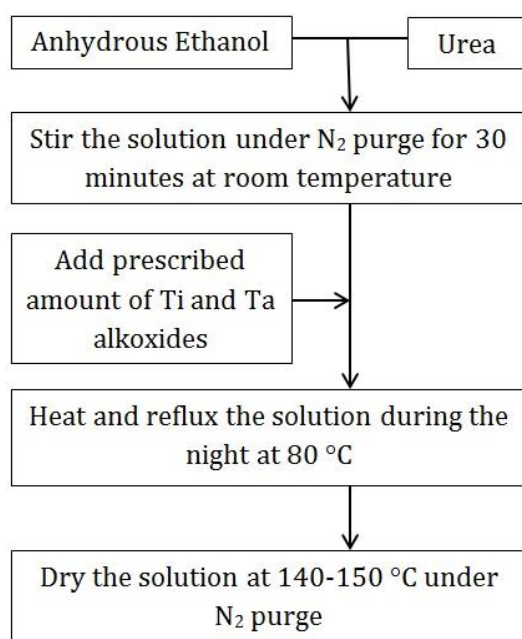


Fig. 1. Schematic flowchart of the preparation of Ti-Ta-ON precursor using urea-based sol-gel method.

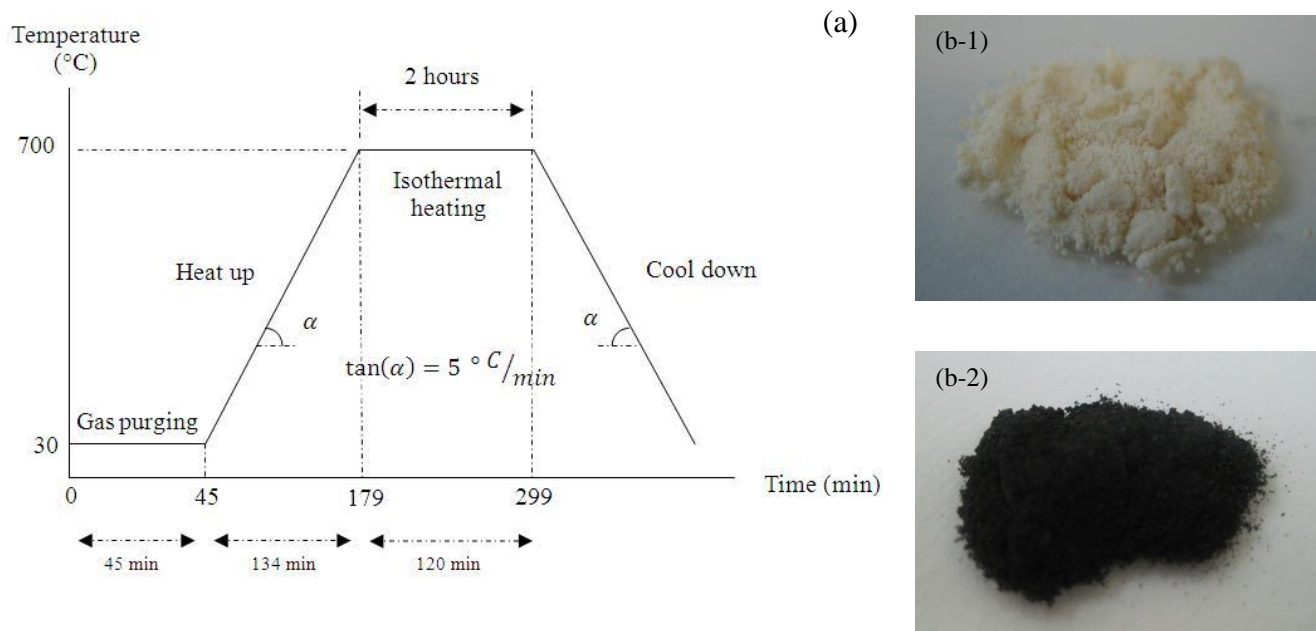


Figure 2. (a) Heating step of the calcination process, (b-1) light yellow powder before calcination, (b-2) fine shiny black powder after 700 °C heat treatment for 2 hours

## 6.2.4 Physicochemical Characterizations

In order to characterize the crystalline structure and phase identification, powder X-ray diffraction (XRD) data were collected using a Philips X'Pert diffractometer equipped with Cu K $\alpha$  radiation ( $\lambda = 1.5406 \text{ \AA}$ ) (at 50 kV and 40 mA) in a scan range ( $2\theta$ ) from  $10^\circ$  to  $85^\circ$  at a speed of  $2^\circ \text{ min}^{-1}$ . The surface morphologies were examined through a scanning electron microscope (SEM, JEOL JSM-840) equipped with an Energy Dispersive X-Ray Spectroscopy (EDS) to analyse the Ti, Ta, O, N and C contents of different samples.

## 6.2.5 Electrochemical Measurements

All electrochemical experiments were conducted through a conventional 3-electrode cell containing 0.5 M sulphuric acid ( $0.5 \text{ mol.dm}^{-3} \text{ H}_2\text{SO}_4$ ) saturated with  $\text{N}_2$  or  $\text{O}_2$  at atmospheric pressure and room temperature. The silver-silver chloride electrode (Ag/AgCl sat. KCl) and the platinum (Pt) mesh were used as the reference and counter electrodes, respectively. To prepare the working electrode, 10 mg of the catalyst without any addition of carbon black was added to a mixture of 480  $\mu\text{L}$  absolute ethanol and 20  $\mu\text{L}$  Nafion 5 % wt by 10 minutes ultrasonic treatment.

Then, ca. 20  $\mu\text{L}$  of this ink was placed slowly and layer by layer on a glassy carbon rod (CHI Instruments Inc. CHI 104, diameter = 3 mm). Before adding the next layer, the previous one should be completely dried to obtain a uniform and fully covered surface. This step is very important to avoid the oxidation and reduction peaks related to the glassy carbon rod during the measurements. The catalyst loading was ca. 10 mg per geometric  $\text{cm}^2$ . All electrode potentials referred to the Normal Hydrogen Electrode (NHE) scale.

Cyclic voltammetry (CV) in the range of 0.0 to 1.2 V (versus NHE) was performed to evaluate the electrochemical stability of the prepared catalysts. The scan rate was adjusted to  $100 \text{ mV}\cdot\text{s}^{-1}$  and  $\text{N}_2$  gas was bubbled into the 0.5 M  $\text{H}_2\text{SO}_4$  solution at 30 °C. After the cyclic voltammetry had reached a steady state, slow scan voltammetry (SSV) was performed at  $5 \text{ mV}\cdot\text{s}^{-1}$  scan rate in both  $\text{N}_2$  and  $\text{O}_2$  atmosphere to evaluate catalytic activity for the ORR. Because the particle sizes of the specimens are different, the real surface area is hardly estimated. Therefore, the current reflects the ORR activity for a determined amount of the powder. So, in this study the current density is expressed based on the geometric surface area (standardized current) of the working electrode.

## 6.3 Results and Discussions

### 6.3.1 Physicochemical Characterizations

Figure 3 shows the XRD patterns of the  $\text{TiO}_x\text{N}_y$  catalysts obtained from the urea-based sol-gel method after calcination at 700 °C and 900 °C for 2 hours. Pure anatase  $\text{TiO}_2$  and TiN purchased from Fisher Scientific and Sigma-Aldrich, respectively, were used as references. The five diffraction peaks at  $2\theta$  of  $36.56^\circ$ ,  $42.54^\circ$ ,  $61.71^\circ$ ,  $73.99^\circ$  and  $77.89^\circ$  can be indexed as the cubic Fm3m unit cell of TiN [(111), (200), (220), (311) and (222)] with  $a=4.2417 \text{ \AA}$  and  $\alpha=90^\circ$  cell parameters. These peaks are identified with a small blue triangle on top of them. As well, strong diffraction peaks at  $25.25^\circ$ ,  $37.75^\circ$ ,  $47.95^\circ$ ,  $53.79^\circ$  and  $55.05^\circ$  are respectively assigned to (101), (004), (200), (105) and (211) facets of the anatase structure of titanium dioxide micro powder. All peaks are in good agreement with the standard spectrum (JCPDS No. 38-1420 for TiN and No. 21-1272 for  $\text{TiO}_2$ ).

From these patterns it is obvious that the (101) anatase  $\text{TiO}_2$  peak at  $25.25^\circ$  in both samples vanished and changed to a (110) rutile structure at  $27.8^\circ$ . Also, by increasing the temperature from 700 to 900 °C the intensity of this peak was reduced. As well, the intensity of (200), (105) and (211)  $\text{TiO}_2$  anatase peaks is reduced by increasing the temperature. Meanwhile, the growth of the (111), (200), (220), (311) and (222) peaks related to the TiN is obvious in the sample heat treated at 900 °C. These results prove the nitrogen is embedded into the lattice using this method. From the XRD patterns we conclude that the nitrogen content ratio relative to the oxygen content in the prepared samples is considerable. In addition, diffraction intensity increases with increasing particle size. These results suggested that the nano-sized powders were obtained by the sol-gel method and heat treatment, because of their relatively low intensity compared to the  $\text{TiO}_2$  and TiN micro powders. However, increasing the temperature made the peaks much sharper, which indicates the growth of the crystallite structures.

Figure 4 shows the Scanning Electron Microscopy images (SEM) and the Energy Dispersive Spectra (EDS) of the  $\text{TiO}_x\text{N}_y$  electrocatalyst heat treated at 900 °C. Figures a-1 and a-2 show respectively the SEM images and the EDS of the electrocatalyst prepared by the urea-based sol-gel method. Figures b-1 and b-2 are the respective SEM images and EDS for the sample prepared by the regular oxide-based sol-gel method without the addition of urea. Comparing the EDS results shows that the electrocatalyst prepared using the urea-based method contains more nitrogen and carbon than the regular oxide based sol-gel method. The particle size of the sample prepared from the oxide-based method (spheres in figure 4) is much smaller than those of the sample prepared using urea. These results show that inserting nitrogen (which comes from urea) inside the catalyst structures leads to sintering and bigger particles size. It seems that using the oxide-based sol-gel method of preparation leads to a sample which like an oxide based electrocatalyst without defects in the electrocatalyst. Conversely using the urea-based sol-gel method of preparation leads a nitrogen-doped sample which contains more defects in the structure. These defects might contribute in the improvement of the ORR by easing the oxygen adsorption.

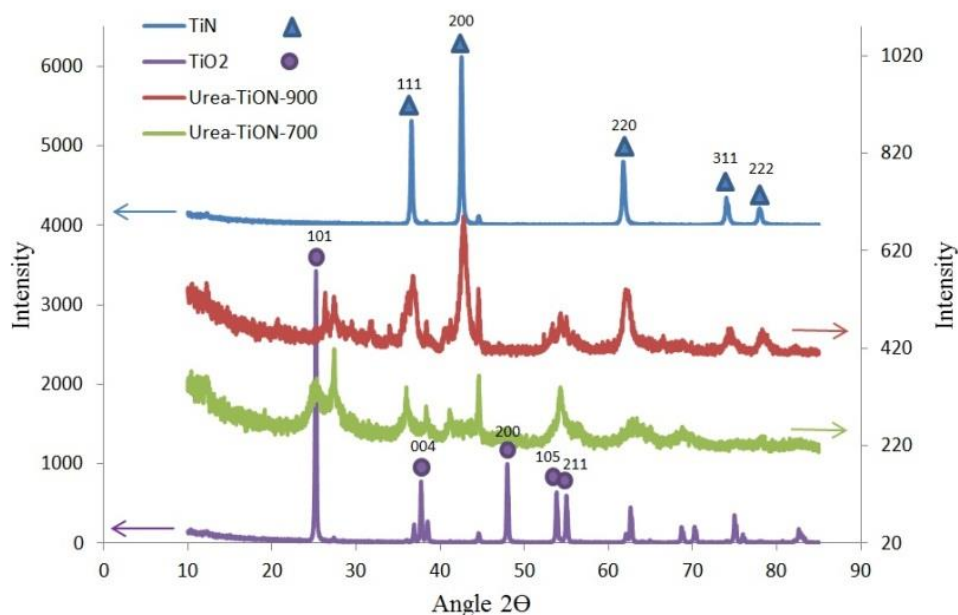


Figure 3. XRD patterns of titanium oxy-nitride powder annealed at 700 °C (Urea-TiON-700) and 900 °C (Urea-TiON-900) for 2 hours; TiN and TiO<sub>2</sub> reference materials were purchased from Sigma-Aldrich and Fisher Scientific, respectively.

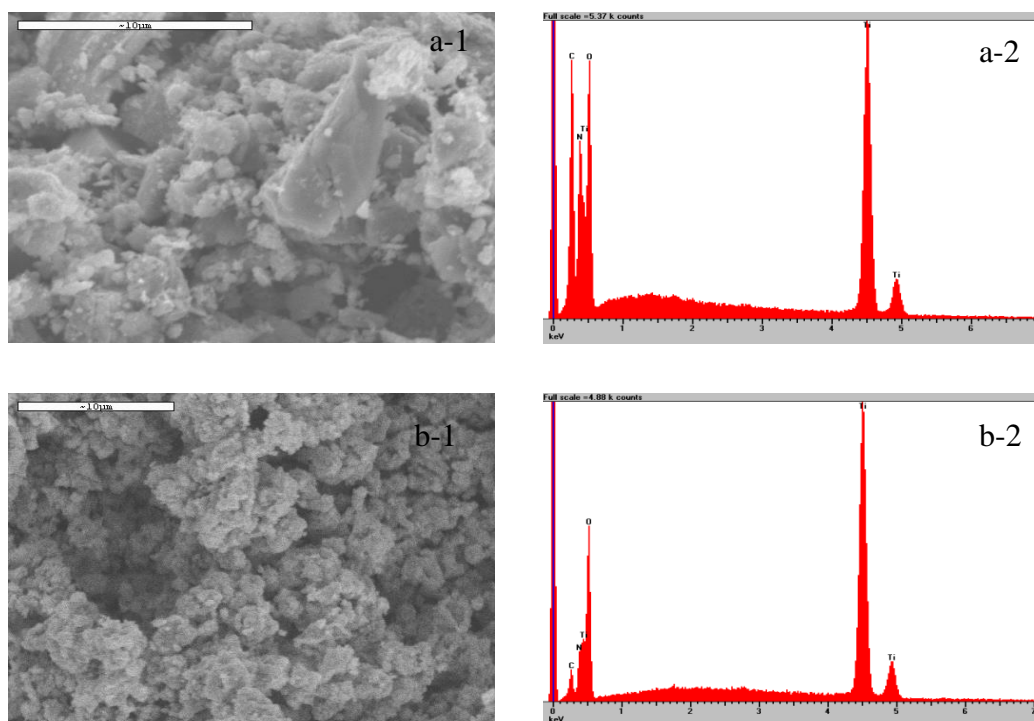


Figure 4. (a) SEM images and EDS of the TiO<sub>x</sub>N<sub>y</sub> prepared from urea-based sol-gel method and (b) TiO<sub>x</sub>N<sub>y</sub> prepared from regular oxide-based sol-gel method without the addition of urea

### 6.3.2 Electrochemical Stability

Figure 5 shows the cyclic voltammogram (CV) in a nitrogen atmosphere of the samples containing 25 % Ta and 75 % Ti, which were heat treated at 500 and 900°C. The shape of the CV for the sample heat treated at 500°C is significantly different from those of the sample annealed at 900°C. But in both cases after several potential cycles (100 cycles at the rate of 100 mV/s scan rate) the first scan and the last one were almost the same. The CVs of the specimens with different Ta amounts and heat-treated at 500, 700 and 900 °C also reached a similar steady state. These results revealed that the heat treated mixture of Ti and Ta oxy-nitrides had high electrochemical stability in an acidic solution. Furthermore, there was no specific anodic peak because of catalyst oxidation and dissolution. The current density at any potential of the sample annealed at 500°C is smaller than those of the sample heated at 900°C. This might be related to the increase of the electrochemical active surface area with the sample heating temperature. The calculated cathodic and anodic electric charge densities at steady state were almost the same, which confirms the surface stability of the specimens. These electric charges in the CV were calculated using the following equation:

$$Q = \int i \cdot dt = \int i \frac{dE}{v} = \frac{1}{v} \int i \cdot dE$$

Where  $Q$ ,  $I$ ,  $t$ ,  $v$  and  $E$  are respectively charge (C), current density (Amp/cm<sup>2</sup>), time (second), scan rate (mV/second), and electrode potential (Volt).

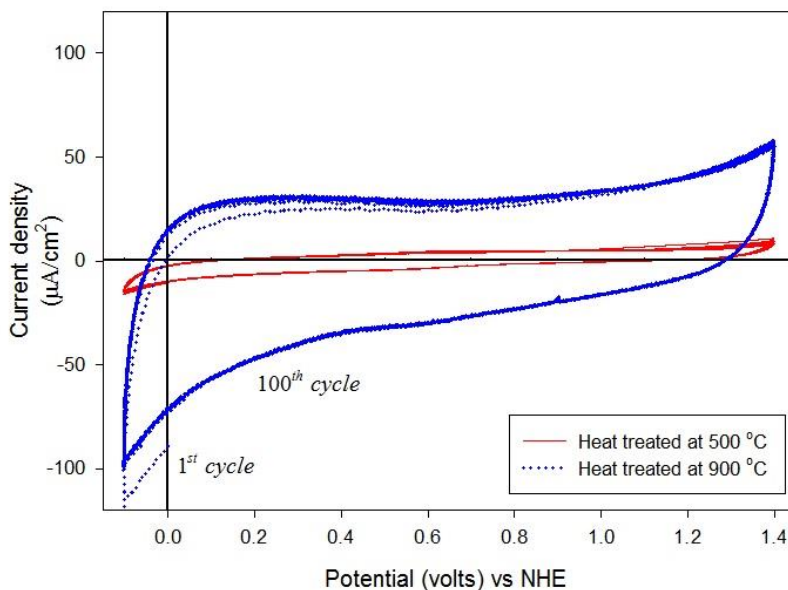


Figure 5. Cyclic voltammetry (under nitrogen and with 100 mV/s scan rate) of the samples containing 25 % Ta and 75 % Ti heat treated at 500 °C (red line) and 900 °C (blue dot).

Comparing the CVs of the samples heat treated at 500 and 900 °C, in figure 5, shows that the amount of the electric charge density increases with the isothermal heat treatment temperature. This behaviour might be owing to the increased active surface area as a result of the rising temperature. The calculated amount of these charges for different samples is depicted in Figure 6. There is a linear relationship between the anodic and cathodic electric charge density values that agree well with each other. This is mostly due to the same charge and discharge of the electric double layer, indicating that no one-direction oxidation or reduction reaction of the catalyst occurred. As shown in this figure, in all the cases, the charge increased with the heat-treatment temperature up to 700 °C, and then decreased. This amount decreased when the Ta content in the sample increased. Assuming that the real surface area is proportional to the charge of the electric double layer, the specimens heat-treated at 700 °C had the highest real surface area. This charge value for tantalum oxy-nitride is in good agreement with the literature [4, 10, 24, 41]. However, the comparison between the surface area of the pure titanium oxide and our prepared titanium oxy-nitride shows there is much more surface area in titanium oxy-nitride. This is supported by the work of Kim et al. [32] who reported that titanium oxide exhibited less than  $100 \mu\text{C}\cdot\text{cm}^{-2}$  charges; while this amount is around  $2000 \mu\text{C}\cdot\text{cm}^{-2}$  for titanium oxy-nitride heat treated at 700 °C.

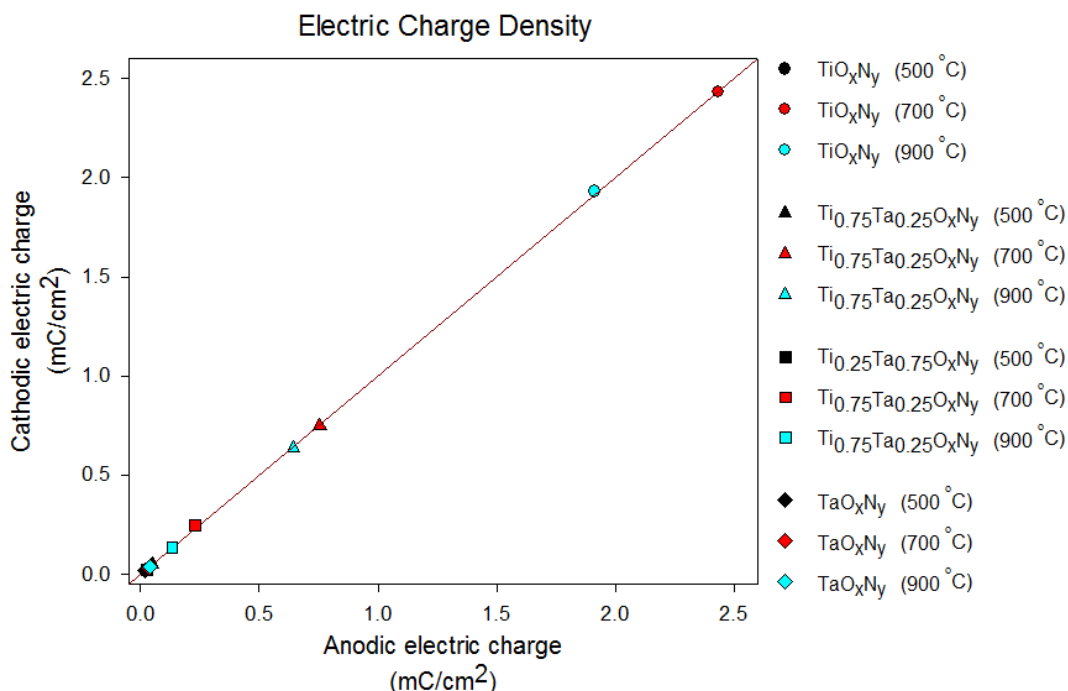


Figure 6. Comparison of the anodic and cathodic charges calculated from the cyclic voltammogram

### 6.3.3 Catalytic Activity for the ORR

After the CVs reached steady state, slow scan voltammetry (SSV) (scan rate:  $5 \text{ mV}\cdot\text{s}^{-1}$ , 1.2 V to 0 V vs. NHE) was performed in a nitrogen and oxygen atmosphere. However, the potential–current curves in the slow scan voltammetry immediately reached steady state, the curve at the 3<sup>rd</sup> cycle with the cathodic scan was used to avoid the effect of the initial state. The cathodic current obtained under O<sub>2</sub> atmosphere increased when the potential was decreasing, however such an increase in the obtained cathodic current under N<sub>2</sub> was not observed. The obtained current under N<sub>2</sub> atmosphere is the charge current of the double layer capacitance. The difference between the current under O<sub>2</sub> atmosphere ( $i_{O_2}$ ) and that under N<sub>2</sub> atmosphere ( $i_{N_2}$ ) corresponded to the oxygen reduction current ( $i_{ORR}$ ), that is,  $i_{ORR} = i_{O_2} - i_{N_2}$ . This current density is evaluated on the basis of the geometric surface area of the working electrode. The onset potential for the ORR,  $E_{ORR}$ , was defined as the electrode potential at the  $i_{ORR} = -0.2 \text{ }\mu\text{A}\cdot\text{cm}^{-2}$  and it is utilized to evaluate the electrocatalytic activity for the ORR.

Figure 7 demonstrates the SSV of all specimens heat treated at 500, 700 and 900 °C for 2 hours under  $N_2 + 3\% H_2$  atmosphere. According to these curves, it is revealed that by increasing the heat treatment temperature from 500 to 700 or 900 °C, the  $i_{ORR}$  and  $E_{ORR}$  increased significantly, however the specimen heat treated at 700 °C had the highest electric charge density. These results indicate that the electrocatalytic activity for the ORR significantly depends on the heat-treatment temperature, so that the onset potential of titanium oxy-nitride increased from ca. 0.05 V to 0.65 V vs. NHE by increasing the temperature from 500 to 700 °C. This is an indication that the electrocatalytic activity of the ORR increases when the temperature of the heat treatment increases. In addition, by increasing the Ta content in the mixture, the defined onset potential increased; the electric charge, however, drastically decreased. It might be related to the poor electrical conductivity of the electrocatalysts. Therefore, the increase of the onset potential with the content of the embedding Ta in the electrocatalyst improved its electrocatalytic activity for the ORR. On the other hand, because of the big particle size and small surface area of the electrocatalysts containing Ta, the obtained current density was small compared to that of the titanium oxy-nitride. For instance, onset potential for the ORR for pure tantalum oxy-nitride heat treated at 700 °C was ca. 0.85 V vs. NHE while this value was ca. 0.65 V vs. NHE for pure titanium oxy-nitride. However, the ORR current was 100 times smaller for tantalum oxy-nitride based electrocatalyst, when compared to those of titanium oxy-nitride based electrocatalyst. In this study, we did not mix the prepared electrocatalysts with carbon black to increase the active surface area for the ORR and, hence, the obtained current was small in comparison with the literature. So, it is assumed that finding the optimum amount of Ta to insert inside the Ti-based electrocatalyst is critical to have both good activity and a highly active surface area. This optimization is still under development.

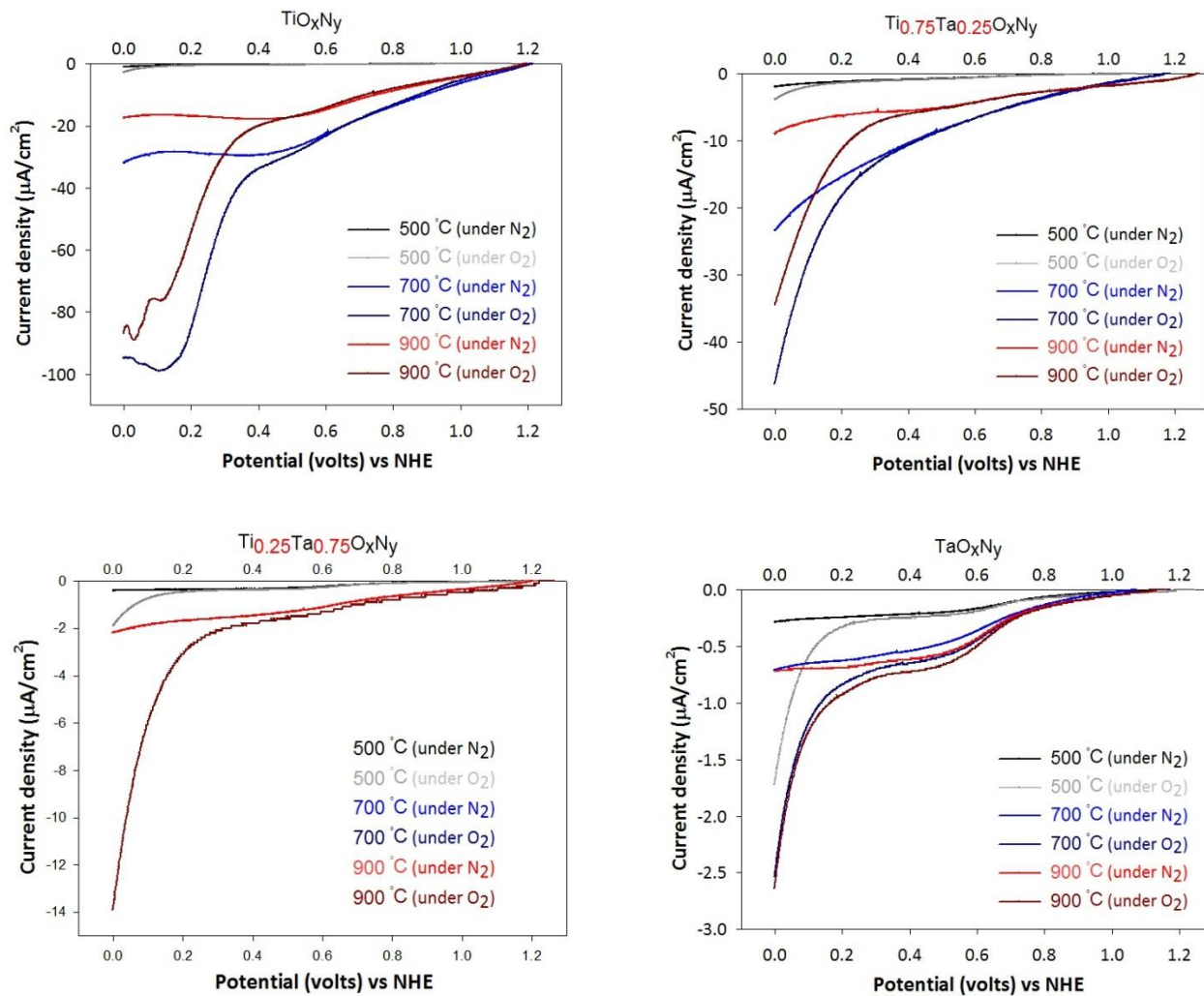


Figure 7. Comparison of the SSV (scan rate: 5 mV/s) results of different specimens with various Ta percentages heat-treated at 500, 700 and 900 °C

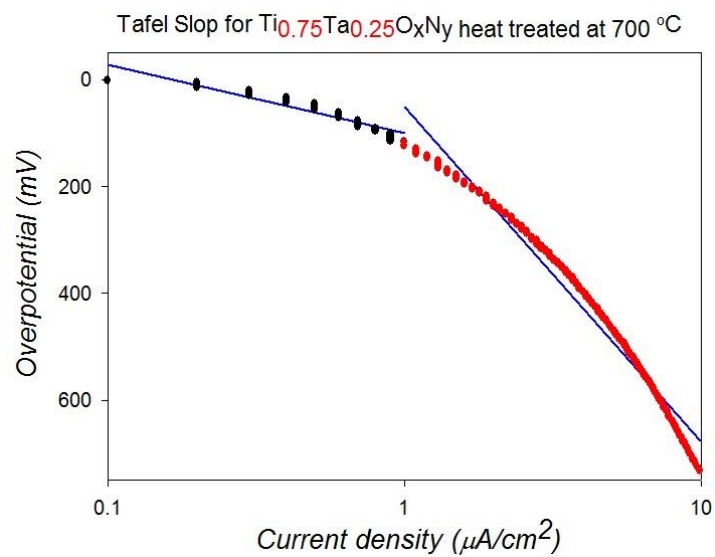
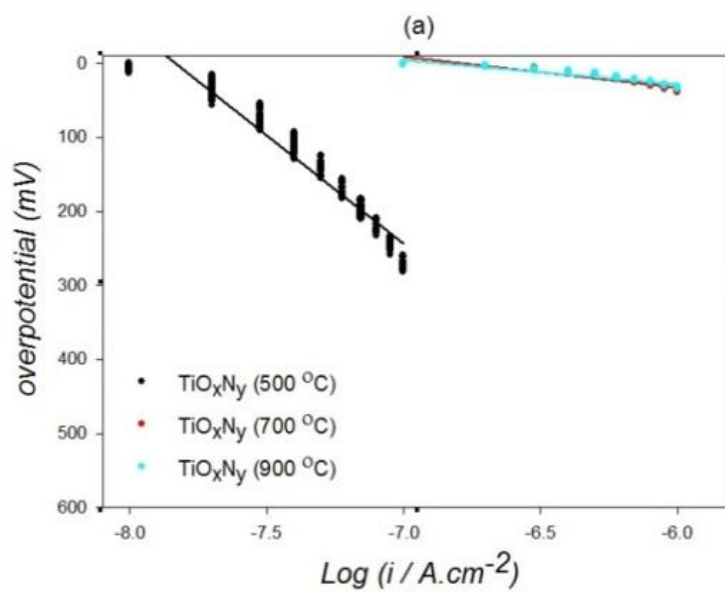
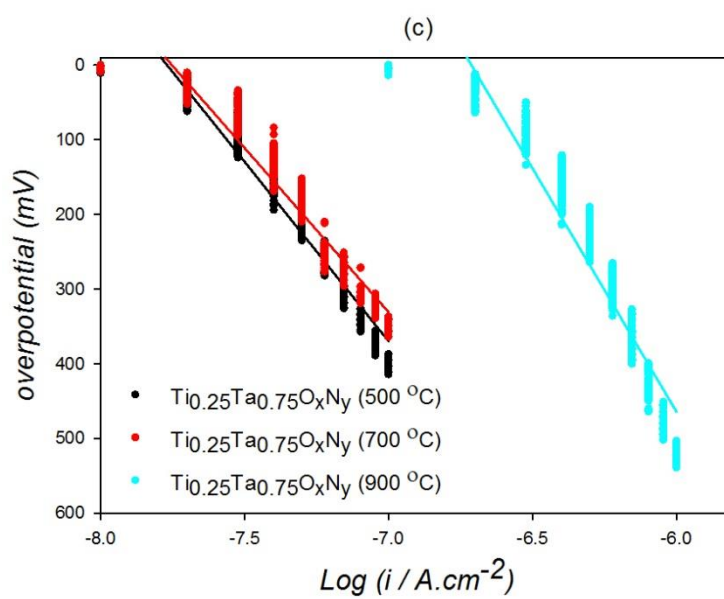
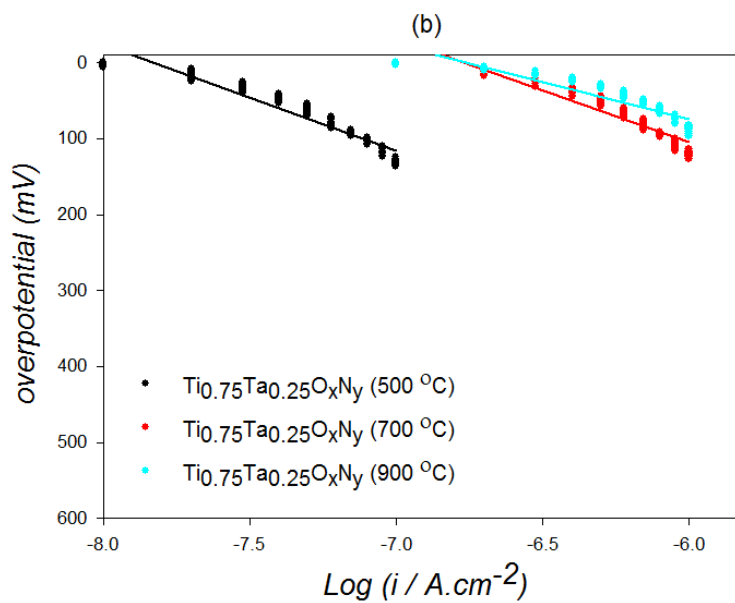


Figure 8. The Tafel plot of the ORR for the sample containing 25 % Ta and heat treated at  $700\text{ }^\circ\text{C}$  for 2 hours





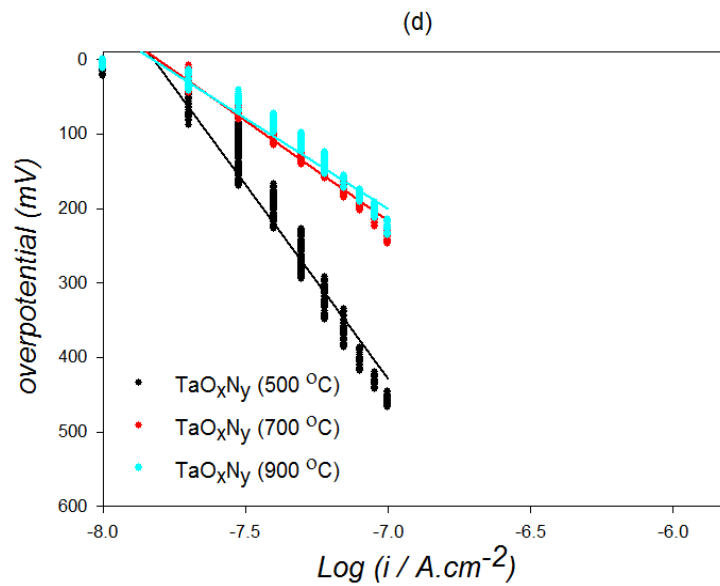
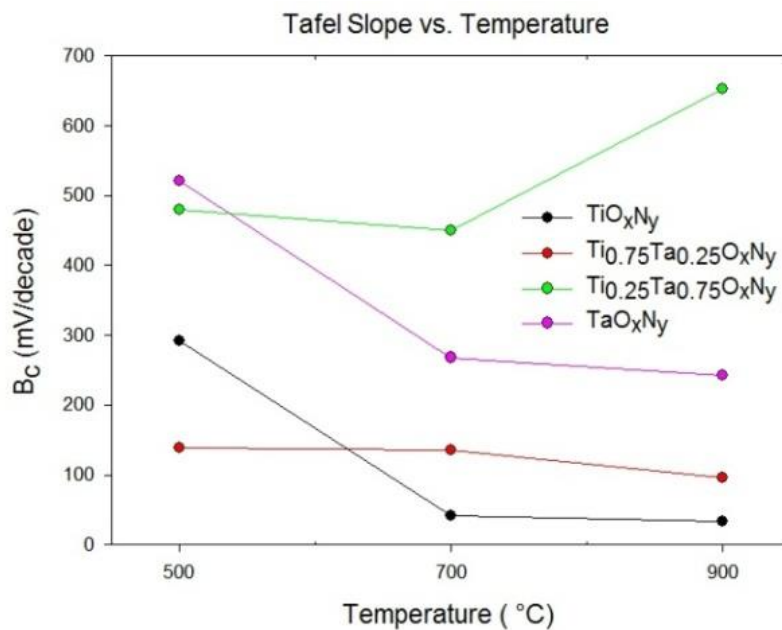
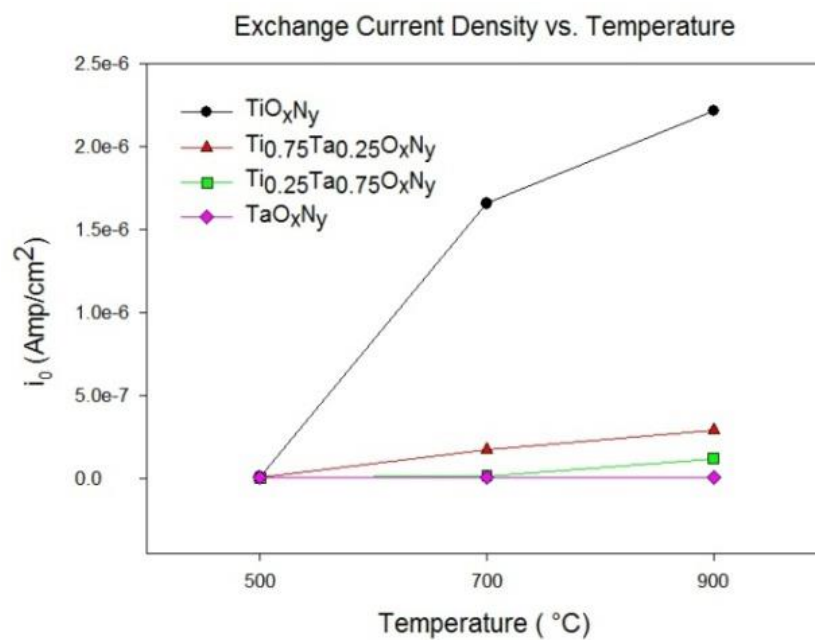


Figure 9. Tafel plots of different samples heat treated at 500, 700 and 900 °C under N<sub>2</sub> for 2 hours: (a) TiO<sub>x</sub>N<sub>y</sub> electrocatalysts; (b) Ti<sub>0.75</sub>Ta<sub>0.25</sub>O<sub>x</sub>N<sub>y</sub> electrocatalysts; (c) Ti<sub>0.25</sub>Ta<sub>0.75</sub>O<sub>x</sub>N<sub>y</sub> electrocatalysts; (d) TaO<sub>x</sub>N<sub>y</sub> electrocatalysts

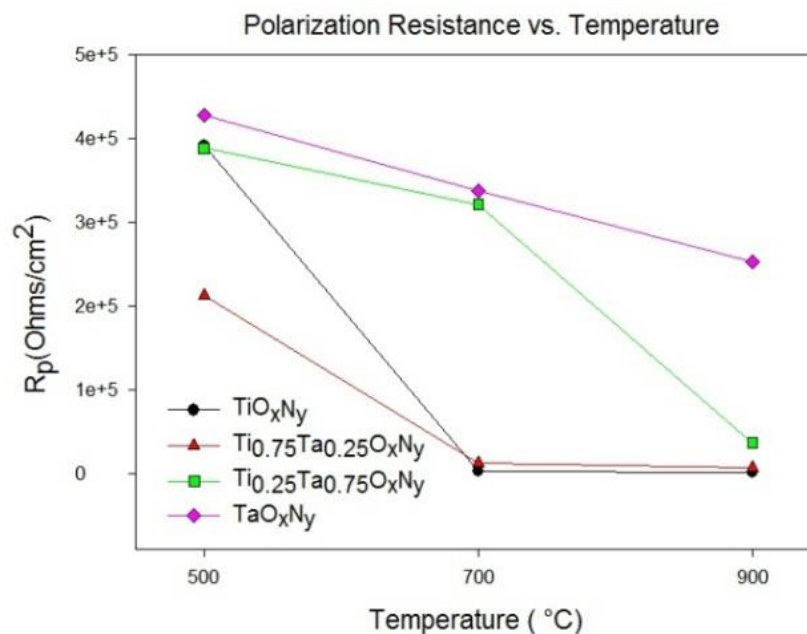
The Tafel plot of the ORR for the sample containing 25 % Ta and heat treated at 700 °C for 2 hours is shown in figure 8. In the low current density regions the Tafel slope of about 128 mV/decade  $\pm$  10 mV/decade was observed, indicating the high reaction rate in comparison with the high Tafel slope obtained for the other annealing temperature. However, in the most high current density regions, this amount increased significantly. As it is accepted classically, the change of the Tafel slope appears to be related to the change in the nature of the adsorbed oxygen-containing species with potential, a transition that strongly affects the ORR. The Tafel plots of all other electrocatalysts are represented in various curves of figure 9. The changes in the Tafel slope can be observed from these curves and the calculated exchange current density and polarization resistance are presented in the various curves of figures 10.



(a)



(b)



(c)

Figure 10. Effect of the annealing temperature on the basic electrocatalytic parameters: (a) Variation of the Tafel slope vs annealing temperature; (b) Variation of the exchange current density vs annealing temperature; and (c) variation of the polarization resistance vs temperature for different samples.

Fig.10.a shows that when the sample is annealed at 500°C, the lowest Tafel Slope (about 120 mV/decade) is obtained for Ti<sub>0.75</sub>Ta<sub>0.25</sub>O<sub>x</sub>N<sub>y</sub> electrocatalyst and it does not change when the annealing temperature increases. The highest Tafel slope is obtained with TaO<sub>x</sub>N<sub>y</sub> electrocatalyst and it decreases when the annealing temperature increases. But at 900°C its Tafel slope is still higher (~250 mV/decade) than those of Ti<sub>0.75</sub>Ta<sub>0.25</sub>O<sub>x</sub>N<sub>y</sub> (~120 mV/decade). The TiO<sub>x</sub>N<sub>y</sub> electrocatalyst exhibited a Tafel slope of about 300 mV/decade when annealed at 500°C but decreases to less than 60 mV/decade when annealed at 900°C. On the other hand its exchange current density (Fig.10.b) increases from 2×10<sup>-9</sup> A/cm<sup>2</sup> to 2×10<sup>-6</sup> A/cm<sup>2</sup> when its annealing temperature increases from 500°C to 900°C. The other electrocatalysts exhibit exchange current densities for sample annealed at 500°C which are lower than the TiO<sub>x</sub>N<sub>y</sub> electrocatalyst annealed at the same temperature. The exchange current densities of these other samples (Fig.10.b) do not increase significantly (less than 2×10<sup>-7</sup> A/cm<sup>2</sup>) with the annealing temperature, up to 900°C. Fig.10.c shows a decrease of the polarization resistance with the annealing temperature and the

lowest resistance polarization is respectively obtained for  $\text{Ti}_{0.75}\text{Ta}_{0.25}\text{O}_x\text{N}_y$  and  $\text{TiO}_x\text{N}_y$  based electrocatalysts annealed at  $900^\circ\text{C}$ . Based on these various basic parameters, the performance for the ORR of these electrodes increases in the following orders:  $\text{TaO}_x\text{N}_y < \text{Ti}_{0.25}\text{Ta}_{0.75}\text{O}_x\text{N}_y < \text{Ti}_{0.75}\text{Ta}_{0.25}\text{O}_x\text{N}_y < \text{TiO}_x\text{N}_y$ . Also, inserting a small amount of Ta could improve the onset potential for the ORR besides having an acceptable Tafel slope and exchange current density. The best electrocatalyst for the ORR is obtained with  $\text{TiO}_x\text{N}_y$  based electrocatalyst.

## 6.4 Conclusion

Using a new urea-based sol-gel method in this study led to the preparation of a mixture of titanium and tantalum oxy-nitride nano-powder as a non-Pt cathode catalyst for the ORR at a relatively low temperature. XRD and EDS results revealed that a considerable amount of nitrogen and carbon was inserted into the metal oxide structure to enhance the catalytic activity most likely by improving the electrical properties and also introducing the defects in the surface. Compared to the other method explained in the literature, this investigation shows that preparing the  $\text{TiO}_x\text{N}_y$  and/or  $\text{TaO}_x\text{N}_y$  is possible at  $900^\circ\text{C}$  instead of  $1600^\circ\text{C}$ . Electrochemical stability determined by CV curves shows that the  $\text{TaO}_x\text{N}_y$ ,  $\text{Ti}_{0.25}\text{Ta}_{0.75}\text{O}_x\text{N}_y$ ,  $\text{Ti}_{0.75}\text{Ta}_{0.25}\text{O}_x\text{N}_y$  and  $\text{TiO}_x\text{N}_y$  are significantly stable after 100 scans between  $-0.2$  and  $1.4$  Volts. Heat treatment had a major effect on the onset potential by changing the crystallinity of the catalyst, so that the onset potential of titanium oxy-nitride increased from ca.  $0.05$  V to  $0.65$  V vs. NHE by increasing the temperature from  $500$  to  $700^\circ\text{C}$ . Increasing the Ta concentration also led to have a higher onset potential but lower ORR current. For instance, the onset potential for the ORR for pure tantalum oxy-nitride heat treated at  $700^\circ\text{C}$  was ca.  $0.85$  V vs. NHE while this amount was ca.  $0.65$  V vs. NHE for pure titanium oxy-nitride. However, the ORR current was 100 times smaller in tantalum oxy-nitride than in titanium oxy-nitride, probably because of the low electrochemical active surface area. Electrochemical measurements suggested that an appropriate composition of titanium and tantalum was required to have both a good onset potential and ORR current by improving the catalytic activity and increasing the active surface area and electrical conductivity. In particular based on these various results, it can be concluded that the performance for the ORR of these electrodes increases in the following orders:

$\text{TaO}_x\text{N}_y < \text{Ti}_{0.25}\text{Ta}_{0.75}\text{O}_x\text{N}_y < \text{Ti}_{0.75}\text{Ta}_{0.25}\text{O}_x\text{N}_y < \text{TiO}_x\text{N}_y$ .

## 6.5 Acknowledgements:

The author wishes to acknowledge the help of Jeff Lullo in commenting on an early draft of this article.

## 6.6 References

- [1] Bin Wang, *J. Power Sources*, 152, 1 (2005).
- [2] Drew C. Higgins, Doralice Meza, Zhongwei Chen, *The Journal of Physical Chemistry C*, 114, 21982 (2010).
- [3] Wei Xiong, Feng Du, Yong Liu, Albert Perez, Michael Supp, Terizhandur S. Ramakrishnan, Liming Dai, Li Jiang, *J. Am. Chem. Soc.*, 132, 15839 (2010).
- [4] A. Ishihara, Y. Shibata, S. Mitsushima, K. Ota, *Journal of The Electrochemical Society*, 155, B400 (2008).
- [5] Yuyan Shao, Geping Yin, Yunzhi Gao, *J. Power Sources*, 171, 558 (2007).
- [6] Deli Wang, Huolin L. Xin, Yingchao Yu, Hongsen Wang, Eric Rus, David A. Muller, Hector D. Abruña, *J. Am. Chem. Soc.*, 132, 17664 (2010).
- [7] Ke Zhang, Qiaoli Yue, Guifen Chen, Yanling Zhai, Lei Wang, Huaisheng Wang, Jinsheng Zhao, Jifeng Liu, Jianbo Jia, Haibo Li, *The Journal of Physical Chemistry C*, 115, 379 (2010).
- [8] Yan Liu, Akimitsu Ishihara, Shigenori Mitsushima, Nobuyuki Kamiya, Ken-ichiro Ota, *Journal of The Electrochemical Society*, 154, B664 (2007).
- [9] F. Fouda-Onana, S. Bah, O. Savadogo, *Journal of Electroanalytical Chemistry*, 636, 1 (2009).
- [10] Akimitsu Ishihara, Motoko Tamura, Koichi Matsuzawa, Shigenori Mitsushima, Ken-ichiro Ota, *Electrochimica Acta*, 55, 7581 (2010).
- [11] Takako Toda, Hiroshi Igarashi, Masahiro Watanabe, *Journal of Electroanalytical Chemistry*, 460, 258 (1999).
- [12] Yongfu Tang, Huamin Zhang, Hexiang Zhong, Ting Xu, Hong Jin, *J. Power Sources*, In Press, Corrected Proof, (2011).

- [13] Hui Yang, Walter Vogel, Claude Lamy, Nicolás Alonso-Vante, *The Journal of Physical Chemistry B*, 108, 11024 (2004).
- [14] Vojislav R. Stamenkovic, Ben Fowler, Bongjin Simon Mun, Guofeng Wang, Philip N. Ross, Christopher A. Lucas, Nenad M. Marković, *Science*, 315, 493 (2007).
- [15] Shuo Chen, Paulo J. Ferreira, Wenchao Sheng, Naoaki Yabuuchi, Lawrence F. Allard, Yang Shao-Horn, *J. Am. Chem. Soc.*, 130, 13818 (2008).
- [16] Juan Zhao, Arumugam Manthiram, *Journal of The Electrochemical Society*, 158, B208 (2011).
- [17] V. Stamenković, T. J. Schmidt, P. N. Ross, N. M. Marković, *The Journal of Physical Chemistry B*, 106, 11970 (2002).
- [18] Sanjeev Mukerjee, Supramaniam Srinivasan, *Journal of Electroanalytical Chemistry*, 357, 201 (1993).
- [19] Huimin Wu, David Wexler, Huakun Liu, O. Savadogo, Jungho Ahn, Guoxiu Wang, *Mater. Chem. Phys.*, 124, 841 (2010).
- [20] Guoxiu Wang, Huimin Wu, David Wexler, Huakun Liu, Oumarou Savadogo, *J. Alloy. Compd.*, 503, L1 (2010).
- [21] G. Selvarani, S. Maheswari, P. Sridhar, S. Pitchumani, A. K. Shukla, *Journal of Fuel Cell Science and Technology*, 8, 021003 (2011).
- [22] Ken-ichiro Ota, Yoshiro Ohgi, Kyung-Don Nam, Koichi Matsuzawa, Shigenori Mitsushima, Akimitsu Ishihara, *J. Power Sources*, 196, 5256 (2011).
- [23] S. Venkataraj, D. Severin, S. H. Mohamed, J. Ngaruiya, O. Kappertz, M. Wuttig, *Thin Solid Films*, 502, 228 (2006).
- [24] Akimitsu Ishihara, Shotaro Doi, Shigenori Mitsushima, Ken-ichiro Ota, *Electrochimica Acta*, 53, 5442 (2008).
- [25] Shotaro Doi, Akimitsu Ishihara, Shigenori Mitsushima, Nobuyuki Kamiya, Ken-ichiro Ota, *Journal of The Electrochemical Society*, 154, B362 (2007).

- [26] Akimitsu Ishihara, Kunchan Lee, Shotaro Doi, Shigenori Mitsushima, Nobuyuki Kamiya, Michikazu Hara, Kazunari Domen, Kenzo Fukuda, Ken-ichiro Ota, *Electrochemical and Solid-State Letters*, 8, A201 (2005).
- [27] Youta Maekawa, Akimitsu Ishihara, Jin-Hwan Kim, Shigenori Mitsushima, Ken-ichiro Ota, *Electrochemical and Solid-State Letters*, 11, B109 (2008).
- [28] Kyung Don Nam, Akimitsu Ishihara, Koichi Matsuzawa, Shigenori Mitsushima, Ken-ichiro Ota, *Electrochemical and Solid-State Letters*, 12, B158 (2009).
- [29] Kunchan Lee, Akimitsu Ishihara, Shigenori Mitsushima, Nobuyuki Kamiya, Ken-ichiro Ota, *Electrochimica Acta*, 49, 3479 (2004).
- [30] Yan Liu, Akimitsu Ishihara, Shigenori Mitsushima, Nobuyuki Kamiya, Ken-ichiro Ota, *Electrochemical and Solid-State Letters*, 8, A400 (2005).
- [31] Yan Liu, Akimitsu Ishihara, Shigenori Mitsushima, Ken-ichiro Ota, *Electrochimica Acta*, 55, 1239 (2010).
- [32] Jin-Hwan Kim, Akimitsu Ishihara, Shigenori Mitsushima, Nobuyuki Kamiya, Ken-ichiro Ota, *Electrochimica Acta*, 52, 2492 (2007).
- [33] Akimitsu Ishihara, Yoshiro Ohgi, Koichi Matsuzawa, Shigenori Mitsushima, Ken-ichiro Ota, *Electrochimica Acta*, 55, 8005 (2010).
- [34] Shuya Kawahara, Shigenori Mitsushima, Kenichiro Ota, and Nobuyuki Kamiya, *ECS Transaction*, 3, 619 (2006).
- [35] Wang-Jae Chun, Akio Ishikawa, Hideki Fujisawa, Tsuyoshi Takata, Junko N. Kondo, Michikazu Hara, Maki Kawai, Yasumichi Matsumoto, Kazunari Domen, *The Journal of Physical Chemistry B*, 107, 1798 (2003).
- [36] A. Ishihara J.-H. Kim, S. Mitsushima, N. Kamiya and K. Ota, *Chem. Lett.*, 36, 514 (2007).
- [37] Jin-Hwan Kim, Akimitsu Ishihara, Shigenori Mitsushima, Nobuyuki Kamiya, Ken-ichiro Ota, *Electrochemistry*, 75, 166 (2007).
- [38] Shiro Shimada, *Solid State Ionics*, 141–142, 99 (2001).
- [39] Shiro Shimada, Mats Johnsson, Sigita Urbonaite, *Thermochimica Acta*, 419, 143 (2004).

- [40] Akimitsu Ishihara, Motoko Tamura, Koichi Matsuzawa, Shigenori Mitsushima, Ken-ichiro Ota, *Journal of Fuel Cell Science and Technology*, 8, 031005 (2011).
- [41] Yohei Shibata, Akimitsu Ishihara, Shigenori Mitsushima, Nobuyuki Kamiya, Ken-ichiro Ota, *Electrochemical and Solid-State Letters*, 10, B43 (2007).
- [42] Akimitsu Ishihara Yoshiro Ohgi, Yohei Shibata, Shigenori Mitsushima and Ken-ichiro Ota, *Chemistry Letters*, 37, 608 (2008).
- [43] Gang Liu, Hua Min Zhang, Mei Ri Wang, He Xiang Zhong, Jian Chen, *J. Power Sources*, 172, 503 (2007).

**CHAPTER 7      ARTICLE 4: DENSITY FUNCTIONAL THEORY (DFT)  
COMPUTATION OF THE OXYGEN REDUCTION REACTION (ORR)  
ON TITANIUM NITRIDE (TiN) SURFACE**

A. Seifitokaldani <sup>a,b</sup>, M. Perrier <sup>a</sup>, O. Savadogo <sup>a,b</sup>

<sup>a</sup> Chemical Engineering Department, Polytechnique Montréal, Montréal, QC, Canada

<sup>b</sup> Laboratory of New Materials for Electrochemistry and Energy, Polytechnique Montréal,  
C.P.6079, Succursale Centre-Ville, Montréal, Québec H3C 3A7, Canada

Submitted to: *Electrochimica Acta*

Two different facets of the TiN were studied as the possible electro-catalyst for the ORR. ORR was considered to take place in three different sequential steps namely oxygen adsorption, hydroxide production and water desorption. These steps were simulated by Vienna *ab initio* Simulation Package (VASP) on different adsorption sites on both TiN(111) and TiN(200). Their corresponding energy was determined. The comparison of the adsorption energies of the different species involved on the ORR was done. The type of the facets which allow the strong dissociative adsorption of oxygen, the relatively strong OH adsorption and the water production was respectively identified. Accordingly it was shown that the TiN(200) surface exhibits active sites for the ORR while the TiN(111) surface was poisoned by strong OH adsorption. Furthermore, the results of the simulation of these sequential reactions on two possible bridge and top adsorption sites on the TiN(200), indicates that the hydroxide production and water desorption as the rate determining steps of the ORR in bridge and top sites, respectively. The electron density of states (DOS) obtained from these calculations for these two surfaces were used to calculate their d-band center and fractional filling in different situations.

**Keywords:** *Density Functional Theory, DFT, Computation, VASP, Oxygen Reduction Reaction, ORR, Titanium Nitride, TiN*

## 7.1 Introduction

The state of the art electro-catalyst for the Polymer Electrolyte Membrane Fuel Cells (PEMFCs) is the Pt or Pt alloys nano-particles on the carbon support (Pt/C) [1-17]. Although, because of some drawbacks such as sintering, dissolution and deposition of extremely dispersed Pt nano-particles in the electrolyte and consequently low durability of this type of catalysts, which limit its utilization for mass production of PEMFCs, developing a new non-Pt electro-catalyst is a big challenge for decades [18-23].

Transition metal oxides and nitrides are the most potential candidates as a probable alternative electro-catalyst to the Pt based compounds [24-28] because they exhibit high chemical and electrochemical stability in corrosive media such as PEMFC acidic environment. Different oxide compounds such as zirconium oxide [29-31], titanium oxide [32-34], manganese oxide [35], tungsten oxide [36, 37], niobium oxide [32, 38, 39], cobalt and tin oxide [39], have been evaluated as catalysts or catalyst-supports for the ORR. Although these compounds had shown to some extent a catalytic activity for the ORR and also a good stability, it was not enough to be considered as an alternative active electro-catalyst. Specially, their low electrical conductivity inspired researchers to work on the nitrides and carbides of the transition metals which have better electrical properties than the transition metal oxides. Therefore, zirconium nitride, niobium nitride [40], cobalt nitride [41], tungsten carbide [42], chromium carbo-nitride and tantalum carbo-nitride [43, 44] were studied. In spite of the better electrical conductivity of these materials, because transition metal oxides are thermodynamically more stable than carbo-nitrides and nitrides, these nitrides and carbo-nitrides were essentially unstable under the ORR conditions and were oxidized at high oxidation potentials [45, 46].

Currently, most of the investigations in this area are devoted to the transition metal oxy-nitrides which satisfy both the chemical and electrochemical stability and electrocatalytic activity [47-56]. But, due to its great abundance, titanium oxy-nitride (TiON) is one of the most appealing electro-catalysts and has been the subject of many investigations on its preparation, stability, and catalytic activity [57-61]. Interestingly, in our group preliminary results have shown that the ratio of TiN and TiO<sub>2</sub> in the TiON affects its catalytic activity, so that increasing the N portion led to a better electro catalytic activity. Finding an answer for the reason of this phenomenon is the subject of this article.

The utilisation of the computational chemistry tools to study the reactions taking place on the surface of solid catalysts is as long as the development of computer science. A lot of studies on fundamental properties of surfaces have been made in view to determine appropriate materials as catalyst for specific reactions. In particular, Nørskov and coworkers made significant contributions in the study of transition metal's catalytic activity from DFT simulation. They have studied a vast variety of solid catalysts including the transition metals, in which it has led to development of the d-band theory [62-68]. In the case of the electro-catalysts used in PEMFCs, some studies on the simulation of the ORR steps on platinum [69-75] or platinum based materials [76-79] have been done. The oxygen and the hydroxide adsorption were mostly evaluated. In addition to Pt based compound, some other non-Pt precious materials such as gold or palladium alloys [80-84] and non-precious materials [85-90] have been also studied.

To the best of our knowledge there is no simulation on the determination of the surface energies involved in the ORR steps using VASP on the transition metal's nitride. So, for the first time, in this article titanium nitride was studied using the DFT simulation in view to reveal its electro-catalytic activity towards the ORR steps. As already mentioned, increasing the TiN portion in the TiON structure led to a better electro-catalytic activity. Therefore, the electro-catalytic activity of two major facets of titanium nitride namely TiN(200) and TiN(111) which mostly make up the bulk of the TiN, was evaluated in this article. A noteworthy point in the present article is that in addition to the oxygen and hydroxide adsorption evaluation, water desorption was also investigated.

## 7.2 Computational Approach

Vienna *ab initio* Simulation Package (VASP) [91-94] based on the Density Functional Theory (DFT) was used in the present article to simulate different steps of the ORR on the TiN(200), TiN(111) and Pt(111) surfaces by solving the Kohn-Sham equation of a many-body system with an iterative approach. The system was under the periodic boundary condition and computation was done in a reciprocal space. Plane-Wave basis sets with an adequate cutoff energy of 400 eV and accurate precision was used. Electron-ion core interactions were represented by the Projected Augmented Wave (PAW) approach [95, 96], while the General Gradient Approximation (GGA) of *Perdew, Burke and Ernzerhof* [97, 98] (PBE) was used as the exchange-correlational functional to describe the interactions among electrons. The Brillouin zone integration was done

on a grid of  $4 \times 4 \times 1$  with a Gaussian smearing parameter  $\sigma$  of 0.2 eV and a Self-Consistence-Field (SCF) convergence criterion of  $1 \times 10^{-5}$  eV. Initial structures were optimized by allowing the atoms positions to be relaxed while the iterative algorithm was updated by the Conjugate Gradient approach with a convergence criteria of 0.02 eV/Å for each loop.

TiN(200) and TiN(111) surfaces were modeled with a four layer slab using a  $2 \times 2 \times 1$  supercell in which there were four Ti atoms and four N atoms per layer. In order to separate two subsequent slabs and reduce their mutual effects, a vacuum gap of 12 and 14.7 Å was considered for the TiN (200) and TiN (111), respectively. This vacuum gap which was almost identical to 6 layers in each case, demonstrated in figure (1), was enough since the surface work function calculated as 4.43 eV agrees well with the experimental value of 4.2~4.5 eV [99, 100]. Figure (1) also shows different sites of oxygen adsorption on these surfaces namely: top and bridge for the TiN (200), and also (t-b-t)<sup>15</sup>, (t-h-b)<sup>16</sup>, (t-f-b)<sup>17</sup> and top sites for the TiN (111). Adsorbates including oxygen, hydroxide, water and all other transient species were placed on one side of the slab. Excluding these species and the top layer of the slab that were allowed to relax in their positions to reach the most stable configuration, all other atoms were frozen at their ideal bulk positions to simulate the bulk and reduce the computational cost.

---

<sup>15</sup> (t-b-t): top bridge, also simply called bridge site

<sup>16</sup> (t-h-b): top hcp bridge, also called hollow hcp bridge (hcp: hexagonal close packed)

<sup>17</sup> (t-f-b): top fcc bridge, also called hollow fcc bridge (fcc: face centered cubic)

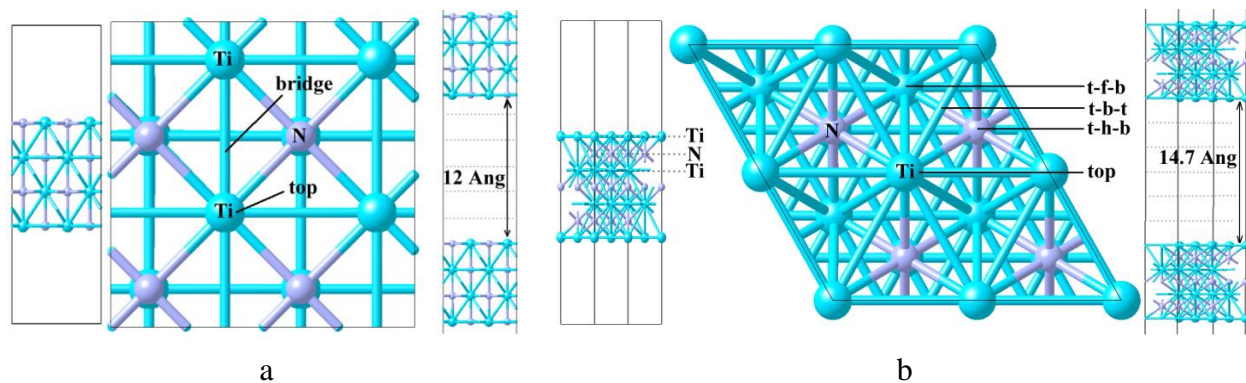


Figure 1.(a) TiN (200) with two top and bridge possible sites and (b) TiN (111) with four top, (t-b-t), (t-h-b) and (t-f-b) possible sites for the oxygen adsorption. The left and middle pictures are the side and top views of a slab, respectively, while the right pictures show two subsequent slabs with the related vacuum gap between them.

Adsorption energy of  $O_2$ , OH and  $H_2O$  for both the TiN (200) and TiN (111) surfaces at different sites were calculated and discussed. Generally speaking, equation (1) was used to calculate the adsorption energy of a component A on a surface B:

$$E_{ads} = E_{A+B} - (E_A + E_B) \quad (1)$$

Where,  $E_{A+B}$  is the total energy of the system including both adsorbate A and adsorbent B at their final relaxed state,  $E_A$  is the energy of the adsorbate A alone inside the simulation cell and  $E_B$  is the energy of the adsorbent B alone inside the simulation cell. Notice that the simulation cells in all cases must be identical. According to this definition more negative adsorption energy means a more favorable adsorption and vice versa less negative (more positive) energy means a less favorable one.

Some electronic properties which are helpful in understanding and justifying different behaviors in oxygen, hydroxide or water adsorption on different surfaces, such as fractional d-band filling, d-band width and specifically d-band center were calculated and discussed in the next section. Equations (2) to (4) were used to calculate the fractional d-band filling ( $f_d$ ), d-band center ( $\epsilon_d$ ) and d-band width ( $W_d$ ), respectively.

$$f_d = \frac{\text{Number of Occupied States}}{\text{Number of states}} = \frac{\int_{-\infty}^{\epsilon_F} \rho \cdot d\epsilon}{\int_{-\infty}^{\infty} \rho \cdot d\epsilon} \quad (2)$$

$$\epsilon_d = \frac{\int_{-\infty}^{\epsilon_F} \rho E \cdot d\epsilon}{\int_{-\infty}^{\epsilon_F} \rho \cdot d\epsilon} \quad (3)$$

$$W_d^2 = \frac{\int_{-\infty}^{\epsilon_F} \rho E^2 \cdot d\epsilon}{\int_{-\infty}^{\epsilon_F} \rho \cdot d\epsilon} \quad (4)$$

Where,  $\rho, E$  and  $\epsilon_F$  are the density of electronic state per volume, energy of the electron and Fermi energy, respectively.

### 7.3 Results and Discussions

The determination of the energies involved in the following essential sequences of the ORR on the TiN surfaces is important to understand the performance of the titanium oxy nitride based electro-catalyst for the ORR. These sequences are: the oxygen adsorption, the hydroxide production and the water desorption. Using the VASP simulation, Figure (2-a) shows the adsorption energies of O<sub>2</sub> calculated from equation (1) on the TiN(200) and TiN(111) surfaces. The oxygen adsorption energies change with the type of the adsorption site. When the O-O distance increases, the adsorption energy is more negative and it is more positive when the distance from the surface increases (top site). However in almost all cases, TiN(111) which exhibits a more adsorption energy shows a stronger oxygen adsorption than TiN(200). The top sites for the adsorption of oxygen in both TiN surfaces are not favourable to break up the O-O bond and create atomic adsorbed oxygen. While for all other adsorption sites of the TiN facets, a strong dissociative adsorption of oxygen was observed. Specially, in two t-h-b and t-f-b cases of TiN(111), the adsorption energy is -10.58 and -9.71 eV, respectively. These energies compared to those calculated for the Pt(111), -0.53 and -0.67 eV on the same adsorption sites of t-h-b and t-f-b, respectively, proved a very strong oxygen adsorption on the TiN(111). In the both top sites which had smaller oxygen adsorption energy (smaller in magnitude) than the other sites, distance between the oxygen atoms as well as the distance of the molecule from the surface remained almost unchanged, while in all other sites oxygen bond was broken to separate the atoms up to 3 angstrom. In addition, distance of the oxygen atoms from the surface was reduced. Figure (5) in

parts a and b show the initial and final states of oxygen on two adsorption sites (top and bridge) of TiN(200), respectively. The same is demonstrated for the TiN(111) in figure (6).

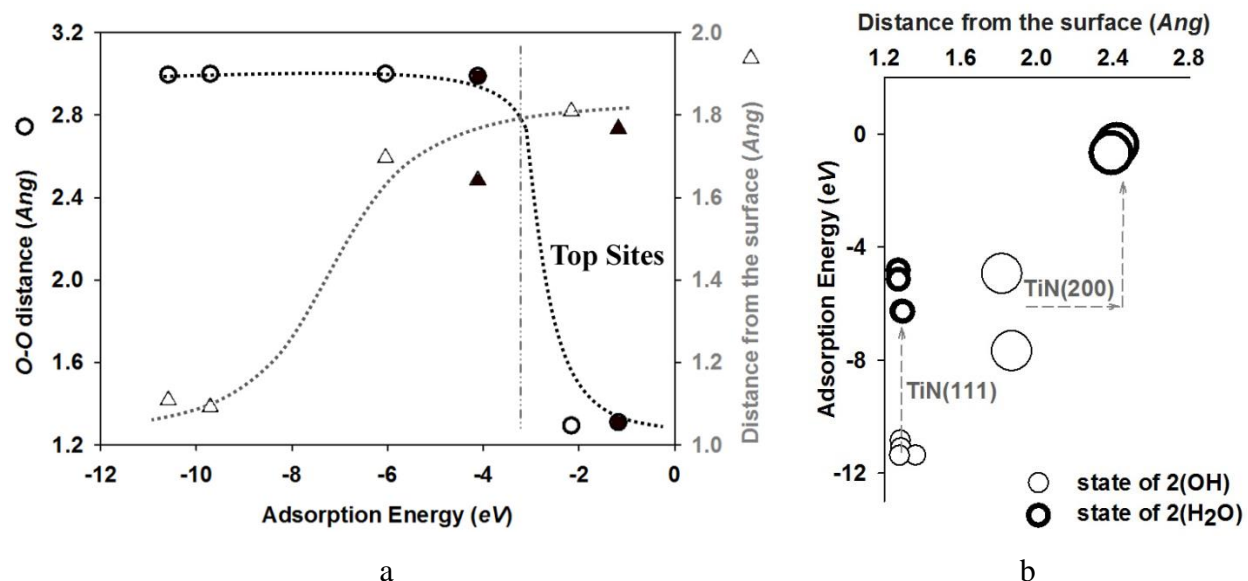
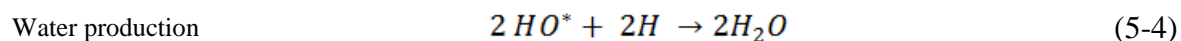
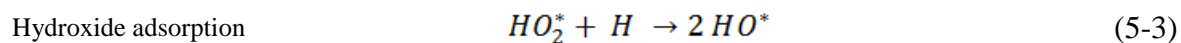
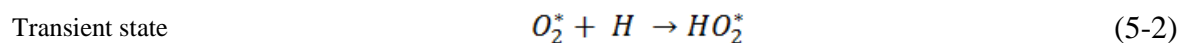
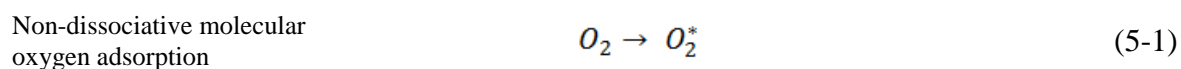


Figure 2.(a) Oxygen-Oxygen bond distance (circles) and molecule distance from the TiN surface (triangles) versus adsorption energy. Hollow circles and triangles are related to the TiN(111) and the filled black ones are related to the TiN(200). In the both top sites which there were no dissociative adsorption, adsorption energy magnitude was less than 3 eV (right side of the vertical dash-line). (b) Molecule distance from the surface versus the adsorption energy is depicted for the hydroxide and water states, respectively by thin and thick circles.

Although TiN(111) showed a very strong dissociative adsorption of oxygen which makes this surface not favorable as the TiN(200) for the second and third steps of the ORR. To happen, it is necessary to be able to provide water molecule and repel it from the surface. It is the case on TiN(200) for both sites (Top and Bridge) of adsorption. Figure (2-b) shows the variation of the adsorption energy with the molecule distance from the TiN surface for the hydroxide state and the water state. In the case of TiN(111), the adsorption energy of OH<sub>2</sub> is reduced to almost half of that of the hydroxide; however it is still negative enough to not let the surface repel it. In comparison to the water adsorption energy on the TiN(200) surface which is around -0.5 eV, those on TiN(111) is almost -5 eV. Accordingly, the water adsorption energy on TiN(111) is at

least 10 times more than that of TiN(200). This help to keep the water molecule on its (TiN(111)) surface .This tendency does not allow the OH to react with the upcoming proton to create water molecule. On the other hand, the calculated adsorption energy on TiN(200) in both cases of the top and the bridge sites shows a very feeble adsorption bond to keep produced water on its surface. Moreover, its lower tendency to adsorb water when compared to that of the oxygen molecule resulted in repelling the produced water to provide new available sites for adsorbing new oxygen molecules. Water repelling from the TiN(200) surface is demonstrated in figure (2-b), by increasing the molecule distance from the surface. Therefore, both lowering the magnitude of adsorption energy and taking distance from the surface existed for the TiN(200) surface, passing from the hydroxide state to the water state. While in the case of TiN(111) just there was reduction of adsorption energy magnitude without considerable change in distance. Then the comparison of the top view of figure (6-c) with (6-d) showed a so stable OH state that does not change even by adding the next hydrogen atom. This stable OH state had three strong bonds with Ti atoms which do not depend on the type of the adsorption site. On the other hand, from figure (5-c) and (5-d), it is obvious that in both top and bridge sites of the TiN(200), adding the second hydrogen atom to the hydroxide, led to the creation of water molecule which is far from the TiN(200) surface. Although, it must be noted that in this case the top site needed one more step than the bridge site to make 2(OH). It means that after the weak and non-dissociative oxygen adsorption on this site, a transient  $O_2H$  state (depicted in figure (3)) was created, which transferred to 2(OH) by adding the other hydrogen atom. Considering the \* sign as the Ti active site, the ORR is suggested to take place on the top and bridge sites, respectively by the equations (5) and (6):

Top site:



Bridge site:

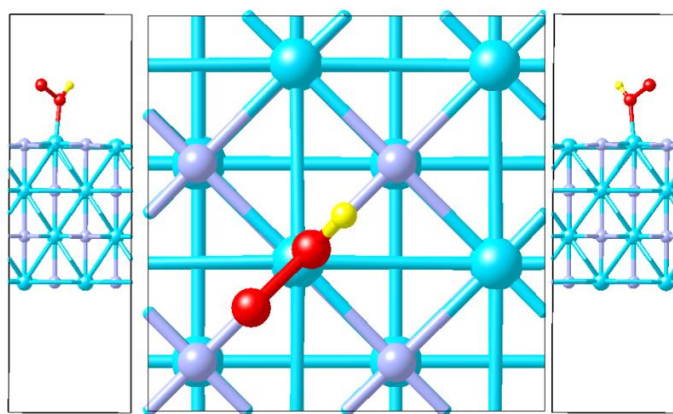
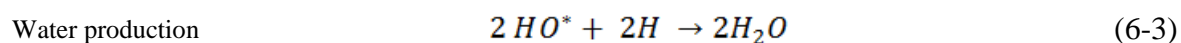
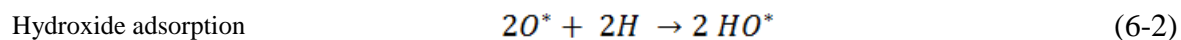
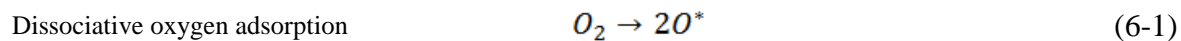


Figure 3. Transition  $O_2H$  state between  $O_2$  adsorption and  $OH$  production on top site of  $TiN(200)$

The extra transition step mentioned in equation (5-2) arises because of the weak and non-dissociative oxygen adsorption on the top site. In fact, a fairly low oxygen adsorption energy (in magnitude) associated to the top site is a significant obstacle in the ORR progress on that site, at least compared to the bridge site in which adsorption is dissociative and strong. Figure (4-a) compares all adsorption energies in three oxygen, hydroxide and water states for all sites in both  $TiN(200)$  and  $TiN(111)$  surfaces. Based on the adsorption energy amounts, it could be concluded that the oxygen adsorption is the rate determining step for the top site of  $TiN(200)$  because the next hydroxide production is very favourable. Also, it should be noted that since the water adsorption energy in top site is almost identical to the oxygen adsorption energy, it would not be favorable to make the surface site free for the new oxygen molecules. However in the case of bridge site, both oxygen adsorption and water repletion were favourable, but the hydroxide production does not happen as quickly as on the other sites. Therefore, the hydroxide production step can be considered as the rate determining step to control the ORR rate for the bridge site. In the case of  $TiN(111)$ , figure (4-a) shows that  $OH$  by having a high negative adsorption energy is in a so stable state that it is not transformed to water molecule. Also figure (4-b) proves that in

TiN(111), at the final step, the molecule remains close to the surface, while in TiN(200) it is far from the surface.

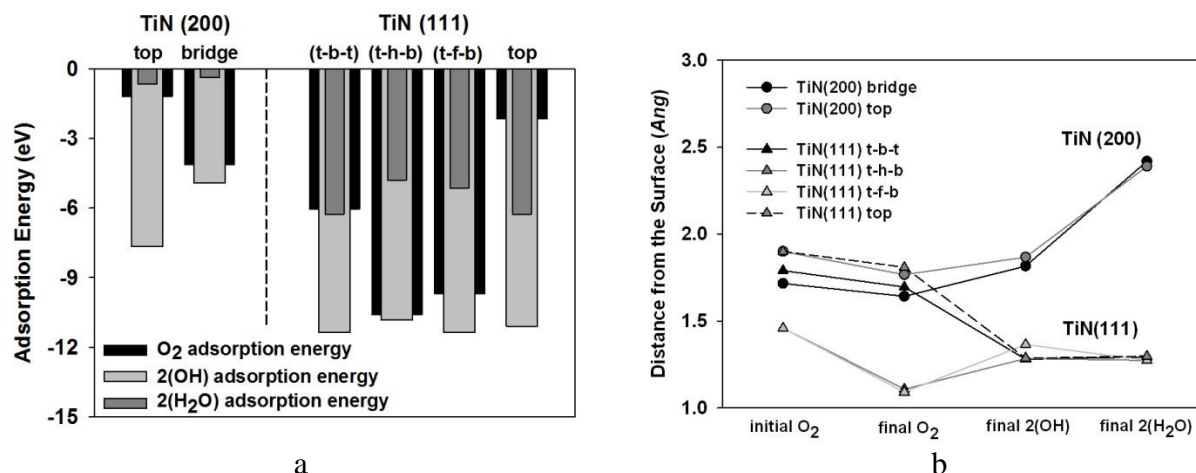


Figure 4. (a) Adsorption energies of O<sub>2</sub>, 2(OH) and 2(H<sub>2</sub>O) on different sites of TiN(200) and TiN(111), (b) Distances of the species from the surfaces

Figure (7) represents the Density of electronic State (DOS) of the top layer titanium atoms, as the active sites, for all adsorption sites in four different situations: TiN without any adsorbate, TiN with adsorbed oxygen, TiN with adsorbed hydroxide and also TiN with water. These figures show qualitatively the change in the DOS of the titanium active sites in interaction with atoms at different steps. The black filled areas are those occupied with electrons, while the gray regions represent the available electronic states above the Fermi level (set as 0 eV) which are empty. The dash-line  $\epsilon_d$  is the d-band center of the DOS in each case. These figures show the change in the shape of the DOS and the amount of the d-band center. From the sole TiN to the TiN-2(H<sub>2</sub>O), DOS changed step by step according to the interaction between the titanium and the adsorbate atoms, but only in the case of TiN(200), it went back to the initial DOS of TiN(200) at the final step where there was water molecule on top of the surface. In addition, comparing the d-band center amount of the initial sole TiN and the final step, confirms the existence of an interaction between the TiN(111) and 2(H<sub>2</sub>O) adsorbates in all cases. In general, in TiN(111) there was no change in the DOS shape and the related d-band center's amount between the TiN-2(OH) state and the TiN-2(H<sub>2</sub>O) state, reconfirming the high stability of adsorbed hydroxide on this surface.

However, in TiN(200) specially for the bridge site, the obvious change of the DOS from TiN-2(OH) to TiN-2(H<sub>2</sub>O) is an indication of the release of the surface from the interaction with adsorbates.

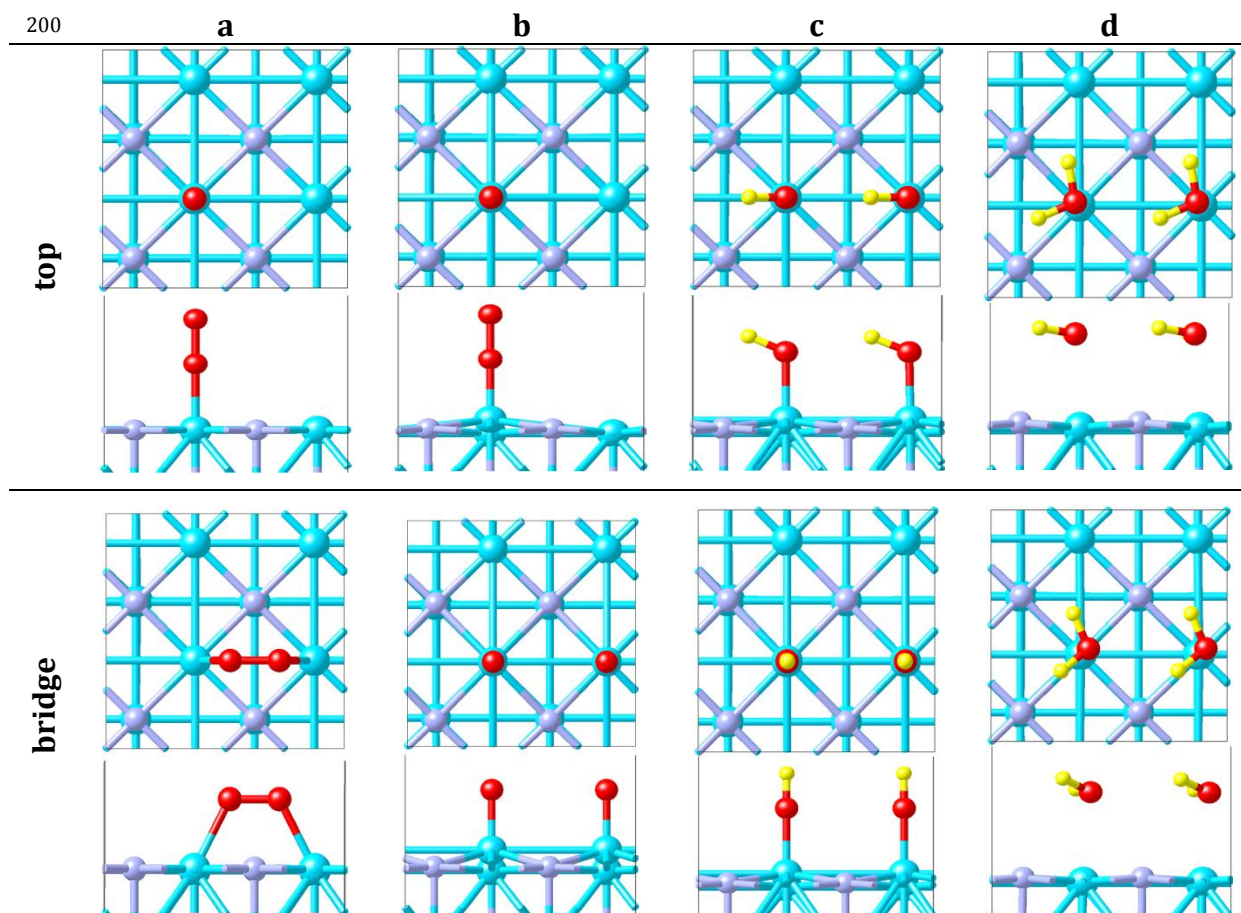


Figure 5. Top and side views of initial and final states of different adsorbates on TiN(200) surface. States a, b, c and d are related to initial configuration of oxygen molecule, final state of O<sub>2</sub>, final state of 2(OH) and final state of 2(H<sub>2</sub>O), respectively. These states are demonstrated for the two top and bridge sites of TiN(200).

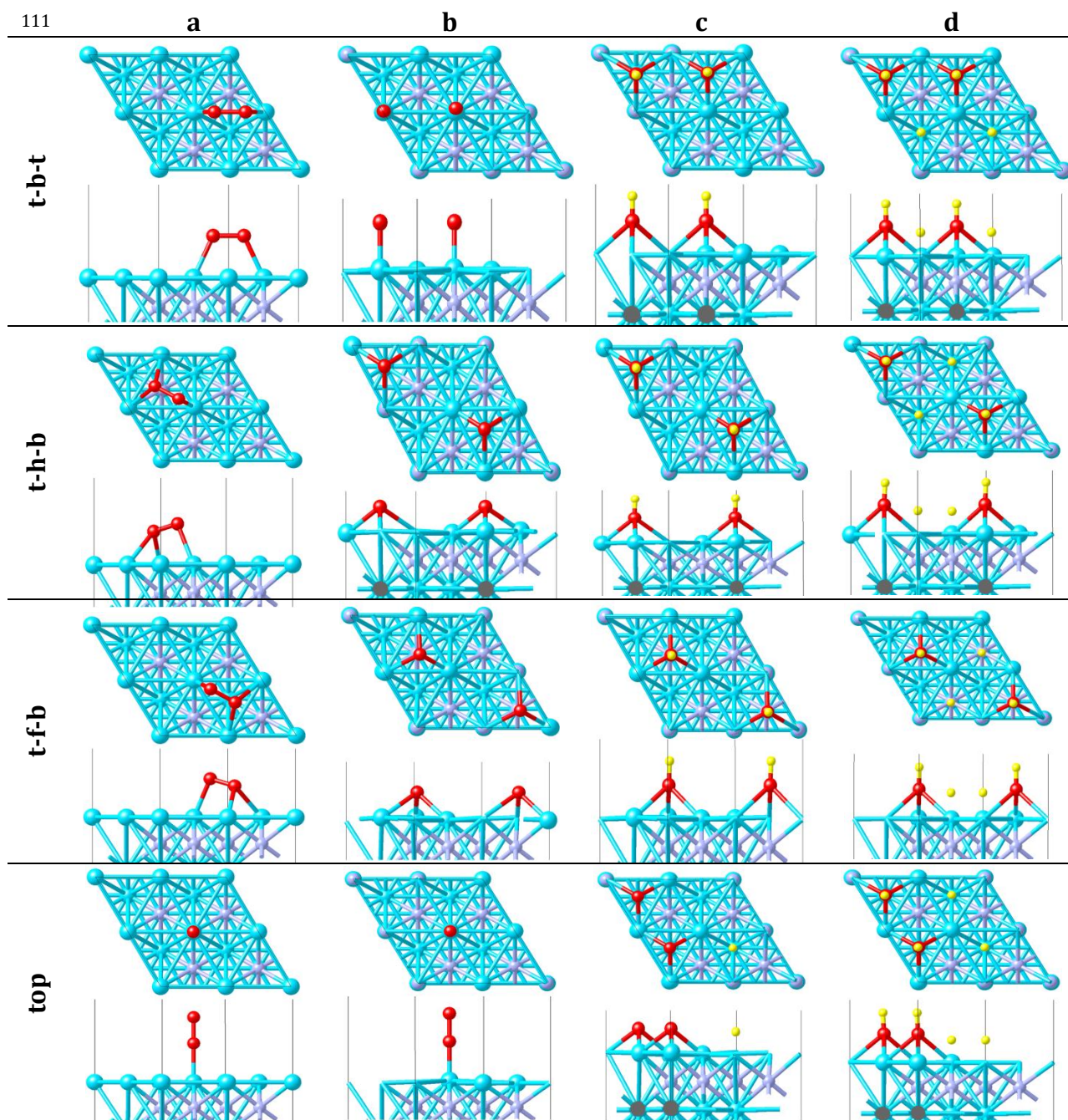


Figure 6. Top and side views of initial and final states of different adsorbates on TiN(111) surface. States a, b, c and d are related to initial configuration of oxygen molecule, final state of  $O_2$ , final state of  $2(OH)$  and final state of  $2(H_2O)$ , respectively. These states are demonstrated for the four t-b-t, t-h-b, t-f-b and top sites of TiN(111).

The amounts of the d-band centers, fractional d-band filling, d-band width and also adsorption energy for the top and bridge sites on TiN(200) are summarised in table 1. It is clear that both sites should have the same amounts for these parameters in initial state, including only TiN(200). Interestingly, both of them had also similar properties at the last step, where we had TiN(200) and 2(H<sub>2</sub>O). At the first step, d-band center on the bridge site was significantly altered and reduced by oxygen adsorption, while it did not change a lot in the top site. Once again, this indicates a strong interaction between oxygen molecule and Ti atoms in bridge site. This reduction in d-band center consequently led to higher d-band filling, so that it increased from 0.26 to 0.4 in the bridge site's case. The more negative adsorption energy obtained on the bridge site in comparison to that of the top site is also consistent with this strong interaction. At the second step in which we had hydroxide production, the top site is more favorable than the bridge site to adsorb the OH species. On the top site we had a lower d-band center and consequently a higher d-band filling compared to the bridge site, indicating a stronger adsorption of hydroxide on the top site with lower adsorption energy. However, at the last step, bridge site showed a less favourable possibility to adsorb the water molecule with less negative adsorption energy, which is more favorable for the ORR.

Table 1. Comparison of Bridge and Top sites on TiN(200) in four different situations from the electronic structure property's point of view.

	Active site	d-band center $\epsilon_d$ (eV)	Fractional d-band filling $f_d$	d-band width $W_d$ (eV)	Adsorption energy (eV)
TiN(200)	bridge	0.16	0.26	0.30	---
	top	0.16	0.26	0.30	---
TiN(200)-O <sub>2</sub>	bridge	<b>0.06</b>	<b>0.40</b>	0.29	<b>-4.11</b>
	top	0.12	0.28	0.29	-1.18
TiN(200)-2(OH)	bridge	0.17	0.26	0.32	-4.93
	top	<b>0.15</b>	<b>0.27</b>	0.30	<b>-7.66</b>
TiN(200)-2(H <sub>2</sub> O)	bridge	0.21	0.24	0.32	<b>-0.37</b>
	top	0.20	0.24	0.32	-0.66

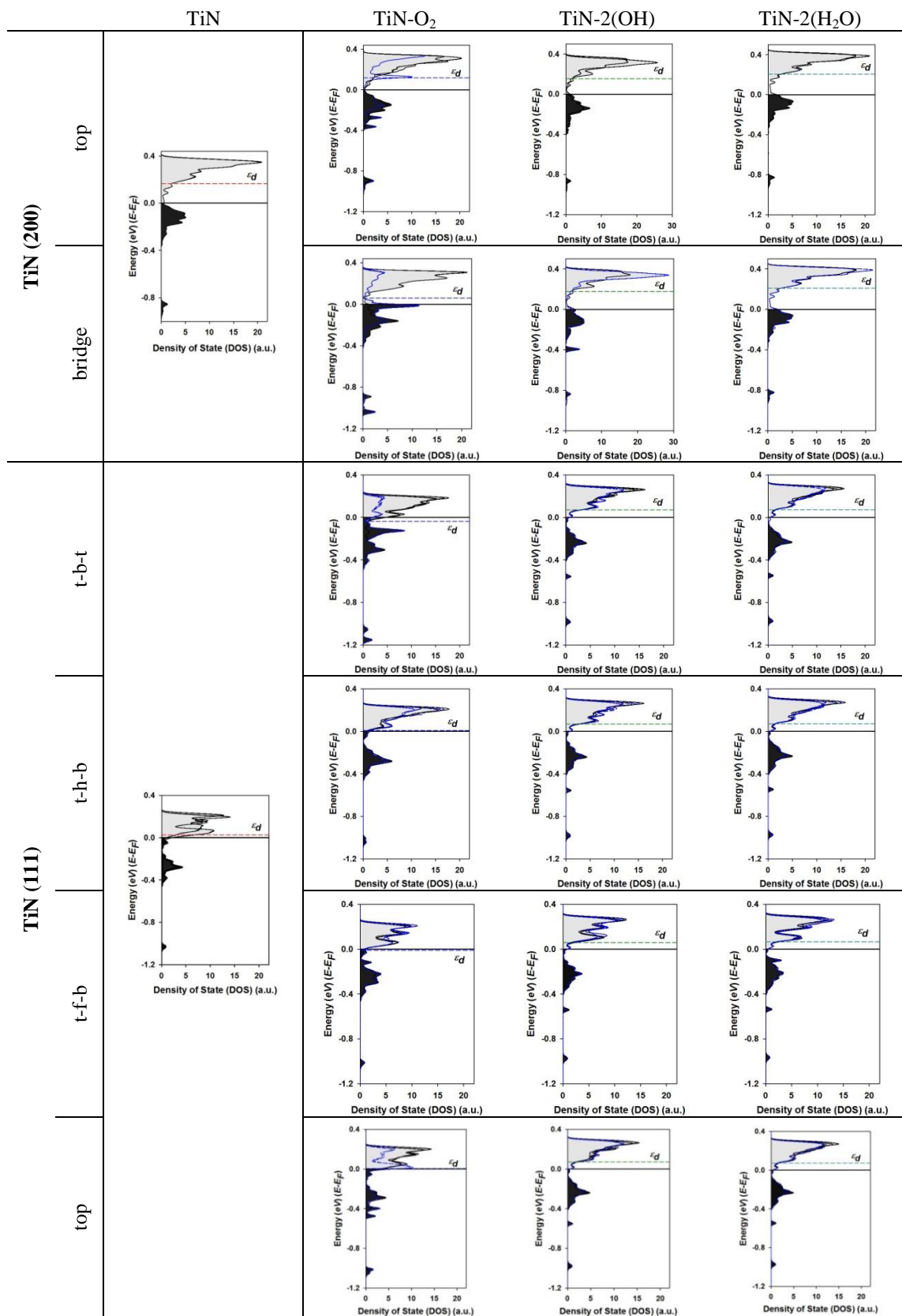


Figure 7. Density of States (DOS) of the top layer titanium atoms in different situations. Black region represents the filled states and the grey regions are those above the Fermi level that are empty.

## 7.4 Conclusion

DFT computation based on the Plane-Wave basis sets and the Projected Augmented Wave (PAW) approach with the General Gradient Approximation (GGA) of *Perdew, Burke and Ernzerhof* (PBE) exchange-correlational functional was used to simulate the ORR steps on two different surfaces of the TiN. Both TiN(200) and TiN(111) showed a very strong interaction with oxygen molecule which led to a dissociative adsorption, except for the top adsorption site. Having a fairly strong and stable bond with hydroxide molecule ceased the ORR progress on the TiN(111) facet, in which water molecule could not be produced. However, on the other hand, TiN(200) showed a good activity to produce water molecule and then to repel it. In fact, production of water molecule and repulsion provides new available sites for the next oxygen molecule adsorption. Comparison of the DOS patterns and also d-band center and fractional filling in different situations, demonstrated the strong interaction of TiN(111) with OH molecule, while in the case of TiN(200) this interaction weakened by adding a second proton to the adsorbed OH molecule. Therefore, having more TiN(200) rather than TiN(111) in the TiON structure improves its catalytic activity for the ORR.

Having close adsorption energies of water and oxygen molecules, made these two steps the most important of the ORR for the top site in TiN(200). In the other word, having a fairly weak oxygen adsorption or fairly strong water adsorption provides a competition between keeping the water molecule on the surface and adsorbing a new oxygen molecule. While, for the bridge site, water adsorption was not comparable to the strong oxygen adsorption, and undoubtedly adsorbing a new oxygen molecule is favourable of this competition to let the ORR proceed. However, in this case hydroxide production is not as spontaneous as the other sites, indicating a fairly slow rate in this step for the bridge site. Comparing the d-band center and d-band fractional filling changes in oxygen adsorption and hydroxide production steps supported this issue. Therefore, bridge site is the most favourable site for the ORR on the TiN(200).

## 7.5 References

- [1] T. Toda, H. Igarashi, M. Watanabe, *Journal of Electroanalytical Chemistry*, 460 (1999) 258-262.
- [2] Y. Tang, H. Zhang, H. Zhong, T. Xu, H. Jin, *J. Power Sources*, In Press, Corrected Proof (2011).
- [3] D.W. Jung, S. Park, C.Y. Ahn, J.B. Kim, E.S. Oh, *Fuel Cells*, 12 (2012) 398-405.
- [4] Z. Peng, H. Yang, *J. Am. Chem. Soc.*, 131 (2009) 7542-7543.
- [5] H. Yang, W. Vogel, C. Lamy, N. Alonso-Vante, *The Journal of Physical Chemistry B*, 108 (2004) 11024-11034.
- [6] V.R. Stamenkovic, B. Fowler, B.S. Mun, G. Wang, P.N. Ross, C.A. Lucas, N.M. Marković, *Science*, 315 (2007) 493-497.
- [7] G. Wang, H. Wu, D. Wexler, H. Liu, O. Savadogo, *J. Alloy. Compd.*, 503 (2010) L1-L4.
- [8] J. Zhao, A. Manthiram, *Journal of The Electrochemical Society*, 158 (2011) B208-B214.
- [9] H. Wu, D. Wexler, H. Liu, O. Savadogo, J. Ahn, G. Wang, *Mater. Chem. Phys.*, 124 (2010) 841-844.
- [10] V. Stamenković, T.J. Schmidt, P.N. Ross, N.M. Marković, *The Journal of Physical Chemistry B*, 106 (2002) 11970-11979.
- [11] S. Mukerjee, S. Srinivasan, *Journal of Electroanalytical Chemistry*, 357 (1993) 201-224.
- [12] P. Mani, R. Srivastava, P. Strasser, *The Journal of Physical Chemistry C*, 112 (2008) 2770-2778.
- [13] I.E.L. Stephens, A.S. Bondarenko, F.J. Perez-Alonso, F. Calle-Vallejo, L. Bech, T.P. Johansson, A.K. Jepsen, R. Frydendal, B.P. Knudsen, J. Rossmeisl, I. Chorkendorff, *J. Am. Chem. Soc.*, 133 (2011) 5485-5491.
- [14] M. Nie, P.K. Shen, M. Wu, Z. Wei, H. Meng, *J. Power Sources*, 162 (2006) 173-176.
- [15] T. Toda, H. Igarashi, H. Uchida, M. Watanabe, *Journal of The Electrochemical Society*, 146 (1999) 3750-3756.

- [16] M.K. Jeon, C.H. Lee, G.I.L. Park, K.H. Kang, *J. Power Sources*, 216 (2012) 400-408.
- [17] M.B. Vukmirovic, J. Zhang, K. Sasaki, A.U. Nilekar, F. Uribe, M. Mavrikakis, R.R. Adzic, *Electrochimica Acta*, 52 (2007) 2257-2263.
- [18] J. Wu, X.Z. Yuan, J.J. Martin, H. Wang, J. Zhang, J. Shen, S. Wu, W. Merida, *Journal of Power Sources*, 184 (2008) 104-119.
- [19] X. Yu, S. Ye, *J. Power Sources*, 172 (2007) 145-154.
- [20] Y. Shao, G. Yin, Y. Gao, *J. Power Sources*, 171 (2007) 558-566.
- [21] S.G. Rinaldo, W. Lee, J. Stumper, M. Eikerling, *Electrochemical and Solid-State Letters*, 14 (2011) B47-B49.
- [22] Z.-M. Zhou, Z.-G. Shao, X.-P. Qin, X.-G. Chen, Z.-D. Wei, B.-L. Yi, *International Journal of Hydrogen Energy*, 35 (2010) 1719-1726.
- [23] V. Mazumder, M. Chi, K.L. More, S. Sun, *J. Am. Chem. Soc.*, 132 (2010) 7848-7849.
- [24] B. Wang, *J. Power Sources*, 152 (2005) 1-15.
- [25] T. Oh, J.Y. Kim, Y. Shin, M. Engelhard, K.S. Weil, *J. Power Sources*, 196 (2011) 6099-6103.
- [26] A. Ishihara, M. Tamura, K. Matsuzawa, S. Mitsushima, K.-i. Ota, *Electrochimica Acta*, 55 (2010) 7581-7589.
- [27] R. Othman, A.L. Dicks, Z. Zhu, *International Journal of Hydrogen Energy*, 37 (2012) 357-372.
- [28] Y. Takasu, M. Suzuki, H. Yang, T. Ohashi, W. Sugimoto, *Electrochimica Acta*, 55 (2010) 8220-8229.
- [29] Y. Suzuki, A. Ishihara, S. Mitsushima, N. Kamiya, K.-i. Ota, *Electrochemical and Solid-State Letters*, 10 (2007) B105-B107.
- [30] Y. Liu, A. Ishihara, S. Mitsushima, N. Kamiya, K.-i. Ota, *Electrochemical and Solid-State Letters*, 8 (2005) A400-A402.
- [31] Y. Liu, A. Ishihara, S. Mitsushima, K.-i. Ota, *Electrochimica Acta*, 55 (2010) 1239-1244.

- [32] G. Chen, C.C. Waraksa, H. Cho, D.D. Macdonald, T.E. Mallouka, *Journal of The Electrochemical Society*, 150 (2003) E423-E428.
- [33] T. Ioroi, Z. Siroma, N. Fujiwara, S.-i. Yamazaki, K. Yasuda, *Electrochemistry Communications*, 7 (2005) 183-188.
- [34] L. Timperman, Y.J. Feng, W. Vogel, N. Alonso-Vante, *Electrochimica Acta*, 55 (2010) 7558-7563.
- [35] N.R. Elezovic, B.M. Babic, V.R. Radmilovic, L.M. Vracar, N.V. Krstajic, *Electrochimica Acta*, 54 (2009) 2404-2409.
- [36] M.S. Saha, M.N. Banis, Y. Zhang, R. Li, X. Sun, M. Cai, F.T. Wagner, *Journal of Power Sources*, 192 (2009) 330-335.
- [37] J. Shim, C.-R. Lee, H.-K. Lee, J.-S. Lee, E.J. Cairns, *Journal of Power Sources*, 102 (2001) 172-177.
- [38] K. Sasaki, L. Zhang, R.R. Adzic, *Physical Chemistry Chemical Physics*, 10 (2008) 159-167.
- [39] A. Ishihara, Y. Ohgi, K. Matsuzawa, S. Mitsushima, K.-i. Ota, *Electrochimica Acta*, 55 (2010) 8005-8012.
- [40] K.-i. Ota, Y. Ohgi, K.-D. Nam, K. Matsuzawa, S. Mitsushima, A. Ishihara, *J. Power Sources*, 196 (2011) 5256-5263.
- [41] M. Azuma, M. Kashihara, Y. Nakato, H. Tsubomura, *Journal of Electroanalytical Chemistry and Interfacial Electrochemistry*, 250 (1988) 73-82.
- [42] K. Lee, A. Ishihara, S. Mitsushima, N. Kamiya, K.-i. Ota, *Electrochimica Acta*, 49 (2004) 3479-3485.
- [43] Jin-Hwan Kim, Akimitsu Ishihara, Shigenori Mitsushima, Nobuyuki Kamiya, K.-i. Ota, *Chem. Lett.*, 36 (2007) 514.
- [44] J.-H. Kim, A. Ishihara, S. Mitsushima, N. Kamiya, K.-i. Ota, *Electrochemistry*, 75 (2007) 166-168.
- [45] S. Shimada, *Solid State Ionics*, 141-142 (2001) 99-104.
- [46] S. Shimada, M. Johnsson, S. Urbonaitė, *Thermochimica Acta*, 419 (2004) 143-148.

- [47] A. Ishihara, Y. Shibata, S. Mitsushima, K. Ota, *Journal of The Electrochemical Society*, 155 (2008) B400-B406.
- [48] A. Ishihara, M. Tamura, K. Matsuzawa, S. Mitsushima, K.-i. Ota, *Journal of Fuel Cell Science and Technology*, 8 (2011) 031005-031006.
- [49] A. Ishihara, K. Lee, S. Doi, S. Mitsushima, N. Kamiya, M. Hara, K. Domen, K. Fukuda, K.-i. Ota, *Electrochemical and Solid-State Letters*, 8 (2005) A201-A203.
- [50] Y. Shibata, A. Ishihara, S. Mitsushima, N. Kamiya, K.-i. Ota, *Electrochemical and Solid-State Letters*, 10 (2007) B43-B46.
- [51] A. Ishihara, S. Doi, S. Mitsushima, K.-i. Ota, *Electrochimica Acta*, 53 (2008) 5442-5450.
- [52] A.I. Yoshiro Ohgi, Yohei Shibata, Shigenori Mitsushima and Ken-ichiro Ota, *Chemistry Letters*, 37 (2008) 608.
- [53] S. Doi, A. Ishihara, S. Mitsushima, N. Kamiya, K.-i. Ota, *Journal of The Electrochemical Society*, 154 (2007) B362-B369.
- [54] Y. Maekawa, A. Ishihara, J.-H. Kim, S. Mitsushima, K.-i. Ota, *Electrochemical and Solid-State Letters*, 11 (2008) B109-B112.
- [55] G. Liu, H.M. Zhang, M.R. Wang, H.X. Zhong, J. Chen, *J. Power Sources*, 172 (2007) 503-510.
- [56] K.D. Nam, A. Ishihara, K. Matsuzawa, S. Mitsushima, K.-i. Ota, *Electrochemical and Solid-State Letters*, 12 (2009) B158-B160.
- [57] J. Shim, C.-R. Lee, H.-K. Lee, J.-S. Lee, E.J. Cairns, *J. Power Sources*, 102 (2001) 172-177.
- [58] C. Di Valentin, E. Finazzi, G. Pacchioni, A. Selloni, S. Livraghi, M.C. Paganini, E. Giamello, *Chemical Physics*, 339 (2007) 44-56.
- [59] E. Martínez-Ferrero, Y. Sakatani, C. Boissière, D. Grosso, A. Fuertes, J. Fraxedas, C. Sanchez, *Advanced Functional Materials*, 17 (2007) 3348-3354.
- [60] W.L. Wang, O. Savadogo, Z.F. Ma, *International Journal of Hydrogen Energy*, 37 (2012) 7405-7417.
- [61] W. Wang, O. Savadogo, Z.-F. Ma, *Journal of Applied Electrochemistry*, 42 (2012) 857-866.

- [62] J.K. Nørskov, *Progress in Surface Science*, 38 (1991) 103-144.
- [63] B. Hammer, J.K. Nørskov, *Surface Science*, 343 (1995) 211-220.
- [64] M. Mavrikakis, B. Hammer, J.K. Nørskov, *Physical Review Letters*, 81 (1998) 2819-2822.
- [65] A. Nilsson, L.G.M. Pettersson, B. Hammer, T. Bligaard, C.H. Christensen, J.K. Nørskov, *Catalysis Letters*, 100 (2005) 111-114.
- [66] J.K. Nørskov, F. Abild-Pedersen, F. Studt, T. Bligaard, *Proceedings of the National Academy of Sciences*, 108 (2011) 937-943.
- [67] J.K. Nørskov, T. Bligaard, J. Rossmeisl, C.H. Christensen, *Nat Chem*, 1 (2009) 37-46.
- [68] J.R. Kitchin, J.K. Nørskov, M.A. Barteau, J.G. Chen, *The Journal of Chemical Physics*, 120 (2004) 10240-10246.
- [69] M. Lynch, P. Hu, *Surface Science*, 458 (2000) 1-14.
- [70] A. Michaelides, P. Hu, *J. Am. Chem. Soc.*, 123 (2001) 4235-4242.
- [71] A. Michaelides, P. Hu, *The Journal of Chemical Physics*, 114 (2001) 513-519.
- [72] R.A. Sidik, A.B. Anderson, *Journal of Electroanalytical Chemistry*, 528 (2002) 69-76.
- [73] Z. Shi, J. Zhang, Z.-S. Liu, H. Wang, D.P. Wilkinson, *Electrochimica Acta*, 51 (2006) 1905-1916.
- [74] L. Ou, F. Yang, Y. Liu, S. Chen, *The Journal of Physical Chemistry C*, 113 (2009) 20657-20665.
- [75] Z. Yang, J. Wang, X. Yu, *Physics Letters A*, 374 (2010) 4713-4717.
- [76] Z. Yang, J. Wang, X. Yu, *Chem. Phys. Lett.*, 499 (2010) 83-88.
- [77] I. Matanović, F.H. Garzon, N.J. Henson, *The Journal of Physical Chemistry C*, 115 (2011) 10640-10650.
- [78] L. Wang, J.I. Williams, T. Lin, C.-J. Zhong, *Catalysis Today*, 165 (2011) 150-159.
- [79] W. Xu, D. Cheng, M. Niu, X. Shao, W. Wang, *Electrochimica Acta*, 76 (2012) 440-445.
- [80] Y. Xu, M. Mavrikakis, *The Journal of Physical Chemistry B*, 107 (2003) 9298-9307.
- [81] X. Liu, C. Meng, Y. Han, *The Journal of Physical Chemistry C*, 117 (2013) 1350-1357.

- [82] X. Liu, L. Li, C. Meng, Y. Han, *The Journal of Physical Chemistry C*, 116 (2011) 2710-2719.
- [83] F. Fouda-Onana, O. Savadogo, *Electrochimica Acta*, 54 (2009) 1769-1776.
- [84] F. Fouda-Onana, S. Bah, O. Savadogo, *Journal of Electroanalytical Chemistry*, 636 (2009) 1-9.
- [85] E. Vayner, R.A. Sidik, A.B. Anderson, B.N. Popov, *The Journal of Physical Chemistry C*, 111 (2007) 10508-10513.
- [86] Y. Okamoto, *Appl. Surf. Sci.*, 255 (2008) 3434-3441.
- [87] L. Li, Z. Wei, S. Chen, X. Qi, W. Ding, M. Xia, R. Li, K. Xiong, Z. Deng, Y. Gao, *Chem. Phys. Lett.*, 539–540 (2012) 89-93.
- [88] X. Chen, F. Li, X. Wang, S. Sun, D. Xia, *The Journal of Physical Chemistry C*, 116 (2012) 12553-12558.
- [89] W. Orellana, *Chem. Phys. Lett.*, 541 (2012) 81-84.
- [90] S. Sun, N. Jiang, D. Xia, *The Journal of Physical Chemistry C*, 115 (2011) 9511-9517.
- [91] G. Kresse, J. Hafner, *Physical Review B*, 47 (1993) 558-561.
- [92] G. Kresse, J. Hafner, *Physical Review B*, 49 (1994) 14251-14269.
- [93] G. Kresse, J. Furthmuller, *Computational Materials Science*, 6 (1996) 15-50.
- [94] G. Kresse, J. Furthmuller, *Physical Review B*, 54 (1996) 11169-11186.
- [95] P.E. Blochl, *Physical Review B*, 50 (1994) 17953-17979.
- [96] G. Kresse, D. Joubert, *Physical Review B*, 59 (1999) 1758-1775.
- [97] J.P. Perdew, K. Burke, M. Ernzerhof, *Physical Review Letters*, 77 (1996) 3865-3868.
- [98] J.P. Perdew, K. Burke, M. Ernzerhof, *Physical Review Letters*, 78 (1997) 1396-1396.
- [99] L.P.B. Lima, J.A. Diniz, I. Doi, J. Godoy Fo, *Microelectronic Engineering*, 92 (2012) 86-90.
- [100] F. Fillot, T. Morel, S. Minoret, I. Matko, S. Maîtrejean, B. Guillaumot, B. Chenevier, T. Billon, *Microelectronic Engineering*, 82 (2005) 248-253.

## CHAPTER 8 GENERAL DISCUSSION

According to the objectives of this project, finding a stable and active alternative to the commercially used Pt/C electro-catalyst for the oxygen reduction reaction (ORR) was the main goal of this research. In this regards, titanium oxy-nitride ( $\text{TiO}_x\text{N}_y$ ) was produced by a new urea-based sol-gel method (simply called U method) as a non-noble electro-catalyst for the ORR. A comprehensive comparison between four different sol-gel methods was carried out to evaluate the physicochemical and electrochemical properties of the produced electro-catalysts.

In the first section, it has been shown that the  $\text{TiO}_x\text{N}_y$  produced by the U method, had more nitrogen — and consequently titanium nitride — in its structure than the  $\text{TiO}_x\text{N}_y$  produced by the other sol-gel methods, under a similar heat treatment condition. So that, the TiN characteristic peaks in XRD results of the samples prepared by the U method were obvious even at low temperature heat treatments (700 °C), while for the samples prepared by the other methods these peaks were considerable just after a heat treatment at a high temperature (1100 °C). Heat treatment showed a key role in determining the titanium nitride to titanium oxide ratio. For instance, based on the EDS elemental analysis nitrogen percentage in the bulk material of the sample produced by the U method increased from 9 to 24 percent by increasing the temperature from 700 to 1100 °C, while the oxygen percentage was decreasing inversely. In addition, crystallite size of the samples prepared by the U method was almost in the same range of the TiN crystallite size (20 to 40 nm), but the crystallite size of the samples prepared by the other sol-gel methods was in the same range of the  $\text{TiO}_2$  crystallite size (40 to 60 nm). Furthermore, at low temperature the phase transfer took place from anatase to rutile titanium oxide. So that, the lattice parameters ( $a = 4.5668$  and  $c = 2.0117$  Ang) were consistent with those of the rutile  $\text{TiO}_2$  for the sample prepared at 700 °C. While, at higher temperatures (900 and 1100 °C) there was another phase transfer from the tetragonal rutile structure to the cubic TiN structure with lattice parameters ( $a = 4.4782$  and  $c = 4.9578$  Ang) in consistent with the reference pure titanium nitride. Comparing the XRD results of the samples prepared by the in-situ and ex-situ using of the urea as a reagent, revealed that, although, increasing the temperature to 1100 °C led to the characteristic peaks of TiN appearing in ex-situ method as well, the calculated lattice parameters had a more tetragonal anatase structure than a cubic one. Therefore, it was evident that the in-situ urea-based method was more efficient than the other sol-gel methods for preparing titanium oxy-nitride with a high quantity of titanium nitride.

In the second part, other physicochemical properties of the prepared samples such as morphology, particle size and surface area were acquired. SEM images indicated that the particle size was completely dependent on the preparation method and calcination temperature. For instance, for the samples prepared by the U method, particle size was less than 200 nm, and by increasing the temperature it was even reduced to 20-40 nm. But, for the samples prepared by the other sol-gel methods it was bigger than 250 nm and in some cases it went rise to 800 nm. This factor greatly affected the amount of the surface area. Having a very high B.E.T. surface area ( $93.5132 \text{ m}^2/\text{g}$ ) with the U method was a consequence of the particles that were too small.

Evaluating the electrochemical properties of the prepared electro-catalysts and their catalytic activity toward the ORR was another objective of this project. In this regard, in the third part, cyclic voltammetry (CV), polarization, and electrochemical impedance spectroscopy (EIS) techniques were used. According to the slow scan voltammetry with scan rate of 5 mV/s and polarization curves, Tafel slope, exchange current density and onset potential for the oxygen reduction reaction on different samples were obtained. Based on these information, the electro-catalyst prepared by the U method which was annealed at 1100 °C, showed the best catalytic activity among all other samples. Its Tafel slope, exchange current density and onset potential were -203 mV/decade,  $4\text{E-}04 \text{ mA/mg}$  and close to 0.8 volt vs. NHE, respectively. Although the samples prepared by the U method had generally bigger exchange current density and smaller Tafel slope, its big advantage to the other sol-gel methods was a much higher onset potential amount. EIS measurements also supported the assertion that this electro-catalyst had the best catalytic activity. In fact it was shown that this sample had the biggest specific capacitance ( $\sim 3.3 \text{ F/g}$ ) — which was in accordance with B.E.T. result — and also the lowest charge transfer resistance.

In the next part of this project, ICP-TOF-MS was used to evaluate the chemical and electrochemical stability of the prepared electro-catalysts under the PEMFC working condition. Heretofore, measuring the dissolved metal concentration by ICP-TOF-MS was done just to evaluate its chemical stability. However, in this project this technique was used also during the CV, to evaluate the electro-catalyst's electrochemical stability as well, which was more realistic and similar to the PEMFC's working condition. The sample with the best catalytic activity (prepared by the U method) showed a less stability than the others, probably because of its much higher surface area. Nevertheless, its stability was better than the commercially used Pt/C electro-

catalyst, both chemically and electrochemically. Dissolved titanium concentration in 10 mM sulfuric acid at 50 °C and after 24 hours was less than 0.1 % of its amount at the beginning, while this amount for the commercial Pt/C electro-catalyst was around 0.15 %. This amount under a harsh oxidation condition (potential more than 2 volts vs. NHE) and after 100 cyclic voltammetry, was less than 0.2 % for our best electro-catalyst, indicating its high electrochemical stability, as well. Because, after the oxidation at the high potential the catalytic activity of the electro-catalyst was decreased via increasing the Tafel Slope and decreasing the exchange current density, its surface change was evaluated by the XPS before and after the oxidation. XPS revealed that there was a surface change from titanium nitride to titanium oxide. So that nitrogen amount on the surface decreased from 11 % before the oxidation to 5 % after the oxidation. Thus, decreasing the titanium nitride's amount in the titanium oxy-nitride surface reduced its catalytic activity.

In the other part of this project, titanium nitride's activity toward the ORR was studied theoretically. For this purpose, Vienna *ab initio* Simulation Package (VASP) based on the density functional theory (DFT) was used to follow the ORR in three sequential steps: oxygen adsorption, hydroxide production and water desorption. Two different facets of the titanium nitride, TiN(111) and TiN(200) were considered as the catalyst surfaces with different possible adsorption sites. First of all, all adsorption energies were calculated to reveal which surface with which adsorption site was more favorable for the oxygen and hydroxide adsorption. Although oxygen adsorption on both surfaces was very strong and dissociative — stronger than the oxygen adsorption on the Pt(111) —, TiN(111) showed a stronger adsorption. Produced hydroxide on the TiN(111) was very stable and consequently disinclined to react with another proton to produce water. In the other word, TiN(111) surface became poisoned very soon by strong adsorption of the hydroxide species. But, TiN(200) was a favorable surface for production and desorption of water. Analysis of the adsorption energies also showed that the bridge site on the TiN(200) was more active than the top site on this surface for the ORR. Then, some fundamental properties of the surfaces such as d-band center and d-band fractional filling were obtained from the electron density of states (DOS). Considering two possible bridge and top adsorption sites on the TiN(200), these information indicated the hydroxide production and water desorption as the rate determining steps for the ORR in bridge and top sites, respectively. Therefore, it is been revealed

that the TiN, specially TiN(200) had a catalytic activity for the ORR, and losing this material from the titanium oxy-nitride's surface causes diminishing of the catalytic activity.

In the last part, effect of the mixing titanium with another transition metal was investigated. In this regard, titanium and tantalum oxy-nitride was produced by the U method. Increasing the Ta concentration led to have a higher onset potential but lower ORR current density. For instance, the onset potential for the ORR for pure tantalum oxy-nitride heat treated at 700 °C was ca. 0.85 V vs. NHE while this value was ca. 0.65 V vs. NHE for pure titanium oxy-nitride. However, the ORR current was 100 times smaller in tantalum oxy-nitride, probably because of the low electrochemical active surface area. Electrochemical measurements suggested that an appropriate composition of titanium and tantalum was required to have both a good onset potential and ORR current density by improving the catalytic activity and increasing the active surface area and electrical conductivity.

In summary, in-situ urea-based sol-gel method provided a titanium oxy-nitride with fairly high amount of titanium nitride at relatively lower temperature than the previous works. This electro-catalyst showed more stability than the commercially used Pt/C electro-catalyst, both chemically and electrochemically. Besides a very high surface area it had better catalytic activity than the electro-catalysts produced by the other sol-gel methods. Also, titanium nitride, specially TiN(200) was discovered as an active surface for the ORR. This work might be considered as the starting point in developing a stable and active titanium oxy-nitride at low temperature and consequently low cost for PEMFC applications, with a quantum chemistry computation sight.

## CONCLUSIONS AND RECOMMENDATIONS

### Conclusions:

According to the objectives of this thesis, the results show that titanium and tantalum oxy-nitrides were produced by a new introduced in-situ urea-based sol-gel method. This method showed that it is possible to produce transition metal oxy-nitrides with high quantity of nitrogen at fairly low time and temperature. However, there is a need to study the effect of the effective parameters in sol-gel method such as ratio of nitrogen source and metal source, ratio of solution and metal precursor, and also heat treatment duration and type of the nitridizing gas.

Later, physicochemical characterizations proved the existence of significant amount of titanium nitride in titanium oxy-nitride structure and the effect of heat treatment on this quantity. Electrochemical characterizations also showed the effect of this high amount of titanium nitride on the activity of the electro-catalyst for the ORR. In general, it was deduced that the sample heat treated at the highest temperature is the sample which content the highest titanium nitride and which exhibit the highest surface area and the highest catalytic activity. Then, its chemical and electrochemical stability showed a better stability than the commercially used Pt/C electro-catalyst. However, catalytic activity of our produced titanium oxy-nitride was not comparable to that of the platinum or platinum based electro-catalysts. But its better chemical and electrochemical stability is a promising point to continue the research on these types of materials.

Finally, ab initio simulation showed that the TiN(200) was an active surface for the ORR, but TiN(111) in spite of a very strong and dissociative oxygen adsorption was not. It revealed that on the TiN(200), for the bridge site, which was the most favorable adsorption site, producing the hydroxide was the rate determining step, while for the top site water desorption was the rate determining step. Although this theoretical study gave us a fundamental understanding of the oxygen reduction reaction on the surface of titanium nitride, it is necessary to do more investigations to be able to figure out what is exactly happening on this surface. Specially, if we are looking for to understand the reaction steps on the surface of a more complex system such as titanium oxy-nitride, we have to study this reaction on titanium oxide, and also a mixture of titanium oxide and titanium nitride as well. In this project, effect of the surrounding species on the surface such as water and oxygen molecules was not considered, however it is recommended for the future studies that these species also be involved in the reaction.

## Recommendations

At the end, as a recommendation for the future works, it is suggested to:

- 1) Make *ab initio* computation on  $\text{TiO}_2$  surface (on the most common structure obtained from XRD on this thesis);
- 2) Determine the role of the precursor on the electro-catalyst composition;
- 3) Determine the relation between the surface chemical composition and the onset potential;
- 4) Prepare MEA (Membrane electrode assembly) based on various titanium-oxy-nitrides electro-catalysts and characterize them in a single PEMFC cell;
- 5) Make correlation between the PEMFC performances, the electrochemical data and the *ab initio* computation parameters;
- 6) Evaluate the titanium oxy-nitride as a support for the commercially used Pt based electro-catalysts instead of the carbon, certainly because of its better stability, catalytic activity and also its high surface area.

## LIST OF REFERENCES

- [1] S. M. Haile, "Fuel cell materials and components," *Acta Materialia*, vol. 51, pp. 5981-6000, 2003.
- [2] U. S. D. o. Energy. (2011). *Types of Fuel Cells*:  
[http://www1.eere.energy.gov/hydrogenandfuelcells/fuelcells/fc\\_types.html#pem](http://www1.eere.energy.gov/hydrogenandfuelcells/fuelcells/fc_types.html#pem).  
Available:  
[http://www1.eere.energy.gov/hydrogenandfuelcells/fuelcells/fc\\_types.html#pem](http://www1.eere.energy.gov/hydrogenandfuelcells/fuelcells/fc_types.html#pem)
- [3] W. Xiong, *et al.*, "3-D Carbon Nanotube Structures Used as High Performance Catalyst for Oxygen Reduction Reaction," *Journal of the American Chemical Society*, vol. 132, pp. 15839-15841, 2010.
- [4] J. Zhao and A. Manthiram, "In Situ Electrochemical Characterization of Proton Exchange Membrane Fuel Cells Fabricated with Pd--Pt--Ni Cathode Catalysts," *Journal of The Electrochemical Society*, vol. 158, pp. B208-B214, 2011.
- [5] A. Ishihara, *et al.*, "Partially Oxidized Tantalum Carbonitrides as a New Nonplatinum Cathode for PEFC--1," *Journal of The Electrochemical Society*, vol. 155, pp. B400-B406, 2008.
- [6] Y. Tang, *et al.*, "Carbon-supported Pd-Pt cathode electrocatalysts for proton exchange membrane fuel cells," *Journal of Power Sources*, vol. In Press, Corrected Proof, 2011.
- [7] A. Ishihara, *et al.*, "Tantalum (oxy)nitrides prepared using reactive sputtering for new nonplatinum cathodes of polymer electrolyte fuel cell," *Electrochimica Acta*, vol. 53, pp. 5442-5450, 2008.
- [8] S. Doi, *et al.*, "Zirconium-Based Compounds for Cathode of Polymer Electrolyte Fuel Cell," *Journal of The Electrochemical Society*, vol. 154, pp. B362-B369, 2007.
- [9] W.-J. Chou, *et al.*, "Corrosion resistance of ZrN films on AISI 304 stainless steel substrate," *Surface and Coatings Technology*, vol. 167, pp. 59-67, 2003.
- [10] A. Ishihara, *et al.*, "Tantalum Oxynitride for a Novel Cathode of PEFC," *Electrochemical and Solid-State Letters*, vol. 8, pp. A201-A203, 2005.
- [11] Y. Maekawa, *et al.*, "Catalytic Activity of Zirconium Oxynitride Prepared by Reactive Sputtering for ORR in Sulfuric Acid," *Electrochemical and Solid-State Letters*, vol. 11, pp. B109-B112, 2008.
- [12] K. D. Nam, *et al.*, "Partially Oxidized Niobium Carbonitride as Non-Platinum Cathode for PEFC," *Electrochemical and Solid-State Letters*, vol. 12, pp. B158-B160, 2009.
- [13] G. Selvarani, *et al.*, "A PEFC With Pt--TiO<sub>2</sub>/C as Oxygen-Reduction Catalyst," *Journal of Fuel Cell Science and Technology*, vol. 8, pp. 021003-8, 2011.
- [14] J. Larminie and A. Dicks, *Fuel Cell Systems Explained*: John Wiley & Sons, Ltd, 2000.
- [15] R. O'Hayre, *et al.*, *Fuel Cell Fundamentals*: John Wiley & Sons, INC, 2006.
- [16] S. Basu, *Recent Trends in Fuel Cell Science and Technology*. New Dehli, India: Springer, 2007.

- [17] J. Zhang, *et al.*, "Effects of hot pressing conditions on the performances of MEAs for direct methanol fuel cells," *Journal of Power Sources*, vol. 165, pp. 73-81, 2007.
- [18] N. Rajalakshmi and K. S. Dhathathreyan, "Catalyst layer in PEMFC electrodes—Fabrication, characterisation and analysis," *Chemical Engineering Journal*, vol. 129, pp. 31-40, 2007.
- [19] M.S. Wilson and S. Gottesfeld, "High performance catalyzed membranes of ultra-low Pt loadings for polymer electrolyte fuel cells," *J Electrochem Soc*, vol. 139, p. L28, 1992.
- [20] M. S. Wilson and S. Gottesfeld, "Thin-film catalyst layers for polymer electrolyte fuel cell electrodes," *Journal of Applied Electrochemistry*, vol. 22, pp. 1-7, 1992/01/01 1992.
- [21] G. S. Kumar, *et al.*, "High performance electrodes with very low platinum loading for polymer electrolyte fuel cells," *Electrochimica Acta*, vol. 40, pp. 285-290, 1995.
- [22] D. Bevers, *et al.*, "Innovative production procedure for low cost PEFC electrodes and electrode/membrane structures," *International Journal of Hydrogen Energy*, vol. 23, pp. 57-63, 1998.
- [23] E. J. Taylor, *et al.*, "Preparation of High-Platinum Utilization Gas Diffusion Electrodes for Proton Exchange Membrane Fuel Cells," *Journal of The Electrochemical Society*, vol. 139, pp. L45-L46, May 1, 1992 1992.
- [24] P. S. Fedkiw and W. H. Her, "An Impregnation-Reduction Method to Prepare Electrodes on Nafion SPE," *Journal of The Electrochemical Society*, vol. 136, pp. 899-900, March 1, 1989 1989.
- [25] E. Gülzow, *et al.*, "Dry layer preparation and characterisation of polymer electrolyte fuel cell components," *Journal of Power Sources*, vol. 86, pp. 352-362, 2000.
- [26] H. Liu, *et al.*, "A review of anode catalysis in the direct methanol fuel cell," *Journal of Power Sources*, vol. 155, pp. 95-110, 2006.
- [27] J. Zhang, *PEM Fuel Cell Electrocatalysts and Catalyst Layers, Fundamentals and Applications*. Canada: Springer, 2008.
- [28] I. EG&G Technical Services, *Fuel Cell Handbook*, Seventh Edition ed. West Virginia: U.S. Department of Energy, 2004.
- [29] S. von Kraemer, *et al.*, "Gas Diffusion Electrodes and Membrane Electrode Assemblies Based on a Sulfonated Polysulfone for High-Temperature PEMFC," *Journal of The Electrochemical Society*, vol. 153, pp. A2077-A2084, November 1, 2006 2006.
- [30] M. A. Hickner, *et al.*, "Alternative Polymer Systems for Proton Exchange Membranes (PEMs)," *Chemical Reviews*, vol. 104, pp. 4587-4612, 2004/10/01 2004.
- [31] Q. Li, *et al.*, "Approaches and Recent Development of Polymer Electrolyte Membranes for Fuel Cells Operating above 100 °C," *Chemistry of Materials*, vol. 15, pp. 4896-4915, 2003/12/01 2003.
- [32] E. A. Ticianelli, *et al.*, "Methods to Advance Technology of Proton Exchange Membrane Fuel Cells," *Journal of The Electrochemical Society*, vol. 135, pp. 2209-2214, September 1, 1988 1988.

- [33] M. S. Wilson and S. Gottesfeld, "High Performance Catalyzed Membranes of Ultra-low Pt Loadings for Polymer Electrolyte Fuel Cells," *Journal of The Electrochemical Society*, vol. 139, pp. L28-L30, February 1, 1992 1992.
- [34] G. Sasikumar, *et al.*, "Dependence of optimum Nafion content in catalyst layer on platinum loading," *Journal of Power Sources*, vol. 132, pp. 11-17, 2004.
- [35] J. M. Song, *et al.*, "Optimal composition of polymer electrolyte fuel cell electrodes determined by the AC impedance method," *Journal of Power Sources*, vol. 94, pp. 78-84, 2001.
- [36] M. M. P. Janssen and J. Moolhuysen, "Binary systems of platinum and a second metal as oxidation catalysts for methanol fuel cells," *Electrochimica Acta*, vol. 21, pp. 869-878, 1976.
- [37] T. J. Schmidt, *et al.*, "On the CO tolerance of novel colloidal PdAu/carbon electrocatalysts," *Journal of Electroanalytical Chemistry*, vol. 501, pp. 132-140, 2001.
- [38] H. A. Gasteiger, *et al.*, "H<sub>2</sub> and CO Electrooxidation on Well-Characterized Pt, Ru, and Pt-Ru. 2. Rotating Disk Electrode Studies of CO/H<sub>2</sub> Mixtures at 62 .degree.C," *The Journal of Physical Chemistry*, vol. 99, pp. 16757-16767, 1995/11/01 1995.
- [39] M. R. Andrew, *et al.*, "Electrolytes for methanol-air fuel cells. I. The performance of methanol electro-oxidation catalysts in sulphuric acid and phosphoric acid electrolytes," *Journal of Applied Electrochemistry*, vol. 7, pp. 153-160, 1977/03/01 1977.
- [40] P. N. Ross, *et al.*, "Electrocatalysis on binary alloys: I. Oxidation of molecular hydrogen on supported Pt-Rh alloys," *Journal of Electroanalytical Chemistry and Interfacial Electrochemistry*, vol. 59, pp. 177-189, 1975.
- [41] B. N. Grgur, *et al.*, "Electrooxidation of H<sub>2</sub>/CO Mixtures on a Well-Characterized Pt<sub>75</sub>Mo<sub>25</sub> Alloy Surface," *The Journal of Physical Chemistry B*, vol. 101, pp. 3910-3913, 1997/05/01 1997.
- [42] B. N. Grgur, *et al.*, "Electrooxidation of H<sub>2</sub>, CO and H<sub>2</sub>/CO mixtures on a well-characterized Pt-Re bulk alloy electrode and comparison with other Pt binary alloys," *Electrochimica Acta*, vol. 43, pp. 3631-3635, 1998.
- [43] A. Morozan, *et al.*, "Low-platinum and platinum-free catalysts for the oxygen reduction reaction at fuel cell cathodes," *Energy & Environmental Science*, vol. 4, pp. 1238-1254, 2011.
- [44] B. Wang, "Recent development of non-platinum catalysts for oxygen reduction reaction," *Journal of Power Sources*, vol. 152, pp. 1-15, 2005.
- [45] V. P. Zhdanov and B. Kasemo, "Kinetics of electrochemical O<sub>2</sub> reduction on Pt," *Electrochemistry Communications*, vol. 8, pp. 1132-1136, 2006.
- [46] J. K. Nørskov, *et al.*, "Origin of the Overpotential for Oxygen Reduction at a Fuel-Cell Cathode," *The Journal of Physical Chemistry B*, vol. 108, pp. 17886-17892, 2004/11/01 2004.
- [47] Z. Shi, *et al.*, "Current status of ab initio quantum chemistry study for oxygen electroreduction on fuel cell catalysts," *Electrochimica Acta*, vol. 51, pp. 1905-1916, 2006.

- [48] A. J. Bard and L. R. Faulkner, *Electrochemical Methods: Fundamentals and Applications*, 2nd eddition ed.: John Wiley & Sons, Inc., 2001.
- [49] A. Parthasarathy, *et al.*, "Temperature Dependence of the Electrode Kinetics of Oxygen Reduction at the Platinum/Nafion[registered sign] Interface---A Microelectrode Investigation," *Journal of The Electrochemical Society*, vol. 139, pp. 2530-2537, 1992.
- [50] Y. Gochi-Ponce, *et al.*, "Synthesis and electrochemical characterization of a novel platinum chalcogenide electrocatalyst with an enhanced tolerance to methanol in the oxygen reduction reaction," *Electrochemistry Communications*, vol. 8, pp. 1487-1491, 2006.
- [51] Z. Xie and S. Holdcroft, "Polarization-dependent mass transport parameters for orr in perfluorosulfonic acid ionomer membranes: an EIS study using microelectrodes," *Journal of Electroanalytical Chemistry*, vol. 568, pp. 247-260, 2004.
- [52] M. Itagaki, *et al.*, "Electroreduction mechanism of oxygen investigated by electrochemical impedance spectroscopy," *Journal of Electroanalytical Chemistry*, vol. 557, pp. 59-73, 2003.
- [53] A. M. Dhirde, *et al.*, "Equivalent Electric Circuit Modeling and Performance Analysis of a PEM Fuel Cell Stack Using Impedance Spectroscopy," *Energy Conversion, IEEE Transactions on*, vol. 25, pp. 778-786, 2010.
- [54] X.-Z. Yuan, *et al.*, *Electrochemical Impedance Spectroscopy in PEM Fuel Cells: Fundamentals and Applications*. London: Springer, 2010.
- [55] M. E. Orazem and B. Tribollet, *Electrochemical Impedance Spectroscopy*. NJ: Wiley, 2008.
- [56] V. F. Lvovich, *Impedance Spectroscopy : Applications to Electrochemical and Dielectric Phenomena*. NJ: Wiley, 2012.
- [57] A. Stassi, *et al.*, "Electrocatalytic behaviour for oxygen reduction reaction of small nanostructured crystalline bimetallic Pt-M supported catalysts," *Journal of Applied Electrochemistry*, vol. 36, pp. 1143-1149, 2006/10/01 2006.
- [58] C. M. Sánchez-Sánchez, *et al.*, "Imaging Structure Sensitive Catalysis on Different Shape-Controlled Platinum Nanoparticles," *Journal of the American Chemical Society*, vol. 132, pp. 5622-5624, 2010.
- [59] C. Koenigsmann, *et al.*, "Size-Dependent Enhancement of Electrocatalytic Performance in Relatively Defect-Free, Processed Ultrathin Platinum Nanowires," *Nano Letters*, vol. 10, pp. 2806-2811, 2010.
- [60] H.-W. Liang, *et al.*, "Ultrathin Te Nanowires: An Excellent Platform for Controlled Synthesis of Ultrathin Platinum and Palladium Nanowires/Nanotubes with Very High Aspect Ratio," *Advanced Materials*, vol. 21, pp. 1850-1854, 2009.
- [61] Z. Chen, *et al.*, "Supportless Pt and PtPd Nanotubes as Electrocatalysts for Oxygen-Reduction Reactions," *Angewandte Chemie International Edition*, vol. 46, pp. 4060-4063, 2007.

- [62] J. Zhang, *et al.*, "Controlling the Catalytic Activity of Platinum-Monolayer Electrocatalysts for Oxygen Reduction with Different Substrates," *Angewandte Chemie International Edition*, vol. 44, pp. 2132-2135, 2005.
- [63] W.-P. Zhou, *et al.*, "Improving Electrocatalysts for O<sub>2</sub> Reduction by Fine-Tuning the Pt-Support Interaction: Pt Monolayer on the Surfaces of a Pd<sub>3</sub>Fe(111) Single-Crystal Alloy," *Journal of the American Chemical Society*, vol. 131, pp. 12755-12762, 2009.
- [64] M. B. Vukmirovic, *et al.*, "Platinum monolayer electrocatalysts for oxygen reduction," *Electrochimica Acta*, vol. 52, pp. 2257-2263, 2007.
- [65] J. Zhang, *et al.*, "Mixed-Metal Pt Monolayer Electrocatalysts for Enhanced Oxygen Reduction Kinetics," *Journal of the American Chemical Society*, vol. 127, pp. 12480-12481, 2005.
- [66] V. R. Stamenkovic, *et al.*, "Trends in electrocatalysis on extended and nanoscale Pt-bimetallic alloy surfaces," *Nat Mater*, vol. 6, pp. 241-247, 2007.
- [67] U. A. Paulus, *et al.*, "Oxygen Reduction on Carbon-Supported Pt-Ni and Pt-Co Alloy Catalysts," *The Journal of Physical Chemistry B*, vol. 106, pp. 4181-4191, 2002.
- [68] J. Yang, *et al.*, "Carbon-Supported Pseudo-Core-Shell Pd-Pt Nanoparticles for ORR with and Without Methanol," *Journal of The Electrochemical Society*, vol. 155, pp. B776-B781, 2008.
- [69] Z.-M. Zhou, *et al.*, "Durability study of Pt-Pd/C as PEMFC cathode catalyst," *International Journal of Hydrogen Energy*, vol. 35, pp. 1719-1726, 2010.
- [70] W. He, *et al.*, "Simple preparation of Pd-Pt nanoalloy catalysts for methanol-tolerant oxygen reduction," *Journal of Power Sources*, vol. 195, pp. 1046-1050, 2010.
- [71] W. Wang, *et al.*, "One-step synthesis of carbon-supported Pd-Pt alloy electrocatalysts for methanol tolerant oxygen reduction," *Electrochemistry Communications*, vol. 10, pp. 1396-1399, 2008.
- [72] V. R. Stamenkovic, *et al.*, "Improved Oxygen Reduction Activity on Pt<sub>3</sub>Ni(111) via Increased Surface Site Availability," *Science*, vol. 315, pp. 493-497, January 26, 2007
- [73] H. Wu, *et al.*, "Pt<sub>1-x</sub>Co<sub>x</sub> nanoparticles as cathode catalyst for proton exchange membrane fuel cells with enhanced catalytic activity," *Materials Chemistry and Physics*, vol. 124, pp. 841-844, 2010.
- [74] P. Mani, *et al.*, "Dealloyed Pt-Cu Core-Shell Nanoparticle Electrocatalysts for Use in PEM Fuel Cell Cathodes," *The Journal of Physical Chemistry C*, vol. 112, pp. 2770-2778, 2008.
- [75] G. Gupta, *et al.*, "Highly Stable and Active Pt-Cu Oxygen Reduction Electrocatalysts Based on Mesoporous Graphitic Carbon Supports," *Chemistry of Materials*, vol. 21, pp. 4515-4526, 2009.
- [76] M. Wakisaka, *et al.*, "Increased Oxygen Coverage at Pt-Fe Alloy Cathode for the Enhanced Oxygen Reduction Reaction Studied by EC-XPS," *The Journal of Physical Chemistry C*, vol. 112, pp. 2750-2755, 2008.

- [77] D.-H. Lim, *et al.*, "Effect of ceria nanoparticles into the Pt/C catalyst as cathode material on the electrocatalytic activity and durability for low-temperature fuel cell," *Applied Catalysis B: Environmental*, vol. 94, pp. 85-96, 2010.
- [78] K. H. Lee, *et al.*, "Synthesis and characterization of nanostructured PtCo-CeO<sub>x</sub>/C for oxygen reduction reaction," *Journal of Power Sources*, vol. 185, pp. 871-875, 2008.
- [79] V. Mazumder, *et al.*, "Core/Shell Pd/FePt Nanoparticles as an Active and Durable Catalyst for the Oxygen Reduction Reaction," *Journal of the American Chemical Society*, vol. 132, pp. 7848-7849, 2010.
- [80] J. Kim, *et al.*, "Structurally Ordered FePt Nanoparticles and Their Enhanced Catalysis for Oxygen Reduction Reaction," *Journal of the American Chemical Society*, vol. 132, pp. 4996-4997, 2010.
- [81] L. M. Vracar, *et al.*, "Palladium Electrode in Oxygen-Saturated Aqueous Solutions," *Journal of The Electrochemical Society*, vol. 133, pp. 1835-1839, 1986.
- [82] M. Tarasevich, *et al.*, "Corrosion stability of nanosize Pd/C, PdCo/C, and PdCoCr/C catalytic systems in acidic media for fuel cell cathodes," *Protection of Metals and Physical Chemistry of Surfaces*, vol. 45, pp. 782-786, 2009.
- [83] A. Sarkar, *et al.*, "Low cost Pd-W nanoalloy electrocatalysts for oxygen reduction reaction in fuel cells," *Journal of Materials Chemistry*, vol. 19, pp. 159-165, 2009.
- [84] F. Fouda-Onana and O. Savadogo, "Study of O<sub>2</sub> and OH adsorption energies on Pd-Cu alloys surface with a quantum chemistry approach," *Electrochimica Acta*, vol. 54, pp. 1769-1776, 2009.
- [85] F. Fouda-Onana, *et al.*, "Palladium-copper alloys as catalysts for the oxygen reduction reaction in an acidic media I: Correlation between the ORR kinetic parameters and intrinsic physical properties of the alloys," *Journal of Electroanalytical Chemistry*, vol. 636, pp. 1-9, Nov 2009.
- [86] N. N. Kariuki, *et al.*, "Colloidal Synthesis and Characterization of Carbon-Supported Pd-Cu Nanoparticle Oxygen Reduction Electrocatalysts," *Chemistry of Materials*, vol. 22, pp. 4144-4152, 2010.
- [87] C. Xu, *et al.*, "Nanotubular Mesoporous PdCu Bimetallic Electrocatalysts toward Oxygen Reduction Reaction," *Chemistry of Materials*, vol. 21, pp. 3110-3116, 2009.
- [88] Y.-C. Yeh, *et al.*, "Pd-C-Fe Nanoparticles Investigated by X-ray Absorption Spectroscopy as Electrocatalysts for Oxygen Reduction," *Chemistry of Materials*, vol. 21, pp. 4030-4036, 2009.
- [89] J. Guo, *et al.*, "Improving Oxygen Reduction Reaction Activities on Carbon-Supported Ag Nanoparticles in Alkaline Solutions," *The Journal of Physical Chemistry C*, vol. 114, pp. 4324-4330, 2010.
- [90] J. Zhang, *et al.*, "Stabilization of Platinum Oxygen-Reduction Electrocatalysts Using Gold Clusters," *Science*, vol. 315, pp. 220-222, January 12, 2007 2007.
- [91] L. Demarconay, *et al.*, "Electroreduction of dioxygen (ORR) in alkaline medium on Ag/C and Pt/C nanostructured catalysts--effect of the presence of methanol," *Electrochimica Acta*, vol. 49, pp. 4513-4521, 2004.

- [92] H. Tributsch, *et al.*, "Methanol-resistant cathodic oxygen reduction catalysts for methanol fuel cells," *Journal of Applied Electrochemistry*, vol. 31, pp. 739-748, 2001.
- [93] R. Otero, *et al.*, "Tailoring surface electronic states via strain to control adsorption: O/Cu/Ru(0 0 0 1)," *Surface Science*, vol. 550, pp. 65-72, 2004.
- [94] J. D. Stiehl, *et al.*, "Formation of Molecularly Chemisorbed Oxygen on TiO<sub>2</sub>-Supported Gold Nanoclusters and Au(111) from Exposure to an Oxygen Plasma Jet," *The Journal of Physical Chemistry B*, vol. 109, pp. 6316-6322, 2005.
- [95] J. L. Fernández, *et al.*, "Thermodynamic Guidelines for the Design of Bimetallic Catalysts for Oxygen Electoreduction and Rapid Screening by Scanning Electrochemical Microscopy. M-Co (M: Pd, Ag, Au)," *Journal of the American Chemical Society*, vol. 127, pp. 357-365, 2004.
- [96] A. H. C. Sirk, *et al.*, "Oxygen Reduction by Sol Derived [Co, N, C, O]-Based Catalysts for Use in Proton Exchange Membrane Fuel Cells," *Electrochemical and Solid-State Letters*, vol. 8, pp. A104-A107, 2005.
- [97] R. Bashyam and P. Zelenay, "A class of non-precious metal composite catalysts for fuel cells," *Nature*, vol. 443, pp. 63-66, 2006.
- [98] M. Lefèvre, *et al.*, "Iron-Based Catalysts with Improved Oxygen Reduction Activity in Polymer Electrolyte Fuel Cells," *Science*, vol. 324, pp. 71-74, April 3, 2009 2009.
- [99] N. A. Vante and H. Tributsch, "Energy conversion catalysis using semiconducting transition metal cluster compounds," *Nature*, vol. 323, pp. 431-432, 1986.
- [100] K. Lee, *et al.*, "Ternary non-noble metal chalcogenide (W-Co-Se) as electrocatalyst for oxygen reduction reaction," *Electrochemistry Communications*, vol. 9, pp. 1704-1708, 2007.
- [101] T. Oh, *et al.*, "Effects of tungsten oxide addition on the electrochemical performance of nanoscale tantalum oxide-based electrocatalysts for proton exchange membrane (PEM) fuel cells," *Journal of Power Sources*, vol. 196, pp. 6099-6103, 2011.
- [102] A. Ishihara, *et al.*, "Tantalum oxide-based compounds as new non-noble cathodes for polymer electrolyte fuel cell," *Electrochimica Acta*, vol. 55, pp. 7581-7589, 2010.
- [103] Y. Liu, *et al.*, "Transition Metal Oxides as DMFC Cathodes Without Platinum," *Journal of The Electrochemical Society*, vol. 154, pp. B664-B669, 2007.
- [104] J.-H. Kim, *et al.*, "Catalytic activity of titanium oxide for oxygen reduction reaction as a non-platinum catalyst for PEFC," *Electrochimica Acta*, vol. 52, pp. 2492-2497, 2007.
- [105] Y. Liu, *et al.*, "Zirconium Oxide for PEFC Cathodes," *Electrochemical and Solid-State Letters*, vol. 8, pp. A400-A402, 2005.
- [106] Y. Takasu, *et al.*, "Oxygen reduction behavior of RuO<sub>2</sub>/Ti, IrO<sub>2</sub>/Ti and IrM (M: Ru, Mo, W, V) Ox/Ti binary oxide electrodes in a sulfuric acid solution," *Electrochemistry Communications*, vol. 10, pp. 668-672, 2008.
- [107] N. Yoshinaga, *et al.*, "Oxygen reduction behavior of rutile-type iridium oxide in sulfuric acid solution," *Electrochimica Acta*, vol. 54, pp. 566-573, 2008.

- [108] Y. Takasu, *et al.*, "Oxygen reduction characteristics of several valve metal oxide electrodes in HClO<sub>4</sub> solution," *Electrochimica Acta*, vol. 55, pp. 8220-8229, 2010.
- [109] M. Nie, *et al.*, "A study of oxygen reduction on improved Pt-WC/C electrocatalysts," *Journal of Power Sources*, vol. 162, pp. 173-176, 2006.
- [110] F. Jaouen and J.-P. Dodelet, "Average turn-over frequency of O<sub>2</sub> electro-reduction for Fe/N/C and Co/N/C catalysts in PEFCs," *Electrochimica Acta*, vol. 52, pp. 5975-5984, 2007.
- [111] Y. Shibata, *et al.*, "Effect of Heat Treatment on Catalytic Activity for Oxygen Reduction Reaction of TaOxNy/Ti Prepared by Electrophoretic Deposition," *Electrochemical and Solid-State Letters*, vol. 10, pp. B43-B46, 2007.
- [112] Y. Ohgi, *et al.*, "Zirconium Oxide-Based Compound as New Cathode Without Platinum Group Metals for PEFC," *Journal of The Electrochemical Society*, vol. 157, pp. B885-B891, 2010.
- [113] M. Pattabi, *et al.*, "Electrochemical characterization of tungsten carbonyl compound for oxygen reduction reaction," *International Journal of Hydrogen Energy*, vol. 26, pp. 171-174, 2001.
- [114] K. Lee, *et al.*, "Stability and electrocatalytic activity for oxygen reduction in WC + Ta catalyst," *Electrochimica Acta*, vol. 49, pp. 3479-3485, 2004.
- [115] C. Z. Deng and M. J. Dignam, "Sputtered Cobalt-Carbon-Nitrogen Thin Films as Oxygen Reduction Electrocatalysts," *Journal of The Electrochemical Society*, vol. 145, pp. 3513-3520, 1998.
- [116] S. V. Mentus, "Oxygen reduction on anodically formed titanium dioxide," *Electrochimica Acta*, vol. 50, pp. 27-32, 2004.
- [117] E. G. a. D. P. V.B. Baez, "The reduction of oxygen on titanium oxide electrodes," *J. Electroanal. Chem.*, vol. 340 p. 273, 1992.
- [118] J. Y. Kim, *et al.*, "A novel non-platinum group electrocatalyst for PEM fuel cell application," *International Journal of Hydrogen Energy*, vol. 36, pp. 4557-4564, 2011.
- [119] J. Ribeiro, *et al.*, "Morphological and electrochemical investigation of RuO<sub>2</sub>-Ta<sub>2</sub>O<sub>5</sub> oxide films prepared by the Pechini-Adams method," *Journal of Applied Electrochemistry*, vol. 38, pp. 767-775, 2008.
- [120] H.-R. Chen, *et al.*, "Annealing effect on the performance of RuO<sub>2</sub>-Ta<sub>2</sub>O<sub>5</sub>/Ti electrodes for use in supercapacitors," *Materials Chemistry and Physics*, vol. 125, pp. 652-655, 2011.
- [121] B. R. Limoges, *et al.*, "Electrocatalyst materials for fuel cells based on the polyoxometalates [PMo(12 - n)VnO<sub>40</sub>](3 + n)- (n = 0-3)," *Electrochimica Acta*, vol. 50, pp. 1169-1179, 2005.
- [122] W. Sun, *et al.*, "Carbon-supported tetragonal MnOOH catalysts for oxygen reduction reaction in alkaline media," *Journal of Power Sources*, vol. 196, pp. 627-635, 2011.

- [123] A. Ishihara, *et al.*, "Partially Oxidized Tantalum Carbonitride as New Cathodes Without Platinum Group Metals for Polymer Electrolyte Fuel Cell," *Journal of Fuel Cell Science and Technology*, vol. 8, pp. 031005-6, 2011.
- [124] S. T. Oyama, "Preparation and catalytic properties of transition metal carbides and nitrides," *Catalysis Today*, vol. 15, pp. 179-200, 1992.
- [125] C. Angelkort, *et al.*, "Formation of tantalum nitride films by rapid thermal processing," *Thin Solid Films*, vol. 437, pp. 108-115, 2003.
- [126] K. Baba and R. Hatada, "Synthesis and properties of tantalum nitride films formed by ion beam assisted deposition," *Surface and Coatings Technology*, vol. 84, pp. 429-433, 1996.
- [127] S. Boughaba, *et al.*, "Synthesis of tantalum pentoxide films by pulsed laser deposition: material characterization and scale-up," *Thin Solid Films*, vol. 358, pp. 104-113, 2000.
- [128] M. Kerlau, *et al.*, "Synthesis of crystallized TaON and Ta<sub>3</sub>N<sub>5</sub> by nitridation of Ta<sub>2</sub>O<sub>5</sub> thin films grown by pulsed laser deposition," *Solid State Sciences*, vol. 6, pp. 101-107, 2004.
- [129] Y. Makino, *et al.*, "Characterization of Ti(N<sub>x</sub>O<sub>y</sub>) coatings produced by the arc ion plating method," *Surface and Coatings Technology*, vol. 98, pp. 934-938, 1998.
- [130] D. M. Hoffman, "Chemical vapour deposition of nitride thin films," *Polyhedron*, vol. 13, pp. 1169-1179, 1994.
- [131] F. Fabreguette, *et al.*, "Temperature and substrate influence on the structure of TiN<sub>x</sub>O<sub>y</sub> thin films grown by low pressure metal organic chemical vapour deposition," *Surface and Coatings Technology*, vol. 125, pp. 396-399, 2000.
- [132] J. Guillot, *et al.*, "Phase mixture in MOCVD and reactive sputtering TiO<sub>x</sub>N<sub>y</sub> thin films revealed and quantified by XPS factorial analysis," *Acta Materialia*, vol. 54, pp. 3067-3074, 2006.
- [133] M. Ritala, *et al.*, "Controlled Growth of TaN, Ta<sub>3</sub>N<sub>5</sub>, and TaO<sub>x</sub>N<sub>y</sub> Thin Films by Atomic Layer Deposition," *Chemistry of Materials*, vol. 11, pp. 1712-1718, 1999.
- [134] G. Brauer and J. R. Weidlein, "Synthesis and Properties of Tantalum Oxide Nitride, TaON," *Angewandte Chemie International Edition in English*, vol. 4, pp. 875-875, 1965.
- [135] M. Stavrev, *et al.*, "Crystallographic and morphological characterization of reactively sputtered Ta, TaN and TaNO thin films," *Thin Solid Films*, vol. 307, pp. 79-88, 1997.
- [136] I. Ayerdi, *et al.*, "Characterization of tantalum oxynitride thin films as high-temperature strain gauges," *Sensors and Actuators A: Physical*, vol. 46, pp. 218-221.
- [137] V. Zhabrev, *et al.*, "The effect of thermal treatment on the structure of tantalum oxide films grown on titanium," *Technical Physics Letters*, vol. 30, pp. 396-398, 2004.
- [138] S. Venkataraj, *et al.*, "Towards understanding the superior properties of transition metal oxynitrides prepared by reactive DC magnetron sputtering," *Thin Solid Films*, vol. 502, pp. 228-234, 2006.
- [139] J. M. Mwabora, *et al.*, "Structure, Composition, and Morphology of Photoelectrochemically Active TiO<sub>2</sub>-xN<sub>x</sub> Thin Films Deposited by Reactive DC

- Magnetron Sputtering," *The Journal of Physical Chemistry B*, vol. 108, pp. 20193-20198, 2004.
- [140] F. Vaz, *et al.*, "Preparation of magnetron sputtered TiN<sub>x</sub>O<sub>y</sub> thin films," *Surface and Coatings Technology*, vol. 174-175, pp. 197-203.
- [141] K. Mauritz, "Sol-Gel Chemistry."
- [142] K. H. J. Buschow, *et al.*, "Encyclopedia of Materials - Science and Technology, Volumes 1-11," Elsevier, pp. 1090-1095.
- [143] K. Kamiya, *et al.*, "Preparation of TiO<sub>2</sub> fibres by hydrolysis and polycondensation of Ti(O—C<sub>3</sub>H<sub>7</sub>)<sub>4</sub>," *Journal of Materials Science Letters*, vol. 5, pp. 402-404, 1986.
- [144] I. Ichinose, *et al.*, "A Surface Sol–Gel Process of TiO<sub>2</sub> and Other Metal Oxide Films with Molecular Precision," *Chemistry of Materials*, vol. 9, pp. 1296-1298, 1997.
- [145] M. Fang, *et al.*, "Surface Sol–gel Synthesis of Ultrathin Titanium and Tantalum Oxide Films," *Journal of Nanoparticle Research*, vol. 1, pp. 43-49, 1999.
- [146] M. Niederberger, *et al.*, "Benzyl Alcohol and Titanium Tetrachloride A Versatile Reaction System for the Nonaqueous and Low-Temperature Preparation of Crystalline and Luminescent Titania Nanoparticles," *Chemistry of Materials*, vol. 14, pp. 4364-4370, 2002.
- [147] G. Garnweitner, *et al.*, "Nonaqueous synthesis of crystalline anatase nanoparticles in simple ketones and aldehydes as oxygen-supplying agents," *Chemical Communications*, pp. 397-399, 2005.
- [148] M. A. Worsley, *et al.*, "Route to high surface area TiO<sub>2</sub>/C and TiCN/C composites," *Journal of Materials Chemistry*, vol. 19, pp. 7146-7150, 2009.
- [149] W. R. Matizamhuka, *et al.*, "Synthesis, sintering and characterisation of TaON materials," *Ceramics International*, vol. 34, pp. 1481-1486, 2008.
- [150] N. P. Bansal, "Low-temperature synthesis, pyrolysis and crystallization of tantalum oxide gels," *Journal of Materials Science*, vol. 29, pp. 5065-5070, 1994.
- [151] F. Z. Tepehan, *et al.*, "Optical properties of sol-gel dip-coated Ta<sub>2</sub>O<sub>5</sub> films for electrochromic applications," *Solar Energy Materials and Solar Cells*, vol. 59, pp. 265-275, 1999.
- [152] Y. Shin, *et al.*, "Controlled deposition of covalently bonded tantalum oxide on carbon supports by solvent evaporation sol-gel process," *Surface Science*, vol. 603, pp. 2290-2293, 2009.
- [153] A. Cappellani, *et al.*, "Processing and characterisation of sol-gel deposited Ta<sub>2</sub>O<sub>5</sub> and TiO<sub>2</sub>-Ta<sub>2</sub>O<sub>5</sub> dielectric thin films," *Solid-State Electronics*, vol. 43, pp. 1095-1099, 1999.
- [154] C. Arnould, *et al.*, "Fabrication of tantalum oxide/carbon nanotubes thin film composite on titanium substrate," *Journal of Colloid and Interface Science*, vol. 344, pp. 390-394, 2010.

- [155] C. Arnould, *et al.*, "Titanium modified with layer-by-layer sol-gel tantalum oxide and an organodiphosphonic acid: A coating for hydroxyapatite growth," *Journal of Colloid and Interface Science*, vol. 336, pp. 497-503, 2009.
- [156] J. Buha, *et al.*, "Thermal Transformation of Metal Oxide Nanoparticles into Nanocrystalline Metal Nitrides Using Cyanamide and Urea as Nitrogen Source," *Chemistry of Materials*, vol. 19, pp. 3499-3505, 2007.
- [157] E. Orhan, *et al.*, "Synthesis and energetics of yellow TaON," *Solid State Sciences*, vol. 4, pp. 1071-1076, 2002.
- [158] Y. Kurokawa, *et al.*, "Preparation of refractory nitride fibers by thermal decomposition of transition metal (Ti, Nb) alkoxide-cellulose precursor gel fibers in NH<sub>3</sub> atmosphere," *Journal of Materials Science*, vol. 36, pp. 301-306, 2001.
- [159] K. Kamiya, *et al.*, "Nitridation of TiO<sub>2</sub> fibres prepared by the sol-gel method," *Journal of Materials Science*, vol. 22, pp. 937-941, 1987.
- [160] K. Kohno, "Nitridation of the sol-gel derived TiO<sub>2</sub> coating films and the infrared ray reflection," *Journal of Materials Science*, vol. 27, pp. 658-660, 1992.
- [161] M. A. Centeno, *et al.*, "Catalytic combustion of volatile organic compounds on gold/titanium oxynitride catalysts," *Applied Catalysis B: Environmental*, vol. 61, pp. 177-183, 2005.
- [162] Z. Wu, *et al.*, "Visible light induced electron transfer process over nitrogen doped TiO<sub>2</sub> nanocrystals prepared by oxidation of titanium nitride," *Journal of Hazardous Materials*, vol. 157, pp. 57-63, 2008.
- [163] H. Zhang, *et al.*, "Preparation of titanium nitride ultrafine powders by sol-gel and microwave carbothermal reduction nitridation methods," *Ceramics International*, vol. 35, pp. 1071-1075, 2009.
- [164] A. Gomathi and C. N. R. Rao, "Nanostructures of the binary nitrides, BN, TiN, and NbN, prepared by the urea-route," *Materials Research Bulletin*, vol. 41, pp. 941-947, 2006.
- [165] C. Giordano, *et al.*, "Metal Nitride and Metal Carbide Nanoparticles by a Soft Urea Pathway," *Chemistry of Materials*, vol. 21, pp. 5136-5144, 2009.
- [166] A. W. Jackson, *et al.*, "Amorphous and nanocrystalline titanium nitride and carbonitride materials obtained by solution phase ammonolysis of Ti(NMe<sub>2</sub>)<sub>4</sub>," *Journal of Solid State Chemistry*, vol. 179, pp. 1383-1393, 2006.
- [167] A. W. Jackson and A. L. Hector, "A nonoxidic sol-gel route to titanium nitride and carbonitride films by primary aminecondensation," *Journal of Materials Chemistry*, vol. 17, pp. 1016-1022, 2007.
- [168] I.-s. Kim and P. N. Kumta, "Hydrazide sol-gel process: A novel approach, for synthesizing nanostructured titanium nitride," *Materials Science and Engineering B*, vol. 98, pp. 123-134, 2003.
- [169] F. Jensen, *Introduction to Computational Chemistry*. England: John Wiley & Sons Ltd, 2007.

- [170] R. M. Martin, *Electronic Structure: Basic Theory and Practical Methods*. Cambridge: Cambridge University Press, 2004.
- [171] I. B. BERSUKER, *Electronic Structure and Properties of Transition Metal Compounds: Introduction to the Theory*. New Jersey: John Wiley & Sons, INC., 2010.
- [172] E. Engel and R. M. Dreizler, *Density Functional Theory: An Advanced Course*. New York: Springer, 2011.
- [173] E. Engel and R. M. Dreizler, *Density Functional Theory (an advanced course)* Verlag Berlin Heidelberg: Springer, 2011.
- [174] S. Basri, *et al.*, "Nanocatalyst for direct methanol fuel cell (DMFC)," *International Journal of Hydrogen Energy*, vol. 35, pp. 7957-7970, 2010.
- [175] P. Hohenberg and W. Kohn, "Inhomogeneous Electron Gas," *PHYSICAL REVIEW*, vol. 136, p. B 864, 9 November 1964 1964.
- [176] W. Kohn and L. J. Sham, "Self-Consistent Equations Including Exchange and Correlation Effects," *Physical Review*, vol. 140, pp. A1133-A1138, 1965.
- [177] S. H. Vosko, *et al.*, "Accurate spin-dependent electron liquid correlation energies for local spin density calculations: a critical analysis," *Canadian Journal of Physics*, vol. 58, pp. 1200-1211, 1980/08/01 1980.
- [178] J. P. Perdew and Y. Wang, "Accurate and simple analytic representation of the electron-gas correlation energy," *Physical Review B*, vol. 45, pp. 13244-13249, 1992.
- [179] A. D. Becke, "Density-functional exchange-energy approximation with correct asymptotic behavior," *Physical Review A*, vol. 38, p. 3098, 1988.
- [180] Wikipedia. (14 August 2011). *List of quantum chemistry and solid state physics software*. Available: [http://en.wikipedia.org/wiki/List\\_of\\_quantum\\_chemistry\\_and\\_solid\\_state\\_physics\\_software](http://en.wikipedia.org/wiki/List_of_quantum_chemistry_and_solid_state_physics_software)
- [181] G. Kresse and J. Hafner, "ABINITIO MOLECULAR-DYNAMICS FOR LIQUID-METALS," *Physical Review B*, vol. 47, pp. 558-561, Jan 1993.
- [182] G. Kresse and J. Hafner, "AB-INITIO MOLECULAR-DYNAMICS SIMULATION OF THE LIQUID-METAL AMORPHOUS-SEMICONDUCTOR TRANSITION IN GERMANIUM," *Physical Review B*, vol. 49, pp. 14251-14269, May 1994.
- [183] G. Kresse and J. Furthmuller, "Efficiency of ab-initio total energy calculations for metals and semiconductors using a plane-wave basis set," *Computational Materials Science*, vol. 6, pp. 15-50, Jul 1996.
- [184] G. Kresse and J. Furthmuller, "Efficient iterative schemes for ab initio total-energy calculations using a plane-wave basis set," *Physical Review B*, vol. 54, pp. 11169-11186, Oct 1996.
- [185] P. E. Blochl, "PROJECTOR AUGMENTED-WAVE METHOD," *Physical Review B*, vol. 50, pp. 17953-17979, Dec 1994.
- [186] G. Kresse and D. Joubert, "From ultrasoft pseudopotentials to the projector augmented-wave method," *Physical Review B*, vol. 59, pp. 1758-1775, Jan 1999.

- [187] J. P. Perdew, *et al.*, "Generalized gradient approximation made simple," *Physical Review Letters*, vol. 77, pp. 3865-3868, Oct 1996.
- [188] J. P. Perdew, *et al.*, "Generalized gradient approximation made simple (vol 77, pg 3865, 1996)," *Physical Review Letters*, vol. 78, pp. 1396-1396, Feb 1997.
- [189] P. J. Feibelman and D. R. Hamann, "Electronic Structure of a "Poisoned" Transition-Metal Surface," *Physical Review Letters*, vol. 52, pp. 61-64, 1984.
- [190] P. J. Feibelman and D. R. Hamann, "Modification of transition metal electronic structure by P, S, Cl, and Li adatoms," *Surface Science*, vol. 149, pp. 48-66, 1985.
- [191] L. M. Falicov and G. A. Somorjai, "Correlation between catalytic activity and bonding and coordination number of atoms and molecules on transition metal surfaces: Theory and experimental evidence," *Proceedings of the National Academy of Sciences of the United States of America*, vol. 82, pp. 2207-2211, 1985.
- [192] W. Yang and R. G. Parr, "Hardness, softness, and the Fukui function in the electronic theory of metals and catalysis," *Proceedings of the National Academy of Sciences of the United States of America*, vol. 82, pp. 6723-6726, 1985.
- [193] J. Harris and S. Andersson, "H<sub>2</sub> Dissociation at Metal Surfaces," *Physical Review Letters*, vol. 55, pp. 1583-1586, 1985.
- [194] B. Hammer and J. K. Nørskov, "Electronic factors determining the reactivity of metal surfaces," *Surface Science*, vol. 343, pp. 211-220, 1995.
- [195] J. R. Kitchin, *et al.*, "Modification of the surface electronic and chemical properties of Pt(111) by subsurface 3d transition metals," *The Journal of Chemical Physics*, vol. 120, pp. 10240-10246, 2004.
- [196] A. Nilsson, *et al.*, "The electronic structure effect in heterogeneous catalysis," *Catalysis Letters*, vol. 100, pp. 111-114, 2005/04/01 2005.
- [197] J. K. Nørskov, *et al.*, "Density functional theory in surface chemistry and catalysis," *Proceedings of the National Academy of Sciences*, vol. 108, pp. 937-943, January 18, 2011.